THE UNIVERSITY *of* EDINBURGH

Engineering synucleinopathy-resistant human dopaminergic neurons by CRISPR-mediated mutation of the *SNCA* gene

Yixi Chen

Doctor of Philosophy

The University of Edinburgh

2020

Acknowledgements

First of all, I would like to express my gratitude towards my supervisor Dr Tilo Kunath, for shaping my research career since my MSc and for arranging my PhD funding which made this work possible. I am immensely thankful for his support and guidance throughout.

I would like to thank all members of Kunath lab, especially Dr Karamjit Singh Dolt, for the invaluable support during CRISPR targeting. I am thankful to Dr Maurice Canham, who trained me for the dopaminergic differentiation and help me with SNP analysis. I am grateful to Nicola Drummond for her persistent support in differentiation and always taking care of the lab. I would also like to thank Dr Stephen West, Ammar Natalwala, Craig Leighton, Sophie Glendinning, Dr Catarina Dias, Dr Fergus McWhinnie and Dr David McNay, for constructive comments and discussions.

I am thankful to the facilities staff at the Centre for Regenerative Medicine, especially to Dr Bertrand Vernay and Dr Matthieu Vermeren for numerous supports in imaging and analysis, and to Dr Fiona Rossi and Dr Claire Cryer for training and support in flow cytometry.

I would like to thank Dr Marco Kriek and Dr Terry Baker of UCB Pharma Ltd. and Dr Patrick Downey of UCB BioPharma Sprl. for the fruitful collaboration and the production of α-Syn PFFs. I would like to thank Dr Natalie Homer and Dr Joanna Simpson, without whom the dopamine UPLC-MS/MS experiment would not have been possible. I am grateful to Dr Marti Colom Cadena and Prof Tara Spires-Jones for their help with the synaptic staining analysis, and to Dr Graham Robertson and Dr Michele Zagnoni for their support in calcium imaging and analysis.

I am thankful to my thesis committee members, Prof Susan Rosser, Dr Abdenour Soufi and Prof Tara Spires-Jones for their support and encouragement throughout my PhD. I am grateful to the Centre of Mammalian Synthetic Biology for funding my PhD and organising academic development workshops, which I found very helpful.

I am grateful to my Mum and Dad, who support my interests and are always there for me. Finally, I would like to thank my boyfriend Dr Abhishek Gupta for keeping me sane and supporting me in all possible ways.

Abstract

An experimental treatment for Parkinson's disease (PD) involved the transplantation of fetal midbrain tissue, a source of midbrain dopaminergic (mDA) progenitors, into the striatum of patients to restore dopaminergic innervation. Although clinical benefits were experienced by some patients, this heterogeneous and scarce source of tissue is not sustainable. Recently, mDA progenitors differentiated from human embryonic stem cells (hESCs) and induced pluripotent stem cells (iPSCs) are comparably potent and efficient as fetal midbrain tissue in rescuing dopaminergic deficits in PD animal models and clinical trials using this cell product are progressing. However, the hESC/hiPSC-derived mDA grafts are still susceptible to the development of Lewy body pathology, as found in clinical trials using fetal tissues. The clinical benefits of the fetal grafts reduced in correlation with the accumulation of Lewy body pathology, therefore, a pathology-resistant graft would be longer-lasting and beneficial to patients. For *in vitro* modelling of Lewy body pathology, which is an inclusion pathology mainly consist of misfolded α-Synuclein (α-Syn) aggregates, I treated hESC-derived mDA neurons with α-Syn pre-formed fibrils (PFFs). PFFs recruit endogenous α-Syn to form Lewy body-like aggregates which are positive for phospho-serine 129 α-Syn (pS129-αSyn), ubiquitin and p62. The PFF models also recapitulate other aspects of PD, such as synaptic and mitochondrial dysfunction, neuroinflammation and neurodegeneration. Since endogenous α-Syn is essential for the development of aggregates, I attempted to produce pathology-resistant neurons by knocking out α-Syn (*SNCA*) in hESCs with CRISPR/Cas9n and subsequently differentiating the $SNCA^{+/-}$ and $SNCA^{-/-}$ hESCs into mDA neurons. As α-Syn might play physiological roles which are not yet fully elucidated, I created a single amino acid (S87E) mutation in α-Syn, aiming to reduce α-Syn aggregation without disruption of α-Syn physiological functions. Half of the resulting CRISPR-engineered $SNCA^{+/-}$, $SNCA^{-/-}$ and $SNCA^{S87E/S87E}$ hESC clones exhibited normal genomic integrity, free from detectable copy number variations (CNVs), large copy-neutral loss of heterozygosity (CN-LOH), off-target events and integration of targeting plasmids. Subsequently, mDA neurons were differentiated from $SNCA^{+/-}$, $SNCA^{-/-}$ and $SNCA^{S87E/S87E}$ hESCs and they highly resembled mDA neurons derived from WT parental hESCs based on marker analysis and RNAseq. This data suggested that the α-Syn mutations, as well as the selection and cloning process, did not impair mDA differentiation. Synapse formation, spontaneous

activities and dopamine secretion were readily observed in mDA neurons of all tested genotypes. The WT mDA neurons treated with PFFs recapitulated pS129-αSyn pathology, but did not result in detectable cell death or significant impairment of synapse formation, mitochondrial morphology or spontaneous neuronal activities within the timeframe of the current study. *SNCA*$^{+/-}$, *SNCA*$^{-/-}$ and *SNCA*$^{S87E/S87E}$ mDA neurons treated with PFFs revealed that *SNCA*$^{+/-}$ exhibited significantly less, while *SNCA*$^{-/-}$ showed no pS129-αSyn pathology and *SNCA*$^{S87E/S87E}$ exhibited a reduced level of pathology compared to WT mDA neurons. The PFF-treated hESC-derived mDA neuron model established in this study could be used as an effective platform for drug screening. In addition, *SNCA*$^{+/-}$ and *SNCA*$^{-/-}$ hESC-derived cells could be valuable cell models for studying the physiological role of α-Syn. On the condition of satisfactory validation in animal models, *SNCA*$^{+/-}$ and *SNCA*$^{-/-}$ hESC-derived mDA progenitors would have significant potential in cell replacement therapy for PD.

Lay Summary

In cell replacement therapy for Parkinson's disease (PD), the scarce and inconsistent embryo-derived tissues are now being replaced by sustainable and reliable laboratory grown cells. Transplantable midbrain dopaminergic (mDA) progenitors can be produced from human embryonic stem cells (hESCs) or induced pluripotent stem cells (iPSCs). However, they are still susceptible to the development of Lewy body pathology, the hallmark of PD, which was observed in the clinical trials using embryo-derived tissues. To generate disease resistant grafts, I targeted the main component of Lewy body, a misfolded protein named α-Synuclein (α-Syn). Endogenous α-Syn is essential for the formation of Lewy body-like pathology, therefore, I generated α-Syn deficient hESCs by removing the α-Syn gene, *SNCA*, in order to produce disease resistant grafts. As α-Syn might play physiological roles which are not yet fully understood, I substituted a single amino acid (S87) in α-Syn with the one that is predicted to reduce the level of pathology (E87), aiming to provide resistance without disruption of α-Syn physiological functions. mDA neurons were subsequently produced from these α-Syn mutant hESCs and tested for susceptibility to the Lewy body-like pathology using a seeding model. The results showed that S87E substitution in α-Syn conveyed some resistance, while partial removal of α-Syn (*SNCA*$^{+/-}$) resulted in considerable resistance and complete removal of α-Syn (*SNCA*$^{-/-}$) resulted in full resistance to Lewy body-like pathology in this model. Provided they exhibit satisfactory performance in animal models, mDA cells produced from *SNCA*$^{+/-}$ and *SNCA*$^{-/-}$ hESCs could be longer-lasting novel cell products for PD cell replacement therapy.

Table of Contents

List of Figures

List of Tables

List of Abbreviations

5’ UTR	5’ untranslated region
6-OHDA	6-hydroxydopamine
AA	ascorbic acid
AADC	aromatic amino acid decarboxylase
AAV	adeno-associated virus
BARHL1	BarH like homeobox 1
BBB	blood-brain barrier
BDNF	brain-derived neurotrophic factor
BMP	bone morphogenic protein
CAD	catecholaminergic neuron-like
Cas9n	Cas9-D10A
CHIR	CHIR99021
CN-LOH	copy-neutral loss of heterozygosity
CNS	central nervous system
CNV	copy number variation
COL1A1	collagen type I alpha 1
CSPα	cysteine string protein α
DAPT	N-[N-(3,5-difluorophenacetyl)-l-alanyl]-S-phenylglycine t-butyl
DAT	dopamine transporter
db-cAMP	dibutyryl cyclic AMP
DBS	deep brain stimulation
DLB	dementia with Lewy bodies
DOPAC	3,4-dihydroxyphenylacetic acid
DSB	double-strand break

EN1	engrailed-1
FACS	fluorescence-activated cell sorting
FCCP	carbonyl cyanide 4-(trifluoromethoxy)phenylhydrazone
FDR	false discovery rate
FGF	fibroblast growth factor
FIAU	1-(2-deoxy-2-fluoro-1-β-D-arabinofuranosyl)-5-iodouracil
FOXA2	forkhead box protein A2, or hepatocyte nuclear factor 3-beta (HNF-3B)
GAD	glutamic acid decarboxylase
GBX2	gastrulation brain homeobox 2
GDNF	glial cell line-derived neurotrophic factor
GID	graft-induced dyskinesia
GMP	good manufacturing practice
gRNA	guide RNA
GSK3β	glycogen synthase kinase 3β
HA	homology arm
HDR	homology directed repair
hESC	human embryonic stem cell
hfVM	human fetal ventral midbrain
hiPSC	human induces pluripotent stem cell
HSPG	heparin sulfate proteoglycan
HVA	homovanillic acid
IAP	integrin-associated protein, or CD47
L-Glu	L-glutamate
LAG3	lymphocyte-activation gene 3
LAMP1	lysosomal markers l ysosomal-associated membrane protein 1

LAMP2	lysosomal markers l ysosomal-associated membrane protein 2
LDH	lactate dehydrogenase
LDN	LDN193189
LMX1A	LIM homeobox transcription factor 1α
LRTM1	leucine-rich repeat and transmembrane domain-containing protein 1
mDA	midbrain dopaminergic
MEAs	microelectrode arrays
mEPSC	miniature excitatory postsynaptic currents
MHC	major histocompatibility complex class
mIPSC	miniature inhibitory postsynaptic currents
MPTP	1-methyl-4-phenyl-1,2,3,6-tetrahydropyridine
NAC	hydrophobic non-amyloid component
NDM	Neural Differentiation Medium
NGS	next generation sequencing
NHEJ	non-homologous end-joining
NIM	Neural Induction Medium
NPM	Neural Patterning Medium
NURR1	nuclear receptor subfamily 4, group A, member 2 (NR4A2)
OCT4	octamer-binding transcription factor 4, or POU5F1
OTX2	orthodenticle homeobox 2
p62	ubiquitin-binding protein p62, or sequestosome 1 (SQSTM1)
PAM	protospacer adjacent motif
PCA	principal component analysis
PD	Parkinson’s disease
PDGFRα	platelet-derived growth factor receptor α

PFF	pre-formed fibril
poly-O	poly-ornithine
pS129-αSyn	phospho-serine129 α-Syn
PSD95	post-synaptic density protein 95
ROI	regions of interest
RT-qPCR	reverse transcription quantitative PCR
SB	SB431542
SDS-PAGE	sodium dodecyl sulphate-polyacrylamide gel electrophoresis
sEPSC	spontaneous excitatory postsynaptic currents
SHH	Sonic Hedgehog
siRNA	small-interfering RNA
SIX3	SIX homeobox 3
SN	*substantia nigra*
SNAP25	synaptosome associated protein 25
SNP	single nucleotide polymorphism
SOX6	SRY-box transcription factor 6
T7E1	T7 endonuclease 1
TBP	TATA-binding protein
TGF-β	transforming growth factor β
TH	tyrosine hydroxylase
ThT	Thioflavin T
UPL	Universal Probe Library
UPLC-MS/MS	ultra-performance liquid chromatography with tandem mass spectrometer
VAMP2	vesicle-associated membrane protein 2
VEEV	Venezuelan equine encephalitis virus

VLMCs	vascular and leptomeningeal cells
VMAT2	vesicular monoamine transporter 2
WNV	West Nile virus
WT	wildtype
α-Syn	α-Synuclein

Chapter 1: Introduction

1.1. Parkinson's disease (PD) and loss of *substantia nigra* neurons

Parkinson's disease (PD) is the second most common neurodegenerative disease, estimated to be affecting 6.1 million people worldwide in 2016 (Dorsey et al., 2018) and 145,000 people in UK alone in 2018 (Parkinson's UK, 2018). First described as the 'shaking palsy' by James Parkinson in 1817 (Parkinson, 1817), PD is characterised by motor symptoms such as tremor and rigidity, as well as non-motor symptoms including pain, sleep disorder and dementia (Jankovic, 2008). Neuropathologically, PD patients have an excessive loss of midbrain dopaminergic (mDA) neurons which originate in *substantia nigra* (SN) *pars compacta* (Tretiakoff, 1919). The mDA neurons innervate the dorsal striatum, where they release the neurotransmitter dopamine that is critical for the modulation of motor activities. This population of DA neurons (A9) is relatively vulnerable in PD compared to A10 DA neurons which originate from ventral tegmental area (Pacelli et al., 2015). At the onset of motor symptoms in PD patients, around 60% of mDA neurons in the SN *pars compacta* are lost, along with a ~80% depletion of the striatal dopamine content (Dauer and Przedborski, 2003).

The primary treatment for PD is the medication levodopa, a precursor of dopamine (Barbeau, 1969; Birkmayer and Hornykiewicz, 1961). Although levodopa provides marked symptomatic relief to early-stage patients, it induces complications such as dyskinesia and wears off after several years of administration (Barbeau, 1969; Obeso et al., 2000). In addition, systemic administration of levodopa does not mimic the natural dopamine release and does not work solely at the site of mDA neuronal loss. Another popular therapy is deep brain stimulation (DBS) by implanting electrodes in the pallidum or subthalamic nucleus (Benabid, 2003). The electrodes are connected to a neuro-pacemaker which generate pulses that disrupt abnormal neuronal activities. DBS is proven to improve motor functions of PD patients (Benabid, 2003), but it provides limited alleviation of non-motor symptoms (Kurtis et al., 2017) and does not halt or reverse the neurodegeneration progress (Constantinescu et al., 2017). Therefore, the dopaminergic system needs to be restored in a more physiological manner, which could be achieved by cell replacement therapy.

1.2. Grafting of fetal tissues in pre-clinical animal models of PD

Since the midbrain dopaminergic neurons lost during PD originate from SN, the first successful cell replacement therapy dissected SN from 16-17-day rat embryos and transplanted them into the SN of 6-hydroxydopamine (6-OHDA)-lesioned rats (Björklund et al., 1981). The 6-OHDA model is a widely used pre-clinical PD model where unilateral injection of the neurotoxin 6-OHDA was used to lesion the nigrostriatal dopaminergic system (Ungerstedt and Arbuthnott, 1970). The SN grafts restored the striatal dopaminergic neurotransmission and rescued behavioural defects, such as spontaneous as well as amphetamine-induced asymmetric motor behaviour (Björklund et al., 1981).

With the success of using rat embryos, a following study grafted 6-OHDA-lesioned rats with human fetal ventral midbrain (hfVM) tissues (Brundin et al., 1986). Tissues from 9-week-old fetal donors gave rise to robust graft survival and re-innervation of the striatum, and reversed the motor asymmetry, while tissues from 11-19-week-old donors resulted in poor graft survival (Brundin et al., 1986). This suggests that an optimal timing of tissue harvest, which is during early development, is crucial for graft survival in this cell replacement therapy.

1.3. Clinical trials for cell replacement therapy for PD

Based on the success in pre-clinical animal models, hfVM tissues were used in the cell replacement therapy clinical trials for PD (Figure 1.1). Following the initial clinical success (Lindvall et al., 1989), the open-label Lund series were performed, where most patients experienced decent graft survival and functionality for years and were even off levodopa medication (Kefalopoulou et al., 2014; Li et al., 2008, 2016; Lindvall et al., 1994, 1990; Wenning et al., 1997; Widner et al., 1992). A few other groups around the world have since performed multiple open-label clinical trials with encouraging results, where patients showed improvement to different extents (Freed et al., 1992; Freeman et al., 1995; Kordower et al., 1995; Mendez et al., 2002).

This led to two subsequent NIH-funded double-blind studies, in which however, the overall improvement was insignificant (Freed et al., 2001; Olanow et al., 2003). In addition, 15% (Freed et al., 2001) to 50% (Olanow et al., 2003) of patients developed graft-induced dyskinesia (GID), some of them so severe that further neurosurgery such as DBS was required to ameliorate the condition. Followed-up study found that GID is most likely to be

caused by the serotonergic neurons in the graft tissues (Politis et al., 2011). Retrospective analysis revealed that younger patients (Freed et al., 2001) and those at earlier stage of PD benefited more from the transplantation (Olanow et al., 2003). It was also found that at least 1 year of multiple immunotherapy seemed crucial for an optimal graft survival (Piccini et al., 2005), as the two NIH-funded double-blind studies either used no immunosuppression (Freed et al., 2001) or cyclosporin A only for 6 months (Olanow et al., 2003).

Based on these findings, a revisit of the hfVM cell replacement therapy, TRANSEURO, was designed and initiated in 2009 with strict patient selection criteria, including that they must be at a relatively early stage of PD, respond well to levodopa and do not have significant levodopa-induced dyskinesia (TRANSEURO consortium and Barker, 2019). Nonetheless, the use of fetal tissues makes it an unsustainable therapy. A high demand of embryo availability – 3 embryos to provide sufficient cells for each side of the transplant (TRANSEURO consortium and Barker, 2019), as well as ethical issues related to the use of embryos largely limits the prevalence of this therapy. In fact, 87 out of 128 scheduled transplantation surgeries were cancelled due to the lack of embryo donors (TRANSEURO consortium and Barker, 2019).

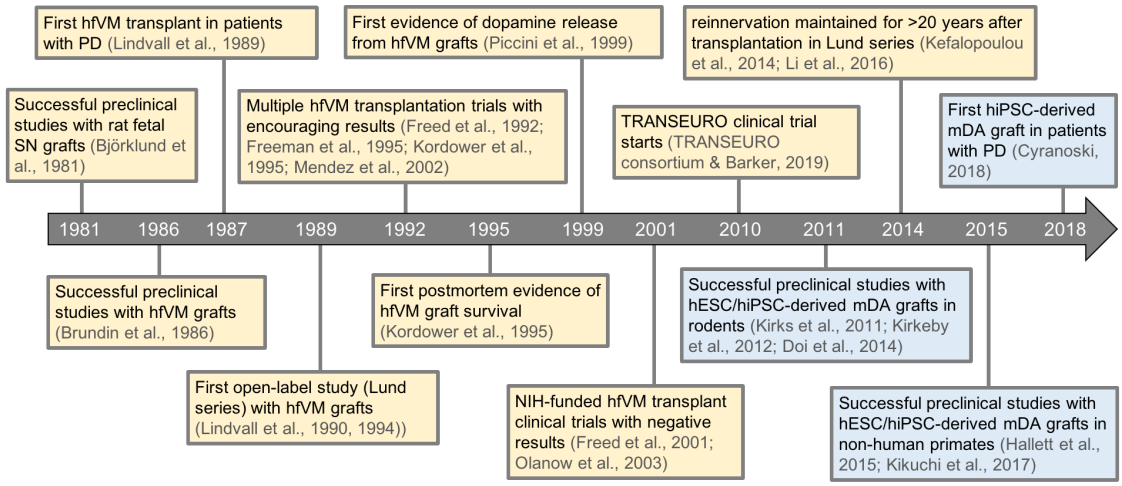

Figure 1.1 Timeline of cell replacement therapy for PD using human fetal midbrain tissues (yellow boxes) **or hESC/hiPSC-derived mDA progenitors** (blue boxes) (adapted from (Barker et al., 2015)).

1.4. α-Synuclein (α-Syn) and PD

α-Synuclein (α-Syn, gene *SNCA*) was implicated in PD initially in familial PD cases with α-Syn A53T mutation, which results from a G to A substitution in *SNCA* exon 4 (Polymeropoulos, 1997). The *SNCA* gene is located at chromosome 4q21-q23 and consists of 6 exons, of which 5 are coding exons (Figure 1.2). The translational product, the α-Syn protein, is a 140 amino acid protein (Uéda et al., 1993) comprising 3 domains: a positively charged α-helical N-terminal region, a highly hydrophobic non-amyloid component (NAC) region and a negatively charged acidic C-terminal region (Figure 1.2). Seven 11-amino-acid imperfect repeats with a highly conserved KTKEGV motif span the N-terminal and NAC regions (orange in Figure 1.2) and give rise to an N-terminal helix. This helical structure participates in the binding of α-Syn to membrane via interactions with lipids, and makes α-Syn less prone to form β-sheet structures which promote α-Syn aggregation (Sode et al., 2007). The NAC region, involved in protein-protein interactions, is the most aggregation-prone part of α-Syn (El-Agnaf et al., 1998; Pawar et al., 2005; Uéda et al., 1993).

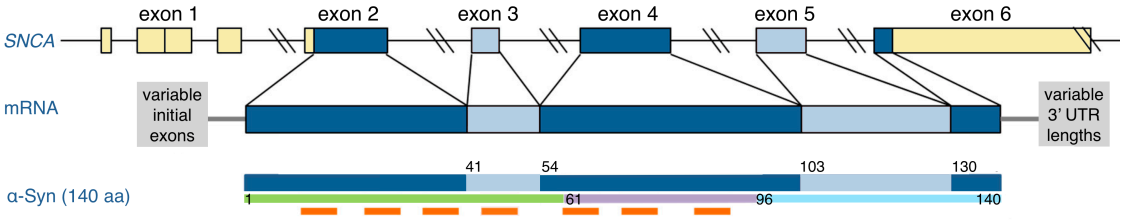

Figure 1.2 *SNCA* gene, mRNA transcript and α-Syn protein (adapted from (Ana Gámez-Valero and Katrin Beyer, 2018)). Coding regions of *SNCA* are coloured in blue and untranslated regions in yellow. α-Syn protein consists of 3 domains: an α-helical N-terminal region (green), a highly hydrophobic non-amyloid component (NAC) region (purple) and a negatively charged acidic C-terminal region (cyan). Orange indicates the 11-amino-acid imperfect repeats containing the highly conserved KTKEGV motif.

α-Syn is expressed primarily in brain, and also found in blood, bone marrow and other tissues. In the brain, α-Syn is expressed predominantly in neurons, but is also found in astrocytes and microglia at a low expression level. In SN dopaminergic neurons, α-Syn initially expressed in nucleus and subsequently distributed to synapses during embryonic development (Galvin et al., 2001). The physiological functions of α-Syn remain to be fully elucidated, but it is suggested that α-Syn is involved in innate immunity and regulation of synaptic vesicles (see section 1.9 for further details).

SNCA triplication results in early onset of PD (at the age of 25 – 49) and rapidly progressive disease course within 10 years (Farrer et al., 2004; Olgiati et al., 2015; Sekine et al., 2010; Singleton, 2003). Clinically, *SNCA* triplication patients exhibit severe Parkinsonian symptoms of resting tremor and bradykinesia. They also suffer from cognitive decline and mental disorders such as depression, behavior disturbances, sleep disorders (Olgiati et al., 2015; Sekine et al., 2010). Such consistency of robust clinical symptoms, early age of onset and fast disease progression are not found in *SNCA* duplication patients. Postmortem analysis of brain tissues from *SNCA* triplication patients revealed extensive Lewy pathology and severe SN and hippocampal neurodegeneration (Farrer et al., 2004; Singleton, 2003). In *SNCA* triplication patients, the levels of α-Syn protein in blood and α-Syn mRNA in brain are double of those in healthy controls (Farrer et al., 2004), and an extensive amount of brain α-Syn protein is found in aggregated form, which is absent in healthy controls (Miller et al., 2004).

The misfolded aggregated form of α-Syn is involved in several neurodegenerative disorders, collectively termed as synucleinopathies, the most common of which being PD. The histological hallmark of PD, Lewy body, was first described by Friederich H. Lewy in 1912 (Lewy, 1912). This inclusion body pathology is widely distributed in the central nervous system (CNS) (Braak et al., 2003; Wakabayashi et al., 2013). According the Braak staging system, the Lewy body pathology is initiated in the medulla oblongata (stage 1) and propagated to the pontine tegmentum (stage 2), subsequently progressed to the midbrain, in particular SN *pars compacta* (stage 3) and then the basal procencephalon and mesocortex (stage 4), and eventually into the neocortex (stages 5 and 6) (Braak et al., 2003).

The major component of Lewy bodies is aggregated α-Syn (Spillantini et al., 1998, 1997). Phosphorylation of serine 129 in α-Syn (pS129-αSyn) is a reliable marker for Lewy body pathology (Anderson et al., 2006; Fujiwara et al., 2002). More than 90% of α-Syn is phosphorylated at Ser129 in synucleinopathy patients, while less than 4% is phosphorylated under physiological condition (Oueslati, 2016). Apart from α-Syn, hundreds of other proteins and lipids have been identified in Lewy bodies, including components of cytoskeleton, lysosome and mitochondria, as well as molecules involved in cellular stress such as heat-shock proteins (Wakabayashi et al., 2013). Ubiquitin (Braak et al., 2003; Kuusisto et al., 2003) and p62 (Kuusisto et al., 2003; Zatloukal et al., 2002),

both of which are involved in the degradation of α-Syn, are also signature components of Lewy bodies and thus commonly used as markers for identification.

1.5. Lewy body pathology in grafts in PD patients

In clinical trials of cell replacement therapy with fetal tissue, grafts exhibited long term survival and functionality in a selected population of patient (section 1.3). However, in the post-mortem brain of these patients, Lewy body pathology was surprisingly found in 11 – 24 year old grafts, suggesting a host-to-graft spread of Lewy body pathology (Kordower et al., 2017, 2008; Kurowska et al., 2011; Li et al., 2008, 2016). The pathology was marked by pS129-αSyn$^+$ and ubiquitin$^+$ aggregates, suggesting they are genuine Lewy bodies (Kordower et al., 2017, 2008; Kurowska et al., 2011; Li et al., 2008, 2016). The pathology was commonly found in grafts more than 10 years old, and no α-Syn aggregates or ubiquitinated aggregates were observed in younger grafts (Figure 1.3 and Table 1.1). The percentage of dopaminergic neurons containing Lewy bodies varied from 1.9% to 27.1% in 12 – 24-year-old post-mortem grafts analysed to date (Table 1.1).

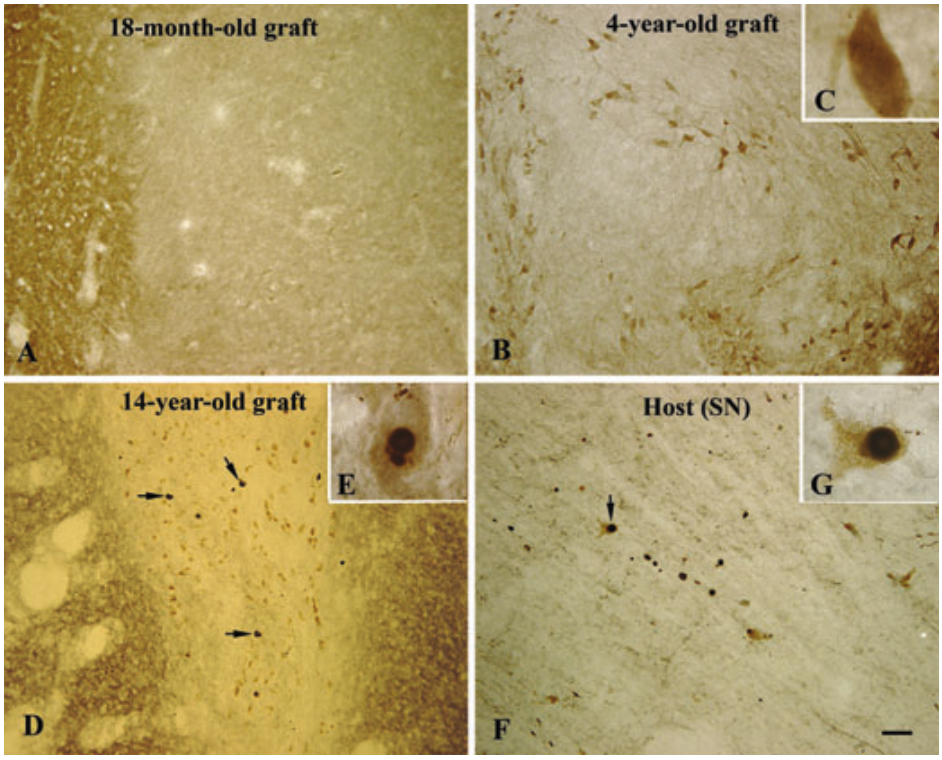

Figure 1.3 Lewy body pathology resembling that in the host, was found in a 14-year-old graft, but was absent in younger grafts (Chu and Kordower, 2010). Scale bar = 80 μm in A, B, D and F, = 8 μm in C, E and G.

Graft age	Dopaminergic neurons with Lewy bodies	Reference
4 months	No	(Mendez et al., 2008)
8 months	No	(Mendez et al., 2008)
4 years	No	(Kordower et al., 2008)
9 years	No	(Mendez et al., 2008)
12 years	Yes (1.9%)	(Li et al., 2010)
14 years	Yes	(Kordower et al., 2008)
14 years	No	(Mendez et al., 2008)
16 years	Yes (5.0%)	(Li et al., 2010)
16 years	Yes (10.5% – right and 27.1% – left)	(Kordower et al., 2017)
22 years	Yes (1.2%)	(Kurowska et al., 2011)
24 years	Yes (12%)	(Li et al., 2016)

Table 1.1 Summary of the presence (and wherever data is available, the percentage) of dopaminergic neurons with Lewy body pathology in post-mortem grafts analysed to date.

The development of Lewy bodies correlated to a decrease in clinical benefits of the grafts, with PD motor symptoms relapsed 11 – 14 years after transplantation (Kordower et al., 2008; Li et al., 2016). In fact, the expression of tyrosine hydroxylase (TH) and dopamine transporter (DAT) in the Lewy body-positive grafts was weaker compared to younger grafts or healthy control (Chu and Kordower, 2010; Kordower et al., 2017, 2008; Kurowska et al., 2011; Li et al., 2010). These findings suggest the accumulation of Lewy body pathology deteriorates functionality of the grafts over time.

The development of Lewy body pathology in grafts has been modelled in mice (Desplats et al., 2009; Hansen et al., 2011) and rats (Angot et al., 2012; Kordower et al., 2011) overexpressing human α-Syn. Host-originated α-Syn was found in the embryonic ventral midbrain tissues grafted in striatum (Angot et al., 2012; Hansen et al., 2011; Kordower et al., 2011), as well as in cortical neuronal stem cells grafted in hippocampus (Desplats et al., 2009). The host-originated α-Syn probably propagated to graft neurons via endocytosis and recruited the aggregation of endogenous α-Syn in graft neurons (Angot et al., 2012).

1.6. Midbrain dopaminergic neurons can be differentiated efficiently from hESCs/hiPSCs *in vitro* using floor plate protocol

The limited access to human embryo material and their previous variable clinical outcomes call for reliable cell source alternatives. Human embryonic stem cells (hESCs) are pluripotent stem cells derived from the inner cell mass of a donated early-stage preimplantation embryo. Human induces pluripotent stem cells (hiPSCs) are stem cells that regain pluripotency by reprogramming with OCT4, SOX2, KLF4 and cMYC (Takahashi and Yamanaka, 2006) or with OCT4, SOX2, KLF4, cMYC, NANOG and LIN28 (Yu et al., 2007). hiPSCs can be reprogrammed from patient's own adult somatic cells, such as skin fibroblasts and blood-derived endothelial progenitor cells, and thus enable autologous grafting. Both hESCs and hiPSCs can provide an unlimited supply of cells through self-renewal and their pluripotency enables differentiation into any cell types of all three germ layers. The mDA progenitors derived from hESCs/hiPSCs are a promising cell source for the cell replacement therapy for PD. Cells differentiated *in vitro* allow for better characterisation and standardisation of the cell components in the grafts, for example, avoiding serotonergic neurons that might cause GID. In addition, the genome of hESCs and hiPSCs can be edited, hence enabling the subsequently differentiated mDA neurons to acquire desirable phenotypes, such as resistance to PD pathologies.

The most efficient protocols to date for *in vitro* mDA differentiation from hESCs/hiPSCs are inspired by the midbrain floor plate origin of mDA neurons during *in vivo* development (Ono et al., 2007). For neural induction, dual SMAD inhibition of bone morphogenic protein (BMP) and transforming growth factor β (TGF-β) pathways is an efficient strategy. In the initial study, this was achieved using BMP inhibitor Noggin and TGF-β inhibitor SB431542 (SB) (Chambers et al., 2009). As a potent and inexpensive alternative, a small molecule BMP inhibitor LDN193189 (LDN) was used instead of Noggin in subsequent studies (Kriks et al., 2011; Xi et al., 2012). With dual SMAD inhibition, an anterior identity is obtained as a default after neural induction (Figure 1.4a). WNT and fibroblast growth factor (FGF) signalling can be used to manipulate the anteroposterior patterning, while Sonic Hedgehog (SHH) can be used for ventralisation (Figure 1.4a). To acquire floor plate identity, a high level of SHH is used to ventralise the progenitors (Fasano et al., 2010). To obtain a midbrain identity, WNT activation is fine-tuned with a potent glycogen synthase kinase 3β (GSK3β) inhibitor CHIR99021 (CHIR)

to adjust the anteroposterior identity of progenitors (Kirkeby et al., 2012; Kriks et al., 2011). CHIR prevents phosphorylation of β-catenin, which is a signal for its degradation. The subsequent stabilisation and accumulation of β-catenin activates canonical WNT signaling (Bennett et al., 2002; MacDonald et al., 2009). Following SHH and WNT activation, FGF8 is applied to boost the number of mDA progenitors (Kirkeby et al., 2017a; Xi et al., 2012). FGF signalling fine-tunes the anteroposterior axis and promotes dopaminergic fate in midbrain progenitors (Lahti et al., 2012).

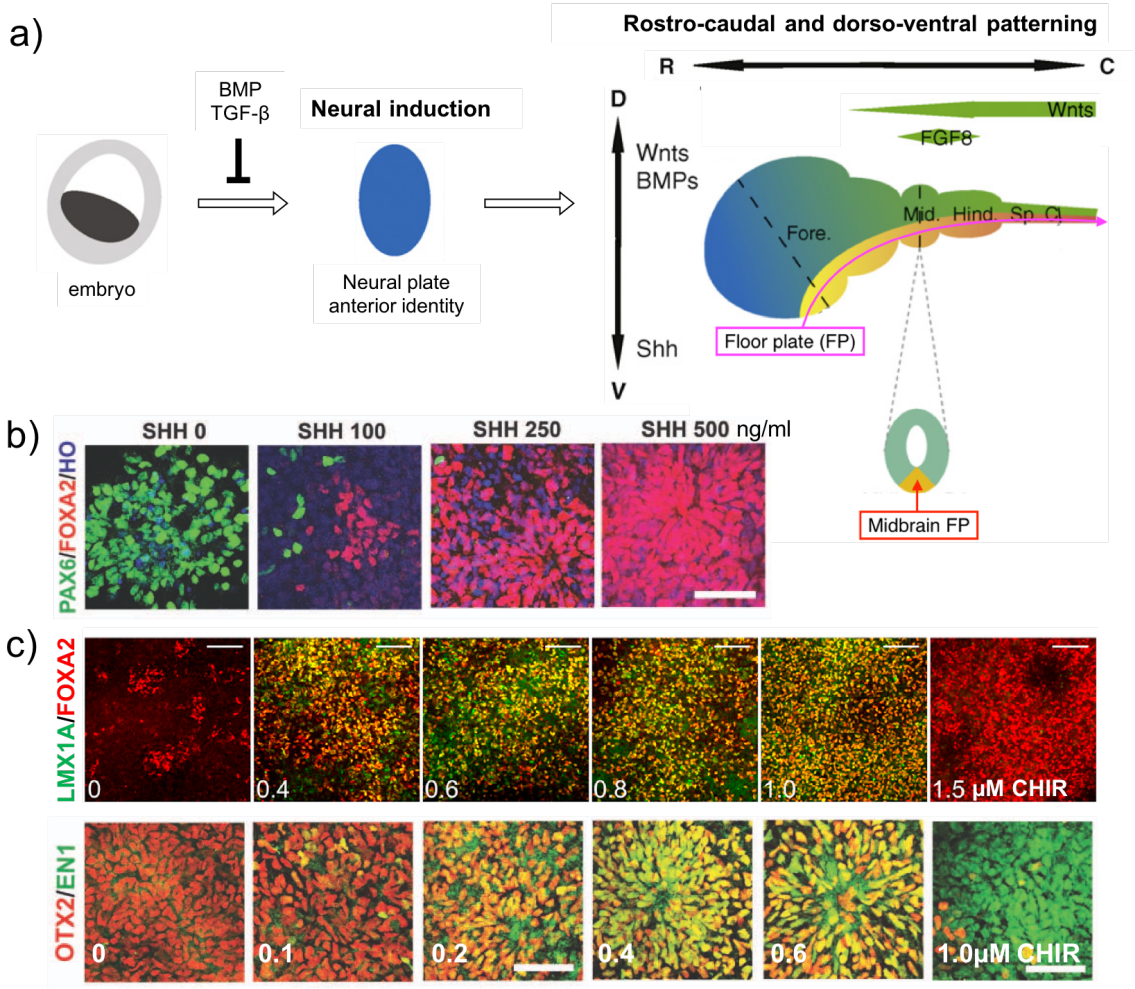

Figure 1.4 *In vitro* mDA differentiation from hESCs/hiPSCs based on the *in vivo* development of midbrain floor plate.

a) Developmental signalling for neural induction, anteroposterior and dorsoventral patterning of ventral midbrain (adapted from (Gaspard and Vanderhaeghen, 2010)).

b) Increased positivity of ventral marker FOXA2 and decreased positivity of dorsal marker PAX6, resulted from the increased ventralisation induced by higher SHH concentration in mDA differentiation *in vitro* (adapted from (Xi et al., 2012)).

c) LMX1A / FOXA2 (adapted from (Kee et al., 2017)) and OTX2 / EN1 (adapted from (Xi et al., 2012)) co-immunostaining identify CHIR concentrations which correctly anteroposteriorly patterned mDA progenitors that are positive for LMX1A / FOXA2 and OTX2 / EN1.

Since mDA neurons are developed from midbrain floor plate, markers for the developing ventral midbrain (Table 1.2) are used as indicators of cell identity during *in vitro* mDA differentiation. Corin, which is expressed ventrally from diencephalon to midbrain and to spinal cord (Kee et al., 2017; Ono et al., 2007; Samata et al., 2016), is used as a marker to assess the floor plate identity of progenitors (Kirkeby et al., 2012; Xi et al., 2012). Since Corin is expressed on the cell surface, it is a useful marker for the isolation and/or quantification of floor plate progenitors by flow cytometry (Doi et al., 2014). Another marker for monitoring the dorsoventral identity of neural progenitors is Foxa2, a transcription factor expressed predominantly in ventral midbrain, but also found in ventral diencephalon and ventral hindbrain (Besnard et al., 2004; Kee et al., 2017; Nouri and Awatramani, 2017). FOXA2 expression is homogenously positive at high SHH condition where the differentiation is sufficiently ventralised (Figure 1.4b).

Markers	Expression regions	Reference
Foxa2	ventral midbrain and ventral hindbrain	(Besnard et al., 2004; Kee et al., 2017; Nouri and Awatramani, 2017)
Corin	floor plate of ventral diencephalon, ventral midbrain and ventral hindbrain	(Kee et al., 2017; Ono et al., 2007; Samata et al., 2016)
Lmx1a	ventral diencephalon and midbrain floor plate	(Andersson et al., 2006; Nouri and Awatramani, 2017)
Otx2	forebrain and midbrain	(Kirkeby et al., 2012; Sunmonu et al., 2011)
En1	caudal midbrain	(Kee et al., 2017; Li and Joyner, 2001; Nouri and Awatramani, 2017)
Barhl1	ventral rostral midbrain and diencephalon	(Kee et al., 2017; Lopes et al., 2006)
Six3	forebrain	(Kirkeby et al., 2012; Li and Joyner, 2001)
Gbx2	hindbrain	(Kirkeby et al., 2012; Sunmonu et al., 2011)

Table 1.2 Markers for monitoring the identity of neural progenitors.

To characterise the anteroposterior identity of the differentiated progenitors, developmental markers with spatially restricted expression in forebrain, midbrain and hindbrain are used (Table 1.2). Lmx1a is a transcription factor expressed in ventral diencephalon and ventral midbrain (Andersson et al., 2006; Nouri and Awatramani, 2017).

Given that FOXA2 is a ventral midbrain and ventral hindbrain marker, co-expression of LMX1A and FOXA2 is unique to the midbrain floor plate and is therefore widely used to identify floor plate mDA progenitors (Figure 1.4c). Other transcription factors that characterise mDA progenitors include Otx2 and En1. Otx2 is expressed predominantly in midbrain but also in a considerably high level in forebrain (Kirkeby et al., 2012; Sunmonu et al., 2011), while En1 is expressed in caudal midbrain (Kee et al., 2017; Li and Joyner, 2001; Nouri and Awatramani, 2017). Hence, co-expression of OTX2 and EN1 reinforces the anteroposterior identity of progenitors (Figure 1.4c).

To further characterise possible contamination with undesired progenitors in the mDA differentiation, ventral rostral midbrain and diencephalon marker Barhl1 (Kee et al., 2017; Lopes et al., 2006), forebrain marker Six3 (Kirkeby et al., 2012; Li and Joyner, 2001) and hindbrain marker Gbx2 (Kirkeby et al., 2012; Sunmonu et al., 2011) are used. Appropriately patterned mDA progenitors exhibit low or undetectable level of these markers (Kirkeby et al., 2012, 2017a; Nolbrant et al., 2017).

To recapitulate the features of SN dopaminergic neurons, dopamine release can be observed from the hESC/hiPSC-derived mDA cultures *in vitro* (Doi et al., 2014; Kikuchi et al., 2017; Kriks et al., 2011; Samata et al., 2016). Whole-cell patch-clamp reveals electrophysiological phenotype characteristics of SN neurons, including spontaneous spiking at a slow rate (1 – 3 Hz) and sub-threshold oscillations of membrane potential (Kriks et al., 2011).

1.7. hESC/hiPSC-derived mDA cell grafts can rescue nigral deficits in multiple pre-clinical animal models of PD

mDA progenitors derived from hESCs or hiPSCs were transplanted into PD animal models, including 6-OHDA-lesioned rats and mice (Doi et al., 2014; Grealish et al., 2014; Kirkeby et al., 2012; Kriks et al., 2011) and 1-methyl-4-phenyl-1,2,3,6-tetrahydropyridine (MPTP)-lesioned monkeys (Kikuchi et al., 2017; Kriks et al., 2011). The unilateral 6-OHDA-lesioned mice and rats exhibit amphetamine-induced rotational asymmetry, which is the key behavioural phenotype assessed in these models. Animals transplanted with hESC/hiPSC-derived mDA progenitors showed significant reversal of this behaviour and was completely restored by the endpoint of some of the studies (Doi et al., 2014; Grealish et al., 2014; Kirkeby et al., 2012; Kriks et al., 2011). In the grafted animals, significantly

fewer contralateral step adjustments were observed in the stepping test which measures forelimb akinesia (Kriks et al., 2011). In addition, grafted animals showed a significant increase in the use of the affected paw in cylinder test (Kirkeby et al., 2012; Kriks et al., 2011). In MPTP-lesioned monkey, significant increase in moving time and significant decrease in PD scoring were observed after transplantation of hiPSC-derived mDA progenitors (Kikuchi et al., 2017). The PD scoring was based on the facial expression, head checking movements, spontaneous movement, movement in response to stimuli, tremor, posture instability and gait of the animals (Kikuchi et al., 2017).

These improvements in behavioural defects in rodents were significant by 12 weeks after transplantation and continued to improve during the next a few weeks (Doi et al., 2014; Kirkeby et al., 2012; Kriks et al., 2011). The reversal of amphetamine-induced rotation behaviour was typically among one of the earliest improvements observed (Kirkeby et al., 2012; Kriks et al., 2011). When fewer neurons were grafted, it could take up to 20 weeks after transplantation before significant improvements became evident (Grealish et al., 2014). In MPTP-lesioned monkey models, it took up to 12 months for significant behavioural improvement to be observed (Kikuchi et al., 2017).

Histology analysis of the grafts in these models revealed robust long-term survival and efficient re-innervation of striatum, with no signs of overgrowth (Grealish et al., 2014; Kikuchi et al., 2017; Kirkeby et al., 2012; Kriks et al., 2011). Dopamine release from the grafts was observed *in vivo* (Kirkeby et al., 2012).

When patterned correctly, hESC/hiPSCs-derived grafts were comparable to human fetal grafts in survival and functionality after transplantation in rat and monkey PD models (Grealish et al., 2014; Kikuchi et al., 2017). In addition, purification of mDA progenitors by fluorescence-activated cell sorting (FACS) or magnetic-activated cell sorting using cell surface markers CORIN (Doi et al., 2014), leucine-rich repeat and transmembrane domain-containing protein 1 (LRTM1) (Samata et al., 2016) and integrin-associated protein (IAP) (Lehnen et al., 2017) significantly increased mDA re-innervation and reduced graft overgrowth. Purification of the progenitors using CORIN, LRTM1 or IAP also reduced or eliminated serotonergic neurons which cause GID in fetal graft transplantation (Doi et al., 2014; Lehnen et al., 2017; Samata et al., 2016). Further improvement in the efficiency and potency of hESC/hiPSCs-derived grafts is expected as new markers for high fidelity mDA differentiations are being discovered, giving rise to purer mDA

populations. This is primarily achieved by RNAseq or RNA microarray analysis of embryonic SN (Bye et al., 2015; Poulin et al., 2014; Samata et al., 2016) and hESC/hiPSC-derived mDA progenitors. The progenitors were classified based on their subsequent differentiation into correctly patterned mDA neurons (Kriks et al., 2011; Lehnen et al., 2017; Samata et al., 2016) or their higher yield of mDA neurons *in vivo* after transplantation (Kirkeby et al., 2017a).

Based on the success in animal models, a number of clinical trials have been scheduled worldwide using hESC/hiPSC-derived mDA progenitors produced at good manufacturing practice (GMP) standards. The first hiPSC-derived mDA progenitor transplant in a PD patient was performed in October 2018 by Prof Jun Takahashi's team at CiRA, Kyoto, Japan (Cyranoski, 2018). Other clinical trials, including STEM-PD (Kirkeby et al., 2017b) and NYSTEM (Studer, 2017), are in preparation and very close to operating on their first patients. Based on what was learned from fetal trials, these trials have strict patient selection criteria similar to that in TRANSEURO trial and include immunotherapies for at least 1 year to ensure graft survival.

1.8. α-Syn pre-formed fibrils (PFFs) treatment produces intracellular aggregates with multiple characteristics of Lewy pathology

Abundant *in vitro* and *in vivo* studies have shown that α-Syn pathology propagates from cell to cell in a prion-like manner. Fetal grafts from PD patients who died over a decade after receiving cell replacement therapy contained Lewy pathology, which was proposed to be a prion-like transmission from host to gtaft. In animal models, brian homogenate derived from PD patients (Masuda-Suzukake et al., 2013; Recasens et al., 2014) or Parkinsonian animals (Bétemps et al., 2014; Luk et al., 2012b; Mougenot et al., 2012) induced widespread α-Syn pathology across different brain regions following injection at single or dual sites.

Under pathological conditions, α-Syn aggregates into oligomeric and/or fibrillar forms, which can act templates to recruit α-Syn monomers (Wood et al., 1999). The resulting aggregates can produce small fragments which are released from cells and further transmiss the pathology. The model such process *in vitro*, α-Syn PFFs are generated from recombinant α-Syn monomers (Figure 1.5a) to provide an exogenous template for aggregation. The recombinant α-Syn monomers can be produced in bacteria or HEK 293

cells and subsequently isolated and purified. The purified α-Syn monomers are incubated at 37 °C with constant agitation to first generate fibrils (Figure 1.5b). The fibrils are subsequently sonicated into smaller fragments, PFFs (Figure 1.5c), which are easily internalized into many cell types, including neurons (Karpowicz et al., 2017). The PFFs can propagate from donor to recipient neurons, where they induce α-Syn pathology (Freundt et al., 2012; Gribaudo et al., 2019; Tran et al., 2014).

Trypan blue-facilitated selective imaging of intracellular PFFs revealed that the majority of PFFs remained extracellular after PFF treatment of primary neurons, probably due to either sequestration on cell culture plates or being oversized for endocytosis even after prolonged sonication (Karpowicz et al., 2017). In fact, sufficient sonication which generates fragment size of < 50 nm is vital for inducing robust α-Syn pathology in both *in vitro* cell models and *in vivo* animal models (Abdelmotilib et al., 2017; Tarutani et al., 2016).

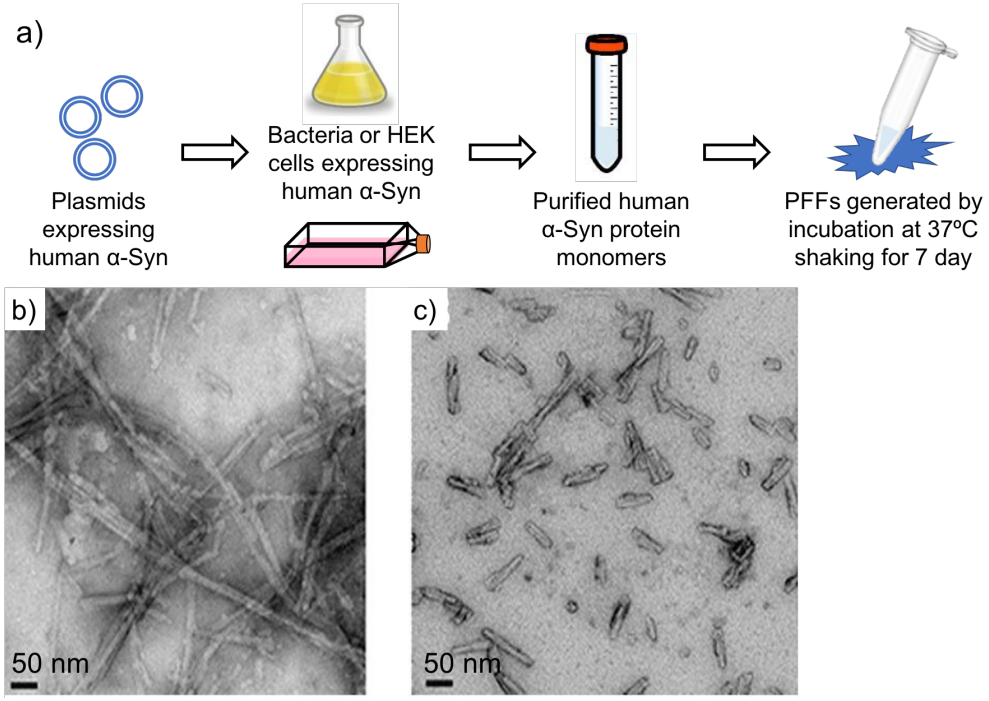

Figure 1.5 Generation of α-Syn pre-formed fibrils (PFFs).

a) Flow chart elucidating the generation of α-Syn PFFs (adapted from (Maneca et al., 2019)).

b-c) Transmission electron microscopy images of PFFs b) before and c) after sonication (adapted from (Polinski et al., 2018).

1.8.1. Application of α-Syn PFFs to cell culture models

Early cell models of PFF-induced synucleinopathy took advantage of non-neuronal cells or immortalized cell lines which are relatively easy to maintain. HEK

293 cells (Figure 1.6a) (Luk et al., 2009; Nonaka et al., 2010; Waxman and Giasson, 2010) and human neuroglioma cells H4 (Jiang et al., 2017) are commonly used, however, they cannot be differentiated into dopaminergic neuronal phenotype. In contrast, another commonly used cell type, human neuroblastoma cells SH-SY5Y (Bousset et al., 2013; Flavin et al., 2017; Luk et al., 2009; Mao et al., 2016; Nonaka et al., 2010; Tarutani et al., 2016; Waxman and Giasson, 2010) is sometimes used undifferentiated, but can also be differentiated to a neuronal phenotype with limited dopaminergic characteristics (Bousset et al., 2013; Domert et al., 2016; Freeman et al., 2013; Lee et al., 2008a). Although these non-neuronal and immortalized cell lines are convenient models for studying the internalisation and propagation of PFFs, their low endogenous α-Syn levels make α-Syn aggregation less efficient. Therefore, α-Syn overexpression is usually required to obtain sufficient levels of endogenous α-Syn expression for PFF-induced aggregation (Jiang et al., 2017; Luk et al., 2009; Nonaka et al., 2010; Tarutani et al., 2016; Waxman and Giasson, 2010). This renders the overexpression models less physiologically relevant, since the endogenous α-Syn level is not elevated in most sporadic PD cases (Quinn et al., 2012; Su et al., 2017). Nonetheless, α-Syn aggregates induced by PFF treatment in these cell models are pS129-αSyn positive, mostly ubiquitinated and thioflavin S positive, resembling the characteristics of Lewy bodies (Luk et al., 2009; Nonaka et al., 2010; Waxman and Giasson, 2010).

In contrast to non-neuronal and immortalized cell lines, mouse or rat primary neurons and hESC/hiPSC-derived neurons are more physiologically relevant models for synucleinopathy induced by PFF treatment (Figure 1.6b). The endogenous α-Syn alone was sufficient for the development of pS129-αSyn^{+} and ubiquitin^{+} aggregates in PFF-treated primary neurons without α-Syn overexpression (Abdelmotilib et al., 2017; Freundt et al., 2012; Gribaudo et al., 2019; Sacino et al., 2013b; Taguchi et al., 2014; Tran et al., 2014; Volpicelli-Daley et al., 2011).

On the contrary, primary neurons derived from *Snca*$^{-/-}$ mice were free from PFF-induced pathologies, including pS129-αSyn^{+} aggregates (Figure 1.6b) (Volpicelli-Daley et al., 2011). In addition, in cells which express no or low levels of α-Syn, such as glutamic acid decarboxylase (GAD) positive hippocampal inhibitory neurons (Taguchi et al., 2014) and astrocytes (Loria et al., 2017), PFF treatment did not give

rise to pS129-αSyn aggregates (Gribaudo et al., 2019; Taguchi et al., 2014; Volpicelli-Daley et al., 2011) or accumulation of its incomplete degradation product (Grassi et al., 2018). Overexpression of α-Syn in GAD$^+$ hippocampal inhibitory neurons resulted in the formation of pS129-αSyn aggregates (Taguchi et al., 2014). These observations suggest that endogenous α-Syn is indispensable for developing PFF-induced pS129-αSyn aggregates. In fact, as revealed by quantification of tagged or truncated PFFs in both primary neurons (Volpicelli-Daley et al., 2011) and non-neuronal cell models (Luk et al., 2009; Nonaka et al., 2010; Waxman and Giasson, 2010), the endogenous α-Syn is recruited as the main component of the aggregates (Figure 1.6a). C-truncated (1-120) and S129A α-Syn PFFs induced robust inclusions at an indistinguishable level (Gribaudo et al., 2019; Luk et al., 2009) or at a similar frequency (Nonaka et al., 2010) as wildtype (WT) PFFs. This suggests that phosphorylation of α-Syn at Ser129 is not required for PFF internalisation or for the subsequent recruitment of endogenous α-Syn.

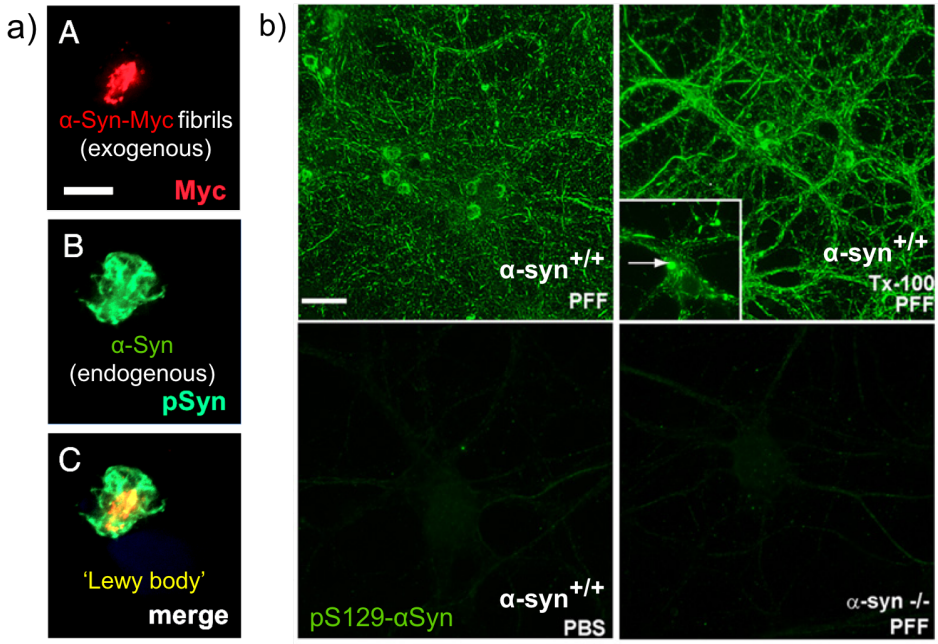

Figure 1.6 PFF treatment in cell models gives rise to Lewy body-like pS129-αSyn$^+$ aggregates.

a) PFF treatment in HEK 293 cells overexpressing α-Syn revealed that endogenous α-Syn was recruited by exogenous Myc-tagged PFFs and formed pS129-αSyn$^+$ aggregates (adapted from (Luk et al., 2009)).

b) Primary neurons derived from WT mice exhibited robust pS129-αSyn$^+$ pathology resistant to Tx-100 when treated with PFFs, but not when treated with PBS vehicle, or when the primary neurons were derived from *Snca*$^{-/-}$ mice (adapted from (Volpicelli-Daley et al., 2011)).

1.8.1.1. Internalisation and propagation of α-Syn PFFs in cell models

Without assisting reagents, PFFs can enter hiPSC-derived cortical neurons (Gribaudo et al., 2019), primary hippocampal, cortical and midbrain dopaminergic neurons (Sacino et al., 2017; Volpicelli-Daley et al., 2011) by endocytosis. The transmembrane protein lymphocyte-activation gene 3 (LAG3) was identified as a binding ligand for endocytosis of α-Syn PFFs (Mao et al., 2016). LAG3 is primarily expressed in neurons but undetectable in astrocytes or microglia. α-Syn PFFs bind to LAG3 with high affinity and specificity, while α-Syn monomers, tau PFFs, β-amyloid oligomers, or β-amyloid PFFs do not bind to LAG3 (Mao et al., 2016). In comparison to WT primary cortical neurons, *LAG3*$^{-/-}$ neurons exhibited significant reduction in α-Syn PFF binding and in PFF-induced calcium influx, which is involved in the PFF-induced neurotoxicity (Mao et al., 2016). Another transmembrane mediator of α-Syn PFF endocytosis identified in the mouse neural progenitor cell line C17.2, is a cell surface receptor, heparin sulfate proteoglycan (HSPG) (Holmes et al., 2013). As validated in both C17.2 cells and primary hippocampal neurons, the internalisation via HSPG is shared with tau PFFs, and potentially with other proteins with a heparin-binding domain (Holmes et al., 2013).

Antibodies targeting LAG3 (Mao et al., 2016) or PFFs themselves (Tran et al., 2014) were shown to reduce the internalisation of α-Syn PFFs and the subsequent aggregated α-Syn pathology in primary neurons. Heparin interfered with the binding of α-Syn PFFs to HSPGs, and thus reduced the internalisation of α-Syn PFFs and subsequent development of aggregates in a dose-dependent manner in C17.2 and HEK 293 cell models (Holmes et al., 2013). These results propose a feasible approach to diminish the propagation of pathology (Henderson et al., 2020). However, intervention at early stage of PD would be essential for efficacious results (Tran et al., 2014).

Following internalisation in primary neurons, the vast majority of PFFs is directed to lysosomes for degradation (Gribaudo et al., 2019; Karpowicz et al., 2017; Lee et al., 2008a; Loria et al., 2017; Sacino et al., 2017). The internalised PFFs showed considerable co-localisation with the lysosomal markers l ysosomal-associated membrane protein 1 (LAMP1) and LAMP2 (Gribaudo et al., 2019; Loria et al., 2017), and inhibition of lysosomal activity accelerated the

formation of α-Syn aggregates (Karpowicz et al., 2017; Sacino et al., 2017). It is believed that the PFFs which evade lysosomal degradation subsequently initiate inclusion formation (Gribaudo et al., 2019; Mahul-Mellier et al., 2019; Sacino et al., 2017). In fact, in non-neuronal cell and hiPSC-derived dopaminergic neuron models, internalisation of PFFs via endocytosis was followed by rupture of endocytic lysosome vesicles (Flavin et al., 2017; Freeman et al., 2013), which accelerated the formation of α-Syn aggregates (Jiang et al., 2017). This is consistent with observation in PD brain sections, that pS129-αSyn^{+} Lewy bodies were surrounded by a corona of ruptured vesicles (Flavin et al., 2017). Interestingly, endocytosis might not be the only, nor the most efficient pathway of internalisation. In H4 neuroglioma cell model, PFFs were found to internalise via direct plasma membrane penetration, which was a more efficient pathway than endocytosis (Jiang et al., 2017). PFFs stored at 4 °C dissociated and showed increased internalisation related to endocytosis pathway and reduced internalisation via direct plasma membrane penetration (Jiang et al., 2017). This might explain the reduction in their capacity to induce aggregation which was observed in prior studies (Bousset et al., 2013; Volpicelli-Daley et al., 2014). Nonetheless, presence of such direct plasma membrane penetration pathway in neurons is yet to be confirmed.

The level of pS129-αSyn pathology induced by PFFs is dependent on the concentration of PFFs as well as the length of culture period after PFF treatment (Gribaudo et al., 2019; Volpicelli-Daley et al., 2011; Wu et al., 2019). Both PFF concentration and culture period must pass a critical threshold to induce pS129-αSyn pathology (Gribaudo et al., 2019; Volpicelli-Daley et al., 2011; Wu et al., 2019). Due to a higher level of endogenous α-Syn (Murphy et al., 2000; Volpicelli-Daley et al., 2011), more mature primary neurons were found to develop more pathology under the same PFF concentration and culture period after PFF treatment (Volpicelli-Daley et al., 2011).

In microfluidic devices where the neuronal processes and cell bodies are isolated, PFF treatment on one side of the devices revealed that PFFs (Brahic et al., 2016; Freundt et al., 2012; Gribaudo et al., 2019) and PFF-induced pS129-αSyn^{+} aggregates (Volpicelli-Daley et al., 2011) could propagate both retrogradely

and anterogradely. The anterograde transportation can reach to second order (Freundt et al., 2012; Gribaudo et al., 2019; Tran et al., 2014) and even third order neurons (Tran et al., 2014), inducing pS129-αSyn aggregates in recipient neurons (Gribaudo et al., 2019). The intracellular propagation of PFFs can also occur without cellular contact between primary neurons (Abounit et al., 2016). Nonetheless, the propagation efficiency is significantly higher in the presence of neuron-to-neuron contact (Abounit et al., 2016). One possible explanation is offered by a mouse catecholaminergic neuron-like (CAD) cell model, where α-Syn PFFs in lysosomal vesicles were transferred from one CAD cell to another via tunnelling nanotubes (Abounit et al., 2016). Although such tunnelling nanotubes were observed in PFF propagation from neurons to CAD cells, they are yet to be identified in neuron-to-neuron transfer.

Interestingly, in the presence of astrocytes, PFF treatment did not result in pS129-αSyn pathology in neuronal cultures (Gribaudo et al., 2019; Sacino et al., 2013b), and only induced few pS129-αSyn puncta when a high concentration of PFFs was used (Sacino et al., 2017). This is probably due to astrocytes trapping and degrading α-Syn. Astrocytes exhibit significantly faster internalisation as well as clearance of PFFs compared to neurons (Lee et al., 2008b). When co-culturing astrocytes with PFF-treated neurons, the PFFs were efficiently transferred from neurons to astrocytes (Loria et al., 2017). This transfer was found significantly less efficient the other way around, from PFF-treated astrocytes to neurons (Loria et al., 2017).

1.8.1.2. α-Syn PFF-induced structural and functional defects in cell models

Cell models treated with PFFs exhibited structural defects such as Golgi fragmentation (Luk et al., 2009), mitochondrial fragmentation (Grassi et al., 2018; Gribaudo et al., 2019) and impaired synaptic structures. Dendritic spine density was reduced in PFF-treated primary neurons (Wu et al., 2019), consistent with prior observations in PFF-injected WT mice and aged human α-Syn-overexpressing mice (Blumenstock et al., 2017). These results parallel the observation of dendritic spine degeneration in dementia with Lewy bodies (DLB) patients (Kramer and Schulz-Schaeffer, 2007). Apart from dendritic spine density,

the co-localisation of post-synaptic density protein 95 (PSD95) and pre-synaptic protein synapsin 1 was found to be significantly reduced in PFF-treated primary neurons (Wu et al., 2019). Furthermore, a subset of synaptic proteins including synaptosome associated protein 25 (SNAP25), vesicle-associated membrane protein 2 (VAMP2), cysteine string protein α (CSPα), synapsin 2, synapsin 1, PSD95 was also significantly reduced in PFF-treated primary neurons (Mahul-Mellier et al., 2019; Tran et al., 2014; Volpicelli-Daley et al., 2011). This agrees with the observation in pS129-αSyn pathology-bearing primary neurons derived from human α-Syn overexpressing mice, where the pre-synaptic localisation of VAMP2, piccolo, synapsin 1 and amphiphysin was depleted (Scott et al., 2010). Consistent with these *in vitro* studies, DLB patients exhibit a diminished synaptic localisation of synapsin 1 (Scott et al., 2010) and reduced levels of synaptophysin, syntaxin, PSD95, and drebrin in brain homogenates (Kramer and Schulz-Schaeffer, 2007).

PFF-treated neurons exhibit multiple functional defects in neuronal activities (Gribaudo et al., 2019; Peelaerts et al., 2015; Volpicelli-Daley et al., 2011). A significant reduction in the frequency of spontaneous action potentials was observed in whole cell patch-clamp and microelectrode arrays (MEAs) of PFF-treated primary cortical neurons (Peelaerts et al., 2015). A similar decrease in the frequency of spontaneous activities was observed by calcium imaging of PFF-treated primary hippocampal neurons (Volpicelli-Daley et al., 2011) and hiPSC-derived cortical neurons (Gribaudo et al., 2019). PFF-treated primary hippocampal neurons also exhibited significant reductions in synchronization, excitatory tone of neurons and functional connectivity of the neuronal network (Volpicelli-Daley et al., 2011). Interestingly, the amplitude of the spontaneous activities was not significantly altered in PFF-treated neurons (Gribaudo et al., 2019).

Whole-cell patch clamp experiments further revealed impairment in synaptic activities of PFF-treated neurons, with reduced frequency of miniature excitatory and inhibitory postsynaptic currents (mEPSC and mIPSC), action potentials and spontaneous excitatory postsynaptic currents (sEPSC) (Peelaerts et al., 2015; Wu et al., 2019). The amplitude of mEPSC remained unaltered while the amplitude of

sEPSC decreased in PFF-treated neurons, which could be due to decreased frequency of action potentials (Wu et al., 2019). The level of these synaptic functional defects was positively correlated with the development of pS129-αSyn pathology (Wu et al., 2019). These findings are consistent with the diminished frequency, but not amplitude of mEPSC observed by whole cell patch-clamp of pS129-αSyn pathology-bearing primary neurons derived from human α-Syn-overexpressing mice (Scott et al., 2010).

Mitochondrial dysfunctions were also observed in PFF-treated neurons. After PFF treatment, pS129-αSyn bearing neurons exhibited a significant increase in mitochondrial oxidisation (Dryanovski et al., 2013) and the loss of mitochondrial membrane potential (Grassi et al., 2018; Mahul-Mellier et al., 2019). These dysfunctions eventually lead to cell death (Mahul-Mellier et al., 2019, 2015; Volpicelli-Daley et al., 2011; Wu et al., 2019), which is likely to be an apoptotic process as supported by caspase activities (Mahul-Mellier et al., 2019, 2015).

1.8.2. Application of α-Syn PFFs to animal models

Henceforth, the applications of PFFs for PD modelling have been extended from cell culture to animal models. The PFF injection model is advantageous for its rapid generation of PD phenotypes, without relying on the aging of transgenic animals overexpressing α-Syn (Giasson et al., 2002; Luk et al., 2012b; Masliah et al., 2000; Mougenot et al., 2012).

As the most extensively used model of α-Syn propagation, intracerebral PFF injection has been applied to model animals including rats (Abdelmotilib et al., 2017; Duffy et al., 2018; Patterson et al., 2019; Paumier et al., 2015; Peelaerts et al., 2015; Thakur et al., 2017), mice (Abdelmotilib et al., 2017; Ayers et al., 2018, 2016; Breid et al., 2016; Karampetsou et al., 2017; Luk et al., 2012a; Masuda-Suzukake et al., 2014, 2013; Okuzumi et al., 2018; Stoyka et al., 2020; Tarutani et al., 2016; Tran et al., 2014; Zhang et al., 2019), and non-human primates (Chu et al., 2019; Recasens et al., 2014; Shimozawa et al., 2017). The host animals can be WT (Abdelmotilib et al., 2017; Blumenstock et al., 2017; Chu et al., 2019; Duffy et al., 2018; Karampetsou et al., 2017; Luk et al., 2012a; Masuda-Suzukake et al., 2014, 2013; Okuzumi et al., 2018; Patterson et al., 2019; Paumier et al., 2015; Peelaerts et al., 2015; Shimozawa et al.,

2017; Stoyka et al., 2020; Tarutani et al., 2016; Tran et al., 2014; Zhang et al., 2019) or overexpressing human α-Syn (Ayers et al., 2018, 2016; Breid et al., 2016; Peelaerts et al., 2015). The development of PFF-induced synucleinopathy was prevalent in both types, although found to be faster and more severe in α-Syn overexpressing animals (Sacino et al., 2013a, 2014c; Thakur et al., 2017).

The PFFs were produced from recombinant mouse (Abdelmotilib et al., 2017; Ayers et al., 2018, 2016; Blumenstock et al., 2017; Duffy et al., 2018; Luk et al., 2012a; Masuda-Suzukake et al., 2014, 2013; Okuzumi et al., 2018; Patterson et al., 2019; Paumier et al., 2015; Shimozawa et al., 2017; Stoyka et al., 2020; Tran et al., 2014; Zhang et al., 2019) or human (Breid et al., 2016; Chu et al., 2019; Masuda-Suzukake et al., 2013; Okuzumi et al., 2018; Peelaerts et al., 2015; Thakur et al., 2017) α-Syn. Most studies treated rodent models with human α-Syn-derived PFFs for the convenience of tracking exogenous α-Syn with species-specific antibodies, but some studies suggest such cross-treatment might induced less α-Syn aggregation (Luk et al., 2016; Masuda-Suzukake et al., 2013; Rey et al., 2018). In fact, the match of protein sequence between the PFF template and α-Syn monomers has substantial impact on the aggregation rate, at least for the initiation stage (Luk et al., 2016). Interestingly, S129 phosphorylation of sonicated α-Syn PFFs indeed induced more aggregates and earlier development of pathologies, although phosphorylation at S129 was not necessary for PFF internalisation or subsequent α-Syn aggregation (Karampetsou et al., 2017; Luk et al., 2009). Rather than a higher potency of pS129-αSyn PFFs, the rapid progression of pathology is most plausibly explained by a lower clearance and hence faster accumulation of pS129-αSyn PFFs in neurons (Karampetsou et al., 2017). It was found that pS129-αSyn PFFs induced an attenuated innate immune response in comparison to WT PFFs (Karampetsou et al., 2017).

The PFF-injected animals exhibit pS129-αSyn^{+} inclusion pathology and loss of dopaminergic neurons (Abdelmotilib et al., 2017; Chu et al., 2019; Duffy et al., 2018; Luk et al., 2012a, 2012b; Masuda-Suzukake et al., 2014, 2013; Patterson et al., 2019; Paumier et al., 2015; Shimozawa et al., 2017; Thakur et al., 2017; Tran et al., 2014; Zhang et al., 2019), resembling the observation in PD patients. The accumulation of α-Syn pathology overtime correlates with dopaminergic degeneration (Abdelmotilib et

al., 2017; Duffy et al., 2018; Patterson et al., 2019; Thakur et al., 2017), and long-term imaging revealed that the inclusion bearing neurons were the ones selectively degenerated (Osterberg et al., 2015). The pathologies observed in PFF-injected animals are similar to those observed in animals injected with α-Syn aggregates-containing brain homogenates, originated from patients with Lewy bodies (Masuda-Suzukake et al., 2013; Recasens et al., 2014) or from aged α-Syn overexpressing mice (Bétemps et al., 2014; Luk et al., 2012b; Mougenot et al., 2012). The PFF-injected rodents developed Parkinsonian behaviours with significant motor impairment in rotarod and wire hang tests (Luk et al., 2012a; Masuda-Suzukake et al., 2014; Tran et al., 2014; Zhang et al., 2019). Some were also reported to have akinesia in stepping test (Patterson et al., 2019; Thakur et al., 2017) and defects in ultrasonic vocalizations (Paumier et al., 2015). Some studies also reported defects in nesting behaviour related to hippocampal dysfunction (Zhang et al., 2019), fear conditioning related to amygdala and social dominance related to prefrontal cortex dysfunction (Stoyka et al., 2020). It is worth noting that there was no change in forelimb use asymmetry measured by cylinder test after unilateral PFF injection (Paumier et al., 2015), or in investigation and anxiety behaviours measured by open field test, according to observations from several studies (Luk et al., 2012a; Patterson et al., 2019; Stoyka et al., 2020).

The pathology was not only detected at the PFF-injected sites, but also in anatomically connected structures. A unilateral striatal injection (the most popular injection site) of PFFs resulted in widespread pathology over the CNS including striatum, SN, amygdala, thalamus and cortex (Abdelmotilib et al., 2017; Blumenstock et al., 2017; Duffy et al., 2018; Grassi et al., 2018; Luk et al., 2012a; Masuda-Suzukake et al., 2014; Okuzumi et al., 2018; Patterson et al., 2019; Paumier et al., 2015; Shimozawa et al., 2017; Stoyka et al., 2020; Tarutani et al., 2016; Tran et al., 2014; Zhang et al., 2019). PFF injection into SN led to relatively restricted pathology, affecting striatum, hippocampus and amygdala (Abdelmotilib et al., 2017; Masuda-Suzukake et al., 2014, 2013). These findings support the cell-to-cell propagation of α-Syn pathology, consolidating the host-to-graft spread hypothesis in PD patients.

Interestingly, peripheral PFF injection in muscle (Ayers et al., 2016; Sacino et al., 2014b; Sorrentino et al., 2018), olfactory bulb (Rey et al., 2018, 2016), sciatic nerve

(Ayers et al., 2018), gut (Challis et al., 2020; Kim et al., 2019) and peritoneum (Ayers et al., 2016; Breid et al., 2016) also resulted in widespread CNS α-Syn pathology, loss of dopaminergic neurons, and even motor and cognitive defects, suggesting a retrograde transport of the pathology (Figure 1.7a). The α-Syn aggregates could be transported to CNS via the vagal nerve following gut injection of PFFs or brain homogenate of PD patients (Holmqvist et al., 2014). In contrast, vagotomy of the vagal nerve abolished this retrograde transport (Kim et al., 2019; Uemura et al., 2018). Similarly, severance of sciatic nerve significantly delayed the retrograde propagation of pathology following intramuscular PFF injection (Sacino et al., 2014b). These studies suggest that retrograde transport via the neuronal projection is a plausible route for the peripheral to CNS propagation of α-Syn, despite a possibility of alternative routes. In fact, PFFs were reported to cross the blood brain barrier and remained in CNS following intravenous injection, although no pS129-αSyn pathology was established by the endpoint of the study (Peelaerts et al., 2015).

Similar to the observations in PFF-treated cell models, α-Syn aggregates induced by PFF injection were found to be mainly host animal-originated, as revealed by western blotting and immunostaining (Blumenstock et al., 2017; Karampetsou et al., 2017; Luk et al., 2012b; Masuda-Suzukake et al., 2013; Peelaerts et al., 2015; Sacino et al., 2014b). This is consistent with the observation in cell models and indicates that endogenous α-Syn expression is essential for PFF-induced α-Syn pathology. In fact, *Snca*$^{-/-}$ mice have been consistently reported to be resistant to synucleinopathy induced by PFFs (Figure 1.7b) (Blumenstock et al., 2017; Karampetsou et al., 2017; Kim et al., 2019; Luk et al., 2012a; Masuda-Suzukake et al., 2014; Sacino et al., 2014b) and by α-Syn aggregate-containing brain homogenates, orginiated from human PD patients (Recasens et al., 2014) or from aged α-Syn overexpressing mice (Bétemps et al., 2014). In comparison, *Snca*$^{+/-}$ mice exhibit an intermediate level of PFF-induced synucleinopathy (Figure 1.7b) (Luk et al., 2012a).

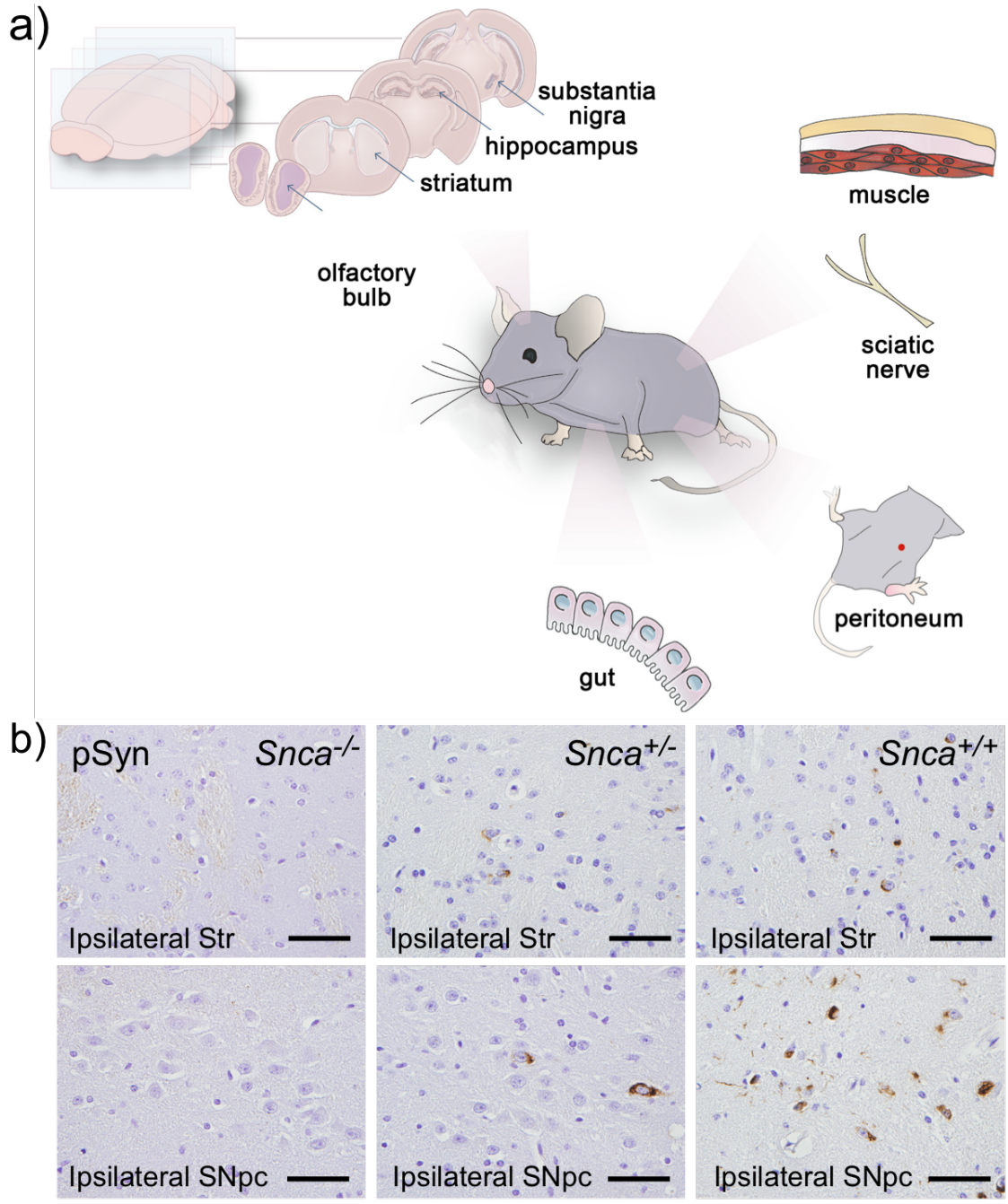

Figure 1.7 PFF injection in animal models.

a) Injection sites that have been reported to cause widespread CNS pathology (adapted from (Chung et al., 2019))

b) Intrastriatal injection of PFFs induced robust Lewy body-like α-Syn pathology in WT mice, no pathology in *Snca*$^{-/-}$ mice and an intermediate level of pathology in *Snca*$^{+/-}$ mice, as demonstrated by pS129-αSyn immunostaining of the ipsilateral striatum (Str) and *substantia nigra pars compacta* (SNpc) 90 days after PFF injection (adapted from (Luk et al., 2012a)).

1.9. Physiological role of α-Syn

1.9.1. α-Syn might play a protective role in innate immunity

Innate immunity is the body's inborn barriers and defenses to pathogens. Braak and Del Tredici proposed that PD might originate from gastrointestinal tract and olfactory bulb, both of which are at the frontlines of host-environment interface (Del Tredici and Braak, 2016). Some patients with encephalitis or other RNA virus infections developed PD symptoms such as tremor and bradykinesia (Haeman Jang et al., 2009; H. Jang et al., 2009; Sejvar, 2003). These findings imply a connection between infections and neurodegeneration. A number of studies suggest that α-Syn, which can be both neuroprotective and neuroinflammatory, is a star player in this connection.

Although *Snca*$^{-/-}$ mice were reported to seemingly lack a phenotype (Al-Wandi et al., 2010; Anwar et al., 2011; Specht and Schoepfer, 2001), recent data suggest that α-Syn might play a role in neuroinflammation. α-Syn knockdown in rat SN, mediated by adeno-associated virus (AAV) expressing small-interfering RNA (siRNA), resulted in a rapid increase in major histocompatibility complex class 1 (MHC-I) expression and recruitment of immune cells (Benskey et al., 2018). This was followed by a decrease in TH^+ neuron (Benskey et al., 2018; Gorbatyuk et al., 2010) and the emergence of Parkinsonian asymmetry in amphetamine-induced rotations, both of which were reversed by co-expression of siRNA insensitive α-Syn (Gorbatyuk et al., 2010). It is worth noting that these studies where α-Syn knockdown resulted in neuroinflammation and death were conducted on adult rats. In contrast, germline α-Syn knockout (*Snca*$^{-/-}$) mice did not result in such alternations (Abeliovich et al., 2000; Al-Wandi et al., 2010; Cabin et al., 2002), suggesting early disruption of this neuroprotective function of α-Syn might be compensated during development.

However, *Snca*$^{-/-}$ mice show strong phenotypes in immune deficiency to neuro-invasive viruses. *Snca*$^{-/-}$ mice did not significantly differ from their WT littermates, in terms of the inoculation efficiency, peripheral epithelial infection, the subsequent systemic dissemination of the virus, the initial brain infection rates and viral titres in the brain, following nose inoculation of reovirus-T3D (Tomlinson et al., 2017). However, once the encephalitis started, *Snca*$^{-/-}$ mice exhibited worse disease course

with significantly lower survival than WT mice (Figure 1.7a) (Tomlinson et al., 2017). Another neuro-invasive RNA virus, West Nile virus (WNV), is lethal to *Snca*$^{-/-}$ mice (Figure 1.8b) (Beatman et al., 2016). A vaccine strain of Venezuelan equine encephalitis virus (VEEV), TC83, could also be lethal to *Snca*$^{-/-}$ mice, which suffered a significantly greater weight loss than *Snca*$^{+/-}$ mice after inoculation of the virus (Beatman et al., 2016). In comparison to WT and *Snca*$^{+/-}$ mice, the absence of α-Syn in *Snca*$^{-/-}$ mice allows significantly higher level of viral growth in brain after WNV or VEEV TC83 inoculation (Beatman et al., 2016). This reinforces the hypothesis that the physiological expression of α-Syn is neuroprotective through an innate immune mechanism. Surprisingly, *SNCA*$^{+/-}$ mice exhibited similar survival and inhibition of WNV viral growth as WT mice within the experimental time frame (Figure 1.8b) (Beatman et al., 2016), supporting the hypothesis that losing up to half of α-Syn expression would not lead to observable immune defects (Benskey et al., 2018). However, α-Syn expression in WT mice increased significantly in response to neuro-invasive virus infection (Beatman et al., 2016), which could expose them to a higher risk of α-Syn aggregation. Accumulation of such infection events during the lifetime of an individual and failure to eradicate α-Syn aggregates could presumably result in synucleinopathy.

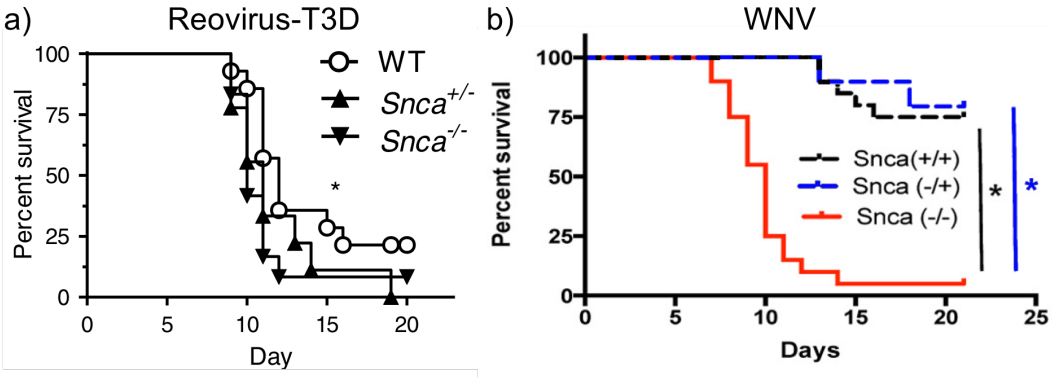

Figure 1.8 Neuroprotective role of α-Syn against neuro-invasive viruses.

a) Following nose inoculation of reovirus-T3D, survival of *Snca*$^{-/-}$ mice was significantly worse than WT mice (* p = 0.042), while *Snca*$^{+/-}$ mice were not significantly different from WT mice (adapted from (Tomlinson et al., 2017)).

b) After WNV inoculation, death rate of *Snca*$^{-/-}$ mice was significantly higher than WT and than *Snca*$^{+/-}$ mice (* p < 0.0001) (adapted from (Beatman et al., 2016)).

Snca$^{-/-}$ mice were also less capable of containing systemic bacterial infection caused by intravenous injection of *Salmonella typhimurium*, which induced lethal

sepsis (Tomlinson et al., 2017). *Snca*$^{-/-}$ mice exhibited a significantly higher bacterial load in their spleens compared to their WT littermates (Tomlinson et al., 2017).

A recent study suggests that α-Syn might also be involved in DNA repair under adverse conditions (Schaser et al., 2019). This provides new insights on how α-Syn might act as a neuronal protective molecule under pathological conditions such as neuro-invasive virus infections. In this study, α-Syn was found to participate in DNA repair by being recruited to double-strand breaks (DSBs), where they facilitated non-homologous end-joining (NHEJ) (Schaser et al., 2019). Under adverse conditions where DSBs occur, the lack of α-Syn, or a reduction in soluble functionable α-Syn monomers due to α-Syn aggregation (Kim et al., 2019; Mahul-Mellier et al., 2019; Osterberg et al., 2015; Volpicelli-Daley et al., 2011), could lead to a delay or insufficiency in DNA repair and result in celluar dysfunctions and eventual death.

1.9.2. α-Syn might contribute to the regulation of synaptic transmission and dopamine release

The onset of α-Syn expression and localisation to synapses are relatively late compared to pre-synaptic proteins such as synapsin 1 and synaptophysin (Galvin et al., 2001; Murphy et al., 2000), suggesting the involvement of α-Syn in synapse formation, if any, is trivial. This is further consolidated by the lack of defects in *Snca*$^{-/-}$ mice, in terms of synaptic morphology and the expression of synaptic proteins (Abeliovich et al., 2000; Cabin et al., 2002). This is unlikely to be a compensation of other members of the synuclein family, namely β- and γ-Synuclein, since the triple knockout mice also exhibited normal expression levels of synaptic proteins (Anwar et al., 2011).

The role of α-Syn in the regulation of dopamine homeostasis has been a controversial topic. Although some studies showed that young *Snca*$^{-/-}$ mice exhibited normal striatal dopamine content (Alerte et al., 2008; Robertson et al., 2004), others reported a lower striatal dopamine content in both young and aged *Snca*$^{-/-}$ mice (Abeliovich et al., 2000; Al-Wandi et al., 2010), as well as in α-Syn/β-Synuclein/γ-Synuclein triple knockout mice (Anwar et al., 2011) compared to their WT littermates. The levels of the dopamine metabolites, 3,4-dihydroxyphenylacetic acid (DOPAC) and homovanillic acid (HVA), were either reduced (Anwar et al., 2011) or unaltered

(Abeliovich et al., 2000; Al-Wandi et al., 2010) in the striatum of these mice. Since dopamine metabolism did not increase in the *Snca*$^{-/-}$ or the triple knockout mice, the lower dopamine content could be due to a decrease in dopamine synthesis, storage, or reuptake.

In both cell culture (Perez et al., 2002) and animal model (Masliah et al., 2000), the overexpression of α-Syn was found to inhibit the activity of TH, the rate limiting enzyme in dopamine synthesis which converts tyrosine to levodopa. Interestingly, in cells bearing α-Syn aggregates, a reduced inhibition on TH activity was observed, suggesting the aggregated form of α-Syn has impaired capacity of inhibiting TH (Alerte et al., 2008). The activity of aromatic amino acid decarboxylase (AADC), which converts levodopa to dopamine, was also inhibited by α-Syn overexpression in dopaminergic cell model (Tehranian et al., 2006). However, the effect of α-Syn overexpression on the protein levels of TH and AADC is controversial, as they were reported to be reduced in some studies (Baptista et al., 2003; Yu et al., 2004) but unaltered in others (Perez et al., 2002; Tehranian et al., 2006). Overall, these findings suggest that α-Syn might negatively regulate the level of dopamine by inhibition of the enzymes involved in dopamine synthesis. Therefore, the lack of α-Syn is unlikely to be responsible for the lower dopamine content in *Snca*$^{-/-}$ and triple knockout mice.

α-Syn might also regulate dopamine homeostasis by affecting dopamine storage. In fact, a significant decrease in the number of reserve vesicles was observed in primary hippocampal neurons derived from *Snca*$^{-/-}$ mice (Cabin et al., 2002) and in α-Syn knockdown primary hippocampal neurons (Murphy et al., 2000). The number of readily releasable vesicles was slightly reduced in primary hippocampal neurons derived from *Snca*$^{-/-}$ mice (Cabin et al., 2002), but not in α-Syn knockdown primary hippocampal neurons (Murphy et al., 2000). However, it is worth noting that these studies were conducted in non-dopaminergic hippocampal neurons and hence these findings await confirmation in mDA neurons relevant to PD. In the mDA system of *Snca*$^{-/-}$ mice, the readily releasable vesicles were replenished faster after initial stimulus and led to a higher dopamine release upon repetitive stimulations, as a possible compensation for the reduced reserve vesicle pool size (Abeliovich et al., 2000; Yavich et al., 2004). In contrast, upon amphetamine or single electrical stimulus, the dopamine release in *Snca*$^{-/-}$ mice was unaltered (Abeliovich et al., 2000). These

findings suggest α-Syn might play a role in maintaining the pool size of reserve/resting vesicles and in the regulation of dopamine release.

In comparison, evidence for the regulation of α-Syn on dopamine reuptake is less compelling. In the striatum, DAT-mediated reuptake of dopamine stops the actions of dopamine. While one study reported reduced striatal DAT level in *Snca*$^{-/-}$ mice (Al-Wandi et al., 2010), another study showed that neither the level nor function of DAT was altered in the striatum of *Snca*$^{-/-}$ mice (Dauer et al., 2002).

1.10. *SNCA*$^{S87E/S87E}$ mutation might reduce α-Syn aggregation with less disruption on its physiological functions

As *Snca*$^{-/-}$ mice are resistant to synucleinopathy (Luk et al., 2012a; Volpicelli-Daley et al., 2011), mDA grafts derived from *SNCA*$^{-/-}$ hESCs are highly likely to harbour the same resistance. However, α-Syn might play physiological roles (section 1.9) that are important for normal functionalities of the grafts, such as innate immunity. Hence, a single amino acid mutation which stops or reduces α-Syn aggregation might be ideal, as it might have less disruption on the physiological functions of α-Syn compared to α-Syn knockout.

Based on literature, I summarized a series of single amino acid mutations that reduced α-Syn aggregation in different settings (Table 1.3). All of them reside in the NAC region (61 – 95) of α-Syn, known to be crucial for α-Syn aggregation (El-Agnaf et al., 1998; Pawar et al., 2005; Uéda et al., 1993). As results from *in vitro* aggregation experiment do not always translate in cell and animal models (Luk et al., 2016), *SNCA*$^{S87E/S87E}$ mutation seems most promising as S87E α-Syn exhibited reduced aggregation in both *in vitro* and *in vivo* experiments (Figure 1.9). Thioflavin T (ThT) fluorometry and sodium dodecyl sulphate-polyacrylamide gel electrophoresis (SDS-PAGE) analysis over time showed that S87E α-Syn exhibited slower aggregation and fibrillisation *in vitro*, which was confirmed by transmission electron microscopy images (Figure 1.9b) (Paleologou et al., 2010). Overexpression of S87E α-Syn in H4 neuroglioma cell model revealed less α-Syn oligomerization and a fewer inclusions per cell compared to cells overexpressing WT α-Syn (Figure 1.9c) (Lázaro et al., 2014). AAV-mediated overexpression of S87E α-Syn in rat SN resulted in significantly fewer α-Syn aggregates (Figure 1.9d), fewer dystrophic fibres and less motor impairment compared to overexpression of WT or S129A α-Syn (Oueslati et al., 2012).

S87E is a phospho-mimicking mutation and phosphorylated S87 was readily found in Lewy bodies and in fact, the level of S87 phosphorylation was significantly higher in Lewy body disease and Alzheimer's disease patients, as well as in synucleinopathy mouse models (Khandelwal et al., 2010; Paleologou et al., 2010). However, whether (and how) S87 phosphorylation modulates pathological pathways in synucleinopathies remains to be elucidated. Given that the phospho-mimicking S87E reduces α-Syn aggregation, S87 phosphorylation is highly likely to be a protective post-translational event. However, the protective effect of S87E mutation is more likely to be resulted from a simple repulsive effect on aggregation rather than a phospho-mimicking effect. The repulsive effect is plausible because S87 and E83 are very close to each other in the Greek-key motif model of α-Syn fibrils (Figure 1.9a) (Tuttle et al., 2016). The negative charge of E83 might be important for inhibiting α-Syn aggregation, as E83A mutation enhanced α-Syn aggregation induced by dopamine or (–)-epigalloca-techin gallate and restored the aggregation ability of Δ74–79, Δ71–82 and Δ76–77 α-Syn (Waxman et al., 2010, 2009). Hence, S87E mutation would put two rows of negatively charged E together and the repulsion would hinder the formation of stable α-Syn fibrils.

Muatation	Effects on α-Syn aggregation
V66P	V66P α-Syn exhibited slower fibrillisation and aggregation in ThT fluorometry, K114 fluorometry and SDS-PAGE analysis over time. HEK 293 cells overexpressing V66P α-Syn showed significantly lower amount of α-Syn aggregates induced by α-Syn PFF treatment. However, when co-incubated or co-expressed with WT α-Syn, V66P α-Syn did not reduce fibrillisation or aggregation in these two models (Waxman and Giasson, 2010).
V66R	Reduced α-Syn protein fibrillisation *in vitro* as shown by ThT fluorometry (Du et al., 2003).
G68E or G68R	Reduced α-Syn protein fibrillisation *in vitro* as shown by ThT fluorometry (Du et al., 2003).
T72P	T72P α-Syn exhibited slower fibrillisation and aggregation in ThT fluorometry, K114 fluorometry and SDS-PAGE analysis over time. HEK 293 cells overexpressing T72P α-Syn showed significantly lower amount of α-Syn aggregates induced by α-Syn PFF treatment. However, when co-incubated or co-expressed with WT α-Syn, T72P α-Syn did not reduce fibrillisation or aggregation in these two models (Waxman and Giasson, 2010).

V74R	Reduced α-Syn protein fibrillisation *in vitro* as shown by ThT fluorometry (Du et al., 2003).
T75P	T75P α-Syn exhibited slower fibrillisation and aggregation in ThT fluorometry, K114 fluorometry and SDS-PAGE analysis over time. When co-incubated with WT α-Syn, T75P α-Syn showed reduced fibrillisation. HEK 293 cells overexpressing T75P α-Syn showed significantly lower amount of α-Syn aggregates induced by α-Syn PFF treatment. When co-expressed with WT α-Syn, T75P α-Syn did not reduce aggregation (Waxman and Giasson, 2010).
A76R or A76E	Reduced α-Syn protein aggregation *in vitro* as shown by SDS-PAGE analysis (Giasson et al., 2001). Decreased α-Syn aggregation in fission yeast model and decreased α-Syn membrane association in budding yeast model (Fiske et al., 2011).
A76P	The P residue strongly inhibited formation of β-sheet structure and reduced α-Syn protein fibrillisation and aggregation *in vitro*, as shown by K114 fluorometry and SDS-PAGE analysis over time (Waxman et al., 2009).
A85P	Reduced α-Syn protein fibrillisation and aggregation *in vitro*, as shown by K114 fluorometry and SDS-PAGE analysis over time. The resulting fibrils had short protrusions, rather than a smooth morphology observed in WT fibrils (Waxman et al., 2009).
S87E	Slower α-Syn protein fibrillisation and aggregation *in vitro* as shown by ThT fluorometry and SDS-PAGE analysis (Paleologou et al., 2010). Reduced α-Syn oligomerization in HEK293 cells overexpressing α-Syn and a marked decrease in the number of inclusions per cell in H4 cells overexpressing α-Syn *in vitro* (Lázaro et al., 2014). AAV-mediated overexpression of S87E α-Syn in rat SN showed no toxic effect on dopaminergic neurons and resulted in significantly fewer α-Syn aggregates, dystrophic fibers, and less motor impairment compared to WT and S87A α-Syn (Oueslati et al., 2012).
F94G	Capable of extending fibrils from pre-existing seeds, but incapable of forming fibrils spontaneously. Exhibited a prolonged lag time of fibril formation but an extension rate similar to WT α-Syn (Yagi et al., 2010).

Table 1.3 Single amino acid mutations of α-Syn which have been reported to reduce α-Syn aggregation.

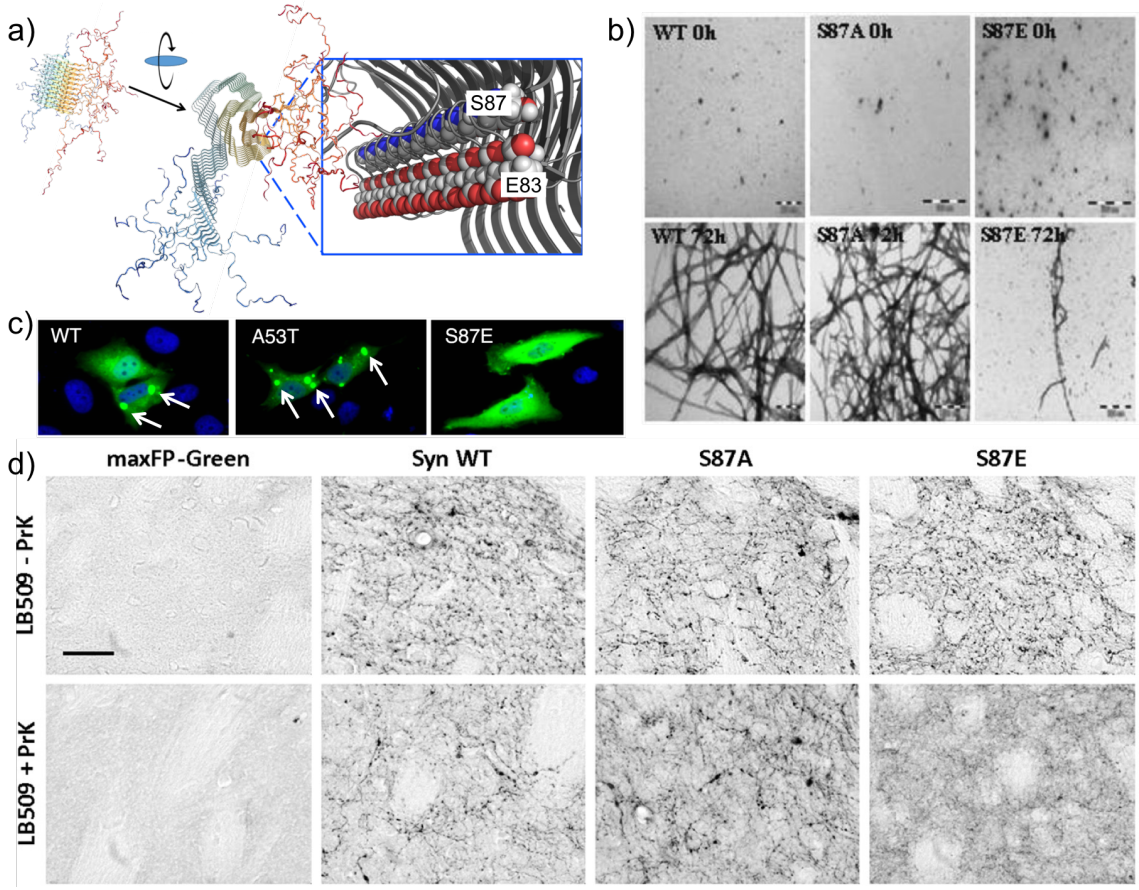

Figure 1.9 S87E mutation of α-Syn reduced α-Syn aggregation.

a) Close localisation of S87 and E83 in the Greek-key motif model of α-Syn fibrils (adapted from PDB accession number 2N0A (Tuttle et al., 2016)). The enlarged insert is credited to Dr Fergus McWhinnie.

b-d) S87E mutation reduced α-Syn aggregation in:

b) protein aggregation *in vitro* (transmission electron microscopy images adapted from (Paleologou et al., 2010))

c) H4 neuroglioma cell model overexpressing S87E α-Syn (adapted from (Lázaro et al., 2014))

d) SN of rat overexpressing S87E α-Syn and treated with protein kinase K (PrK) (adapted from (Oueslati et al., 2012)). LB509 stained for α-Syn.

1.11. Aims and hypotheses of the thesis

The initial aim of this thesis was to generate hESC lines with *SNCA* mutations that were predicted to reduce or eliminate α-Syn pathology. Concretely, I aimed to generate α-Syn homozygous knockout (*SNCA*$^{-/-}$), heterozygous knockout (*SNCA*$^{+/-}$) and S87E homozygous (*SNCA*$^{S87E/S87E}$) hESC lines by CRISPR editing of the *SNCA* gene (Chapter 3). As the CRISPR editing and clonal selection processes might result in off-target and undesired mutations, and targeting plasmids might integrate into the genome, I

subsequently aimed to check the genomic integrity of the clonal lines. Here I hypothesised some of the clonal lines would exhibit undesired mutations, potentially copy number variations (CNVs) at off-target regions or insertion of plasmid sequences.

My next aim was to fine-tune the mDA differentiation of these hESCs and investigate whether their differentiation capacity would alter due to the α-Syn mutation or the selection and cloning process (Chapter 4). Finally, as α-Syn has been reported to play physiological roles in dopamine release, synapse formation and transmission, I aimed to examine whether *SNCA*$^{-/-}$, *SNCA*$^{+/-}$ and *SNCA*$^{S87E/S87E}$ mDA neurons would exhibit changes in these functionalities *in vitro*. Here the hypothesis was that *SNCA*$^{-/-}$ mDA neurons would show some defects in dopamine release or synapse formation and transmission in comparison to WT mDA neurons, while *SNCA*$^{+/-}$ and *SNCA*$^{S87E/S87E}$ mDA neurons would show an intermediate phenotype.

Subsequently, I aimed to use the PFF treatment model of *SNCA*$^{-/-}$, *SNCA*$^{+/-}$ and *SNCA*$^{S87E/S87E}$ mDA neurons to investigate their susceptibility to synucleinopathy (Chapter 5). Here I hypothesised that *SNCA*$^{-/-}$ mDA neurons would be completely resistant to PFF-induced α-Syn pathology, while *SNCA*$^{+/-}$ and *SNCA*$^{S87E/S87E}$ mDA neurons would exhibit some level of resistance. Finally, I aimed to examine a selection of published PFF-induced pathologies *in vitro*, with the hypothesis that PFF-treated neurons would exhibit structural impairment of synapses and mitochondria, functional impairments in spontaneous neuronal activities and subsequent cell death.

Chapter 2: Methods

See Appendix 1 for detailed information of reagent suppliers and catalogue numbers.

2.1. Self-renewing and banking of hESCs

In this study, the use of RC17 hESCs was approved by the MRC Steering Committee for the UK Stem Cell Bank and for the Use of Stem Cell Lines (ref, SCSC13-19). RC17 hESCs (passages 25–29, ~1 million cells / 300 µl per vial when frozen) were retrieved from liquid nitrogen storage and thawed in 10 times volume of StemMACS iPS-Brew XF medium (iPS-B, Miltenyi Biotec). The hESCs were then centrifuged and plated on Laminin-521 (L521, Biolamina, diluted to 5 µg/ml with DPBS (Mg^{2+} Ca^{2+}, Thermo Fisher Scientific))-coated 6-well plates (Corning) for self-renewal and were fed daily with iPS-B. Every 2 or 3 days, once the hESCs reached 70 – 90% confluency, the cells were lifted with EDTA (0.5 mM, Thermo Fisher Scientific) and passaged as clumps at a split ratio of 1:3 to 1:8 depending on confluency. ROCK inhibitor Y27632 (Y2, 10 µM, Tocris) was added in the plating medium when thawing and passaging cells to help cell survival and was subsequently removed the next day. For freezing, ~1 million hESCs were frozen in 300 µl of STEM-CELLBANKER medium (ZENOAQ) supplemented with Y2 (10 µM).

2.2. CRISPR targeting of *SNCA* gene in hESCs

2.2.1. Gibson assembly of gRNA-Cas9n plasmids

For each target site, a series of 20 bp guide RNAs (gRNAs) pairs were designed using the Zhang Lab CRISPR DESIGN webtool (http://crispr.mit.edu) and the top 2 pairs were selected for subsequent cloning into pSpCas9n-2A-Puro (pX462, Addgene) plasmid (Ran et al., 2013b). The pX462 plasmid was obtained under a standard Addgene MTA (Order 152516) with the Provider Organization, Broad Institute, Inc. The gRNA-Cas9n plasmids for *SNCA* knockout were constructed by Karamjit Dolt Singh.

gRNA sequences (5' – 3'):

SNCA knockout 5G1: tgaattcctttacaccacac

SNCA knockout 3G1: gccatggatgtattcatgaa

SNCA knockout 5G4: acaagcaccaaactgacatt

SNCA knockout 3G4: ataatcaatactctaaatgc

SNCA$^{S87E/S87E}$ #1: acagccataccttgcccaac

SNCA$^{S87E/S87E}$ #2: ctttgtcaaaaaggaccagt

SNCA$^{S87E/S87E}$ #5: tttataagctggtgagatta

SNCA$^{S87E/S87E}$ #15: ctgctccctccactgtcttc

The 5'-end most nucleotide of each gRNA (i.e. transcription start site) was substituted by G to increase expression under U6 promotor and also to keep gRNA length at 20 bp for maximal targeting efficiency (Mali et al., 2013). For each gRNA, a 100 bp double-strand DNA fragment was made by PCR amplification of a pair of partially complementary single-stranded DNA where pair-wise complementary sequence was the gRNA and the rest of the sequence was complementary to the pX462 backbone (Ran et al., 2013b).

The pX462 plasmid was digested with dual-cutter *Bbs*I-HF (NEB) in CutSmart® buffer (NEB) and the backbone was isolated by electrophoresis in 0.8% agarose (Thermo Fisher Scientific) gel. The backbone was then purified using Wizard® SV Gel and PCR Clean-Up System (Promega) and ligated with the 100 bp DNA fragment by Gibson assembly using T5 exonuclease (Epicentre) and Phusion® DNA Polymerase (NEB).

Competent *E. coli* Stbl3™ (Thermo Fisher Scientific) was transformed with the assembly product and cultured overnight on Carbenicillin (100 µg/ml, Fisher) supplemented LB/agar plate. I picked 3 colonies for each gRNA and grew them overnight in Carbenicillin supplemented LB medium. Plasmids were then isolated with QIAprep® Spin Miniprep Kit (QIAGEN) and sent for Sanger sequencing. The clones with correct sequences were further scaled up and plasmids were isolated in bulk using PureLink™ HiPure Plasmid Midiprep Kit (Thermo Fisher Scientific).

2.2.2. Gibson assembly of homology-directed repair (HDR) template piggyBac plasmid

The 5' and 3' homology arms (HAs) were PCR amplified from the genomic DNA of paternal hESC line RC17 using Q5® High-Fidelity DNA Polymerase (NEB). The primers contain a sequence complementary to the genomic DNA (in capitals). The rest of the sequence was complementary to the fragment to be ligated using Gibson

assembly, which was the mutation-containing fragment for 5' HA reverse and was the piggyBac plasmid backbone for 5' HA forward, 3' HA forward and 3' HA reverse.

Primer sequences (5' – 3'):

5' HA forward:

attggagctcgtttaaacggCTGCAAATTTAGCTTTTTAAGAACCCTTTGTTTC

5' HA reverse: ccagtggctgctgcaatttcCCCTGCTCCCTCCACTGTC

3' HA forward: atgattatctttctagggttaaCCCAGATAAATGCCATGC

3' HA reverse: tagagcggcccggccttaattaCTACTGTAAGTTGGAAACTCTCC

A mutation-containing double-strand DNA fragment with the following sequence (S87E mutation underlined, synonymous mutations in capitals) was synthesized: gaaattgcagcagccactggctttgtcaaaaaggaTcagCtTggcaaggtatggctgtgtacgtt ttgtgttacatttataagctggtgagattacggttcattttcatgtgaggcctggaggcaggagcaagatacttactgtgg ggaacggctacctgaccctccccttgtgaaaaagtgctacctttatattggtcttgcttgtttcaggcattaaccctagaa agatagtctgcgtaaaattgacgcatgcattcttgaaatattgctctctc

The piggyBac transposon plasmid pMSC-AAT_PB-PGKpuroTK (Yusa, 2013) was obtained from Sanger Institute (Cambridge). The piggyBac plasmid was digested with *Asc*I (NEB) and *Nsi*I (NEB) in CutSmart® buffer and the backbone was isolated by electrophoresis in 0.8% agarose gel. The backbone was then purified and subsequently ligated with the 5' HA and the mutation-containing fragment by Gibson assembly. Competent *E. coli* DH5α cells (NEB) were transformed by the assembly product and grew overnight on Carbenicillin supplemented LB/agar plate. I picked 3 colonies and grew them overnight in Carbenicillin supplemented LB medium. Plasmids were then isolated by miniprep and sent for Sanger sequencing.

The piggyBac plasmid containing the customized 5' HA and mutation-containing fragment was digested with *Pac*I (NEB) and *Hpa*I (NEB) in CutSmart® buffer. The backbone was isolated, purified and subsequently ligated with the 3' HA by Gibson assembly as described above. I picked 8 colonies and grew them overnight in Carbenicillin supplemented LB medium. Plasmids were then isolated by miniprep and sent for Sanger sequencing. The clones with correct sequences were scaled up and plasmids were isolated in bulk by midiprep.

2.2.3. hESCs transfection and clonal selection

For *SNCA* knockout, RC17 hESCs (8 × 10^5 cells) were transfected with 1 µg of each of the 4 gRNA plasmids and GFPiPuroR (a GFP indicator plasmid) using Amaxa™ Human Stem Cell Nucleofector™ Kit 1 (Lonza) and programme B-016 on Nucleofector® II (Lonza). The transfected cells were plated on Matrigel (diluted 1:100 with DMEM/F12 (Thermo Fisher Scientific), Thermo Fisher Scientific)-coated 100 mm TC-treated culture dish (Corning) or L521 (5 µg/ml)-coated 6-well plates. Puromycin (Sigma) selection was applied 24 hours after transfection for 16 hours, at 0.5 µg/ml for cells on Matrigel or at 1.0 µg/ml puromycin for cells on L521. Clones were picked 8 – 14 days after transfection and expanded on L521-coated 96-well plates.

For *SNCA*$^{S87E/S87E}$ mutation, RC17 hESCs (8 × 10^5 cells) were transfected with 3.5 µg of each of the 2 gRNA plasmids and piggyBac HDR template plasmid using Amaxa™ Human Stem Cell Nucleofector™ Kit 1 and programme B-016 on Nucleofector® II. The transfected cells were plated on L521 (5 µg/ml)-coated 6-well plates. Puromycin (1.0 µg/ml, Sigma) selection was applied on the transfected cells 24 hours after transfection and kept until piggyBac cassette removal to avoid silencing of the puroΔTK cassette. Clones were picked 11 days after transfection and expanded on L521-coated 96-well plates.

To remove piggyBac cassette from putative *SNCA*$^{S87E/S87E}$ clones B6 and B21, 8 × 10^5 cells were transfected with 2 – 10 µg (see Table 3.3 for details) of pCMV-HAhyPBase (Yusa, 2013) using Amaxa™ Human Stem Cell Nucleofector™ Kit 1 and programme B-016 on Nucleofector® II. 24 hours after transfection or extra passaging, 1-(2-deoxy-2-fluoro-1-β-D-arabinofuranosyl)-5-iodouracil (FIAU) selection was applied at 200 nM or 500 nM (see Table 3.3 for details). Colonies were fed with FIAU until clones were picked 11 days after transfection or 13 days after extra passaging, and were subsequently expanded on L521-coated 96-well plates.

2.3. Clonal identity verification

2.3.1. PCR genotyping

Genomic DNA was extracted from cell pellets of hESC clones using either MasterPure™ Complete DNA and RNA Purification Kit (Epicentre) or by 1-hour incubation at 98°C in Solution I (25 mM NaOH and 0.2 mM EDTA) followed by

termination with Solution II (40 mM Tris-HCl). PCR reactions flanking the targeted region were performed using Q5® High-Fidelity DNA Polymerase.

For identifying putative *SNCA* knockout and *SNCA*$^{S87E/S87E}$ clones, I designed PCR primers with the following sequences (5′ – 3′):

PCR reaction	Forward (5' – 3')	Reverse (5' – 3')	Product size
SNCA Knockout 449 bp	cacactttggagggtttctc	ctggaaaagcaaacagtcgc	449 bp
SNCA Knockout 943 bp	cagcttccatgcttctaactc	ctttatacacatcacaggggc	943 bp
SNCA Knockout 1927 bp	ccacaagggctgagagat	tggtcatcctccacctga	1927 bp
SNCA$^{S87E/S87E}$ Clones Check 5'	actgtctagctcctgtgctc	tagccgttccccacagtaag	1188 bp
SNCA$^{S87E/S87E}$ Clones Check 3'	caatatgattatctttctagggttaaccc	gttgttgtgcttactcacttcc	1133 bp
SNCA$^{S87E/S87E}$ Clones Cassette Removal Check	ctgctgcaacttacctccgggatg	ccaatcctccccttgctgtcctg	323 bp

Table 2.1 PCR primers for identifying putative *SNCA* knockout and *SNCA*$^{S87E/S87E}$ clones.

Products of the *SNCA*$^{S87E/S87E}$ Clones Check 5' PCR reaction were digested with *Ava*I (NEB) and *Ava*II (NEB) in CutSmart® buffer or with *Bsr*DI (NEB) in NEBuffer™ 2.1 (NEB). PCR or digestion products were electrophoresed in agarose gels with Quick-Load® 100 bp DNA ladder (NEB) or 1 kb DNA ladder (NEB).

2.3.2. Western blotting

Cell pellets of putative *SNCA*$^{-/-}$, *SNCA*$^{+/-}$ and *SNCA*$^{S87E/S87E}$ hESC clones was lysed with RIPA Lysis Buffer System (Santa Cruz) according to manufacturer's instructions. The protein concentration of cell lysate was quantified using BCA assay (Thermo Fisher Scientific). Following the quantification, I incubated cell lysate equivalent to 15 µg of protein with NuPAGE™ LDS loading dye (4x, Thermo Fisher Scientific) and NuPAGE™ Sample Reducing Agent (10x, Thermo Fisher Scientific) at 70°C for 10 minutes, then loaded them on NuPAGE™ 4-12% Bis-Tris Protein Gel (Thermo Fisher Scientific) with SeeBlue™ Plus2 ladder (Thermo Fisher Scientific). The protein was electrophoresed at 50 V until the dye reached 1/3 of the gel and at 100 V for the rest of the gel. The protein was subsequently transferred onto Amersham™ Protran™ Premium 0.45 µm NC nitrocellulose membrane (Amersham) at 300 mA for 1.5 hour at 4°C. The membrane was fixed with 0.4% paraformaldehyde (PFA, Fisher) for 30 minutes and blocked with 10% blocking-grade blocker (BioRad) in 0.05% TBS-N.

Mouse anti-α-Syn primary antibody (BD, 1:1000) was added in 5% blocking-grade blocker in 0.05% TBS-N and rocked at 4°C overnight. The membrane was then washed and rocked in secondary antibody HRP conjugated anti-mouse IgG (Promega, 1:2000) for 2 hours at room temperature. Subsequently, the membrane was washed and incubated with Pierce™ ECL Western Blotting Substrate (Thermo Fisher Scientific) before image acquisition with Odyssey® RC (LI-COR) and Image Studio software. The membrane was exposed for 30 seconds under 700nm and 2 minutes under Chem channel. I then removed the antibodies with Restore™ PLUS Western Blot Stripping Buffer (Thermo Fisher Scientific), blocked and reblotted the membrane with HRP conjugated anti-β-actin antibody (Abcam, 1:1000) in 5% blocking-grade blocker in 0.05% TBS-N for 2 hours at room temperature. Pierce™ ECL Western Blotting Substrate was applied prior to image acquisition.

2.3.3. TOPO-cloning and DNA sequencing

For sequencing, purified PCR products of putative *SNCA*$^{-/-}$, *SNCA*$^{+/-}$ and *SNCA*$^{S87E/S87E}$ hESC clones were incubated with Taq DNA polymerase (NEB) at 72°C for 10 minutes and inserted into pCRTM4-TOPO® vector (TOPO® TA Cloning® Kit for Sequencing, Thermo Fisher Scientific) according to manufacturer's instructions. Alternatively, the purified PCR products were inserted into pCRTM-Blunt II-TOPO® vector (Zero Blunt® TOPO® PCR Cloning Kit, Thermo Fisher Scientific) without Taq DNA polymerase incubation according to manufacturer's instructions. The plasmids were then transfected into competent *E. coli* DH5α cells according to manufacturer's instructions and plated on Carbenicillin (100 µg/ml, for TA Cloning® Kit) or Kanamycin (30 mg/ml, Fisher, for Zero Blunt® kit) supplemented LB/agar plates. The next day, I picked TOPO-clones into Carbenicillin supplemented LB medium. After overnight incubation, plasmids were isolated with QIAprep Spin Miniprep Kit (QIAGEN). The purified plasmids were digested with *Eco*RI (NEB) in NEBuffer™ 2.1 and electrophoresed in 1% agarose gel to check for insertion of alleles. The TOPO-clone plasmids or purified PCR products of putative *SNCA*$^{-/-}$, *SNCA*$^{+/-}$ and *SNCA*$^{S87E/S87E}$ clones were sent for Sanger sequencing at the MRC PPU DNA Sequencing and Services (Dundee), using the following primers (5' – 3') or PCR primers, respectively:

T7: taatacgactcactataggg

M13 reverse: caggaaacagctatgac

2.3.4. Single nucleotide polymorphism (SNP) array analysis

Genomic DNA of *SNCA*$^{-/-}$, *SNCA*$^{+/-}$ and *SNCA*$^{S87E/S87E}$ hESC clones was extracted using MasterPure™ Complete DNA and RNA Purification Kit according to manufacturer's instructions. The samples were sent for SNP analysis at Wellcome Trust Clinical Research Facility (Edinburgh) using Illumina HumanCytoSNP-12 v2.1 BeadChip. The data was analysed following similar approach as in (Canham et al., 2015). To detect copy-neutral loss of heterozygosity (CN-LOH) and CNVs, BeadArray v2–Standard algorithm and genome build GRCh37 were used in BlueFuse Multi (v4.4, Illumina). The algorithm was set to detect CN-LOH larger than 1 Mb with > 200 significant clones and CNVs with > 10 significant clones. β-allele frequency and smoothened Log R ratio plots were generated for identified regions. For *SNCA*$^{-/-}$, *SNCA*$^{+/-}$ and *SNCA*$^{S87E/S87E}$ hESC clones, CN-LOH regions and CNVs in addition to those found in WT parental line were reported.

2.3.5. Off-target analysis

The top 2 predicted off-target sites of gRNAs were obtained from the Zhang Lab CRISPR DESIGN webtool (Table 2.2).

	locus position	locus sequence (5' – 3')	mismatches
off-target #1 of gRNA 5G1	chr15:+46664956	TGTATTCCAGTACACCACACCAG	3
off-target #2 of gRNA 5G1	chr10:+80560295	TGAGTTCCTCTCCACCACACCAG	3
off-target #1 of gRNA 3G1	chr9:+93313553	GCCATGGCTGTATTCAAGAAAAG	2
off-target #2 of gRNA 3G1	chr22:+25774724	GCCCTGGGTGCATTCATGAAGAG	3
off-target #1 of gRNA #1	chr16:-11829783	ACAGAGACACCTTGCCCAACGGG	3
off-target #2 of gRNA #1	chr12:-92057538	ACTGCCATATATTGCCCAACTAG	3
off-target #1 of gRNA #5	chr12:+3380314	TTTGTAAGTTGGTGAGATTAGGG	2

off-target #2 of gRNA #5	chr10:+87437618	TTTGTAGCCTGGTGAGATTAAAG	3

Table 2.2 Location, sequence and number of mismatches of the top 2 off-target sites of gRNAs.

PCR primers were designed to flank these regions (Table 2.3).

PCR reaction	Forward (5' – 3')	Reverse (5' – 3')	Product size
off-target #1 of gRNA 5G1	ccagacttcacaaccaccca	caggatcaagtggggtgtgg	370 bp
off-target #2 of gRNA 5G1	tggcagcaggtttcctactc	gctcttggttgtactggcct	527 bp
off-target #1 of gRNA 3G1	gcttgggcaacacaatgaga	acctgtctatccgtctgccc	532 bp
off-target #2 of gRNA 3G1	catgctctgcctcaaccaga	cagagaggcaggcatgtgaa	311 bp
off-target #1 of gRNA #1	ctagggcagtgattttggg	tatggcaccccaggataag	602 bp
off-target #2 of gRNA #1	ttacccggtcgtggatcatt	gagagcctacgcatcatcttga	817 bp
off-target #1 of gRNA #5	caagccctttgtggagctgg	cctgtctcaaactgaaagttaggc	778 bp
off-target #2 of gRNA #5	gctggtggtgaagaaatgagattc	cccaagtctacatgattttcagc	465 bp

Table 2.3 Sequence and product size of PCR primers used for off-target analysis.

The 449 bp PCR product covering the α-Syn knockout region of *SNCA*$^{+/-}$ clone 4-4 and the 591 bp PCR product covering the S87E region of a DNA mix from *SNCA*$^{S87E/S87E}$ clone B21H4 and WT DNA in equal ratio were used as positive controls. PCR products of these regions were denatured, re-annealed to allow the formation of heteroduplex DNA, and digested by T7 endonuclease 1 (T7E1, NEB) in NEBuffer™ 2 (NEB) at 37°C for 20 minutes. Digestion products were electrophoresed in agarose gel with Quick-Load® 100 bp DNA ladder.

2.3.6. Plasmid integration check

PCR primers were designed to cover plasmid origin, U6 promotor, gRNA, part of Cas9n and part of puroR sequences of gRNA-Cas9n plasmid, as well as partial PGK promotor, partial puroR and partial ΔTK sequences of piggyBac HDR plasmid (Table 2.4).

PCR reaction	Forward (5' – 3')	Reverse (5' – 3')	Coverage	Product size
oug	cttggagcgaa cgacctaca	cggtgtttcgtc ctttccac	plasmid origin, U6 promotor and gRNA sequences of gRNA-Cas9n plasmid	555 bp
Cas	accagagcaa gaacggctac	atccgctcgat gaagctctg	part of the Cas9n sequence	427 bp
cp	gacaaagtgct gtccgccta	gagttcttgcag ctcggtga	part of Cas9n and part of puroR sequences	516 bp
pp	ctcgcacacatt ccacatcca	gagttcttgcag ctcggtga	part of PGK promotor and part of puroR sequences	646 bp

Table 2.4 Sequence and product size of PCR primers used for checking plasmid integration.

As positive control for PCR reactions oug, Cas and cp, I mixed WT DNA with *Not*I linearized gRNA #1 gRNA-Cas9n plasmid. To ensure the copy number of WT DNA equals that of plasmid DNA, the amount of plasmid DNA was calculated according to the ratio of the molar mass of the human genome (2.08×10^{12} g/mol) and that of the plasmid (5.97×10^{6} g/mol).

Similarly, for positive control of PCR reaction pp, I mixed WT DNA with *Not*I linearized piggyBac plasmid and ensured the copy number of WT DNA equals that of plasmid DNA, according to the ratio of the molar mass of the human genome (2.08×10^{12} g/mol) and that of the plasmid (5.51×10^{6} g/mol).

PCR products were electrophoresed in agarose gel with Quick-Load® 100 bp DNA ladder.

2.4. mDA differentiation

For mDA differentiation, hESCs were retrieved from liquid nitrogen storage for self-renewal and passaged once before differentiation. On differentiation day 0, hESCs with a confluency of 70 – 95% were plated on Laminin-111 (L111, Biolamina, diluted to 5 µg/ml with DPBS (Mg^{2+} Ca^{2+}, Thermo Fisher Scientific))-coated 24-well plates (Corning), according to adaption from a published protocol (Nolbrant et al., 2017). The hESCs were plated as clumps of 4-8 cells at a density of 40,000 cells/cm^2. From day 0 to day 4, cells were differentiated in Neural Induction Medium (NIM), which was equal volumes of DMEM/F12 (Thermo Fisher Scientific) and Neurobasal Medium (Thermo Fisher Scientific) supplemented with B27 (without Vitamin A, 1:50, Thermo Fisher Scientific), N2 (1:100,

Thermo Fisher Scientific) and L-Glutamine (2 mM, Thermo Fisher Scientific). From day 4 to day 11, cells were differentiated in Neural Patterning Medium (NPM) which had similar components as NIM, apart from half of the B27 and N2 supplement concentrations. From day 11, cells were differentiated in Neural Differentiation Medium (NDM), which was Neurobasal Medium supplemented with B27 (1:50) and L-Glutamine (2 mM).

From day 0 to day 9, SB431542 (SB, 10 µM, Millipore), LDN-193189 (LDN, 100ng/ml, Miltenyi Biotec), Shh-C24II (SHH, 600ng/ml, R&D Systems) and CHIR99021 (CHIR, 1 µM unless specified, Miltenyi Biotec) were added in NIM or NPM. Medium was changed on day 2, day 4 and day 7. From day 9 to day 11, FGF8b (100 ng/ml, R&D Systems) and heparin (1 µg/ml, Sigma) were added to NPM. On day 11, cells were lifted with Accutase (Sigma) and re-plated on L111-coated 24 or 48-well plates (Corning) as single cells, at a density of 800,000 cells/cm^2. From day 11 to day 16, FGF8b, heparin, ascorbic acid (AA, 0.2 mM, Sigma), brain-derived neurotrophic factor (BDNF, 20 ng/ml, Peprotech) and glial cell line-derived neurotrophic factor (GDNF, 10 ng/ml, Peprotech) were added to NDM. Cells were fed on day 14 and lifted with Accutase on day 16, followed by re-plating on L111-coated 24 or 48-well plates as single cells, at a density of 800,000 cells/cm^2 (unless specified otherwise). From day 16 to day 45, cells were fed every 2 – 3 days with NDM supplemented with BDNF, GDNF, AA, dibutyryl cyclic AMP (db-cAMP, 0.5 mM, Sigma) and N-[N-(3,5-difluorophenacetyl)-l-alanyl]-S-phenylglycine t-butyl (DAPT) (1 µM, Tocris). To obtain cultures with lower density, cells were lifted with Accutase on day 23 and re-plated as clumped of 2-4 cells. The clumps were plated on poly-ornithine (0.0015%, Sigma) and L111-coated 24-well plates or 8-well glass bottom plates (ibidi) at either 25,000 cells/cm^2 or 80,000 cells/cm^2 (unless specified otherwise). After day 23 re-plating, feeding frequency was reduced to weekly replacing half of the culture media with fresh media. From day 45, DAPT was omitted from the feeding medium.

Alternative to re-plating, differentiation was cryopreserved occasionally, either at day 11 or at day 16. The progenitors were frozen in multipes of 100 µl and at a density of 1.2 million cells per 100µl freezing medium, which was STEM-CELLBANKER supplemented with 10 µM of Y2. For thawing, cells were retrieved from liquid nitrogen storage, washed in 10 times volume of NPM (day 11 vials) or NDM (day 16 vials) and re-plated on L111-coated 24-well or 48-well plates at 1.2 million cells per cm^2. For each re-plating (on day 0,

day 11, day 16 and occasionally day 23) and thawing (day 11 and day 16), Y2 (10 μM) was added to help cell survival and was removed at the next medium change.

2.5. Immunostaining

Cells were fixed with 4% PFA (diluted from 37 – 41% with PBS (Thermo Fisher Scientific), Fisher). Depending upon the type of secondary antibodies to be used, cells were blocked with either 2% donkey serum (Sigma) or 2% goat serum (Sigma) in PBS-T (0.1% Triton X-100 (Fisher) in PBS). The blocked cells were incubated with primary antibodies (Table 2.5) in 2% serum in PBS-T at 4°C overnight. The cells were then washed with PBS and incubated with Alexa Fluor secondary antibodies (1:1000 dilution in PBS-T, see Appendix 1 for supplier information) at room temperature for 2 hours. Subsequently, cells were washed with PBS, with an optional incubation with DAPI (1:10000 dilution in PBS, Thermo Fisher Scientific).

Antibody	Dilution	Supplier
goat anti-NANOG	1:500	R&D Systems
mouse IgG2b anti-OCT3/4	1:100	Santa Cruz
rabbit anti-LMX1A	1:1000	Millipore
goat anti-FOXA2	1:100	Santa Cruz
rabbit anti-tyrosine hydroxylase	1:1000	Millipore
mouse IgG2a anti-tyrosine hydroxylase	1:1000	Biolegend
sheep anti-COL1A1	1:200	R&D Systems
rabbit anti-PDGFRα	1:300	Cell Signaling
mouse IgG2b anti-β-III tubulin	1:1000	Abcam
mouse IgG1 anti-α-Syn	1:250	BD
mouse IgG2a anti-PSD95	1:250	Biolegend
rabbit anti-synapsin	1:1000	Millipore
rabbit anti-phospho-S129 α-Syn	1:1000	Abcam
mouse IgG2a anti-p62 (SQSTM1)	1:200	Abcam

Table 2.5 Primary antibodies used in this study.

2.6. CORIN flow cytometry

Cells were lifted at day 16 with Accutase and washed with NDM. Cells were then centrifuged at 800 g for 2 minutes and resuspended in flow cytometry buffer, which was DPBS (without Mg^{2+} and Ca^{2+}, Sigma) supplemented with 2% fetal calf serum (Thermo Fisher Scientific). The resuspended cells were then split into 3 tubes: the first one unstained, the second one stained with rat anti-CORIN antibody (R&D Systems, 1:500) and the final one stained with isotype control (R&D Systems, 1:500). They were incubated on ice for 15 minutes. The stained cells were washed with flow cytometry buffer and incubated with donkey anti-rat IgG Alexa Fluor-488 (Thermo Fisher Scientific) for 15 minutes on ice. Subsequently, the stained cells were washed with flow cytometry buffer and analysed on BD FACS Calibur (BD Biosciences). The data was processed and plotted with FlowJo (version 10.0.7, BD).

2.7. Gene expression analysis

2.7.1. RNA extraction

Total RNA was isolated from cell pellets using either MasterPureTM Complete DNA and RNA Purification Kit (Epicentre) or RNeasy Plus Micro Kit (QIAGEN) according to manufacturer's instructions. RNA concentration was quantified using either NanoDrop® ND-1000 Spectrophotometer (NanoDrop Technologies) or Qubit assay (Thermo Fisher Scientific) following manufacturer's instructions. RIN^e score was obtained using TapeStation (Agilent Technologies) following manufacturer's instructions.

2.7.2. RNAseq

Total RNA was isolated from day 79 cells with RNeasy Plus Micro Kit (QIAGEN) according to manufacturer's instructions. The RNA samples were kept in −80°C at all times and shipped to QIAGEN Genomic Services (Germany) on dry ice for QIAseq UPX 3' Transcriptome RNAseq analysis. For each sample, 10 ng of purified RNA was converted into cDNA NGS libraries using the QIAseq UPX 3' Transcriptome Kit (QIAGEN). During reverse transcription, each sample was tagged with a unique ID and each RNA molecule was tagged with a unique molecular index (UMI). RNA was converted to cDNA and the cDNA was amplified using PCR, during which the PCR indices were added. After PCR the samples were purified and QC using TapeStation

4200 (Agilent) or Agilent Bioanalyzer. Based on quality of the inserts and the concentration measurements, the libraries were pooled in equimolar ratios. The library pool was quantified using qPCR and then sequenced on a NextSeq500 sequencing instrument according to the manufacturer instructions. Raw data was de-multiplexed and FASTQ files were generated using the bcl2fastq software (Illumina Inc.). FASTQ data was checked using the FastQC tool. Primary data analysis was performed using the QIAGEN GeneGlobe bioinformatics tool to demultiplex cells, align reads to reference genome and count UMIs. Secondary analysis was performed using DESeq2 and results were visualised as volcano plots. Principal component analysis (PCA) and unsupervised clustering were performed to quantify the biological differences between the samples. Results were visualised using PCA plot and heatmap, respectively.

2.7.3. cDNA synthesis and reverse transcription quantitative PCR (RT-qPCR)

cDNA was synthesized from 500 ng of total RNA using the SuperScript™ IV Reverse Transcriptase (Thermo Fisher Scientific) according to manufacturer's instructions. qPCR was performed using the Roche LightCycler® 480 System with the Universal Probe Library (UPL) (Roche). Intron-spanning primers were designed using the Roche UPL Assay Design Centre (https://lifescience.roche.com/en_gb/brands/universal-probe-library.html#assay-design-center), with a specific UPL probe for each pair of primers (Table 2.6). Reactions containing cDNA, primers, UPL Probe, LightCycler® 480 Probes Master mix (Roche) and nuclease-free water (total volume 10 µl) were performed in 384-well plates according to manufacturer's instructions. The expression level of genes of interest were calculated using the ΔΔct method and normalised to the expression level of TATA-binding protein (TBP), with primer efficiency = 2, unless calculated otherwise by a serial dilution standard curve. See Appendix 2 for R scripts used for analysing RT-qPCR data. Results were plotted in Prism 8 (version 8.2.1, GraphPad Software, Inc.) as mean of technical replicates.

Gene	Forward primer (5' – 3')	Reverse primer (5' – 3')	Probe number
TBP	gaacatcatggatcagaacaaca	atagggattccgggagtcat	87
LMX1A	tggaggagaacttccaaagc	cagacagacttggggctcac	3

FOXA2	cctggagtgttccagctacg	ccagcaaggtagcactcaaa	80
EN1	gcacacgttattcggatcg	gcttgtcctccttctcgttc	88
OTX2	gcagcctccacacatcaaa	cgggaccccacatttgta	38
BARHL1	tgagccctttggatctaatg	ggacggagttcagccttg	82
SIX3	gtcctcatcgcccctctc	cggaataccatggactgacc	69
GBX2	gctgctcgctttctctgc	gctgtaatccacatcgctctc	63
NANOG	tctccaacatcctgaacctca	ttgctattcttcggccagtt	87
OCT4	tgccgtgaaactggagaag	gcttggcaaattgttcgagt	78
DAT	agactgcccgaagtgtgc	gcagtttcccgttacaccaa	14
NURR1	atttcctcgaaaacgcctgt	catactgcgcctgaacacaa	41
SOX6	gcttctggactcagcccttta	ggcccttagcctttggtta	50
VMAT2	cgggattctgcatcatgttt	tggcaatcagcaggaagg	67

Table 2.6 Primers and probes for RT-qPCR.

2.8. Dopamine ultra-performance liquid chromatography with tandem mass spectrometer (UPLC-MS/MS) analysis

Conditioned media was collected from day 105 mDA cultures after a full media change on day 101. After collecting the 4-day conditioned media, the cultures were equilibrated in media supplemented with 50 mM sucrose overnight and on day 106, the conditioned media was replaced by fresh sucrose supplemented media and incubated for 15 minutes to reduce the osmolarity shock. The conditioned media was again replaced by fresh sucrose supplemented media and incubated for 15 minutes before the conditioned media was collected as an isotonic control. After that, the cultures were exposed to fresh media supplemented with 25 mM KCl and incubated for 15 minutes before the conditioned media was collected. All samples were frozen on dry ice immediately upon collection and sent to Edinburgh Clinical Research Facility (Edinburgh) for dopamine UPLC-MS/MS analysis. The samples were processed by Dr Joanna Simpson and Dr Natalie Homer using the following procedures.

Dopamine was extracted from cell media by solid phase extraction using Strata Strong Cation Exchange (SCX) cartridges (55 µm, 100 mg/mL) and derivatised with proprionic anhydride prior to LC-MS/MS. A published method was as adapted and applied to cell

media analysis (Zhang et al., 2016). All samples were enriched with 1 ng dopamine-1,1,2,2-d_4 hydrochloride (Dopamine-d4, Cerilliant) as internal standard and diluted into 0.1 M hydrochloric acid (400 µl). Cartridges were conditioned with methanol (400 µl) before the sample was loaded. The cartridges was then washed with methanol (400 µl) and 0.1 M HCl (400 µl) and eluted with acetonitrile:propionic anhydride (90:10 v/v) with 2% pyridine (1 mL) and acetonitrile (400 µl). The eluate was collected, capped and heated at 60°C for 20 minutes, to form a proprionate derivative of dopamine. The solution was reduced to dryness under nitrogen at 40°C and reconstituted in mobile phase (100 µl water:acetonitrile (90:10, v/v)). A calibration standard curve of dopamine (0.025–10 ng) was prepared alongside the samples for quantitative analysis of dopamine in the samples.

Chromatographic separation was achieved on a Waters Acquity Classic UPLC system with an Acquity UPLC BEH C18 column (50 x 2.1 mm; 1.7 µm, Waters), protected by an Acquity in-line filter (Waters) and operated at 45°C. The mobile phase consisted of 0.1% formic acid in water (A) and 0.1% formic acid in acetonitrile (B) at a flow rate of 0.5 ml/minute. Gradient elution was achieved with a total run time of 7.5 minutes, from 15% to 85% B. Dopamine was detected on a QTrap 5500 triple quadrupole mass spectrometer (Seiex), operated in positive ion electrospray mode (5.5 kV, 500°C, ion source gas 1 at 60 psig and gas 2 at 40 psig). In multiple reaction mode, transitions monitored were m/z 322.0 -> 136.9 and m/z 326.0 -> 140.9 for dopamine and dopamine-d4, respectively and peaks eluted at 2.3 minutes. The peak area ratio of dopamine/dopamine-d4 was used to calculate the amount of dopamine in the sample by linear regression analysis of the calibration curve (0.025 – 10 ng).

After sample collection for conditioned media, the cultures were fixed with 4% PFA and stained for TH, β-III tubulin and DAPI. For each well, a 14 mm^2 area was imaged as a representative region at 10x with tiling on Nikon TiE. Number of cells were obtained by particle analysis of the DAPI channel and anaylsed for their positivity of TH and β-III tubulin (see Appendix 3 for ImageJ macro script). The number of TH / β-III tubulin double positive cells of each representative image was summarised in Excel. Based on the growth area of each well, the total number of TH / β-III tubulin double positive cells was estimated and used for normalisation of the level of dopamine detected by UPLC-MS/MS.

2.9. Production of PFFs

α-Syn PFFs were produced by Marco Kriek (UCB Pharma Ltd., Slough, UK) using the following procedures (Chen et al., 2019) and shipped on dry ice.

Human *SNCA* cDNA was cloned into a plasmid for mammalian expression, pMKC451, under the control of a CMV promoter. This plasmid (1 mg) was transfected into Expi293 cells (> 97% viability, 2.5 billion cells) grown in Expi293 Expression Medium (Thermo Fisher Scientific) using Expi293fectamine (Thermo Fisher Scientific) and Opti-MEM (Thermo Fisher Scientific), according to manufacturer's instructions. The culture was incubated at 37°C, 120 rpm, 8% CO_2 (Kuhner Shaker X) and after 17 hours Enhancers 1 and 2 (Thermo Fisher Scientific) were added as specified. The culture was harvested 4 days after transfection (typical viability 40%) by centrifugation (90 minutes, 5000 g, JS4.2 rotor in J6-MI Beckman) and filter sterilised through a 0.22 µm filter (Millipak Gammagold, Millipore) using a Sartobran P 0.45 + 0.22 µm prefilter (Sartorius Stedim).

Supernatant was diluted with an equal volume 20 mM Tris/HCl pH 8.0 solution, constituted in FlowFusor pyrogen free water (Fresenius Kabi) and was passed over a 2x 5 ml HiTrap Q FF column (GE Healthcare). Bound protein was eluted with a gradient to 0.4 M NaCl in 20 mM Tris/HCl over 20 column volumes. Fractions with α-Syn were pooled, concentrated using a Centriprep 10K, 10,000 NMWL spin filter (Millipore) and buffer exchanged into 20 mM Tris/HCl pH 8.0 solution using a HiPrep 26/10 desalting column (GE Healthcare). Anion exchange chromatography was repeated using a MonoQ 10/100GL column (GE Healthcare) and fractions with α-Syn were pooled, concentrated and purified over a HiLoad 26/600 Superdex 75 column (GE Healthcare) equilibrated in PBS (Sigma) constituted in FlowFusor pyrogen free water. Analysis throughout the purifications was performed by NuPAGE™ 4-12% Bis/Tris gel electrophoresis using SeeBlue Plus2 ladder. The final pool was concentrated, filter sterilized (0.22 µm Millex GV, Millipore) to 5–10 mg/ml protein and stored at −80°C in BioPur Safe-Lock tubes (Eppendorf).

Protein was analysed by NuPAGE™ gel electrophoresis and a single protein species was observed. Electrospray mass spectrometry (ESI+) gave a deconvoluted mw of 14502 Da (mw calc. 14501 Da for N-acetylated species). Size exclusion chromatography with multi-angle static light scattering (SEC-MALS), JC-1 (Thermo Fisher Scientific) fluorescence (Lee et al., 2009) and attenuated total reflectance Fourier-transform infrared

(ATR-FTIR) spectrometry analysis were implemented to confirm that the recombinant human α-Syn was monomeric. Endotoxin level was measured by Limulus Amebocyte Lysate test (Charles River Laboratories). The protein was not phosphorylated at position serine-129 as determined by the pS129-αSyn antibody (Abcam) following NuPAGE™ gel electrophoresis.

The PFFs were prepared by shaking the purified human α-Syn monomer (7–10 mg/ml, 0.50 ml) in 1.5-ml BioPur Eppendorf vials at 1,200 rpm, 37°C for 10 days, using a VorTemp56 incubator (Labnet). The resulting material was analysed using JC-1 fluorescence on a Varian Cary Eclipse fluorimeter, as well as a 100 g ultracentrifugation (Beckman Optima TLX with a TLA-120.1 rotor) sedimentation to measure residual monomer by NuPAGE™ gel electrophoresis and ATRFTIR spectrometry analysis (Tensor 27, Bruker) (Kaylor et al., 2005). Material with a main JC-1 fluorescence absorbance at 540 nm, < 5% monomer as judged by NuPAGE™ electrophoresis of the ultracentrifugation supernatant and an ATR-FTIR absorption between 1,625 and 1,630 cm^{-1} was sonicated for 4x 10 seconds at 2.5 mg/ml PBS in 1.5-ml BioPur Eppendorf vial on ice using a Soniprep sonicator (MSE). The protein solution was aliquoted and frozen on dry ice and stored at −80°C in BioPur Eppendorf vials.

2.10. PFF treatment

On day 44 of mDA differentiation, neurons were exposed to α-Syn PFFs by a full media change with fresh media containing 5 µg/ml α-Syn PFFs (1:500 of 2.5 mg/ml stock added to fresh media). As negative controls, either 5 µg/ml of α-Syn monomers (diluted from 2.5 mg/ml) or equivalent volume of PBS were added to the fresh media for a full media change in these cultures. Until the cultures were used, half of the conditioned media was replaced weekly with fresh media without PFFs, monomers or PBS.

2.11. Lactate dehydrogenase (LDH) assay

Conditioned media was collected from 25,000 cells/cm^2 and 80,000 cells/cm^2 mDA cultures 3, 4 and 6 weeks after PFF treatment. The samples were processed immediately using Pierce LDH Cytotoxicity Assay Kit (Thermo Fisher Scientific), according to manufacturer's instructions. Briefly, a PBS vehicle-treated well of the same cell density was lysed with the provided lysis buffer (diluted according to instructions) at 37°C for 45 minutes. Samples (conditioned media, cell lysate positive control, LDH positive control or

media negative control) were added to 96-well plates at 50 µl/well in triplicates. Reaction Mix was prepared according to manufacturer's instructions and applied at 50 µl/well. After incubation at room temperature for 30 minutes, 50 µl/well of Stop Solution was added before taking measurements at 490 nm and 680 nm with FLUOstar Omega Microplate Reader (BMG Labtech). The reading at 490 nm was subtracted by the reading at 680 nm (background) and used as indicator of cytotoxicity.

2.12. Image acquisition and processing

2.12.1. pS129-αSyn / β-III tubulin staining

After immunostaining with pS129-αSyn and β-III tubulin, neurons were imaged with 20x or 40x Apo on Axio Observer (Zeiss) or Eclipse Ti-E (Nikon). The 20x images were snapped at one focus plane. The 40x images were taken as z-stack covering a range of 4.2 µm (either 15 slices at a step of 0.3 µm, or 13 slices at a step of 0.32 µm). The stack images were deconvoluted with Huygens Professional (version 19.04, Scientific Volume Imaging BV) using the following settings: number of interactions 50, Signal to Noise Ratio 40, quality threshold 0.01, and saved in .ics format.

The .ics images were processed with ImageJ (version 2.0.0, National Institutes of Health): z-projection images of the two channels were created respectively by projecting maximum intensity over all slices. For each channel, the maximum was lowered to a value where the structures can be seen clearly to aid the selection of binary thresholds. The two channels were then respectively converted to binary images. In order to only quantify pS129-αSyn structures within β-III tubulin-positive neurons, a Boolean "AND" function of the two binary images was performed. Selection over the entire image was created for each binary image (pS129-αSyn binary, β-III tubulin binary and the "AND" image) and the area of selection was measured. Area of the "AND" image was divided by area of the β-III tubulin binary image as a quantification of pS129-αSyn immunostaining in β-III tubulin-positive neurons. For 40x images, particle analysis was performed on the "AND" images to quantify the number, size and shape of pS129-αSyn structures in β-III tubulin-positive neurons. See Appendix 4 for ImageJ macro scripts used for analysing pS129-αSyn / β-III tubulin immunostaining.

Statistical analysis was performed using Prism 8. For area analysis in experimental settings with three parameters (exposure to PFFs, culture density and age), three-way ANOVA was performed on all pairs, with one different parameter. Post hoc tests were corrected for multiple comparisons using Sidak correction. For area analysis in experimental settings with two parameters (genotypes and exposure to PFFs), Welch one-way ANOVA was performed due to significant difference in standard derivations found among groups in Brown-Forsythe test, on all PFF versus control (monomer or PBS) pairs of the same genotype, as well as on pairs formed among different genotypes' PFF condition. Post hoc tests were corrected for multiple comparisons using Dunnett's T3 correction. For particle analysis, unpaired two-tailed Student's t-test was performed between the two genotypes.

Plots were generated using Prism 8, each data point denotes one image field and bars indicate mean ± standard derivation.

2.12.2. Synaptic staining

After immunostaining with PSD95, synapsin and β-III tubulin, neurons were imaged with 60x oil objective on Eclipse Ti-E with z-stack covering a range of 2.4 µm (25 slices at a step of 0.1 µm). The stack images were then deconvoluted with Huygens, using the following settings: number of interactions 50, Signal to Noise Ratio 40, quality threshold 0.01, and saved in .ics format. The .ics images were split into 3 channels and thresholded respectively with ImageJ.

The thresholded images were input to MATLAB, where PSD95 and synapsin particles without overlap with β-III tubulin staining were excluded as noise. Co-localisation of genuine PSD95 and synapsin particles was analysed in 3D and was considered mature, when a particle of the other synaptic marker was found within 1 µm. The MATLAB script output the number of mature PSD95 and synapsin particles, the total number of PSD95 and synapsin particles as well as the total volume of β-III tubulin staining. The number of PSD95 and synapsin particles was then normalised by the total volume of β-III tubulin staining. The percentage of mature particles among the total number of PSD95 and synapsin particles was also calculated.

See Appendix 5 for ImageJ macro script and see http://doi.org/10.25833/m1kq-xq79 for MATLAB script used for analysing PSD95 / synapsin / β-III tubulin

immunostaining. The MATLAB script is credited to Dr Marti Colom Cadena and Prof Tara Spires-Jones (University of Edinburgh).

Statistical analysis was performed in Prism 8 using two-way ANOVA on all PFF versus PBS pairs. Post hoc tests were corrected for multiple comparisons using Sidak correction. Plots were generated using Prism 8, each data point denotes one image field and bars indicate mean ± standard derivation.

2.12.3. Calcium imaging

The cells were incubated with either Fluo-4 (5 μM, Thermo Fisher Scientific) on day 141 cultures or with Fluo-8 (4 μM, Abcam) on day 94–96 cultures in fresh feeding media for 1 hour. The cells were then washed twice with Mg^{2+}-positive live imaging buffer (10 mM HEPES, 140 mM NaCl, 2.5 mM KCl, 2 mM $CaCl_2$, 2 mM $MgCl_2$ and 10 mM D-glucose) and imaged in Mg^{2+}-positive live imaging buffer at 2 frames/second (2 Hz). The day 141 25,000 cell/cm^2 cultures with different genotypes were imaged with 5x on Axio Observer. The day 94–96 80,000 cells/cm^2 WT cultures treated with PFF or PBS control were imaged with 10x on Eclipse Ti-E.

The baseline activities were recorded for 2 minutes (240 frames) before half of the buffer was replaced by Mg^{2+}-free live imaging buffer (10 mM HEPES, 140 mM NaCl, 2.5 mM KCl, 2 mM $CaCl_2$ and 10 mM D-glucose) and recorded for another 2 minutes. The half buffer change followed by 2-minute recording was repeated a few more times, till Mg^{2+} concentration reached 1/8 (day 94–96 cultures) or 1/16 (day 141 cultures) of the original concentration. For day 141 cultures, neurons were stimulated with L-glutamate (L-Glu, 10 μM) in Mg^{2+}-positive live imaging buffer and recorded for 2 minutes, followed by exposure to KCl (20 mM) in Mg^{2+}-positive live imaging buffer and 2-minute recording.

The time lapse stacks were then exported as tiff series images and input to the Cell Detection programme in MATLAB. Regions of interest (ROIs) brighter than surrounding pixels were selected according to their fluorescence intensity change before and after KCl exposure, from the highest to the lower ones. The number and size of ROIs were adjusted according to the density of the cultures and to the microscope objective to make sure most of the cell bodies were captured without including regions that were not cell bodies. The change in fluorescence intensity of

each ROI over the entire recording was extracted with the Batch Extract programme. Signal traces were then input to the Event Detection programme to detect bulk events. During each condition (different Mg^{2+} conditions or exposure to KCl), the number and magnitude of events detected for each ROI was summarised as average magnitude of event, the number of events per cell (ROI) and the percentage of active cells (number of events > 0). The MATLAB scripts used for analysing calcium imaging remained property to Dr Graham Robertson and Dr Michele Zagnoni (University of Strathclyde, Glasgow) and are not published at the moment.

Plots were generated using ggplot 2 (version 3.1.1, http://ggplot2.tidyverse.org) in RStudio (version 1.1.456, RStudio, Inc.). See Appendix 6 for R scripts used for generating these plots.

2.12.4. TMRM live imaging

The cultures were incubated with TMRM (25 nM, Thermo Fisher Scientific) and Hoechst (1:10000, GeneCopoeia) for 15 minutes in Mg^{2+}-positive live imaging buffer and imaged with 60x oil on Eclipse Ti-E with z-stack covering a range of 4.8 µm (25 slices at a step of 0.2 µm). The cultures were then fixed with 4% PFA and stained for β-III tubulin. Based on manual alignment of Hoechst, β-III tubulin channel images of the same field were captured with 60x oil on Eclipse Ti-E with z-stack covering a range of 4.8 µm (25 slices at a step of 0.2 µm). The stack images were then deconvoluted with Huygens, using the following settings: number of interactions 50, Signal to Noise Ratio 40, quality threshold 0.01, and saved in .ics format.

Based on β-III tubulin channel, the cell bodies without any overlapping were selected with the polygon tool. For each cell, the 6 most in-focus stacks in the TMRM channel were selected and auto-thresholded. The thresholded cells were then measured for their cell size, as well as the average size, shape and axes of mitochondria using the 3D Geometrical Measurements, 3D Shape Measurements and 3D ellipsoid fitting functions in the ImageJ 3D analysis plugins (https://imagejdocu.tudor.lu/plugin/analysis/3d_analysis/start), respectively. See Appendix 7 for ImageJ macro scripts for analysing TMRM live imaging.

Statistical analysis was performed in Prism 8 using unpaired two-tailed Student's t-test between PFF and PBS groups. Plots were generated using Prism 8, each data point denotes one cell and bars indicate mean ± standard derivation.

Chapter 3: *SNCA*$^{+/-}$, *SNCA*$^{-/-}$ and *SNCA*$^{S87E/S87E}$ mutants were generated by CRISPR/Cas9n targeting in hESCs

3.1. Introduction

As *Snca*$^{-/-}$ mice were resistant to α-Syn pathology (Bétemps et al., 2014; Blumenstock et al., 2017; Karampetsou et al., 2017; Kim et al., 2019; Luk et al., 2012a; Masuda-Suzukake et al., 2014; Recasens et al., 2014; Sacino et al., 2014b; Volpicelli-Daley et al., 2011), I knocked out *SNCA* in hESCs to produce mDA neurons with resistance to synucleinopathy. However, due to concerns about the physiological functions of α-Syn, I introduced a single amino acid mutation (S87E) in α-Syn, aiming to deliver synucleinopathy resistance (Oueslati et al., 2012; Tuttle et al., 2016) without disrupting physiological functions of α-Syn. For parental hESC line, I chose clinical-grade line RC17 since it has the necessary regulatory paperwork in place to be used in cell therapy clinical trials (De Sousa et al., 2016).

To deliver *SNCA* deletion and S87E mutation, I used the highly efficient and precise CRISPR system. To minimize the off-target effects, I used the nickase mutant of Cas9, Cas9-D10A (Cas9n) (Jinek et al., 2012). Cas9n generates single-strand breaks in DNA and introduces double-strand breaks (DSBs) when a pair of Cas9n/gRNA complexes with appropriate spacing is used. Compared to the DSBs mediated by Cas9, the extra gRNA binding required by Cas9n significantly reduces the number of off-target events (Ran et al., 2013a).

SNCA deletion can be achieved by non-homologous end joining (NHEJ), while *SNCA*$^{S87E/S87E}$ mutation requires a homology-directed repair (HDR) template. For HDR template, I utilized the piggyBac transposon system, which is a highly specific, footprint-free and seamless gene editing technique. Delivered as a plasmid, it allows for drug selection of targeted clones and thus reduces the workload for genotyping (Singh et al., 2015).

Since the emergence of CRISPR/Cas9 technology, off-target insertion, deletion and point mutation have been a prevalent issue (Cradick et al., 2013; Fu et al., 2013; Hsu et al., 2013), although the frequency of off-target indels has been largely reduced by the use of Cas9n (Cho et al., 2014; Fu et al., 2014; Ran et al., 2013a). In addition, cases where

part of the gRNA plasmid and Cas9 plasmid integrated into host genome have been reported (Cradick et al., 2013; Fu et al., 2013). Depending upon the location of insertion, it could disrupt normal functions of genes and induce host immune response.

In this chapter, I presented my work on the generation of putative *SNCA*$^{-/-}$, *SNCA*$^{+/-}$ and *SNCA*$^{S87E/S87E}$ hESC clonal lines by CRISPR/Cas9n targeting, as well as on the assessment of genomic integrity of these clonal lines by detection of single nucleotide polymorphism (SNP), off-target events and plasmid integration.

3.2. *SNCA*$^{+/-}$ and *SNCA*$^{-/-}$ hESC clones were generated by CRISPR/Cas9n targeting

To knockout *SNCA*, I targeted exon 2, the first coding exon of *SNCA* (Figure 1.2). Employing Cas9n requires one pair of guide RNAs (gRNAs) per DNA DSB. Therefore, to delete exon 2, one pair of gRNAs was used for each end of the exon. To identify the gRNA pairs with the highest cleavage efficiency, a series of gRNA pairs were designed using the Zhang Lab CRISPR DESIGN webtool (http://crispr.mit.edu). The top two pairs flanking the 5' end (5G1 + 3G1, 5G2 + 3G2) and the top two pairs flanking the 3' end (5G3 + 3G3, 5G4 + 3G4) of exon 2 were cloned individually into the pSpCas9n-2A-Puro (pX462) plasmid (Ran et al., 2013b) at the *Bbs*I restriction sites (Figure 3.1a). These gRNA-Cas9n plasmid pairs were then tested for deletion efficiency in HEK 293 cells (data not shown). Based on cleavage efficiency in HEK 293 cells, 5G1 and 3G1 gRNAs was picked for targeting the 5′ end of *SNCA* exon 2, and 5G4 and 3G4 gRNAs for targeting the 3′ end (Figure 3.1b).

a)

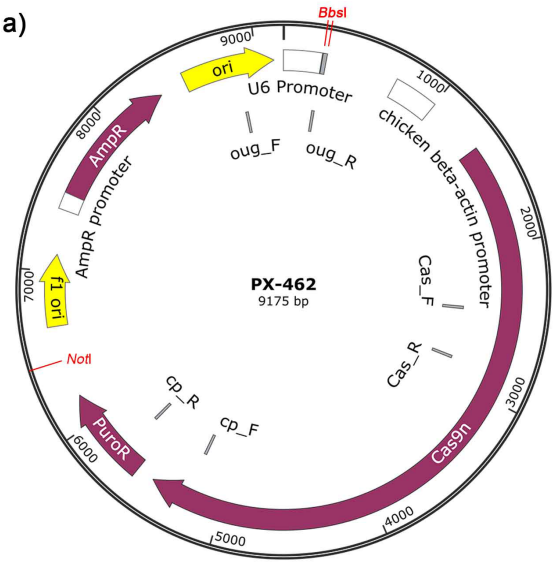

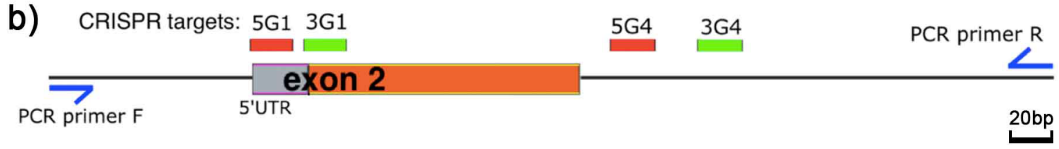

Figure 3.1 Exon 2 of *SNCA* was targeted for α-Syn knockout using gRNA-Cas9n plasmid pX462.

a) Schematic of gRNA-Cas9n plasmid (pX462). A *Bbs*I double digestion was used to insert the gRNA-coding fragment of customized sequence under control of the U6 promoter. The puromycin resistant gene and Cas9n were expressed under the chicken β-actin promoter.

b) Schematic of relative location of gRNAs to *SNCA* genomic sequence. Exon 2, where the α-Syn coding sequence starts, was targeted with Cas9n and 2 pairs of gRNAs flanking exon 2. PCR primers used for detecting exon deletion are indicated with blue arrows. 5G1: 5' gRNA for the 5' end, 3G1: 3' gRNA for the 5' end, 5G4: 5' gRNA for the 3' end, 3G4: 3' gRNA for the 3' end.

I electroporated the hESCs with gRNA-Cas9n plasmids of the four gRNAs and plated the electroporated hESCs sparsely to allow for selection of single cell-derived clones. Since the pX462 plasmid also expresses puromycin resistance gene (puroR, Figure 3.1a), I used puromycin to select transfected hESCs. At 8 – 14 days after selection, I picked 115 hESC colonies into individual wells of 96-well plates (Table 3.1). I replica plated the 51 surviving clones and isolated their genomic DNA. I screened for clones with exon 2 deletion using a PCR assay, which should result in a 449 bp PCR product if exon 2 was intact (Figure 3.2a), as the 5' primer was 90 bp upstream of 5G1 gRNA and 3' primer was 139 bp downstream of 3G4 (Figure 3.1b). In this initial PCR screening, I identified 9 putative *SNCA*$^{-/-}$ clones and 4 putative *SNCA*$^{+/-}$ clones (Table 3.1). The WT PCR band was ~450 bp as expected and the knockout *SNCA* alleles were typically 200 – 400 bp (Figure 3.2a).

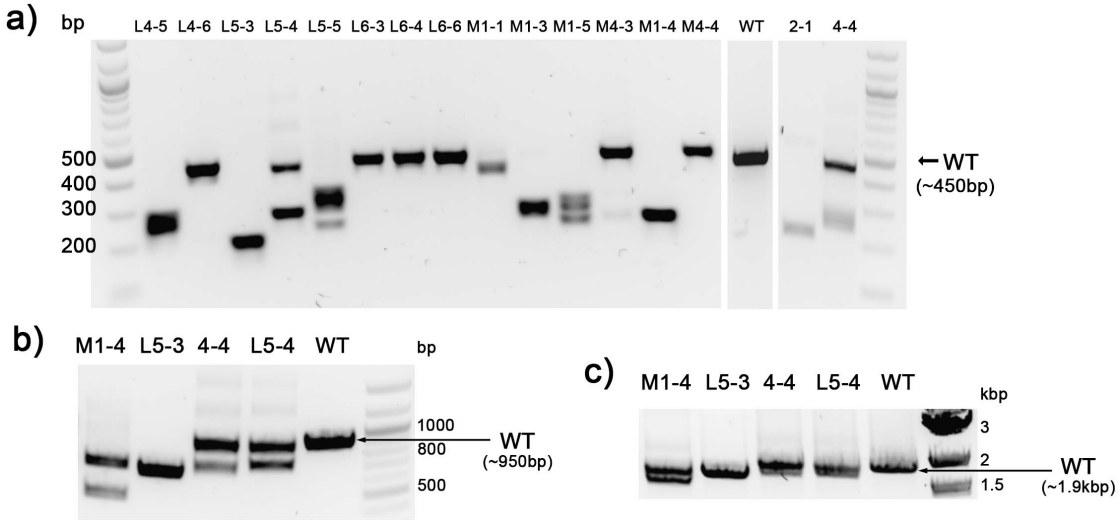

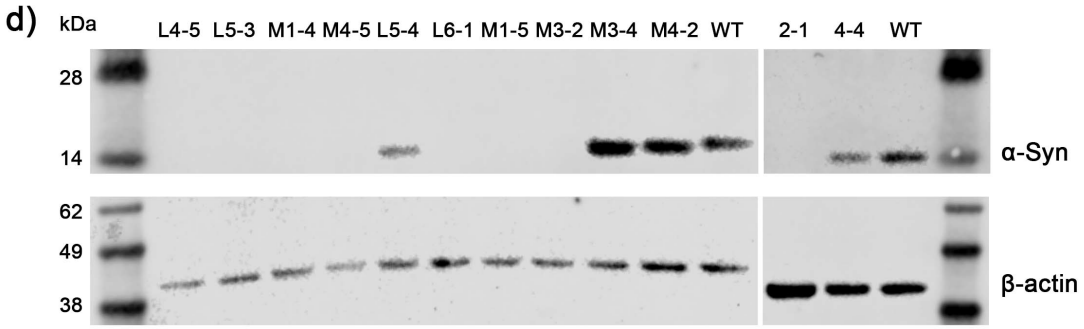

Figure 3.2 Putative α-Syn knockout clones were identified by PCR and western blotting.

a) 449 bp PCR screening of clones revealed several putative *SNCA*$^{-/-}$ clones (including M1-4 and L5-3) and *SNCA*$^{+/-}$ clones (L5-4 and 4-4).

b) 943 bp PCR screening of clones revealed the second allele of putative *SNCA*$^{-/-}$clone M1-4, which had a larger deletion.

c) 1927 bp PCR screening of clones did not reveal another allele of putative *SNCA*$^{-/-}$ clone L5-3.

d) Western blotting screening of clones revealed α-Syn protein was absent in several putative *SNCA*$^{-/-}$ clones (including M1-4 and L5-3) and was expressed at a reduced level in putative *SNCA*$^{+/-}$ clones (L5-4 and 4-4).

	Number of clones picked after puromycin selection	Number of clones survived	Putative clones by PCR	Putative clones by western blotting
Transfection 1 plated on L111	32	3	2 *SNCA*$^{-/-}$ 1 *SNCA*$^{+/-}$	1 *SNCA*$^{-/-}$ 1 *SNCA*$^{+/-}$
Transfection 2 plated on L111	50	17	3 *SNCA*$^{-/-}$ 1 *SNCA*$^{+/-}$	3 *SNCA*$^{-/-}$ 1 *SNCA*$^{+/-}$
Transfection 2 plated on Matrigel	33	31	4 *SNCA*$^{-/-}$ 2 *SNCA*$^{+/-}$	4 *SNCA*$^{-/-}$ 0 *SNCA*$^{+/-}$

Table 3.1 Number of clones derived, putative *SNCA*$^{+/-}$ and *SNCA*$^{-/-}$ clones revealed by PCR and western blotting in *SNCA* knockout targeting.

To investigate if there were larger deletions, especially in putative *SNCA*$^{-/-}$ clones, M1-4 and L5-3, which showed only one apparent allele in short-range PCR, I genotyped putative *SNCA*$^{-/-}$ and *SNCA*$^{+/-}$ clones with long-range PCR assays. I designed a 943 bp PCR (Figure 3.2b), where 5' primer was 338 bp upstream of 5G1 gRNA and 3' primer was 385 bp downstream of 3G4. This 943 bp PCR revealed a second allele of putative *SNCA*$^{-/-}$ clone M1-4, which was ~400 bp shorter than WT allele and was not detected by the short-range PCR assay. However, putative *SNCA*$^{-/-}$ clone L5-3 still showed only one apparent allele, therefore I designed a 1927 bp PCR (Figure 3.2c), where 5' primer was 843 bp upstream of 5G1 gRNA and 3' primer was 864 bp downstream of 3G4. Similar to

two short-range PCRs, only one apparent allele was detected in putative *SNCA*$^{-/-}$ clone L5-3, suggesting that the second allele was of similar size to the other allele or had a large deletion beyond the detection of the 1927 bp PCR reaction.

To investigate whether putative *SNCA*$^{-/-}$ clone L5-3 had alleles of similar sizes but with different sequences, the 449 bp PCR product of L5-3 was TOPO-cloned (Figure 3.3a) and sent for Sanger sequencing. All TOPO-clones reported exactly the same sequence with a 250 bp deletion (traces not shown). To further confirm the absence of an alternative sequence, I sent the 449 bp PCR product of L5-3 for sequencing. The sequencing trace did not show presence of any double peaks, suggesting that the existence of a second allele with a similar deletion size is highly unlikely (Figure 3.3c).

As for putative *SNCA*$^{-/-}$ clone M1-4, two alleles with different deletion sizes were isolated by TOPO-cloning of 943 bp PCR (Figure 3.3b) but not by TOPO-cloning of 449 bp PCR (Figure 3.3a). The TOPO-clones of 943 bp PCR were hence sent for sequencing and revealed one allele with a 214 bp deletion and another with a 428 bp deletion, both of which removed the ATG start codon in exon 2 (Figure 3.3c & e).

Similarly, 449 bp PCR product of putative *SNCA*$^{+/-}$ clones 4-4 and L5-4 were TOPO-cloned for isolation of alleles (Figure 3.3a) and subsequently sent for sequencing. Traces revealed that in one allele of clone 4-4, there was a 210 bp deletion removing the ATG start codon, while the other allele was intact (Figure 3.3d & e). Clone L5-4 had a 175 bp deletion in one allele resulting in the removal of ATG start codon, while in the other allele, there was a 12 bp repeat (insertion) in the 5’ untranslated region (5′ UTR) and a 28 bp deletion in the intron downstream of exon 2 (Figure 3.3d & e).

To validate the level of α-Syn protein expression in these clones and others, I performed western blotting with cell lysate of hESC clones (Figure 3.2d). Eight out of the 9 putative *SNCA*$^{-/-}$ clones originally identified by the 449 bp PCR, including clones M1-4 and L5-3, did not express α-Syn protein at a detectable level. Two out of the 4 putative *SNCA*$^{+/-}$ clones originally identified by the 449 bp PCR, i.e. clones 4-4 and L5-4, exhibited reduced α-Syn expression. This suggested that the 12 bp insertion in the 5’ UTR and the 28 bp deletion in intron 2 did not abolish the α-Syn expression of *SNCA*$^{+/-}$ clone L5-4.

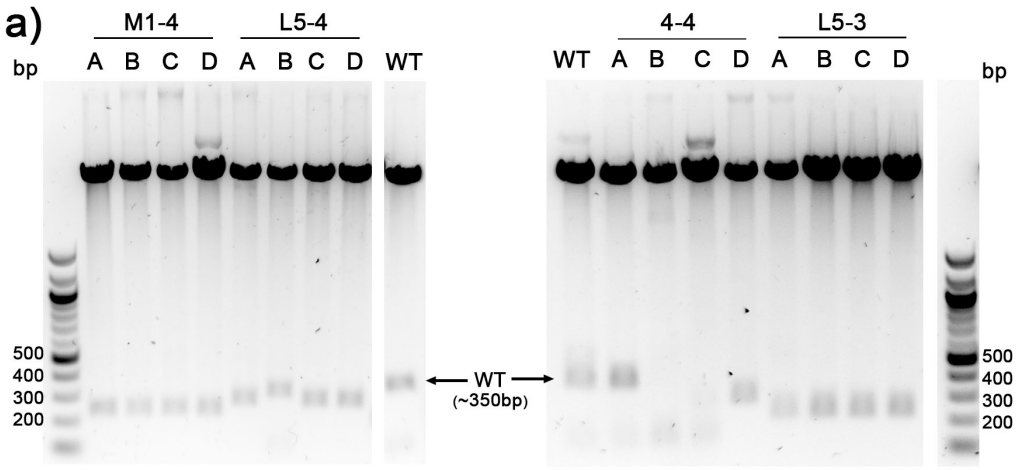
a)
M1-4
L5-4
4-4
L5-3
bp
A B C D A B C D WT
WT A B C D A B C D
bp
500
400
300
200
WT
(~350bp)
500
400
300
200

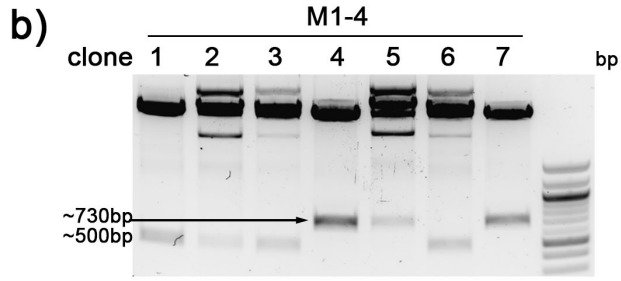
b)
M1-4
clone 1 2 3 4 5 6 7
bp
~730bp
~500bp

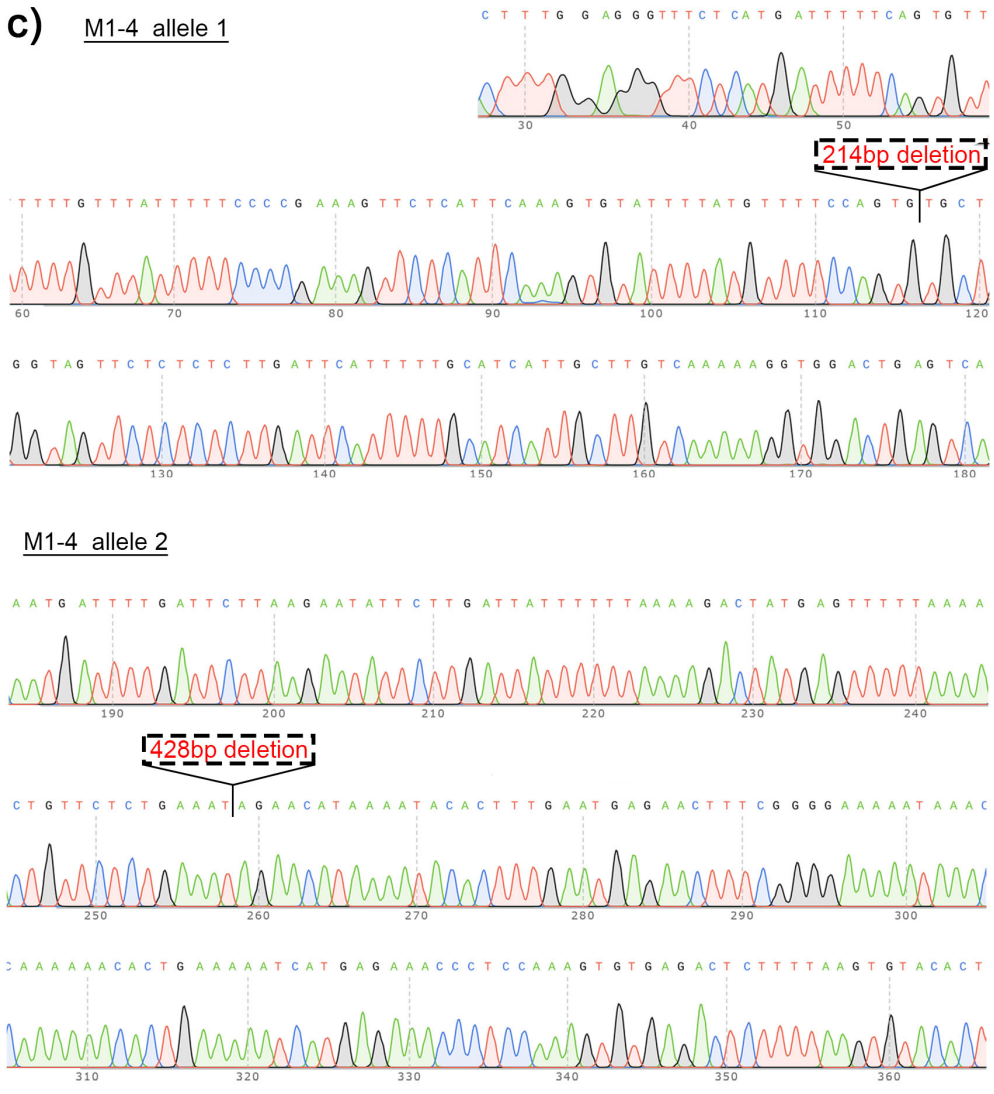
c)
M1-4 allele 1
214bp deletion
M1-4 allele 2
428bp deletion

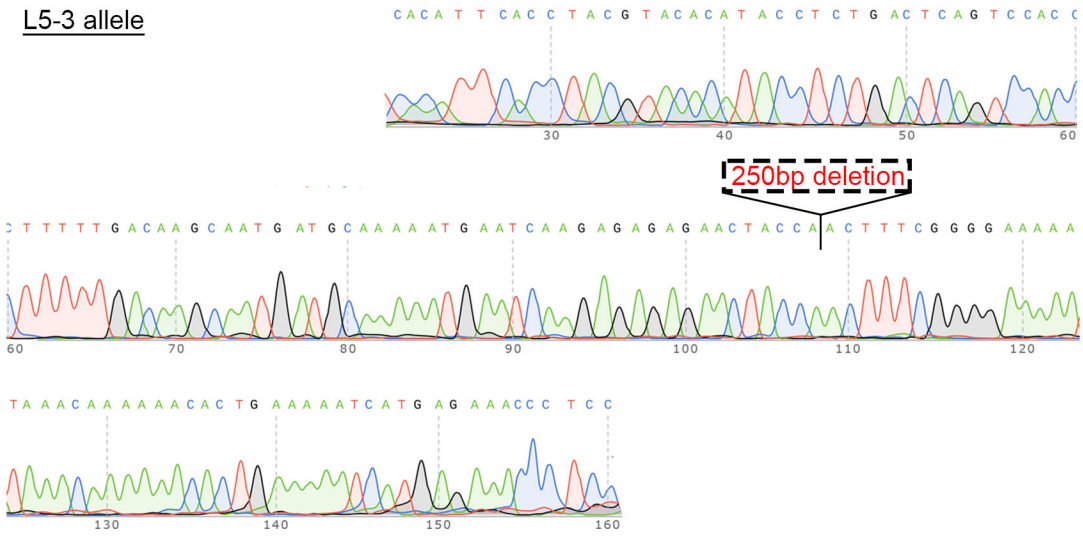
L5-3 allele
250bp deletion

d)

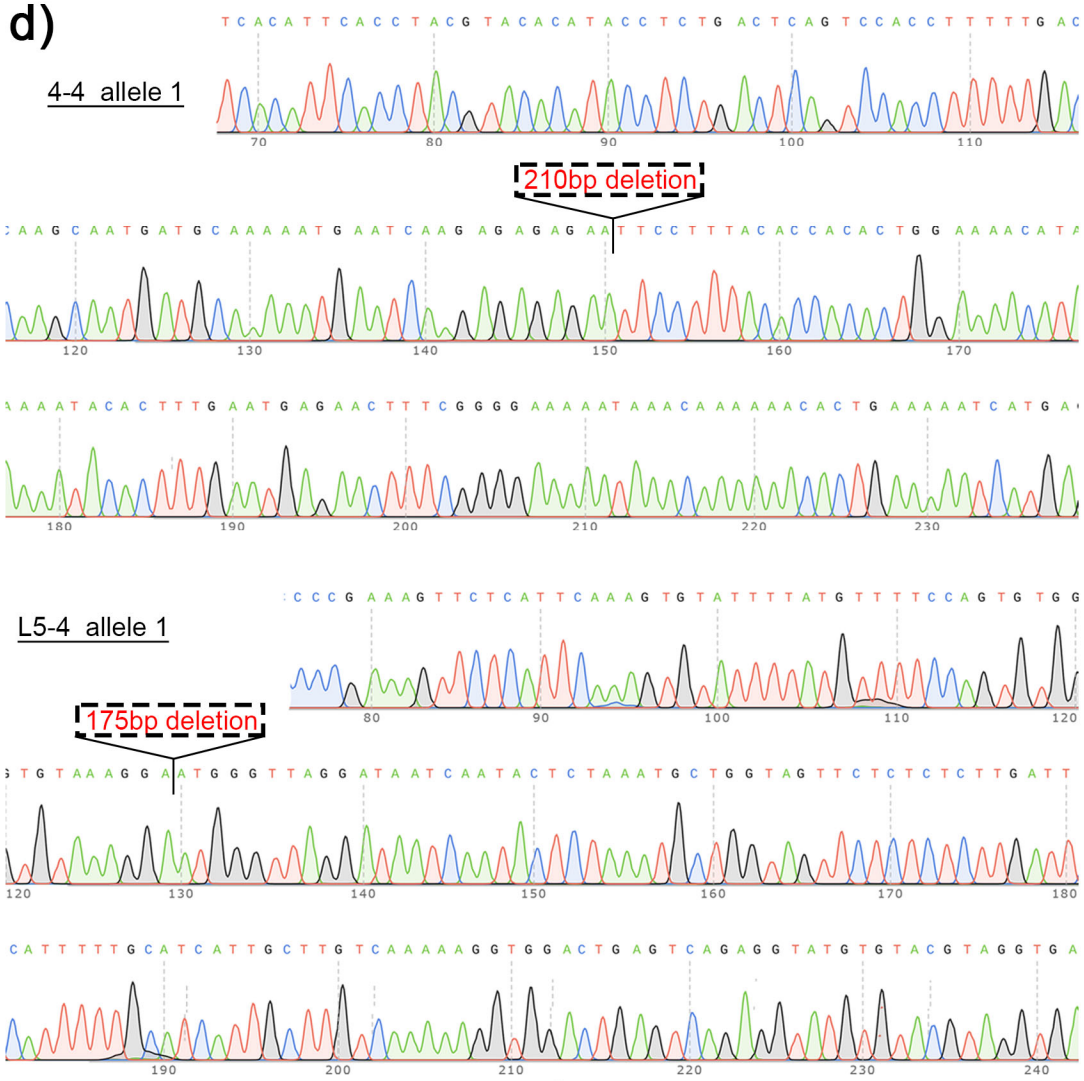
4-4 allele 1
210bp deletion
L5-4 allele 1
175bp deletion

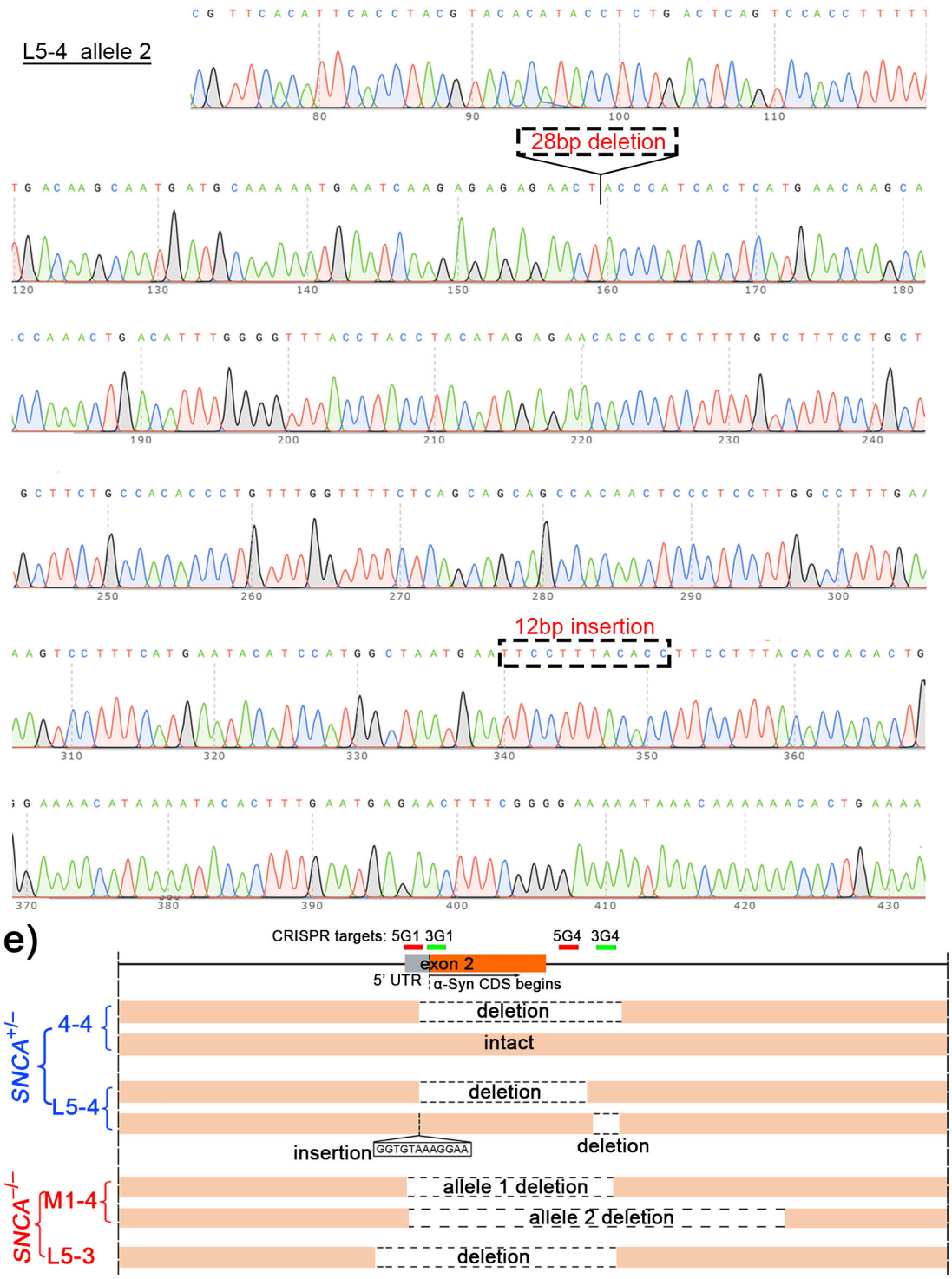

Figure 3.3 Identity of putative *SNCA*$^{+/-}$ and *SNCA*$^{-/-}$ clones was confirmed by restriction enzyme digestion and sequencing of TOPO-clones.

a) *Eco*RI digestion of four independent TOPO-cloned PCR products from 449 bp PCR of putative *SNCA*$^{-/-}$ and *SNCA*$^{+/-}$ clones. Two alleles of different sizes were captured in each *SNCA*$^{+/-}$ clone, while TOPO-clones from each *SNCA*$^{-/-}$ clone had consistent size.

b) *Eco*RI digestion of seven independent TOPO-cloned PCR products from 943 bp PCR of putative *SNCA*$^{-/-}$ clone M1-4, where two alleles of different sizes were captured.

c) Sequencing traces of TOPO-cloned products of *SNCA* alleles from *SNCA*$^{+/-}$ clones 4-4 and L5-4, marking the size and location of indels.
d) Sequencing traces of TOPO-cloned products of *SNCA* alleles from *SNCA*$^{+/-}$ clone M1-4 and PCR product of *SNCA*$^{+/-}$ clone L5-3, marking the size and location of deletions.

e) Schematic summary of sequencing results: two *SNCA*$^{+/-}$ clones (L5-4 and 4-4) and two *SNCA*$^{-/-}$ clones (M1-4 and L5-3) were identified.

3.3. *SNCA*$^{S87E/S87E}$ hESC clones were generated by CRISPR/Cas9n targeting with piggyBac transposon plasmid as HDR template

To generate *SNCA*$^{S87E/S87E}$ homozygous hESC clones, I used CRISPR/Cas9n to create a DNA DSB near S87 and provided a piggyBac transposon plasmid pMSC-AAT_PB-PGKpuroTK (Yusa, 2013) as an HDR template.

Similar to constructing gRNA-Cas9n plasmid for *SNCA* knockout, I designed a series of gRNA pairs flanking S87 in exon 4 of α-Syn with the Zhang Lab CRISPR DESIGN webtool and cloned the top 2 pairs (gRNAs #1 and #5, #2 and #15 in Figure 3.4b) into pX462 plasmid at the *Bbs*I restriction sites (Figure 3.1a).

To construct the piggyBac transposon plasmid, I PCR amplified the 5' homology arm (HA) and 3' HA from the genomic DNA of parental hESC line RC17. Together with a synthetic mutation-containing double-strand DNA fragment, the 5' HA was assembled into the piggyBac transposon plasmid by double digestion with *Asc*I and *Nsi*I. The 3' HA was subsequently integrated by double digestion with *Pac*I and *Hpa*I (Figure 3.4a).

a)

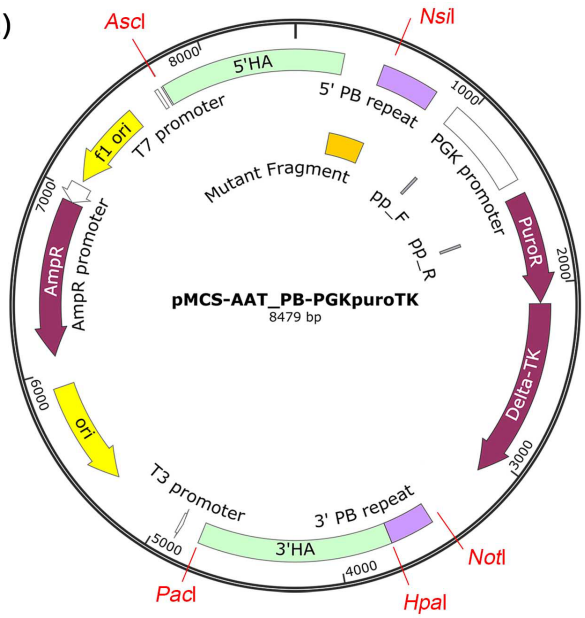

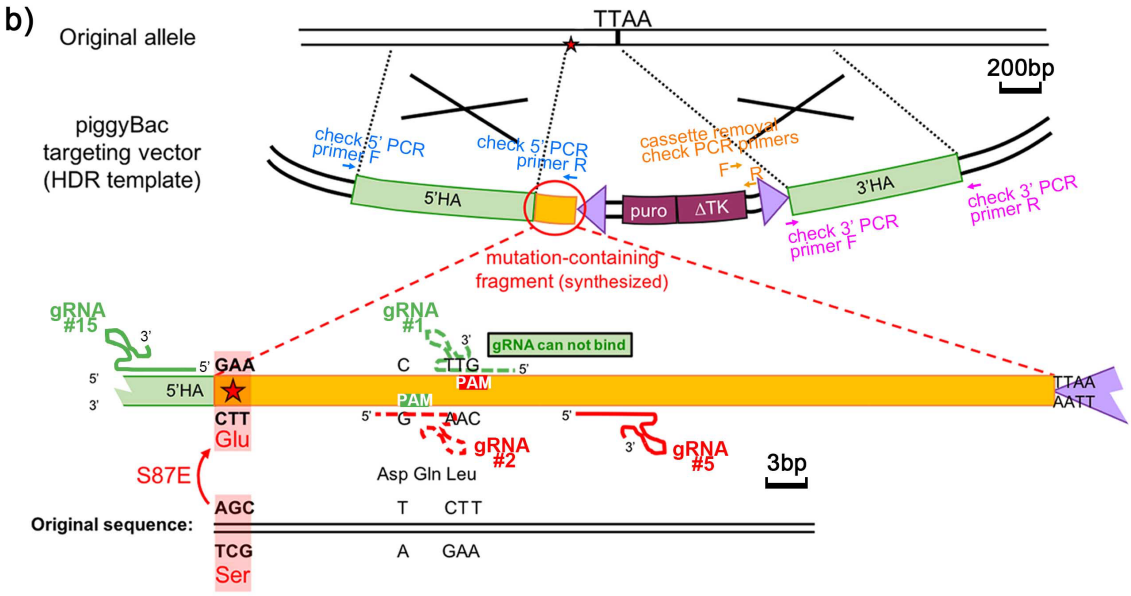

Figure 3.4 Seamless *SNCA*$^{S87E/S87E}$ mutation was delivered by CRISPR/Cas9n targeting with piggyBac transposon plasmid as homology-directed repair (HDR) template.

a) Schematic of piggyBac transposon plasmid showing digestion sites for assembly of homology arm (HAs) and mutated sequence into plasmid backbone. 5' HA and synthesized mutant fragment were Gibson assembled into backbone of piggyBac plasmid, which was obtained by *Asc*I + *Nsi*I double digestion. 3' HA was Gibson assembled into backbone of 5' HA containing piggyBac plasmid, which was obtained by *Pac*I + *Hpa*I double digestion. Puromycin resistant gene and Delta-TK were expressed under PGK promoter, while the former enabled puromycin selection after integration of piggyBac cassette into cell genome, the latter enabled FIAU selection after removal of piggyBac cassette.

b) Upon CRISPR/Cas9n targeting, piggyBac transposon integrated into cell genome with the help of Has and served as an HDR template. The mutations were left seamlessly in the genome after a second round of targeting with hyPBase which removed the piggyBac cassette. A 5' gRNA (#1 or #15) was paired with a 3' gRNA (#5 or #2) to generate a DNA double-strand break. Four nucleotides complementary to gRNA #1 and gRNA #2 and their PAM sites were also mutated in the mutant fragment to prevent gRNA binding (indicated by dash gRNAs) and unintended cleavage of the piggyBac plasmid.

Following a DSB induced by CRISPR/Cas9n, the piggyBac plasmid transposed into a TTAA site close to the DSB with the help of the HAs (Yusa, 2013). This brought in the mutations which were contained in the synthetic DNA fragment, as well as a piggyBac cassette which could be removed in a second transfection, leaving no genomic footprint behind. Since the chosen TTAA site (212 bp downstream of S87E mutation) is not located between any of the gRNA pairs, it was impossible to use the piggyBac cassette insertion to disrupt the CRISPR target site. Thus, to prevent cutting of the piggyBac plasmid and

re-cutting of the edited alleles, it was necessary to introduce synonymous point mutations to the sequence complementary to gRNAs and PAM sites. Therefore, in the synthetic DNA fragment, apart from the intended S87E (agc -> gaa) mutation, 4 other nucleotides complementary to gRNAs or protospacer adjacent motif (PAM) sites were also mutated synonymously (Figure 3.4b). This prevents gRNA #1 and gRNA#2 from binding to the HDR plasmid or the edited allele, and hence prevents the HDR plasmid from being CRISPR/Cas9 targeted and prevents re-cutting of the edited allele. As for the piggyBac cassette, it contains puromycin resistant gene (puroR) and 1-(2-deoxy-2-fluoro-1-β-D-arabinofuranosyl)-5-iodouracil (FIAU) sensitive gene (ΔTK), both of which were used for subsequent clonal selection.

To test the efficiency of the 4 gRNAs with the suggested pairing (B and C), as well as with mix and match (A and D), I electroporated RC17 hESCs with each pairing together with the piggyBac HDR template (Table 3.2). I plated the electroporated hESCs sparsely and used puromycin to select transfected single cell-derived clones. Out of a total of 36 clones I picked, 21 were derived from combination B (Table 3.2), which was the top suggested pairing on the CRISPR DESIGN webtool.

	5' gRNA	3' gRNA	Spacing between PAMs	Number of clones picked	Number of clones survived	Number of putative *SNCA*$^{S87E/S87E}$ clones
A	#1	#2	2	4	4	0
B	#1	#5	57	21	18	2
C	#15	#2	62	6	5	0
D	#15	#5	117	5	3	0

Table 3.2 Summary of gRNAs combinations and number of clones derived in *SNCA*$^{S87E/S87E}$ targeting.

I replica plated 30 surviving clones and isolated their genomic DNA. I screened for clones with S87E (agc -> gaa) mutation with a 1188 bp PCR, where 5' primer was 32 bp upstream of 5' HA and 3' primer was 153 bp downstream of S87E mutation (primers indicated by blue arrows in Figure 3.4b and Figure 3.5a & c). When this PCR product is double digested with *Ava*I and *Ava*II, a WT allele will have 3 fragments of sizes 364 bp, 701 bp and 123 bp, while a S87E allele will have only 2 fragments of sizes 364 bp and 824 bp due to the loss of *Ava*II restriction site (Figure 3.5a). Electrophoresis of the digested products revealed 4 putative *SNCA*$^{S87E/S87E}$ clones (B6, B21, B20 and B16), in

which the ~800 bp S87E band (red arrows) was much stronger than the ~700 bp WT band (green arrows), suggesting a potential mix of *SNCA*$^{S87E/S87E}$ cells with cells harbouring WT allele (Figure 3.5b).

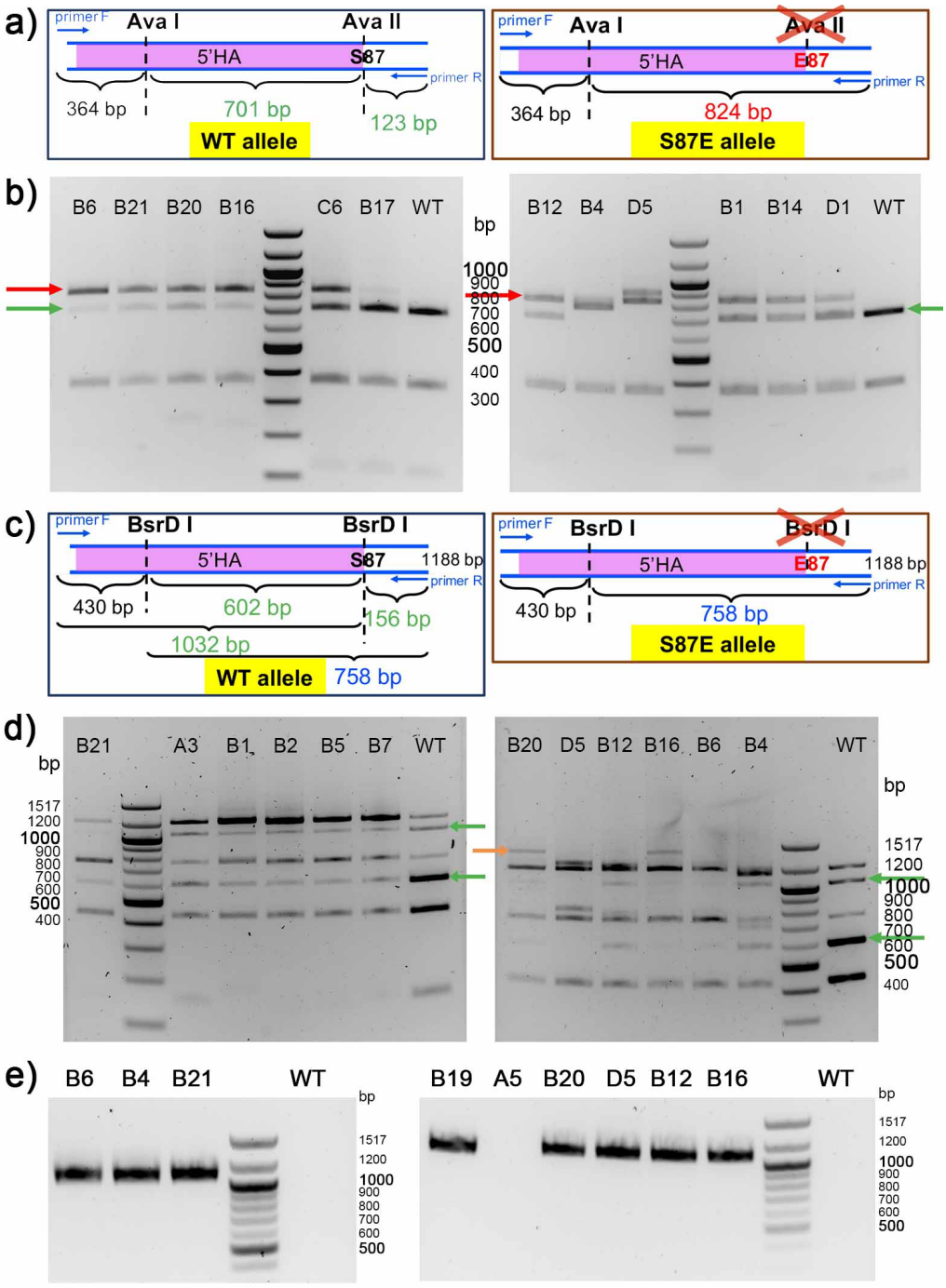

Figure 3.5 PCR screening revealed putative *SNCA*$^{S87E/S87E}$ clones upon piggyBac integration with hESC genome. PCR primers of a-d) are indicated by blue arrows in Figure 3.4b.
a) Upon *Ava*I + *Ava*II double digestion of the PCR product, WT allele had 3 fragments (364 bp, 701 bp and 123 bp) while S87E allele had only 2 fragments (364 bp and 824 bp) due to the loss of *Ava*II site.

b) Putative *SNCA*$^{S87E/S87E}$ clones (B6, B21, B20 and B16) were revealed by double digestion (*Ava*I + *Ava*II) of PCR product in a), where the ~800 bp band (red arrows) is much deeper than the ~700 bp (green arrows), suggesting a potential mix of *SNCA*$^{S87E/S87E}$ cells with cells with WT allele.
c) Due to partial digestion of PCR product with *Bsr*D*I*, WT allele had 6 possible fragments size (1188 bp, 430 bp, 758 bp, 602 bp, 156 bp and 1032 bp) while S87E allele had only 3 fragments (1188 bp, 430 bp and 758 bp) due to the loss of 3' *Bsr*DI site. Fragment sizes 602 bp, 156 bp and 1032 bp were unique to WT allele (indicated by green arrows).
d) Clones B20 and B16 were excluded from further investigation due to unexpected ~1.3 kb bands (orange arrow) in electrophoresis after *Bsr*DI digestion of PCR product in c). Green arrows indicated fragments of WT allele.
e) PCR covering 3' HA revealed that putative *SNCA*$^{S87E/S87E}$ clones B6 and B21 had the expected size (1133 bp), suggesting their 3' HAs are intact. The WT parental line (last lane of the left gel) was amplified as a negative control because the forward primer starts in the piggyBac cassette. PCR primers are indicated by magenta arrows in Figure 3.4b.

To further validate these putative *SNCA*$^{S87E/S87E}$ clones, the 1188 bp PCR product was digested with a different restriction endonuclease *Bsr*DI. Due to partial digestion by this enzyme, WT allele had 6 fragment sizes (1188 bp, 430 bp, 758 bp, 602 bp, 156 bp and 1032 bp) while S87E allele had only 3 fragment sizes (1188 bp, 430 bp and 758 bp) due to the loss of 3' *Bsr*DI site (Figure 3.5c). In agreement with the *Ava*I + *Ava*II digestion data, fragments of sizes 602 bp and 1032 bp, which are unique to WT allele (green arrows in Figure 3.5d), were relatively faint in the putative *SNCA*$^{S87E/S87E}$ clones B6, B21, B20 and B16. However, unexpected bands of ~1.3 kb (orange arrow in Figure 3.5d) were observed in clone B20 and B16, suggesting these two clones had unintended mutations and should be excluded from further investigation. To check the integrity of the 3' HA of putative *SNCA*$^{S87E/S87E}$ clones, I performed a 1133 bp PCR, where 5' primer was 26 bp upstream of 3' HA with 3 bp overlap with 3' HA and 3' primer was 57 bp downstream of 3' HA (primers indicated by magenta arrows in Figure 3.4b). Electrophoresis of PCR products suggested the 3' HAs of putative *SNCA*$^{S87E/S87E}$ clones B21 and B6 were intact.

To remove the piggyBac cassette from *SNCA*$^{S87E/S87E}$ clones B21 and B6, I electroporated these two hESC clones with plasmids expressing pCMV-HAhyPBase, the hyperactive mammalian-codon-optimized piggyBac transposase (Yusa, 2013). It removes the entire piggyBac cassette without leaving any genetic footprint, leaving only the intended mutations in the genome seamlessly. It also came with the desirable byproduct of isolation of *SNCA*$^{S87E/S87E}$ homozygous clones from WT allele-containing cells in clone B21 and B6. While optimizing the clonal selection process, I plated the transfected cells

at various density and selected for the cells free from piggyBac cassette by exposing them to two different concentration of FIAU (Table 3.3). Transfected cells plated at a density 5,000 – 20,000 cells/cm^2 and selected at 200 nM of FIAU gave rise to clones. Plating at low density (353 cells/cm^2) or selection at high FIAU concentration (500 nM) did not give rise to any clones. It is worth noting that an extra passage of the transfected cells (before plating sparsely for FIAU selection) boosted the efficiency of cassette removal (Table 3.3). This was most probably due to the extra passage allowed sufficient time for plasmid expression and transposition events, and more importantly, obviated the *bystander-killing effect*. The metabolised FIAU is toxic and can spread from cassette-retained cells to neighbouring cassette-removed cells. Cassette-retained cells and cassette-removed cells were likely to be located adjacently, since cell proliferation and transposition reactions were co-occurring. An extra passage after the transposition events allows for a redistribution of cells and therefore would largely reduce the bystander-killing effect.

	1st trial	2nd trial	3rd trial	4th trial
Transfection (µg of hyPBase plasmid)	7.5 µg	2 µg / 4 µg	4 µg	10 µg
Plating density (cells/cm^2)	**17.78k / 8.89k**	7.05k	**12.7k** / 0.353k	**10k / 5k**
Passage before FIAU selection	No	No	No	Yes
FIAU selection	200 nM	500 nM	500 nM / **200 nM**	200 nM
Number of clones picked	10 + 12	0	21 + 10	22 + 35
Number of clones without cassette	0 + 1	NA	1 + 0	6 + 6
Number of putative *SNCA*$^{S87E/S87E}$ clones	0 + 1	NA	1 + 0	6 + 6

Table 3.3 Efficiency of piggyBac removal under different transfection and selection conditions in the form of the number of clones picked, survived, cassette removed, and of which *SNCA*$^{S87E/S87E}$ homozygotes. Number of clones are documented in format of 'number of clones derived from B6 + number of clones derived from B21'. Conditions which gave rise to clones were indicated in bold.

After FIAU selection, I isolated single cell-derived clones and extracted their genomic DNA. Similar to the approach for screening putative *SNCA*$^{S87E/S87E}$ clones before cassette removal, I digested the 1188 bp PCR products with *Ava*I and *Ava*II (Figure 3.5a). Electrophoresis of the digested products suggested that the cells containing WT allele were isolated and most of the clones were *SNCA*$^{S87E/S87E}$ homozygotes (Figure 3.6a, where B6L1 was a putative *SNCA*$^{+/S87E}$ heterozygote). To confirm the piggyBac cassette has been successfully removed, I performed a 323 bp PCR with primers indicated by

orange arrows in Figure 3.4b and with the parental clone B21 as a positive control. Electrophoresis of the PCR products identified 14 putative *SNCA*$^{S87E/S87E}$ clones without the piggyBac cassette, including clones B21H4, 6hI, 21fB and 6fC (Figure 3.6b).

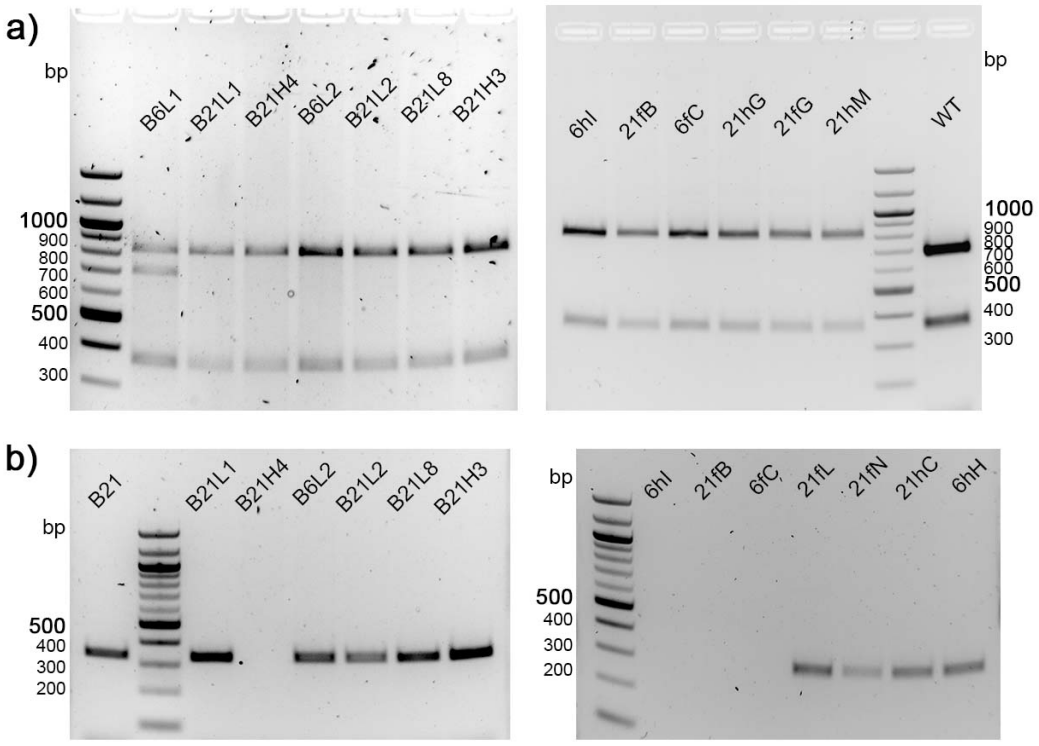

Figure 3.6 PCR screening revealed putative *SNCA*$^{S87E/S87E}$ clones after removal of piggyBac cassette.

a) Putative *SNCA*$^{S87E/S87E}$ clones were revealed by double digestion (*Ava*I + *Ava*II) of PCR product in Figure 3.5 a), where only ~800 bp band, not ~700 bp band was observed. B6L1 harbouring both ~800 and ~700 bp bands was a putative *SNCA*$^{+/S87E}$ heterozygote.

b) Putative *SNCA*$^{S87E/S87E}$ clones (B21H4, 6hI, 21fB and 6fC) with successful removal of piggyBac cassette were revealed by the absence of PCR product when amplifying a partial sequence of the piggyBac cassette. The parental clone B21 (lane 1 of the left gel) was amplified as a positive control. PCR primers are indicated by orange arrows in Figure 3.4b.

To validate the sequence of putative *SNCA*$^{S87E/S87E}$ clones, I PCR amplified a 2358 bp region of clones B6L, B21H4, 6hI, 21fB, 21fG and 6fG with primers check 5' F and check 3' R, covering the entire targeting region and both HAs (Figure 3.4b). I picked 10 – 14 TOPO-clones for each putative *SNCA*$^{S87E/S87E}$ clone and sent for Sanger sequencing. Most of the TOPO-clones were of expected size and reported a correct sequence with the S87E (agc -> gaa) mutation (Figure 3.7). The sequences of the rare atypical TOPO-clones were aligned with human genome using nucleotide BLAST (https://blast.ncbi.nlm.nih.gov). The alignments of the 4 atypical TOPO-clones in Table 3.4 were far from *SNCA*, which is

89724099 to 89838324 of chromosome 4, and were therefore highly likely to be TOPO-cloning artefacts. TOPO-clone 6fG_10 revealed a 370 bp loss 58 bp upstream of S87E, suggesting a small portion of cells in 6fG had a 370 bp deletion.

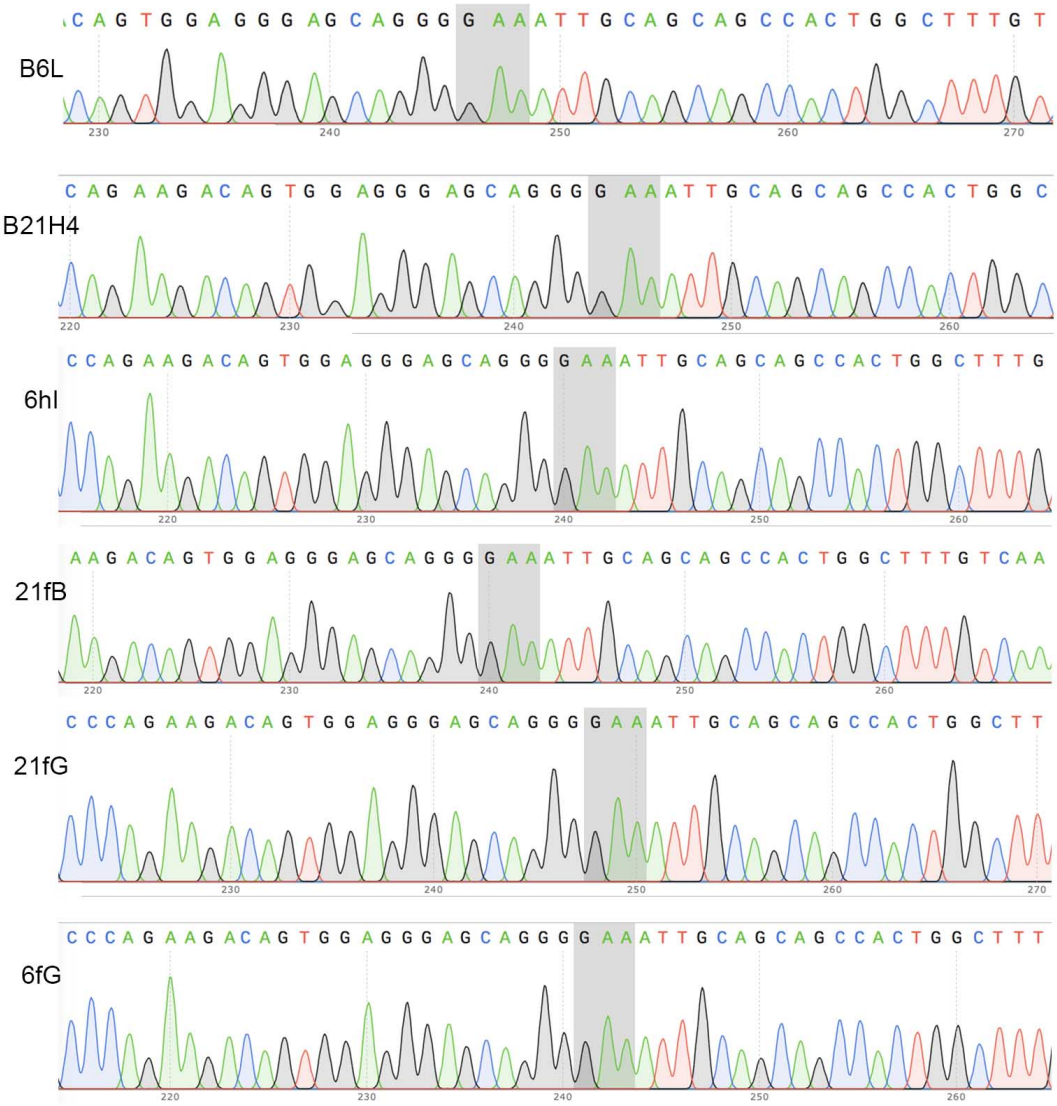

Figure 3.7 Identity of putative SNCAS87E/S87E clones was confirmed by sequencing, with S87E (agc -> gaa) mutation highlighted in grey.

TOPO-clone	Alignment with Homo sapiens genome (GRCh38.p12 primary assembly)
6hI_10	37875167 – 37876448 of chromosome 4
21fB_13	11653992 – 11654961 of chromosome 18
21fG_3	38003560 – 38004232 of chromosome 9
21fG_4	No alignment found

Table 3.4 Alignment of sequences of atypical TOPO-clones with Homo sapiens genome revealed their distal locations to *SNCA*.

3.4. *SNCA*$^{+/-}$, *SNCA*$^{-/-}$ and *SNCA*$^{S87E/S87E}$ hESC clones exhibited normal expression of pluripotency markers and half had normal genomic integrity

3.4.1. Half of the α-Syn mutant hESC clones were free from copy number variations (CNVs) and large copy-neutral loss of heterozygosity (CN-LOH) regions as revealed by whole genome SNP array analysis

To assess the genomic integrity of the α-Syn mutant hESC clones, I purified their genomic DNA and sent for whole genome SNP array. In the parental line RC17, I found 10 CN-LOH regions > 1 Mb (Table 3.5) in addition to the previously reported duplication at chromosome 12p13.31 (Canham et al., 2015). Since the same SNP assay as in (Canham et al., 2015) was used, these CN-LOH might have occurred during the passaging of hESCs, considering the passage I sent for SNP analysis was 12 passages older than (Canham et al., 2015).

Line	Passage	Variation	Region	Start	End	Size (bp)	Number of SNPs
RC17	p29	gain	12p13.31	8,000,336	8,173,254	172,919	19
		CN-LOH	11p11.2	46,029,542	47,969,152	1,939,611	276
		CN-LOH	11q14.3	89,432,891	92,206,818	2,773,928	404
		CN-LOH	14q23.3-24.1	66,266,677	68,977,500	2,710,824	277
		CN-LOH	2q24.3	167,460,233	169,547,991	2,087,759	307
		CN-LOH	2q31.1	169,793,485	171,130,071	1,336,587	208
		CN-LOH	3q11.2	94,807,394	95,848,906	1,041,513	203
		CN-LOH	Xp21.3	26,732,740	28,565,977	1,833,238	264
		CN-LOH	Xq22.1-22.2	100,938,923	102,951,652	2,012,730	271
		CN-LOH	Xq23	109,254,789	111,325,981	2,071,193	234
		CN-LOH	Xq25	125,848,846	127,710,902	1,862,057	244

Table 3.5 SNP analysis summary of parental line RC17. In addition to the previously reported duplication at 12p13.31 (Canham et al., 2015), 10 CN-LOH regions > 1 Mb were detected.

Apart from the CNV and CN-LOH regions found in the parental line, 1 out of 2 *SNCA*$^{-/-}$ clone (L5-3), 2 out of 2 *SNCA*$^{+/-}$ clones (4-4 and L5-4) and 5 out of 14 (with 1 sample failure during SNP assay) *SNCA*$^{S87E/S87E}$ clones (21fB, 21fG, B6L, 6fG and 6hI) did not have any other CNVs or CN-LOH regions > 1 Mb detectable by SNP analysis (Table 3.6).

Genotype	Clone	Passage	Variation	Region	Start	End	Size (bp)	Number of SNPs
SNCA$^{-/-}$	L5-3	p35	none	none	none	none	none	none
SNCA$^{-/-}$	M1-4	p36	CN-LOH	17p13.3-11.2	18,901	16,401,682	16,382,782	2,315
SNCA$^{+/-}$	L5-4	p33	none	None	none	none	none	none
SNCA$^{+/-}$	4-4	p34	none	none	none	none	none	none
SNCA$^{S87E/S87E}$	21fB	p45	none	none	none	none	none	none
SNCA$^{S87E/S87E}$	21fG	p45	none	none	none	none	none	none
SNCA$^{S87E/S87E}$	21fV	p45	loss	20p13-11.1	63,244	62,909,908	62,846,665	3,374
			gain	21p11.2-22.3	10,734,842	48,098,824	37,363,983	4,306
SNCA$^{S87E/S87E}$	21hG	p45	loss	12p12.3	17,182,354	17,339,078	156,725	19
SNCA$^{S87E/S87E}$	21hK	p45	loss	4q25	108,048,977	108,174,195	125,219	21
			loss	5p12	44,422,633	44,499,291	76,659	15
			loss	7q31.1	114,249,733	114,454,337	204,605	20
			loss	8p22	16,260,166	16,645,869	385,704	31
			loss	9q31.2-31.3	111,277,519	111,413,448	135,930	19
SNCA$^{S87E/S87E}$	21hM	p45	loss	8q24.3	144,993,324	145,135,727	142,404	23
SNCA$^{S87E/S87E}$	B21H4	p42	loss	12p13.33	1,236,286	1,401,636	165,351	13
SNCA$^{S87E/S87E}$	B6L	p45	none	none	none	none	none	none
SNCA$^{S87E/S87E}$	6fG	p45	none	none	none	none	none	none
SNCA$^{S87E/S87E}$	6hI	p45	none	none	none	none	none	none
SNCA$^{S87E/S87E}$	6fD	p45	loss	3q24	144,769,891	144,883,424	113,534	17
			loss	8q22.1	96,456,072	96,518,612	62,541	13
			loss	8q24.3	144,990,528	145,135,727	145,200	24
SNCA$^{S87E/S87E}$	6fE	p46	loss	20p13-11.1	63,244	25,730,968	25,667,725	3,374
			gain	20p11.1-q13.33	25,667,725	62,909,908	62,909,908	4,179
SNCA$^{S87E/S87E}$	6fI	p46	loss	Xp22.33	1,961,647	2,036,900	75,254	21
SNCA$^{S87E/S87E}$	6fC	p46	FAILED	NA	NA	NA	NA	NA

Table 3.6 SNP analysis summary of *SNCA*$^{-/-}$, *SNCA*$^{+/-}$ and *SNCA*$^{S87E/S87E}$ clonal hESC lines, other than those found in WT parental line. One out of 2 *SNCA*$^{-/-}$ clones, 2 out of 2 *SNCA*$^{+/-}$ clones and 5 out of 13 *SNCA*$^{S87E/S87E}$ clones (highlighted) were free from CNVs larger than 50 kb and CN-LOH larger than 1 Mb other than those found in WT parental line.

SNCA$^{-/-}$ clone M1-4 had a 16 Mb CN-LOH at chromosome 17p13.3-11.2 (Figure 3.8a). *SNCA*$^{S87E/S87E}$ clone B21H4 had a 165 kb loss at chromosome 12p13.33 (Figure 3.8b) with only one encoding gene *ERC1*, which is related to childhood apraxia of speech (Thevenon et al., 2013). The other 7 *SNCA*$^{S87E/S87E}$ clones (21fV, 21hG, 21fV, 21hM, 6fD, 6fE and 6fI) had 1 to 5 CNVs varied from 62 kb to 63 Mb in size,

with 13 – 4306 SNPs (Table 3.6). Large CNVs with duplication or deletion of hundreds of coding genes could compromise mDA differentiation, and hence these hESC clones were excluded from further *in vitro* mDA differentiation and cell modelling of α-Syn pathology.

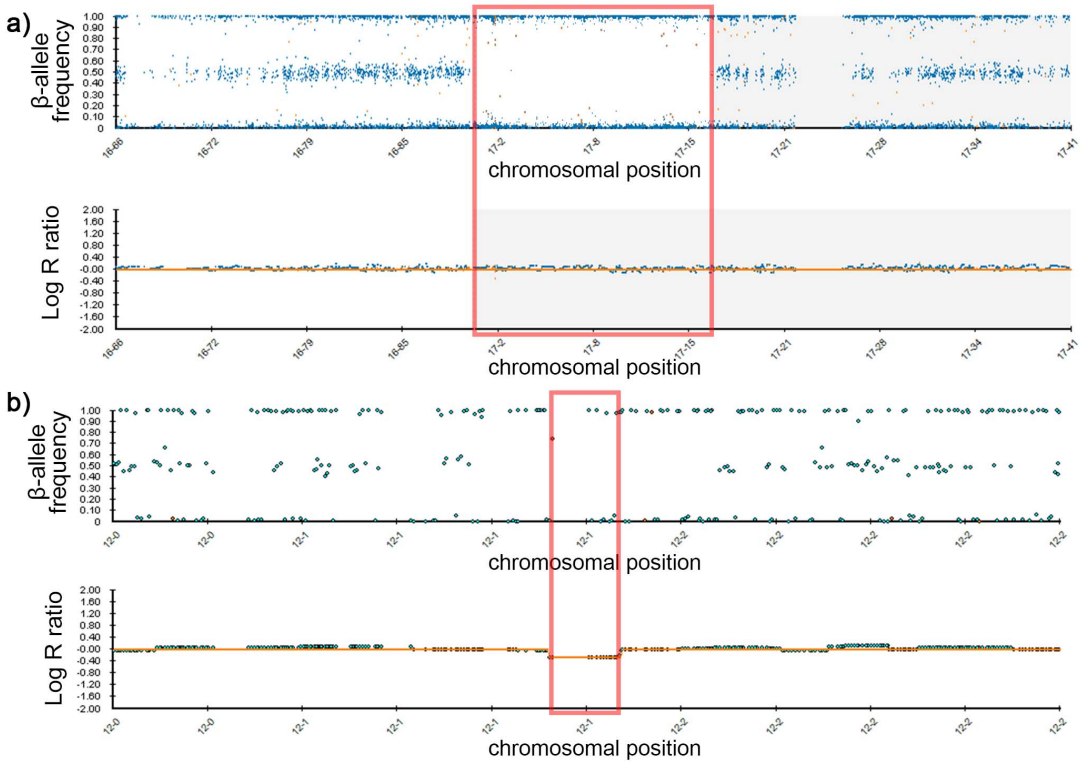

Figure 3.8 Screenshot of SNP analysis illustrating a) a 16 Mb CN-LOH in *SNCA*$^{-/-}$ clone M1-4 and b) a 165 kb deletion in *SNCA*$^{S87E/S87E}$ clone B21H4.

3.4.2. All α-Syn mutant hESC clones were free from CRISPR off-target events detectable by T7 endonuclease 1 (T7E1) assay

To investigate the top off-target sites predicted when designing gRNAs with the Zhang Lab CRISPR DESIGN webtool, I designed PCR primers flanking the top 2 predicted off-target sites of each gRNA.

The PCR product of these regions was denatured and re-annealed to allow the formation of heteroduplex DNA. A T7E1 assay was then used to detect mismatches at these sites. For positive control, I used a 449 bp PCR product covering the *SNCA* knockout region of *SNCA*$^{+/-}$ clone 4-4 (Figure 3.9), or a 591 bp PCR product covering the S87E region of a DNA mix where B21H4 : WT = 1 : 1 (Figure 3.10). In the positive controls where the 2 strands mismatched, T7E1 cleaved the DNA and resulted in a band with smaller size (indicated by red arrows in Figure 3.9 and 3.10).

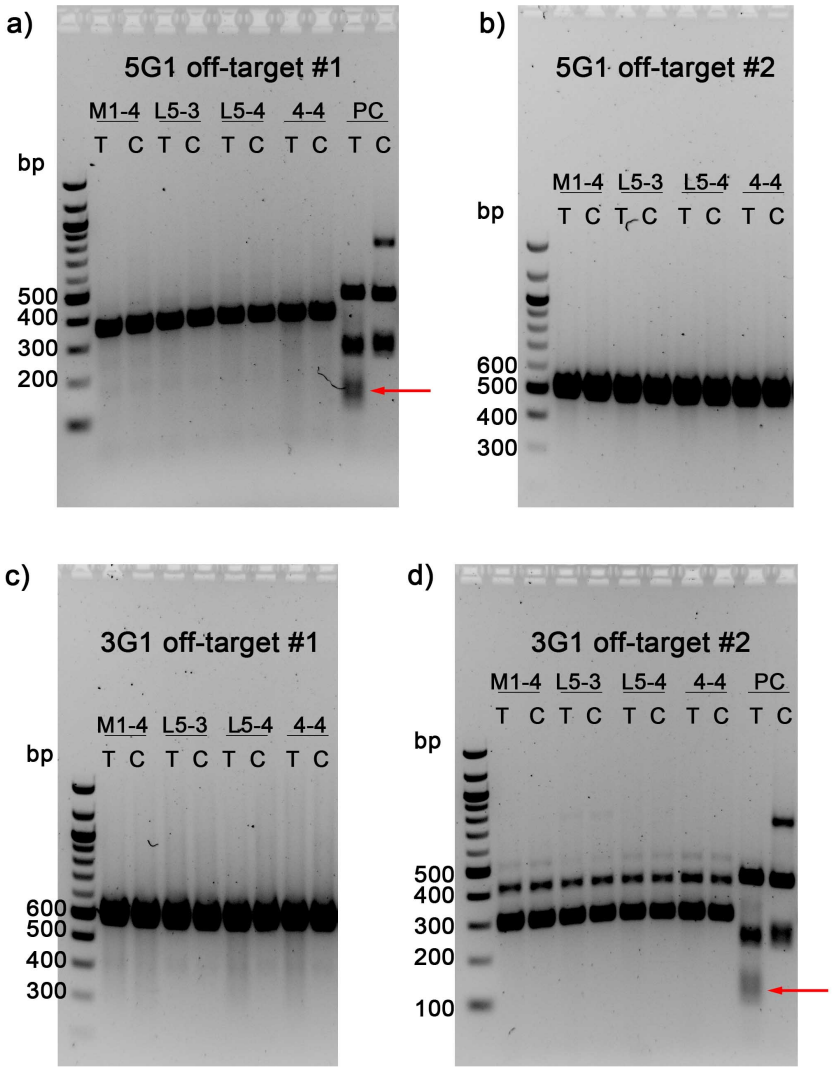

Figure 3.9 In *SNCA*$^{-/-}$ and *SNCA*$^{+/-}$ hESC clones, T7 endonuclease 1 (T7E1) assay revealed no off-target events at the top 2 predicted off-target sites of gRNAs 5G1 and 3G1. The PCR products of these sites were denatured and re-annealed, and subsequently subjected to T7E1 digestion (T) or control reaction (C). A positive control (PC), a 449 bp PCR product covering the α-Syn knockout region of *SNCA*$^{+/-}$ clone 4-4, was included. T7E1 digestion products of mismatched strands in PC are indicated by red arrows.

a) predicted off-target site #1 of 5G1

b) predicted off-target site #2 of 5G1

c) predicted off-target site #1 of 3G1

d) predicted off-target site #2 of 3G1

For all the off-target sites tested, PCR products of all *SNCA*$^{-/-}$, *SNCA*$^{+/-}$ (Figure 3.9) and *SNCA*$^{S87E/S87E}$ clones (Figure 3.10) were of expected sizes in control (C) reaction and had no cleavages upon T7E1 digestion (T). This suggests the clones were highly unlikely to have off-target events at these sites, as anticipated from using

the Cas9n system. However, if the cleavage efficiency was very high and both alleles developed exactly the same indel, this rare incident would have escaped the detection by T7E1 assay. To rule out this possibility, sequencing of the potential off-target regions would be required.

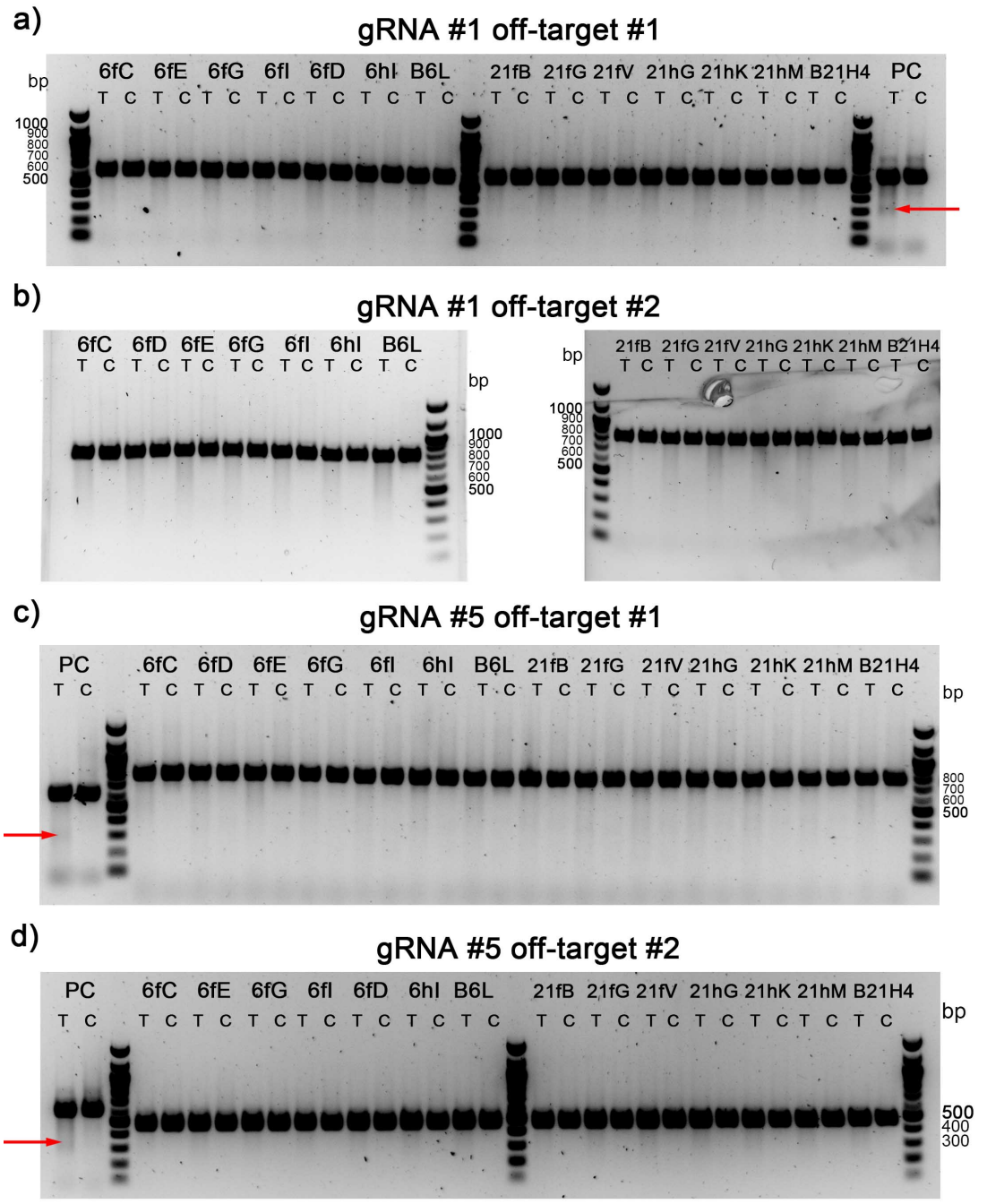

Figure 3.10 In *SNCA*$^{S87E/S87E}$ hESC clones, T7E1 assay revealed no off-target events at the top 2 predicted off-target sites of each gRNA. The PCR products of these sites were denatured and re-annealed, and subsequently subjected to T7E1 digestion (T) or control reaction (C). A positive control (PC), a 591 bp PCR product covering the S87E region of a DNA

mix where B21H4 : WT = 1 : 1, was included. T7E1 digestion products of mismatched strands in PC are indicated by red arrows.

a) predicted off-target site #1 of gRNA #1

b) predicted off-target site #2 of gRNA #1

c) predicted off-target site #1 of gRNA #5

d) predicted off-target site #2 of gRNA #5

3.4.3. All α-Syn mutant hESC clones were free from integration of CRISPR plasmids

As shown previously, the on-target and the top 2 off-target sites were free from insertion of plasmid sequence. To check whether the gRNA-Cas9n plasmid has integrated into other locations in the genome of α-Syn mutant hESC clones, I performed PCR for 3 different regions of the plasmid, with primer pairs indicated in Figure 3.1a (Table 3.7).

Primers	Coverage
oug_F & oug_R	plasmid origin, U6 promotor and gRNA sequences of gRNA-Cas9n plasmid
Cas_F & Cas_R	part of the Cas9n sequence
cp_F & cp_R	part of Cas9n and part of puroR sequences

Table 3.7 Sequence coverage of primers for checking plasmid integration.

For positive control, I spiked WT DNA with *Not*I linearized (site indicated in Figure 3.1a) gRNA #1 pX462 plasmid, the gRNA-Cas9n plasmid for S87E targeting. To ensure the copy number of WT DNA equals that of plasmid DNA, the amount of plasmid for spiking was calculated according to the ratio of the molar mass of the human genome (2.08×10^{12} g/mol) versus that of the plasmid (5.97×10^{6} g/mol). PCR product was absent from all tested *SNCA*$^{-/-}$, *SNCA*$^{+/-}$ and *SNCA*$^{S87E/S87E}$ clones in all 3 PCRs (Figure 3.11a, b & c), suggested these 3 plasmid regions did not integrate into the genome of these clones, and thus would not express gRNA, Cas9n or puroR.

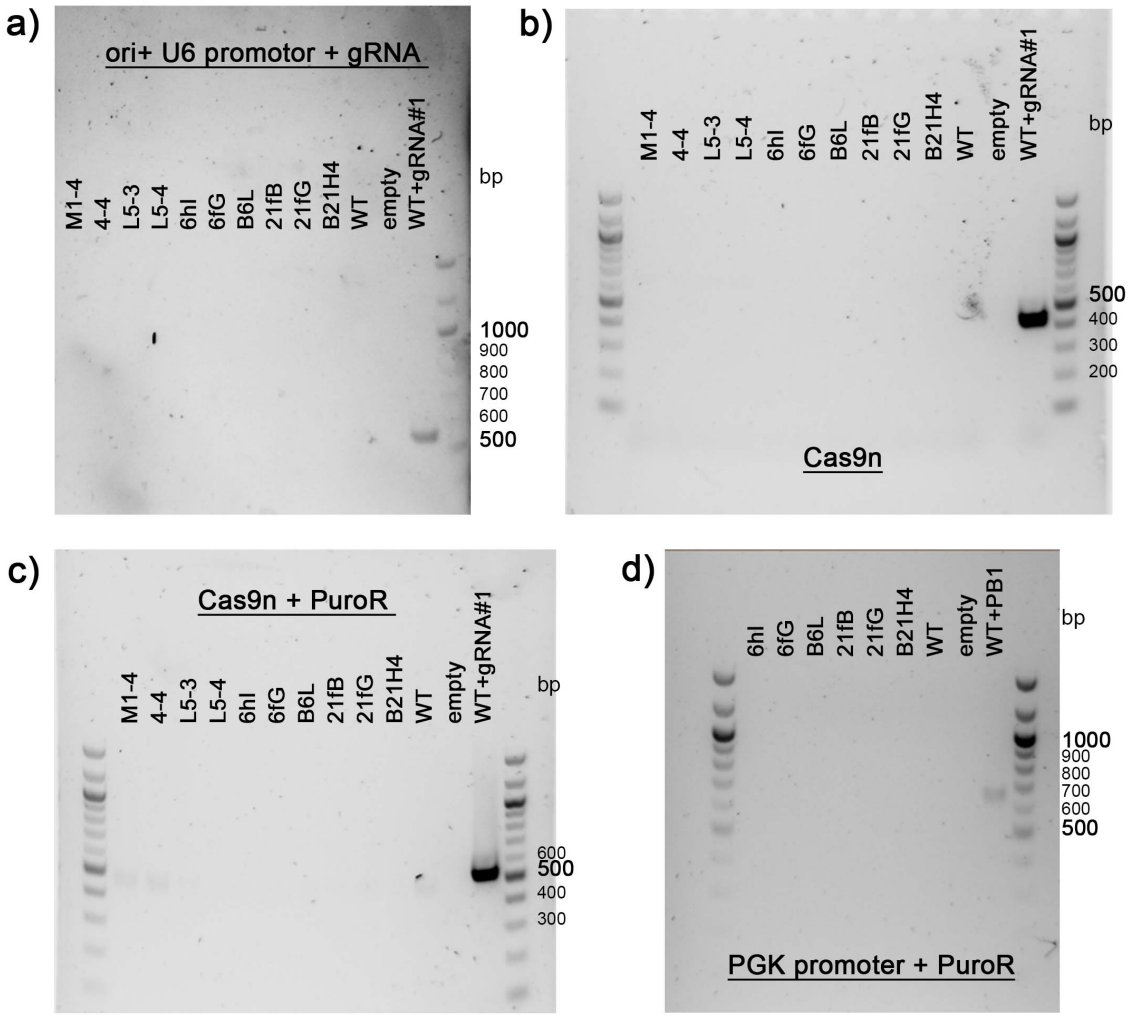

Figure 3.11 Plasmids used during CRISPR targeting did not integrated into genome of *SNCA*$^{-/-}$, *SNCA*$^{+/-}$ and *SNCA*$^{S87E/S87E}$ clones. pX462 and piggyBac transposon plasmids were linearized with Not I and spiked into WT DNA to serve as a positive control. PCR products were absent from targeted clones when amplifying the following partial sequences of the plasmids:
a) primer pair oug_F + oug_R (location illustrated in Figure 3.1a), which covered the plasmid origin, U6 promoter and gRNA sequences of pX462.
b) primer pair Cas_F + Cas_R location illustrated in Figure 3.1a), which covered partial sequence of Cas9n in pX462.
c) primer pair cp_F + cp_R (location illustrated in Figure 3.1a), which covered partial sequence of Cas9n and puroR in pX462.
d) primer pair pp_F + pp_R (location illustrated in Figure 3.4a), which covered partial sequence of PGK promoter and puroR in piggyBac plasmid.

To check whether the piggyBac plasmid has integrated into the genome of *SNCA*$^{S87E/S87E}$ hESC clones, I performed PCR with primer pair pp_F & R (indicated in Figure 3.4a), which covered part of PGK promotor and part of puroR sequences of the piggyBac plasmid. For positive control, I spiked WT DNA with *Not*I linearized (site

indicated in Figure 3.4a) piggyBac plasmid in S87E targeting. Similarly, to ensure the copy number of WT DNA equals that of plasmid DNA, the amount of plasmid for spiking was calculated according to the ratio of the molar mass of the human genome (2.08×10^{12} g/mol) versus that of the plasmid (5.51×10^{6} g/mol). PCR product was absent from all tested *SNCA*$^{S87E/S87E}$ clones (Figure 3.11d), suggesting that this region did not integrate into the genome of the clones, hence would not express PGK promotor or puroR. As previously validated by PCR, these *SNCA*$^{S87E/S87E}$ clones were also free from a partial sequence of ΔTK (Figure 3.6b, primers indicated by orange arrows in Figure 3.4b), and thus would not express ΔTK. As for the pCMV-HAhyPBase plasmid used for removing the piggyBac cassette, its expression does not affect genomic integrity (Yusa et al., 2011).

The limitation of the current detection method is that by PCR amplifying the partial sequences of a plasmid, we cannot guarantee other parts of the plasmid did not integrate. However, considering there was no insertion at the top off-target sites, such integration is highly unlikely.

3.4.4. α-Syn mutation, the selection and cloning process did not impair the expression of pluripotency markers OCT4 and NANOG

To investigate whether the expression of pluripotency markers OCT4 and NANOG was compromised by α-Syn mutation or the selection and cloning process, I performed immunostaining on a selection of *SNCA*$^{-/-}$, *SNCA*$^{+/-}$ and *SNCA*$^{S87E/S87E}$ clones (Figure 3.12). None of the *SNCA*$^{-/-}$, *SNCA*$^{+/-}$ and *SNCA*$^{S87E/S87E}$ clones exhibited defective expression of OCT4 and NANOG compared to WT hESCs, suggesting α-Syn mutation, the selection and cloning process did not impair the expression of these pluripotency markers.

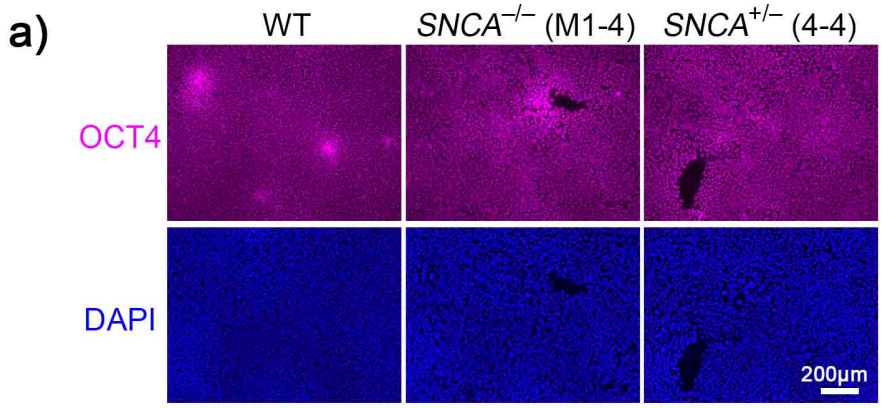

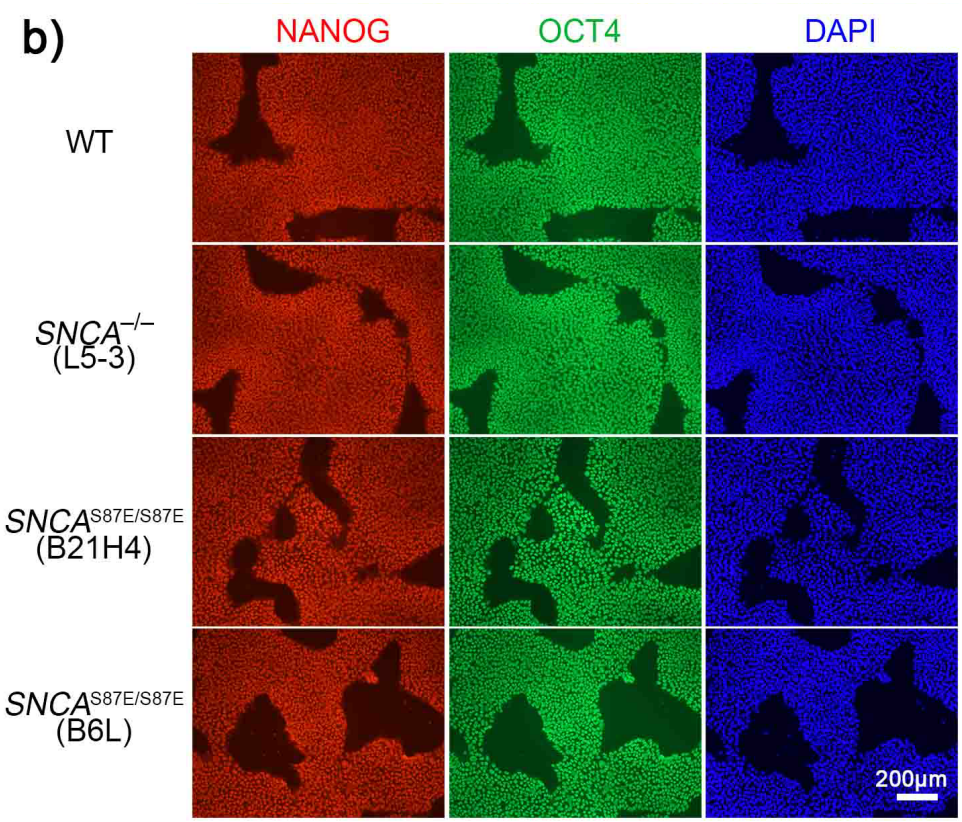

Figure 3.12 Expression of pluripotency markers OCT4 and NANOG was not impaired by α-Syn mutation or cloning process.

a) OCT4 immunostaining of *SNCA*$^{-/-}$ hESC clone M1-4 and *SNCA*$^{+/-}$ hESC clone 4-4 were of similar quality to that of WT.

b) OCT4:NANOG double-immunostaining of *SNCA*$^{S87E/S87E}$ hESC clones B6L and B21H4, *SNCA*$^{-/-}$ hESC clone L5-3 were of similar quality to that of WT hESCs.

3.5. Discussion

In this chapter, I generated putative *SNCA*$^{-/-}$, *SNCA*$^{+/-}$ and *SNCA*$^{S87E/S87E}$ hESC clones by CRISPR/Cas9n gene editing using the clinical-grade hESC line RC17 as the parent cell line. I confirmed the mutations by Sanger DNA sequencing and assessed their genomic integrity, using whole-genome SNP arrays and PCR detection of off-target events and plasmid integration. Results revealed 2 *SNCA*$^{-/-}$, 2 *SNCA*$^{+/-}$ and 5 *SNCA*$^{S87E/S87E}$ clones are suitable for *in vitro* differentiation and cell modelling of α-Syn pathology. *SNCA*$^{-/-}$ clone M1-4 and *SNCA*$^{S87E/S87E}$ clone B21H4 had SNP variations but were still suitable for *in vitro* cell modelling of α-Syn pathology.

SNCA$^{-/-}$ clone M1-4 had a large on-target deletion in one of the alleles, which however, is not unusual. On-target deletions larger than expected have been commonly

identified in various cell types edited with Cas9n, at a comparable frequency to those edited with Cas9 (Owens et al., 2019). Considering that these large on-target deletions are usually several kb in size and the largest reported so far is 42 kb (Parikh et al., 2015), the unidentified allele of *SNCA*$^{-/-}$ clone L5-3 is most probably a deletion larger than 2 kb. For clinical applications, failing to detect a large deletion which could lead to disruptive effects would be unacceptable. The possibility of large deletions also rendered the initial screening for *SNCA*$^{+/-}$ clones less accurate, since an allele with large deletion would be missed by the short-range PCR screening, and consequently a *SNCA*$^{+/-}$ clone could be mis-classified as a WT clone.

There is yet to be an accurate model to predict the distribution of large deletions, which is correlated to the proximity to gRNA cut sites and the gRNA cleavage efficiency (Owens et al., 2019). SNP assay with high resolution, where intermarker spacing can be as small as 700 bp currently, as well as whole genome sequencing, can test whether a clonal line is free from undesired indels and contribute towards the decision that if it can be used for clinical applications. Alternatively, we can perform copy number analysis using qPCR flanking the gRNAs with a region as large as possible to ensure the detection of both alleles.

In S87E targeting, combination B generated the highest number of clones and all putative *SNCA*$^{S87/S87E}$ clones derived from combination B (Table 3.2). This agrees with recent studies (Yan et al., 2017) where the efficiency was highest when the paired gRNAs were 37 – 68 bp apart.

Contrary to the frequently observed off-target events while using CRISPR/Cas9, we did not detect any off-target events when using Cas9n. It is to be noted that the Cas9n provides high fidelity without compromise on efficiency (Cho et al., 2014; Fu et al., 2014; Ran et al., 2013a). Unlike Cas9 where lower gRNA-Cas9 concentration was found to improve the fidelity but render a lower on-target efficiency (Fu et al., 2013; Hsu et al., 2013; Pattanayak et al., 2013), Cas9n and other next generation Cas9 enzymes such as the quadruple substitution variant Cas9-N497A/R661A/Q695A/Q926A (Kleinstiver et al., 2016) improve fidelity without sacrificing efficiency.

Another refinement lies in the delivery method of gRNA and Cas9 enzyme, although it is more costly than plasmid delivery due to requirement in the purification and storage

of RNA and protein. Transfecting with gRNA and Cas9 in the form of ribonucleoprotein complex instead of plasmids largely reduced off-target events (Kim et al., 2014; Liang et al., 2015). Transfecting both gRNA and Cas9 in the form of mRNAs also had similar effect on reducing off-target events (Liang et al., 2015). These results seem intuitive as the ribonucleoprotein was degraded within 24 hours post-transfection, while the plasmid expression lingered for days (Kim et al., 2014). Similarly, the risk of plasmid integration was also avoided by delivering gRNA and Cas9 in the form of mRNAs or ribonucleoprotein.

Delivering gRNA and Cas9 in the form of ribonucleoprotein complex comes with another advantage, that it enhances the on-target efficiency and produces more colonies than plasmid transfection (Kim et al., 2014; Liang et al., 2015). However, the high efficiency would make it difficult to obtain heterozygous knockout clones with one WT allele, and even more difficult for isogenic control clones that retain both WT alleles (Liang et al., 2015). This agrees with our observation that more *SNCA*$^{-/-}$ clones were generated compared to *SNCA*$^{+/-}$ clones. Nonetheless, higher on-target efficiency is always beneficial for generating a homozygous mutation. Cas9-D10A, which produces 5' overhang in a PAM-out design, was more efficient for HDR and less prone to induce large mutations than 3' overhang-producing nickases Cas9-H840A and Cas9-N863A (Bothmer et al., 2017; Yan et al., 2017). A novel CRISPR-Cas effector protein, ErCas12a, exhibited higher efficiency in eliciting strand-annealing-mediated DNA repair than Cas9 (Wierson et al., 2019).

To isolate single cell-derived clone from a pool population after transfection and drug selection, I used cloning cylinder or clone-picking tips in the current study. This resulted in the polyclonal origin of clones B21 and B6. Isolation of single cell-derived clones with high viability remains to be challenging to date. Popular techniques such as limiting dilution, though preserves cell viability, is laborious especially when added to the number of single cell-derived clones needed for genotyping. FACS gives rise to monoclonal cells efficiently, but it requires fluorescence expression in targeted cells and has a negative impact on cell viability. An improvement on the traditional clone-picking method by adding agarose in culture media to form a semisolid 'gel' seems to improve efficiency as well as monoclonality of clone-picking (http://thelindberglab.com/cloning-cells-with-the-agarose-method). To validate monoclonality of individual clones, the best method to date is next

generation sequencing (NGS) such as deep sequencing, which allows for detection of rare genotypes as little as 1% of the original pool population.

In conclusion, for the first time to my knowledge, *SNCA*$^{-/-}$, *SNCA*$^{+/-}$ and *SNCA*$^{S87E/S87E}$ hESCs were generated using state-of-the-art CRISPR/Cas9n techniques. Based on the genomic integrity, the qualified clonal hESC lines were chosen for *in vitro* differentiation and cell modelling of α-Syn pathology. With the evolvement of gene editing, emergence of more efficient and affordable techniques for achieving higher efficiency and fidelity, and for identifying off-target events, can be expected.

Chapter 4: Normal midbrain dopaminergic (mDA) differentiation of *SNCA*$^{-/-}$, *SNCA*$^{+/-}$ and *SNCA*$^{S87E/S87E}$ hESCs with an optimised differentiation protocol

4.1. Introduction

To differentiate mDA neurons from hESCs, I adapted a protocol based on floor plate induction followed by neuronal specification to midbrain identity (Figure 4.1) (Fasano et al., 2010; Kirkeby et al., 2012; Kriks et al., 2011; Nolbrant et al., 2017). Dual SMAD inhibition by SB and LDN converts hESCs into primitive neural ectoderm (Chambers et al., 2009). Early SHH activation with high level of SHH ventralises the neuronal progenitors to a floor plate fate (Fasano et al., 2010). For posterior patterning, canonical WNT signalling is activated using the GSK3β inhibitor, CHIR (Kirkeby et al., 2012; Kriks et al., 2011; Xi et al., 2012). Inhibition of GSK3β prevents the phosphorylation of β-catenin, which is a signal for its degradation. The subsequent stabilisation and accumulation of β-catenin activates canonical WNT signaling (Bennett et al., 2002; MacDonald et al., 2009).

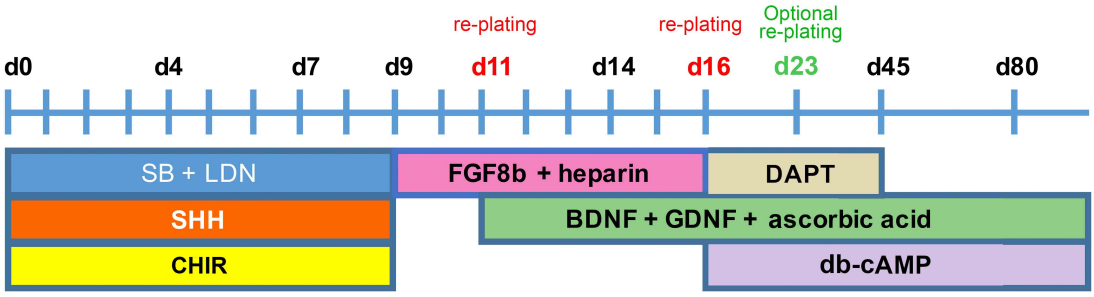

Figure 4.1 Floor plate mDA differentiation protocol for hESCs or hiPSCs. Cell are plated as small clumps at day 0, in the presence of SB431542 (SB) + LDN193189 (LDN) for dual SMAD inhibition, Sonic Hedgehog (SHH) for SHH activation and CHIR99021 (CHIR) for WNT activation. The cells are re-plated at day 11 and day 16, and there is an optional re-plating at day 23 for obtaining neurons of a lower density. SB, LDN, SHH and CHIR are present in cell culture media from differentiation day 0 to day 9. Fibroblast growth factor 8b (FGF8b) and heparin are added from day 9 to day 16. N-[N-(3,5-difluorophenacetyl)-l-alanyl]-S-phenylglycine t-butyl ester (DAPT) is used from day 16 to day 45 to promote neuronal differentiation. Brain-derived neurotrophic factor (BDNF), glial cell-derived neurotrophic factor (GDNF) and ascorbic acid are added from day 11 onwards and dibutyryl-cAMP (db-cAMP) is added from day 16 onwards.

The ventralisation of neuronal progenitors can be monitored by the ventral neural tube marker Foxa2, as well as the floor plate marker Corin (Table 1.2). Since Corin is a cell

surface marker, it can be quantified by flow cytometry to indicate the presence of floor plate cells in a culture (Kikuchi et al., 2017; Ono et al., 2007). Along the anteroposterior axis, several transcription factors are expressed in a spatially restricted manner (Table 1.2). Therefore, these markers have been widely used for monitoring the anteroposterior and dorsoventral identity of the differentiated progenitors. Namely, co-localisation of LMX1A and FOXA2 marks the ventral midbrain, supplemented by the expression of OTX2 and EN1 (Kirkeby et al., 2017a, 2012; Nolbrant et al., 2017; Xi et al., 2012). Rostral ventral midbrain and diencephalon marker BARHL1, forebrain marker SIX3 and hindbrain markers GBX2 are used to identify progenitors which acquired undesired identities (Kirkeby et al., 2017a, 2012; Nolbrant et al., 2017).

As different cell lines vary in the optimal CHIR concentration for mDA differentiation (Kirkeby et al., 2013; Nolbrant et al., 2017), I optimised the CHIR concentration for RC17 using the above markers to indicate the quality of differentiation. In addition, neurons mature in the same well since day 16 re-plating at 800,000 cells/cm^2 in the original protocol, which is too dense for subsequent imaging application in the current study. Hence, I explored conditions for terminal differentiation that would produce sparser DA neurons highly positive for the dopaminergic enzyme TH, and the pan-neuronal marker, β-III tubulin. Based on the optimised protocol, I differentiated *SNCA*$^{-/-}$, *SNCA*$^{+/-}$ and *SNCA*$^{S87E/S87E}$ hESCs into mDA neurons and compared their gene expression profiles to that of WT hESC-derived mDA neurons. In addition, I examined a few crucial mDA neuronal functionalities that might be affected by the deletion or mutation of aSyn.

4.2. Fine-tuning of CHIR concentration, cell culture matrix and re-plating timing for efficient mDA differentiation of hESCs

4.2.1. A narrow range of CHIR concentration efficiently produced correctly specified mDA progenitors

To optimize the CHIR concentration for RC17 hESCs, I used a range of CHIR from 0.7 μM to 1.4 μM. In a successful mDA differentiation, progenitors should be homogenously double positive for LMX1A and FOXA2 on day 11. In this differentiation, LMX1A staining became patchy at 1.3 – 1.4 μM CHIR although FOXA2 staining remained positive (Figure 4.2a), suggesting a transition to hindbrain identity (Kirkeby et al., 2012). At low CHIR concentrations 0.9 – 0.7 μM, both LMX1A and FOXA2

staining were patchy (Figure 4.2a), suggesting a forebrain or ventral rostral midbrain identity (Kirkeby et al., 2012). To further validate the anteroposterior identity, I performed RT-qPCR on day 16 progenitors for a selection of transcription factors (Table 1.2). Day 16 progenitors differentiated with at 0.9 µM CHIR expressed a high level of *BARHL1* and *SIX3* (Figure 4.2b), suggesting an increased presence of forebrain or ventral rostral midbrain progenitors. Low expression level of *GBX2* suggested that none of the CHIR concentration (0.9 – 1.2 µM) gave rise to progenitors of hindbrain identity in this differentiation (Figure 4.2b). Midbrain markers *LMX1A* and *FOXA2* were of similar level among 0.9 – 1.2 µM CHIR, while *EN1* showed an increasing trend and *OTX2* showed a decreasing trend as CHIR concentration increased (Figure 4.2b). This observation is consistent with (Xi et al., 2012), depicting the transition from forebrain / ventral rostral midbrain ($OTX2^{+}EN1^{-}$) to caudal midbrain ($OTX2^{-}EN1^{+}$) characteristics. These results agree with prior observations that only a narrow window of CHIR concentration gave rise to mDA progenitors (Kirkeby et al., 2012; Xi et al., 2012).

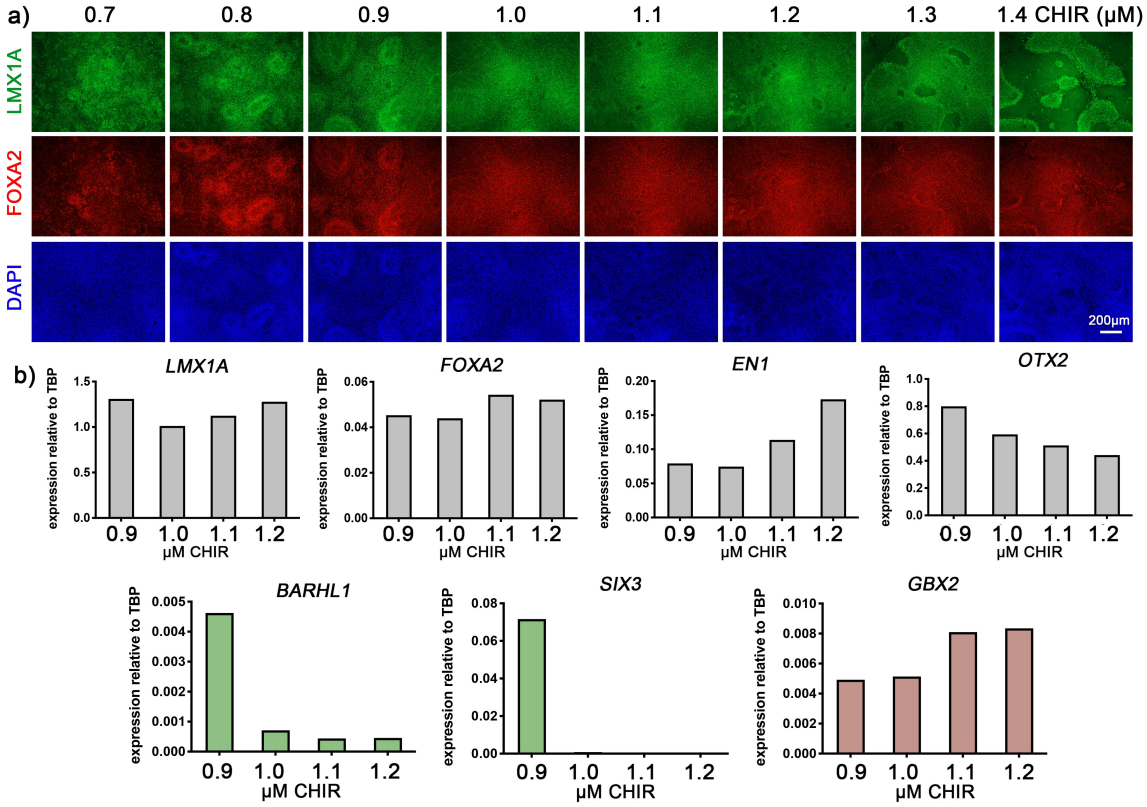

Figure 4.2 A narrow range of CHIR concentration efficiently produced homogenous mDA progenitors.

a) Majority of progenitors were double positive for LMX1A (green) / FOXA2 (red) on day 11 when differentiated at optimal CHIR concentrations. In this differentiation, at CHIR concentrations lower than the optimal 1.0 μM, both LMX1A and FOXA2 staining were patchy. Although FOXA2 staining remained positive even when CHIR concentration was higher than optimal, LMX1A staining became negative drastically.
b) RT-qPCR at day 16 of this differentiation showed that progenitors exhibited increased expression of rostral ventral midbrain and diencephalon gene *BARHL1* and forebrain gene *SIX3* (green) in 0.9 μM CHIR. As for markers expressed in midbrain (grey), *LMX1A* and *FOXA2* were of similar level among 0.9 – 1.2 μM CHIR, but *EN1* showed increasing trend while *OTX2* showed decreasing trend as CHIR concentration increased. The level of hindbrain gene *GBX2* (red) was similarly low in the range of 0.9 – 1.2 μM CHIR. (N = 1)

In this differentiation, day 16 progenitors differentiated with 1.0 – 1.2 μM CHIR formed a single population highly positive for CORIN, while progenitors differentiated with low CHIR concentration (0.9 μM) had a CORIN negative/low subpopulation (Figure 4.3a). This CORIN negative/low subpopulation might have acquired forebrain identity, as CORIN is expressed from midbrain to spinal cord (Ono et al., 2007). In day 16 progenitors differentiated with a different batch of CHIR, the CORIN negative/low subpopulation was not eliminated until CHIR concentration reached 1.2 or 1.3 μM (Figure 4.3b). Nonetheless, the transition to a single CORIN positive population, which resulted from 0.1 μM increment of CHIR concentration, was consistently observed in these differentiations (Figure 4.3b). Considering that 0.1 μM change of CHIR concentration can give rise to progenitors of completely different identity, any batch variation of CHIR stock concentration and/or purity would result in a shift of optimal CHIR concentration. Therefore, optimisation of CHIR concentration should be treated as a delicate matter that batch testing and accurate pipetting with serial dilution are essential.

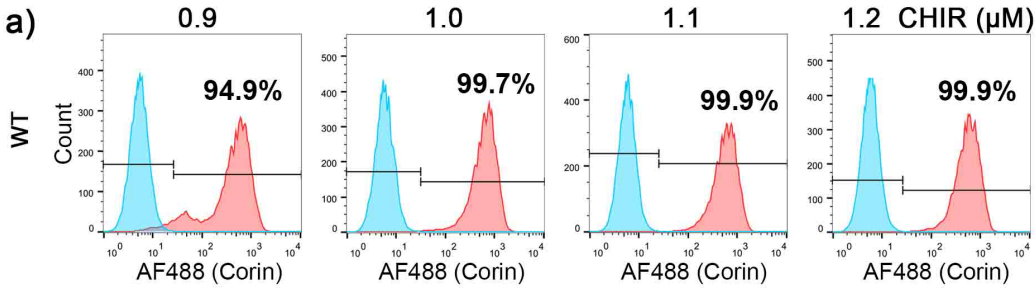

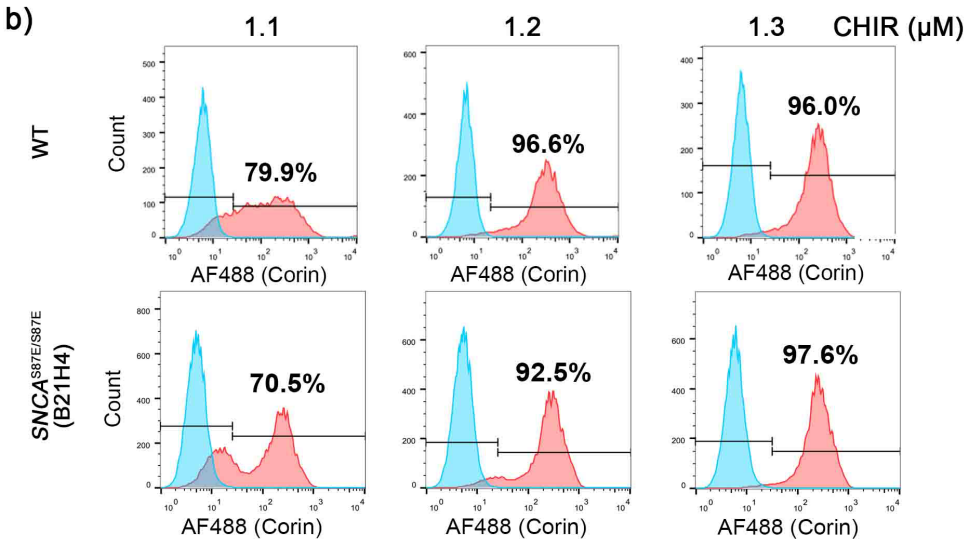

Figure 4.3 Day 16 CORIN flow cytometry revealed that CHIR concentration lower than optimal gave rise to progenitors with forebrain identity.

a) Day 16 flow cytometry of the differentiations in Figure 4.2 revealed a CORIN negative/low subpopulation in low CHIR concentration condition (0.9 μM), while 1.0 – 1.2 μM CHIR formed a single population highly positive for CORIN.

b) When differentiated with a different batch of CHIR, the day 16 progenitors were homogenously positive for CORIN at higher CHIR concentrations (1.2 μM in the WT differentiation and 1.3 μM in the B21H4 differentiation).

4.2.2. Characterisation of fibroblast-like cells

When mDA progenitors were differentiated at an optimal CHIR concentration (1.2 μM for the WT differentiation in Figure 4.3b), most of the cells acquired neuronal morphology at day 38 (Figure 4.4a). In contrast, there were a lot of fibroblast-like cells in the 1.1 μM culture and made the culture more inclined to lift (Figure 4.4a). This suggests that the fibroblast-like cells might be derived from the day 16 CORIN negative progenitors and they are detrimental to the attachment of the *in vitro* maturing neurons in this protocol.

The morphology of the fibroblast-like cells and their co-differentiation with neurons suggested they might be a type of brain fibroblasts cells (Marques et al., 2016) or vascular and leptomeningeal cells (VLMCs) (Vanlandewijck et al., 2018) which are generally positive for collagen type I alpha 1 (COL1A1) and platelet-derived growth factor receptor α (PDGFRα). To investigate the identity of these fibroblast-like cells, I performed immunostaining of TH / COL1A1 / PDGFRα on differentiations with many fibroblast-like cells and a few neurons. The fibroblast-like cells could be identified as

early as day 28 and were TH⁻COL1A1⁺, while TH⁺ cells were COL1A1⁻ (Figure 4.4b). On day 28, PDGFRα staining was not specific for TH⁺ cells, but it did not co-localise with COL1A1 (Figure 4.4b). In day 91 cultures, TH⁺ cells were PDGFRα⁺COL1A1⁻ while the fibroblast-like cells were TH⁻PDGFRα⁻COL1A1⁺ (Figure 4.4c). This suggests they might be arachnoid barrier cells, a subclass of VLMCs that are PDGFRα⁻ (Zeisel et al., 2018).

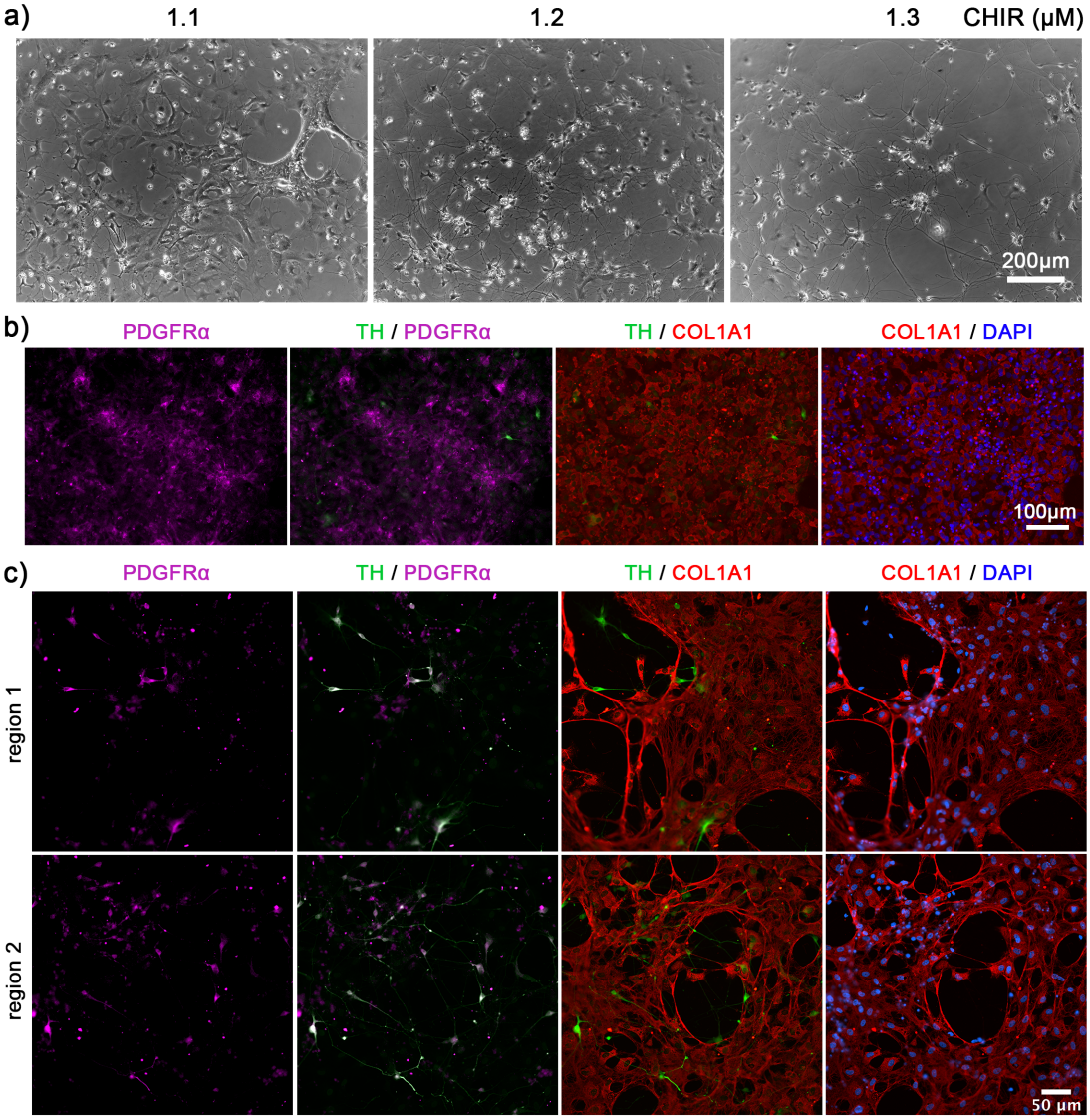

Figure 4.4 Characterisation of fibroblast-like cells which were resulted from with suboptimal CHIR concentration in mDA differentiation.

a) Day 38 bright field images showed that most of the cells acquired neuronal morphology in 1.2 μM CHIR, while plenty of fibroblast-like cells were present in the 1.1 μM condition.

b) The fibroblast-like cells could be identified as early as day 28 and were TH⁻(green) COL1A1⁺(red), while TH⁺ cells are COL1A1⁻. PDGFRα (magenta) staining was not specific for TH⁺ cells but did not co-localise with COL1A1.

c) In day 91 cultures, fibroblast-like cells were $TH^{-}PDGFR\alpha^{-}COL1A1^{+}$, while TH^{+} cells were $PDGFR\alpha^{+}COL1A1^{-}$.

4.2.3. Optimisation of cell culture matrix and re-plating timing for efficient generation of mDA neurons at low density

As an initial attempt, I lowered the re-plating density on day 16 and tested different coating matrices on cell culture plastic plates. On L111 only coating, following the plating density of 800,000 cells/cm^2 in the original protocol gave rise to substantially higher percentage of DA neurons than 400,000 cells/cm^2 by day 40 (Figure 4.5), suggesting a dense population is crucial for neuronal development at this stage. As for matrix, plating on poly-ornithine (poly-O) + L111 did not result in a substantial difference in prevalence of DA neurons compared to L111 at the original plating density 800,000 cells/cm^2 (Figure 4.5). However, at the low density of 400,000 cells/cm^2, poly-O + L111 coating resulted in worse cell attachment (Figure 4.5a). These results suggested that plating at 800,000 cells/cm^2 on L111 only coating would be the best choice for day 16 re-plating among the conditions tested.

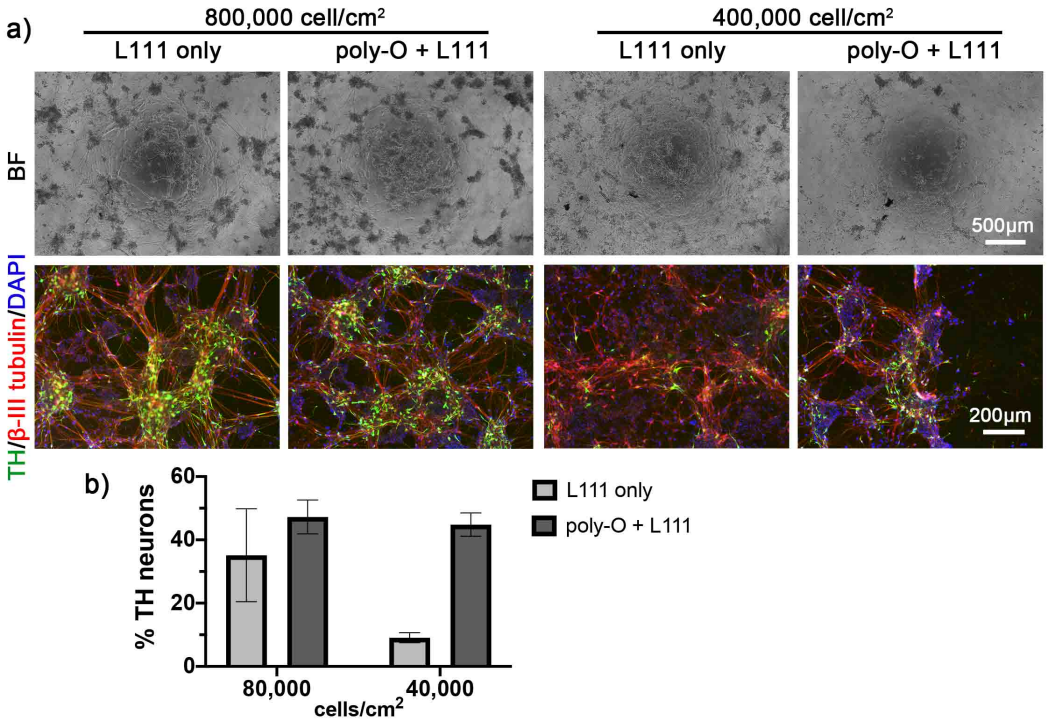

Figure 4.5 On day 16, plating at 800,000 cells/cm^2 on L111 only coating resulted in better cell attachment and a higher percentage of DA neurons.

a) At 400,000 cells/cm^2, plating on L111 only provided better cell attachment compared to poly-ornithine (poly-O) + L111, as shown by day 40 bright field images and TH (green) / β-III tubulin

(red) immunostaining. On L111 only coating, plating at 800,000 cells/cm^2 gave rise to substantially more DA neurons than 400,000 cells/cm^2 as revealed by day 40 TH / β-III tubulin immunostaining.
b) Quantification of percentage of DA neurons, which was calculated by the number of TH$^+$β-III tubulin$^+$ cells over the total number of cells marked by DAPI. Error bars were calculated from standard derivation of duplicate wells.

Therefore, after day 16 re-plating at 800,000 cells/cm^2, I re-plated the mDA progenitors at lower densities at later stage of the differentiation around day 23, when neurites emerge but synapses are not yet formed. A poly-O + L111 coating was essential for plating on glass, as no neurons attached with L111 only coating (data not shown). Unexpectedly, when plating on cell culture plastic plates at 100,000 cells/cm^2, poly-O + L111 coating gave rise to more evenly spread-out neurons compared to L111 only coating, without a major effect on the presence of DA neurons on day 42 (Figure 4.6a). Re-plating at a lower density of 25,000 cells/cm^2 further highlighted the benefit of poly-O + L111 coating, since neurons clumped and began to lift on L111 only coating (Figure 4.6b).

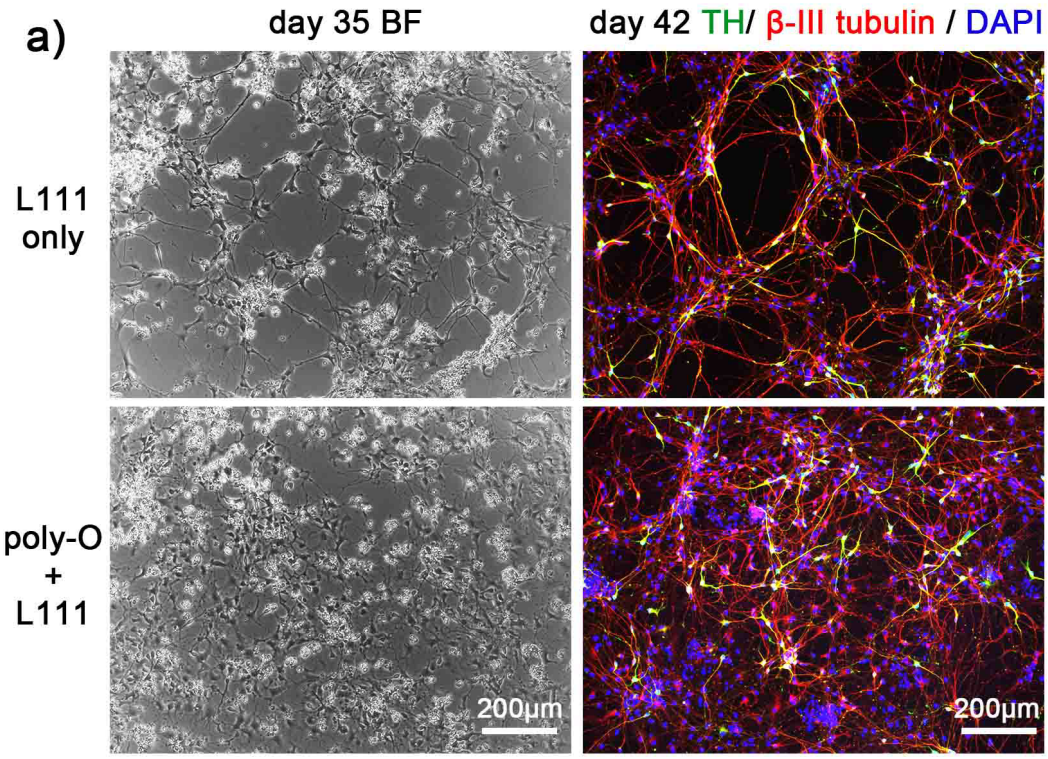

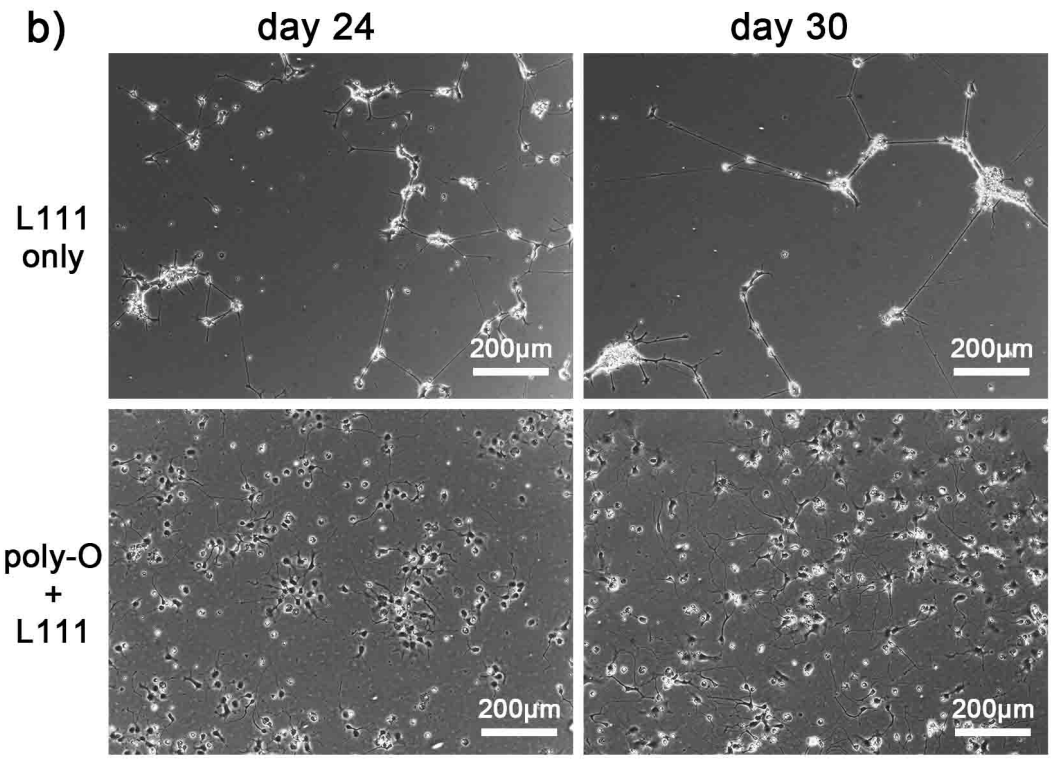

Figure 4.6 On day 23, plating on poly-O + L111 resulted in more evenly spread-out neurons compared to on L111 only without affecting the presence of DA neurons.

a) Day 35 bright field images and day 42 TH (green) / β-III tubulin (red) immunostaining of neurons plated at 100,000 cells/cm^2.

b) Day 24 and day 30 bright field images of a differentiation plated at 25,000 cells/cm^2.

4.3. mDA differentiation of *SNCA*$^{-/-}$, *SNCA*$^{+/-}$ and *SNCA*$^{S87E/S87E}$ hESCs was not impaired by aSyn mutation or the selection and cloning process

4.3.1. mDA neurons derived from hESCs with aSyn deletion or S87E/S87E mutation did not differ from those differentiated from the WT parental line in terms of mDA markers

To investigate whether aSyn deletion or S87E/S87E mutation affects mDA differentiation, I differentiated the hESCs with these mutations following the optimised mDA protocol and checked the expression of mDA markers. All *SNCA*$^{-/-}$, *SNCA*$^{+/-}$ and *SNCA*$^{S87E/S87E}$ hESC lines were successfully differentiated into floor plate progenitors of high purity, as shown by day 16 CORIN flow cytometry (Figure 4.7a). On day 44 of differentiation, down-regulated expression (versus hESCs counterparts) of pluripotent markers *NANOG* and *OCT4*, as well as an up-regulation of the

dopaminergic markers *NURR1*, *SOX6*, *DAT*, and *VMAT2* could be observed in all *SNCA*$^{-/-}$, *SNCA*$^{+/-}$ and WT cultures analysed by RT-qPCR (Figure 4.7b). This suggested *SNCA* deletion did not have a major effect on the mDA differentiation of hESCs. Immunostaining for the ventral neural marker FOXA2 at day 44 (Figure 4.7e&f), dopaminergic enzyme TH and pan-neuronal marker β-III tubulin at day 44 (Figure 4.7c&d) and day 77 (Figure 4.7g&h) further confirmed neither aSyn deletion nor S87E/S87E mutation had a major impact on mDA differentiation.

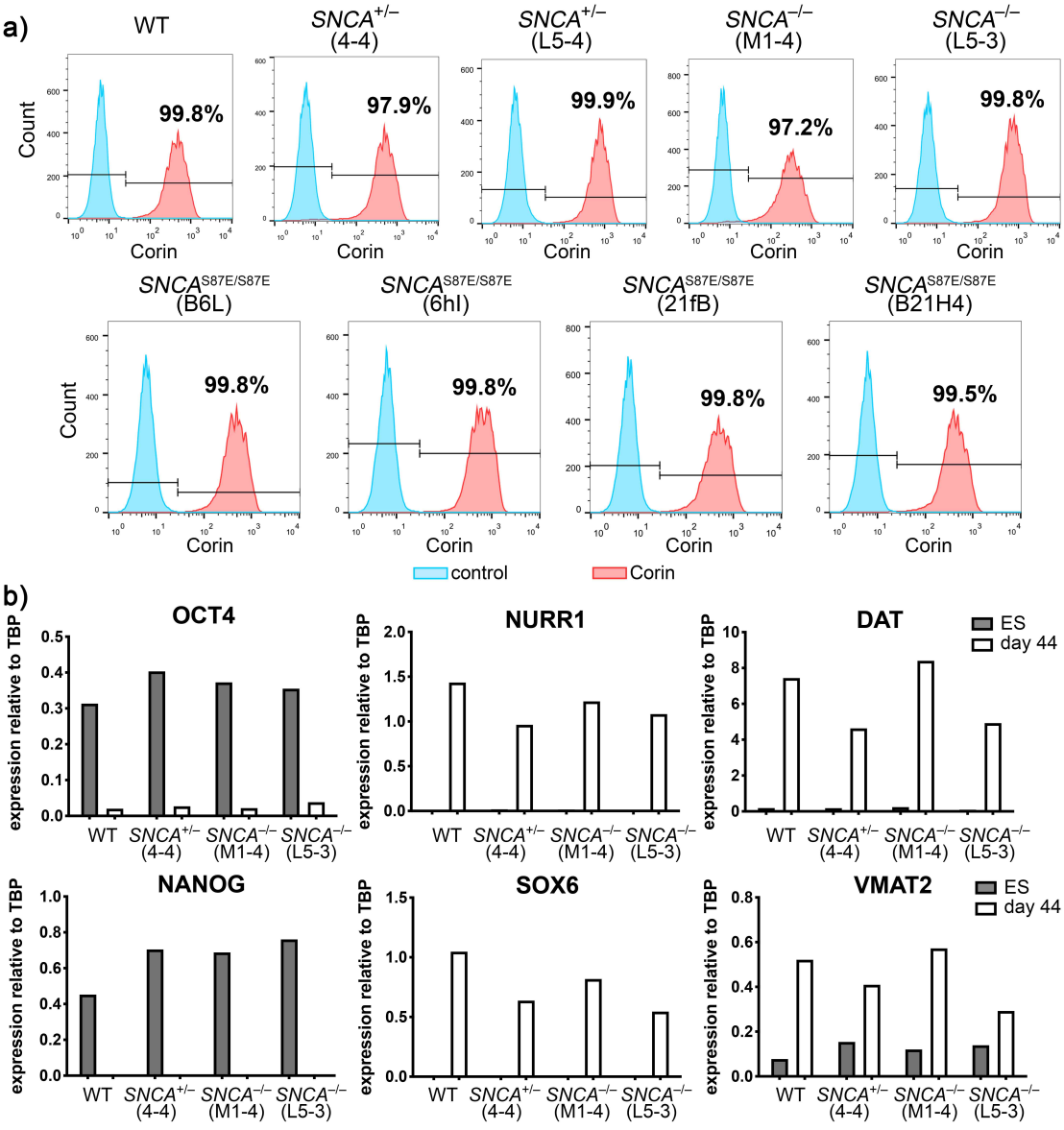

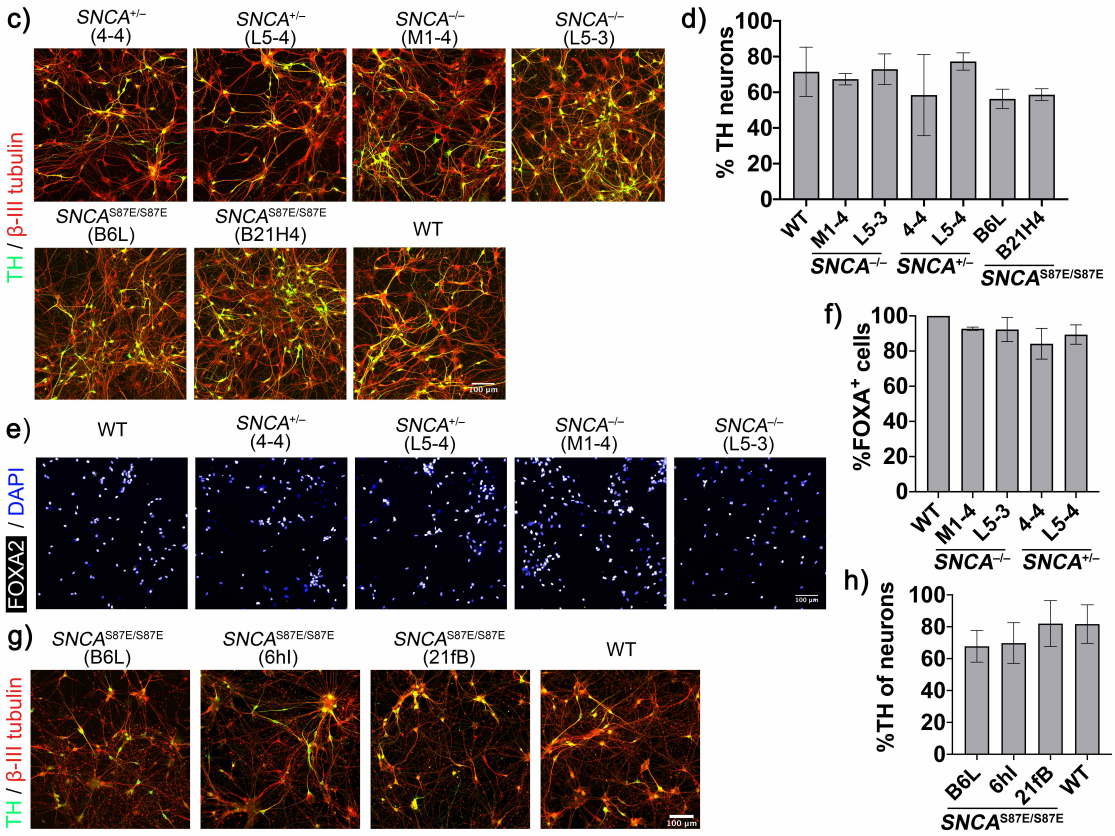

Figure 4.7 mDA neurons differentiated from hESCs with aSyn knockout or *SNCA*$^{S87E/S87E}$ mutation did not significantly differ from their WT parental line.

a) Day 16 CORIN flow cytometry revealed that highly pure floor plate progenitors could be derived from *SNCA*$^{-/-}$, *SNCA*$^{+/-}$ and *SNCA*$^{S87E/S87E}$ hESC lines.

b) RT-qPCR of *SNCA*$^{-/-}$, *SNCA*$^{+/-}$ and WT day 44 cultures revealed a substantial increase in mDA markers *NURR1*, *DAT*, *SOX6* and *VMAT2* and a drastic decrease in pluripotency marker *OCT4* and *NANOG*, compared to their ES counterparts. (N = 1)

c-f) Day 44 immunostaining of mDA neuron marker TH (green) / β-III tubulin (red) and FOXA2 (white) / DAPI and their quantification. Error bars were calculated from standard derivation of replicate wells (N = 1-2 wells, n = 2-5 fields).

g-h) Day 77 immunostaining of TH (green) / β-III tubulin (red) and its quantification. Error bars were calculated from standard derivation of replicate wells (N = 2-3 wells, n = 15-17 fields).

mDA neurons differentiated from WT, *SNCA*$^{+/-}$ and *SNCA*$^{S87E/S87E}$ hESC lines exhibited nuclear and cytoplasmic aSyn expression, while the ones differentiated from *SNCA*$^{-/-}$ lines lacked this expression (Figure 4.8) in agreement with previous western blotting data (Figure 3.2d). The localisation of aSyn was not synaptic in these day 44 neuronal cultures because they were not yet sufficiently mature. Similar mainly cytosolic and rarely synaptic localisation of aSyn has also been observed in immature primary hippocampal neurons (Murphy et al., 2000). This agrees with the observation

that aSyn is not redistributed from the cell body to synapses until 18 weeks of human embryo gestation (Galvin et al., 2001).

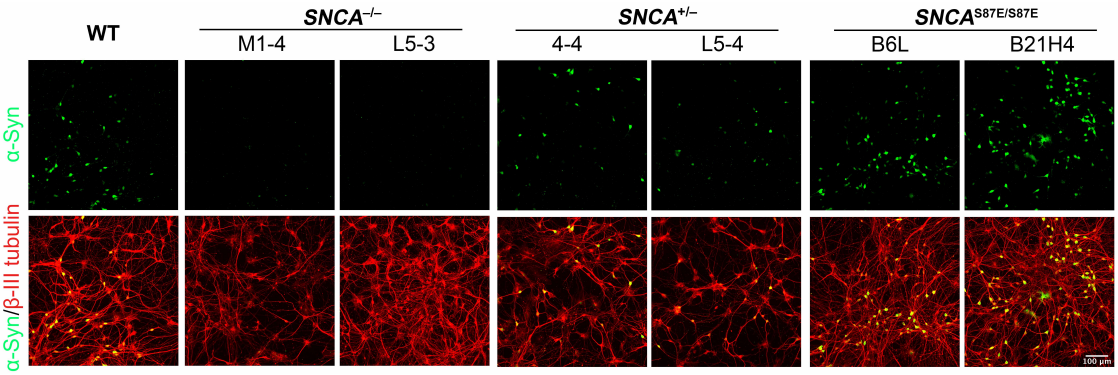

Figure 4.8 aSyn is expressed in DA neurons derived from *SNCA*$^{S87E/S87E}$ and WT hESC lines, is reduced in neurons derived from *SNCA*$^{+/-}$ lines and is absent in neurons derived from *SNCA*$^{-/-}$ lines, as revealed by aSyn (green) / β-III tubulin (red) immunostaining of day 44 cultures.

4.3.2. RNAseq revealed trivial changes in gene expression in *SNCA*$^{+/-}$ and *SNCA*$^{-/-}$ mDA neurons

For an unbiased transcriptome analysis of mDA neurons derived from *SNCA*$^{-/-}$, *SNCA*$^{+/-}$ and WT hESC lines, RNA was extracted from day 79 mDA cultures and sent to QIAGEN Genomic Services (Germany) for QIAseq UPX 3' Transcriptome RNAseq analysis. Similar number of genes were detected in samples of each genotype (Figure 4.9a). Principal component analysis (PCA) did not reveal any clusters, and samples of the 3 genotypes were distributed among each other in both PCA axes (Figure 4.9b). Consistently, in the unsupervised clustering based on the top 50 genes with the largest variance across all samples, samples of the 3 genotypes were distributed alternately in the heatmap (Figure 4.9c). Volcano plots for group-wise comparisons showed that a limited number of genes had fold change < –2 or > 2 with p-value < 0.05 (Figure 4.9d). Only one gene (*AL807752.7*), which is expressed less than 2-fold in *SNCA*$^{+/-}$ mDA neurons compared to *SNCA*$^{-/-}$ (bottom right of Figure 4.9d), passed the significance threshold after p-value adjustment for multiple testing (Benjamini-Hochberg method with false discovery rate (FDR) < 0.05). These findings suggest the transcriptome of *SNCA*$^{-/-}$, *SNCA*$^{+/-}$ and WT mDA neurons highly resemble one another and aSyn deletion is unlikely to have major impact on the expression profiles of mDA neurons.

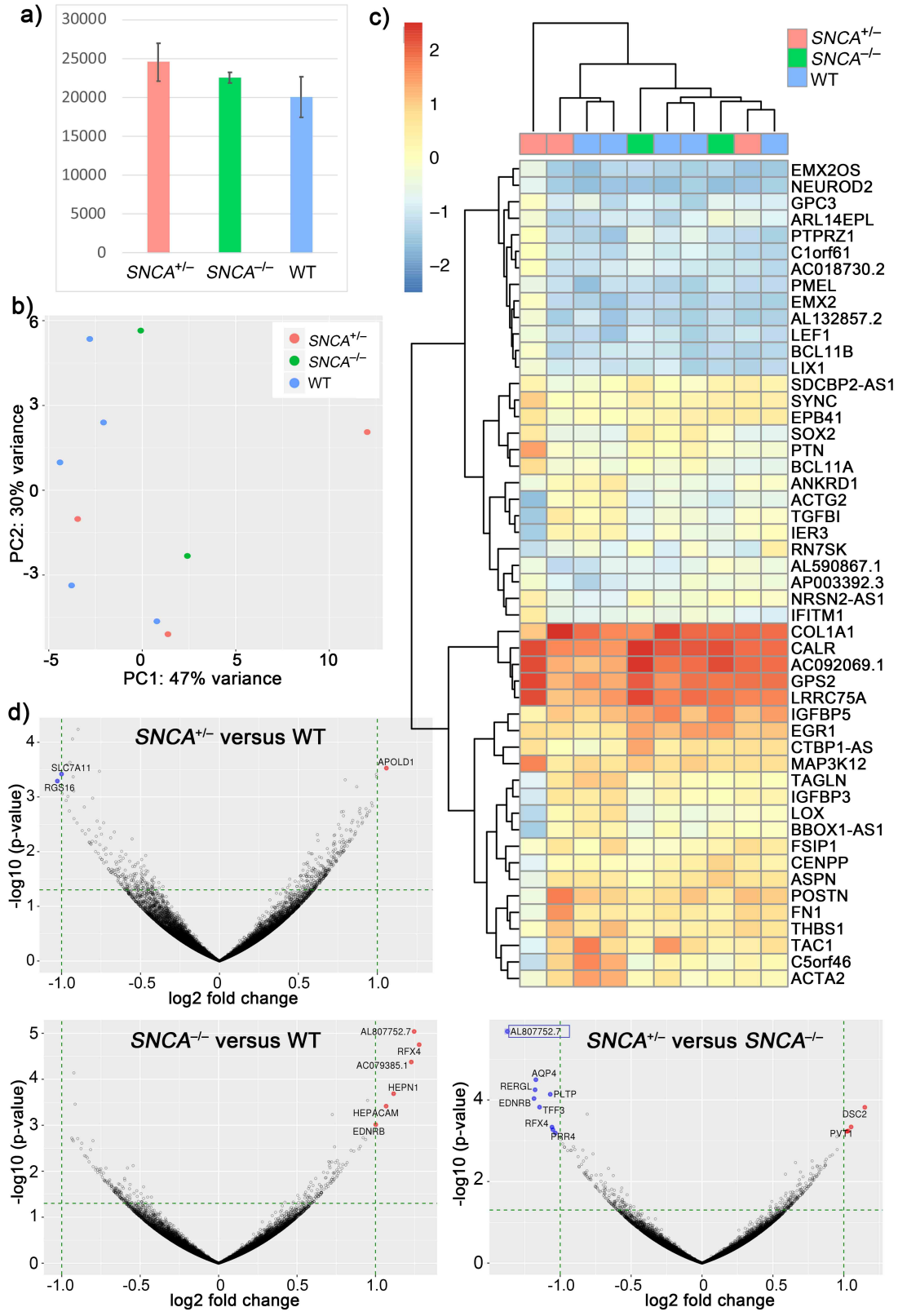

Figure 4.9 RNAseq analysis revealed trivial differences in transcriptome among *SNCA*$^{+/-}$ (n = 3), *SNCA*$^{-/-}$ (n = 2) and WT (n = 5) mDA cultures.

a) Number of genes detected per sample. Bars indicate mean ± standard derivation within the group of each genotype.
b) Principal component analysis (PCA) based on the top 50 genes with the largest variance across all samples.
c) Heatmap showing unsupervised clustering based on the top 50 genes.
d) Volcano plots displaying fold change in expression level and corresponding p-value of each detected gene in group-wise comparisons. Blue dots and red dots correspond to genes with fold change < –2 and > 2 respectively, with p-value < 0.05. The blue box indicates the gene (AL807752.7) with fold change > 2 and adjusted p-value < 0.05.

4.3.3. Deletion or S87E/S87E mutation of aSyn did not affect synapse formation in mDA cultures derived from hESCs of these genotypes

To examine whether aSyn deletion or S87E/S87E mutation impaired the capacity of synapse formation in hESC-derived mDA neurons, I performed immunostaining of pre-synaptic marker synapsin, post-synaptic marker PSD95 and pan-neuronal marker β-III tubulin in day ~80 mDA cultures. To remove background noise, I excluded synapsin and PSD95 particles which were not overlapping with β-III tubulin. Synapsin and PSD95 particles that co-localised within 1 µm with each other were considered part of a mature synapse, while the synapsin or PSD95 overlapping with β-III tubulin alone were regarded as immature (Figure 4.10a). Based on this classification, I quantified the number of total synapsin and PSD95 particles, as well as the number of mature synapsin and PSD95 particles and normalised them to the neuronal volume marked by β-III tubulin. To denote the maturity of synapsin and PSD95, I used the percentage of mature particles among total particles. Co-localisation of synapsin and PSD95 was detected in day 79 (circles) and day 83 mDA cultures (squares) regardless of aSyn deletion or S87E/S87E mutation (Figure 4.10). These findings agree with prior developmental studies (Galvin et al., 2001; Murphy et al., 2000) and observations in *Snca*$^{-/-}$ mice (Abeliovich et al., 2000; Cabin et al., 2002) that aSyn is not essential for synapse formation or development. However, in the current model, the number and maturity of synaptic markers were highly variable between differentiations (such as WT differentiation 1 and 2), suggesting a large number of differentiations would be required to detect subtle differences between genotypes.

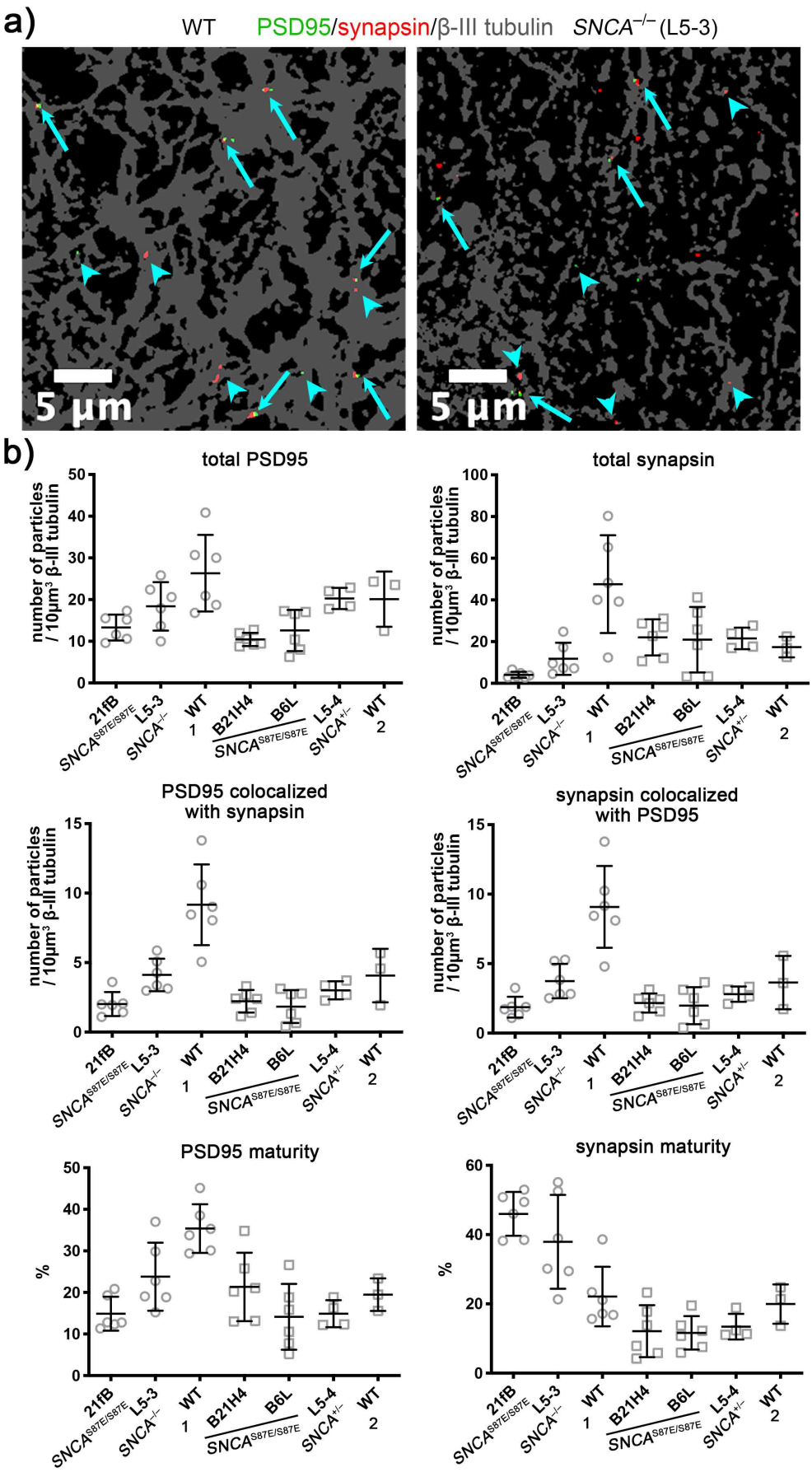
a)
WT
PSD95/synapsin/β-III tubulin
SNCA−/− (L5-3)
5 µm
5 µm
b)
total PSD95
number of particles / 10µm³ β-III tubulin
total synapsin
PSD95 colocalized with synapsin
synapsin colocalized with PSD95
PSD95 maturity
synapsin maturity
%
21fB SNCAS87E/S87E
L5-3 SNCA−/−
WT 1
B21H4 SNCAS87E/S87E
B6L SNCAS87E/S87E
L5-4 SNCA+/−
WT 2

Figure 4.10 Co-localisation of pre-synaptic marker synapsin and post-synaptic marker PSD95 were detected in day ~80 mDA cultures, although number of synapses and maturity of synaptic markers varied between differentiations.

a) Enlarged regions of synapsin / PSD95 / β-III tubulin immunostaining of *SNCA*$^{-/-}$ and WT mDA cultures demonstrating the classification of mature particles (arrows) and immature particles (arrow heads).

b) Quantification of number of total synapsin and PSD95 particles, mature synapsin and PSD95 particles normalised to neuronal volume (as marked by β-III tubulin), as well as maturity of synapsin and PSD95, which was defined as the percentage of total particles that were mature. Circles denote images of day 79 cultures while squares denote images of day 83 cultures. Bars indicate mean ± standard derivation.

4.3.4. Deletion or S87E/S87E mutation of aSyn did not affect spontaneous neuronal activities in mDA cultures derived from hESCs of these genotype

To examine the spontaneous neuronal activity of neurons differentiated from hESCs with aSyn deletion or S87E/S87E mutation, I perform calcium imaging on day 141 neurons. Neurons were loaded with fluo-8 to allow Ca^{2+} influx events to be detected by the change of fluorescence intensity of the cell bodies. To encourage spontaneous activities, I decreased the concentration of Mg^{2+} in the live imaging media stepwise. After recording of spontaneous activities, L-glutamate (L-Glu) and KCl were added to evoke Ca^{2+} influx, enabling the labelling of neurons based on the change of fluo-8 fluorescence intensity (Robertson et al., 2014). Spontaneous neuronal activities could be detected regardless of aSyn deletion or S87E/S87E mutation (Figure 4.11a). Out of the 400 cells analysed per well, many were already active at baseline and more became active as Mg^{2+} concentration decreased by half (Figure 4.11b). In all cultures, the active cells exhibited an increase in frequency of events in at least one of the decreased Mg^{2+} concentrations, compared to baseline (Figure 4.11b). The magnitude of events in active cells did not show any trend in response to the decreasing Mg^{2+} concentration (Figure 4.11b). However, all 3 aspects of the quantification were highly variable, even between sister wells (Figure 4.11b), suggesting only major defects in neuronal activity could be detected by this method.

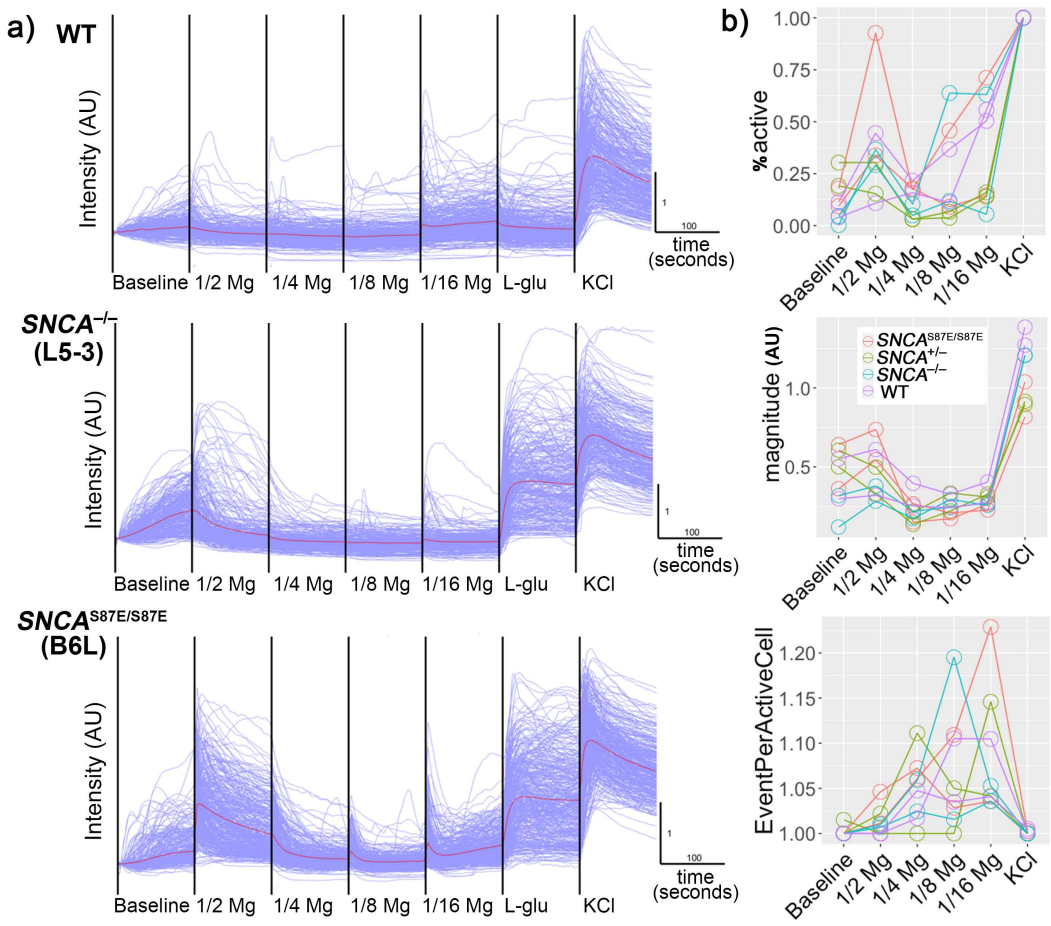

Figure 4.11 Spontaneous neuronal activities were detected by calcium imaging of day 141 *SNCA*$^{+/-}$, *SNCA*$^{-/-}$, *SNCA*$^{S87E/S87E}$ and WT mDA cultures. Concentration of Mg^{2+} in the live imaging media was decreased stepwise to encourage spontaneous activities. L-Glu and KCl were added in the end to distinguish neurons by their response to these stimuli. For each well, 400 cells with the most increase in Fluo-8 fluorescence intensity upon KCl exposure were analysed.

a) Sample traces of calcium imaging of *SNCA*$^{-/-}$, *SNCA*$^{S87E/S87E}$ and WT cultures.

b) Quantification of magnitude of events, events per cell and percentage of active cells during each condition. Results were variable even between sister wells (marked by the same colour, except for *SNCA*$^{S87E/S87E}$, where the 2 cultures were derived from 2 different *SNCA*$^{S87E/S87E}$ clones).

4.3.5. All tested mDA cultures released dopamine into conditioned media under baseline conditions and upon high K^+ stimulus

To examine the capacity of dopamine release in mDA neurons differentiated from *SNCA*$^{-/-}$, *SNCA*$^{+/-}$ and WT hESCs, I quantified the dopamine released by day 105 – 106 mDA cultures using UPLC-MS/MS analysis with a standard curve (Figure 4.12a). To measure the amount of dopamine the neurons produced spontaneously during

routine culture, I harvested the conditioned media which had been in culture for 4 days after a full media change. To measure the amount of dopamine produced by neurons upon high K^+ stimulation, I exposed the culture to fresh media supplemented with 25 mM KCl and collected the conditioned media after 15 min. Before high K^+ stimulation, cells were equilibrised in media supplemented with 50 mM sucrose (which is isotonic to the KCl supplemented media) overnight and exposed to fresh $sucrose^+$ supplemented media for 15 min twice to reduce the effect of osmolarity shock. Conditioned media from the last 15 min $sucrose^+$ media exposure was collected as an isotonic control. A high level of dopamine was released by WT mDA cultures in the media conditioned for 4 days, a moderate level in KCl^+ media conditioned for 15 min, a low level in $sucrose^+$ isotonic control conditioned for 15 min and a background level in the dopamine standard 0 ng/ml (Figure 4.12b). Similar to WT cultures, *SNCA*$^{-/-}$ and *SNCA*$^{+/-}$ mDA cultures released a high level of dopamine spontaneously and in response to high K^+ stimulus (Figure 4.12c).

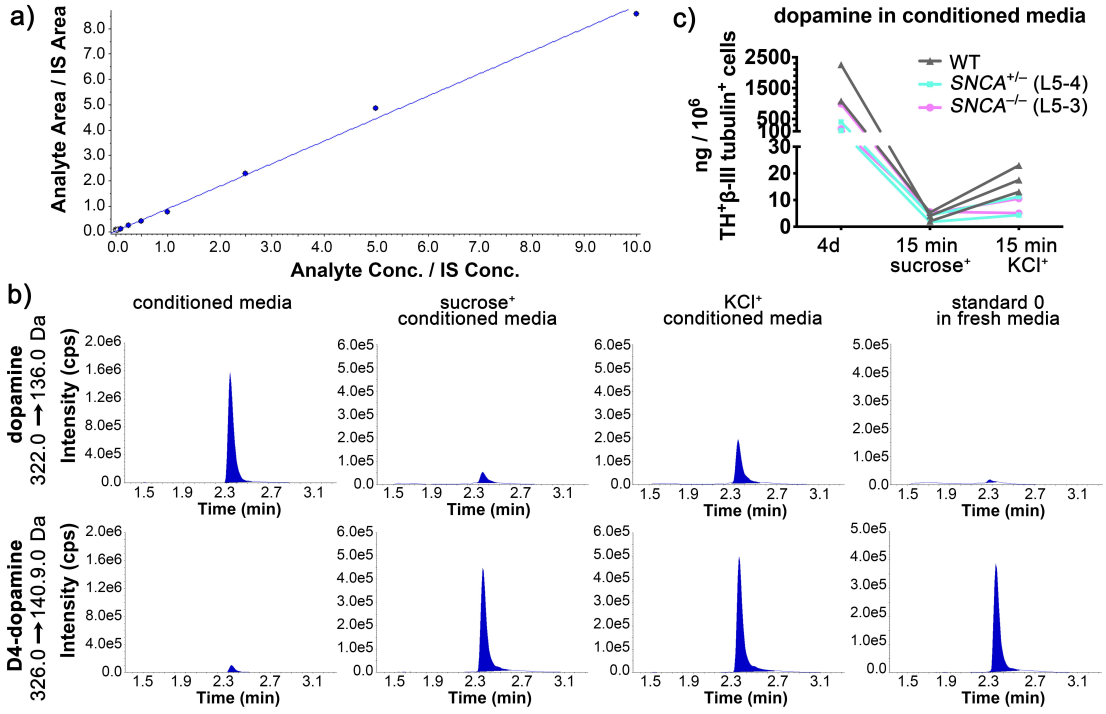

Figure 4.12 All tested mDA cultures released dopamine into conditioned media under baseline conditions as well as upon high K^+ stimulus.

a) A sample standard curve of dopamine in UPLC-MS/MS analysis.

b) UPLC-MS/MS chromatography of dopamine (top) and corresponding internal standard D4-dopamine (bottom) of samples (from left to right): conditioned media (on cells for 4 days) from day 105 WT mDA neurons, $sucrose^+$ conditioned media (on cells for 15 min, isotonic control)

from day 106 WT mDA neurons, KCl^+ conditioned media (on cells for 15 min) from day 106 WT mDA neurons, dopamine standard 0 ng/ml.

c) Quantification of dopamine released in different media types by different genotype of cells, normalised to the number of TH / β-III tubulin double positive cells.

4.4. Discussion

In this chapter, I investigated the differentiation potential of *SNCA*$^{-/-}$, *SNCA*$^{+/-}$ and *SNCA*$^{S87E/S87E}$ hESCs and functions of the resulting mDA neurons. To accomplish this, I optimised the mDA differentiation protocol and demonstrated that the following points were crucial for obtaining dopaminergic neurons with midbrain identity:

- Fine-tuning of CHIR concentration is critical for obtaining progenitors with a correct mDA identity.
- Whether the progenitors obtained a mDA identity can be assessed at the early stage of differentiation by LMX1A and FOXA2 immunostaining at day 11 and CORIN flow cytometry at day 16.
- Day 16 RT-qPCR of anteroposterior and dorsoventral markers can facilitate the determination of optimal CHIR concentrations which give rise to mDA progenitors.
- For applications where the overlap of cell bodies is undesirable, such as calcium imaging and TMRM live imaging, an additional re-plating at day 23 on poly-O + L111 coating would give rise to low density mDA cultures.

Based on the optimized protocol, I demonstrated that *SNCA*$^{-/-}$, *SNCA*$^{+/-}$ and *SNCA*$^{S87E/S87E}$ hESCs can be differentiated into mDA neurons highly resembling those differentiated from WT hESCs. They harboured similar expression profiles as WT mDA neurons and did not have notable defects in synapse formation, spontaneous neuronal activities, or the release of dopamine both spontaneously under baseline conditions and in response to high K^+ stimulus.

Consistent with previous studies (Kirkeby et al., 2012; Xi et al., 2012), I found that only a very narrow window of CHIR concentration (< 0.3 μM) was capable of inducing mDA progenitors. Furthermore, a slight change of 0.1 μM in CHIR concentration could give rise to progenitors with considerably altered gene expression (Figure 4.2 and 4.3). This could be due to several reasons, such as off-target effects and modulation of other signalling pathways. CHIR is a highly potent GSK3β inhibitor that works at nanomolar concentrations (Bain et al., 2007), but it also inhibits other enzymes with nanomolar to

micromolar affinity, which can produce off-target effects. In addition, GSK3β has many substrates other than β-catenin, so the on-target inhibition of GSK3β could alter diverse signalling pathways. Furthermore, endogenous WNT expression can also affect the differentiation, further complicating the effect of exogenous β-catenin activation (Hackland et al., 2017). A baseline activation method, where the unpredictable endogenous WNT secretion is inhibited with a small molecule porcupine inhibitor IWP-2, might enable a tighter control of WNT activation when applying exogenous CHIR (Hackland, 2019).

In prior studies, the optimal CHIR concentration was 0.9 μM for RC17, 0.6 – 1.0 μM for other hESC lines (Nolbrant et al., 2017) and 0.4 – 0.6 μM for hESC line H9 (Xi et al., 2012). Their differences from my optimal CHIR concentration (1.0 – 1.3 μM) could be due to multiple factors, including cell lines and base cell culture medium. While I plated RC17 at 40,000 cells/cm^2 on day 0 of differentiation, (Nolbrant et al., 2017) plated at a lower density of 10,000 cells/cm^2, which could result in less CHIR required to pattern the correct midbrain identity. In contrast to my protocol and (Nolbrant et al., 2017) using CHIR from differentiation day 0 to day 9, (Xi et al., 2012) exposed the differentiation to CHIR for a longer duration from day 0 to day 12, which might also result in the need of a lower CHIR concentration.

A suboptimal CHIR concentration resulted in CORIN negative/low progenitors and gave rise to fibroblast-like cells. This suggests the fibroblast-like cells might be derived from forebrain progenitors, or they were an alternative cell type this protocol gave rise to when CHIR concentration was not optimal for producing mDA neurons. In fact, fibroblast-like cells were only observed in stem cell-derived graft but not in fetal tissue-derived graft, suggesting they might be a cell culture artefact (Tiklová et al., 2019). The exact identity and functions of the fibroblast-like cells also remain unclear. My observation of them being TH$^-$PDGFRα$^-$COL1A1$^+$ suggested they could be arachnoid barrier cells, which required further characterisation of positive markers *SLC47A1*, *ABCG2*, *PGP* and negative marker *LUM* (Zeisel et al., 2018). Once their identity is confirmed, it would be interesting to investigate whether they play a supportive role for the differentiation or functioning of mDA neurons. An early study which achieved mDA neurons isolation with 80-96% purity by striatal injection and retrograde transport of fluorescence dye followed by FACS, found fibroblast-like cells in the sorted midbrain tissue (Kerr et al., 1994). This suggested that the fibroblast-like cells might be functionally and/or spatially related to mDA neurons. As

hESC/hiPSC-derived mDA progenitors are now a promising alternative source for cell replacement therapy for PD (Cyranoski, 2018; Kirkeby et al., 2017b; Studer, 2017), the presence of these fibroblast-like cells in hESC-derived graft after *in vivo* differentiation (Tiklová et al., 2019) should be considered carefully. It is vital to understand how the fibroblast-like cells interact with other cell types and whether they proliferate as they do *in vitro* according to my observation, which could be tumorigenic *in vivo*.

Astrocytes enriched genes RFX4 and AQP4 were picked up as differentially expressed genes in the RNAseq experiment. This is unlikely to be an effect of *SNCA* knockout, as these astrocytes enriched genes were down-regulated in $SNCA^{+/-}$ cultures compared to $SNCA^{-/-}$ cultures, and were not significantly different in pair-wise comparison of $SNCA^{+/-}$ versus WT or $SNCA^{-/-}$ versus WT cultures. Instead, it might indicate some cultures had more astrocytes than others. As astrocytes have the capacity to trap and degrade PFFs (Lee et al., 2008b; Loria et al., 2017), cultures with more astrocytes might form less PFF-induced pS129-αSyn structures.

In this chapter, differentiation-to-differentiation variation was observed in the quantification of synaptic staining and, even well-to-well variation in calcium imaging. The maturity of differentiation and synapse formation might be affected by multiple factors during a lengthy differentiation protocol. One important factor would be the cell viability after day 23 re-plating which could lead to variations in cell density and cell signaling during terminal differentiation. In addition, the presence of unintended cell types such as the fibroblast-like cells might also affect the maturity of cultures. However, such variations in differentiation are difficult to quantify and too complicated to be accounted for by a simple normalization to cell count. Furthermore, the accuracy of the current synaptic staining was limited by the resolution of microscopy. Specific antibody-labelling of target proteins and sufficiently high signal-to-noise ratio are crucial for accurate identification of synapses. However, this is unlikely the case in fluorescence light microscopy where synaptic puncta are labelled with heterogeneous intensity (Wang et al., 2019). With novel analytical tools such as SynQuant (Wang et al., 2019) and DoGNet (Kulikov et al., 2019), it is possible to detect synaptic puncta more accurately with optimized algorithms than with a simple global threshold.

For calcium imaging, well-to-well variation was most probably due to difference in maturity, as less mature cultures tend to be more random in their spontaneous activities.

The variation could also partially result from manual application of solution without a perfusion system, but it is unlikely to be due to the time interval between the recording of wells. In fact, for 8 wells on an ibidi µ-slide, the last well was left in live imaging bugger and imaged ~2 hours later than the first one, but no relation between activities and the sequence of imaging was observed. In addition, intrinsic well-to-well variation in electrophysiology patterns of *in vitro* neuron cultures has been documented in prior study (Wagenaar et al., 2006). In the current imaging condition (2 Hz), only bulk events could be detected while higher frequency events were blurred. Only temporal resolution as high as kHz frame rate (Martens et al., 2014) would enable recording of an action potential. In addition, multi-electrode arrays can be used as an alternative to or in combination with calcium imaging (Shew et al., 2010) to collect data from multiple wells simultaneously, each with thousands of electrodes.

Here, for the first time to my knowledge, dopamine secretion was measured in cell culture media of mDA neurons differentiated from *SNCA*$^{-/-}$ and *SNCA*$^{+/-}$ hESCs. More independent cultures would be required to determine whether aSyn knockout led to a difference in dopamine release. If no differences were observed, it would agree with prior studies where *Snca*$^{-/-}$ mice did not exhibit alternations in the level of dopamine released upon single electric or amphetamine stimuli (Abeliovich et al., 2000; Yavich et al., 2004). Interestingly, *Snca*$^{-/-}$ mice also have a smaller pool of reserve/resting vesicles (Cabin et al., 2002) and the readily releasable vesicles refills faster and results in higher dopamine release upon repetitive stimulations (Abeliovich et al., 2000; Yavich et al., 2004). In addition, the dopamine content in striatum tissue is lower in *Snca*$^{-/-}$ mice compared to WT mice (Abeliovich et al., 2000; Al-Wandi et al., 2010; Anwar et al., 2011). These properties would be interesting to be examined in *SNCA*$^{-/-}$ and *SNCA*$^{+/-}$ hESC-derived mDA neurons using the appropriate electrophysiology and analytical tools.

In summary, mDA neurons could be differentiated from *SNCA*$^{-/-}$, *SNCA*$^{+/-}$ and *SNCA*$^{S87E/S87E}$ hESCs at a comparable quality to those differentiated from WT hESCs. Nonetheless, finer functionalities assays would be required to investigate biological differences between *SNCA*$^{-/-}$, *SNCA*$^{+/-}$, *SNCA*$^{S87E/S87E}$ and WT mDA neurons.

Chapter 5: *SNCA* knockout and *SNCA*$^{S87E/S87E}$ mutation provided resistance to synucleinopathy

5.1. Introduction

To induce α-Syn pathology in human mDA neurons, I used an established α-Syn pre-formed fibrils (PFFs) model (Volpicelli-Daley et al., 2011). α-Syn PFFs induced phosphorylation of α-Syn at Ser129 (pS129-αSyn), a post-translational modification which occurs in Lewy bodies and is a reliable biomarker of aggregated α-Synuclein (Anderson et al., 2006; Fujiwara et al., 2002) that can be detected by immunostaining. α-Syn PFF cell models can also model structural and functional impairments in PD which occur prior to neuron death, including impairment of mitochondria, synapses and spontaneous neuronal activities (see section 1.3.1.2).

In DLB patients, α-Syn aggregates accumulate at pre-synaptic terminals, accompanied by significant decrease in expression of pre- and post-synaptic markers (Kramer and Schulz-Schaeffer, 2007; Scott et al., 2010). In mDA cultures differentiated from A53T PD patient-derived iPSCs, synapse formation was significantly reduced, as marked by synapsin / PSD95 co-localisation and the expression level of various synaptic proteins (Kouroupi et al., 2017). The altitude and frequency of synaptic events were also compromised in these A53T α-Syn mDA neurons (Kouroupi et al., 2017). Exposing primary or hiPSC-derived neurons to α-Syn PFFs represented a cell model with compromised levels of synaptic proteins, impaired synapse formation (Mahul-Mellier et al., 2019; Tran et al., 2014; Volpicelli-Daley et al., 2011; Wu et al., 2019) and defects in spontaneous neuronal activities (Gribaudo et al., 2019; Peelaerts et al., 2015; Volpicelli-Daley et al., 2011; Wu et al., 2019).

In addition, α-Syn accumulation and complex I deficiency were found in the damaged mitochondria in post-mortem brain of PD patients (Devi et al., 2008). PFF model of primary or hiPSC-derived neurons recaptured the fragmentation of mitochondria (Grassi et al., 2018; Gribaudo et al., 2019) and impairment of mitochondrial membrane potential (Grassi et al., 2018; Mahul-Mellier et al., 2019).

In this chapter, I employed the α-Syn PFF model in WT hESC-derived mDA neurons and explored a range of published PFF-induced pathologies. Based on the successful

establishment of this model, I investigated the susceptibility of *SNCA*$^{+/-}$, *SNCA*$^{-/-}$ and *SNCA*$^{S87E/S87E}$ mDA neurons to these pathologies.

5.2. PFFs induced α-Syn pathology in WT mDA cultures, but did not result in detectable cell death or significant impairment of synapse formation, mitochondria or spontaneous neuronal activities

5.2.1. PFFs induced α-Syn pathology which stained for pS129-αSyn and p62 in WT cultures

To produce α-Syn PFFs, human α-Syn protein was expressed and isolated from HEK 293 cells. Fibrillar human α-Syn protein was produced by agitation of monomeric protein and was subsequently sonicated to produce α-Syn PFFs (Chen et al., 2019). The quality of PFFs was assayed to ensure JC-1 fluorescence with a main absorbance at 540 nm, < 5% monomer as judged by NuPAGE™ electrophoresis of the ultracentrifugation supernatant and an ATR-FTIR absorption between 1,625 and 1,630 cm^{-1}. The recombinant α-Syn PFFs, α-Syn monomers, or vehicle control (PBS) were then added to the culture media of day 44 WT mDA neurons at a concentration of 5 µg/ml.

After 5 weeks of additional culture, I performed immunostaining for pS129-αSyn and pan neuronal marker β-III tubulin. WT mDA neurons exposed to α-Syn PFFs developed numerous pS129-αSyn structures within 5 weeks, while α-Syn monomers or PBS vehicle control did not induce such structures (Figure 5.1). To quantify the level of pS129-αSyn pathology in neurons, I thresholded the pS129-αSyn and β-III tubulin immunostaining and converted them to binary images (Figure 5.1). Subsequently, I calculated the percentage of β-III tubulin^{+} space (i.e. neurons) occupied by pS129-αSyn signal to quantify the level of pathology (Figure 5.1).

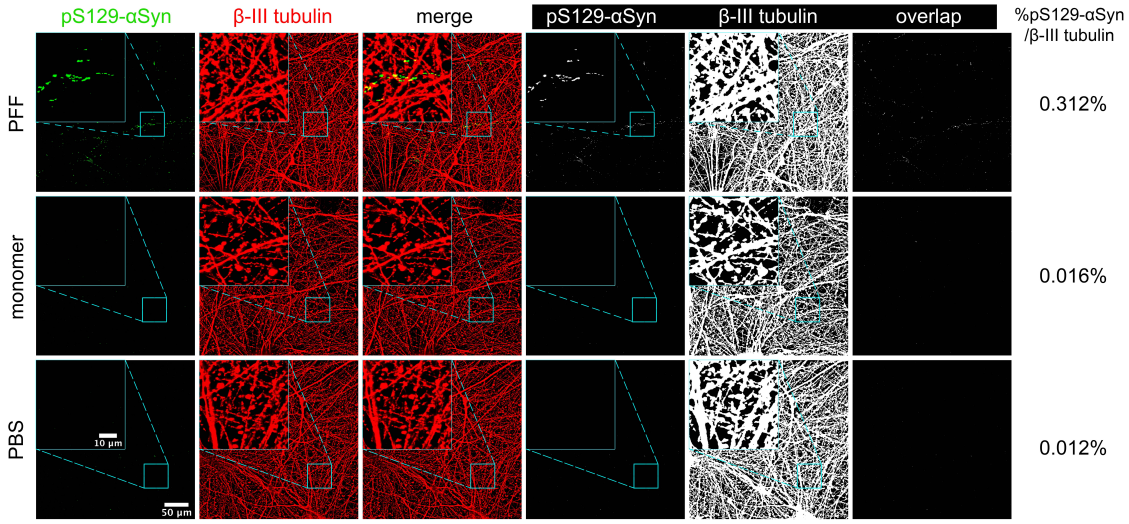

Figure 5.1 pS129-αSyn^{+} structures were found only in cultures treated with PFFs, but not in cultures treated with α-Syn monomers or PBS vehicle control. The fluorescence images were captured at 40x and z-projected before each channel was thresholded into binary image. An overlap binary image of the two channels were made. Quantification for pS129-αSyn pathology was calculated as the percentage of β-III tubulin area occupied by the overlap.

I then decided to investigate whether the amount of pS129-αSyn pathology is affected by the length of culture after PFF treatment and/or the density of neurons. I performed the pS129-αSyn / β-III tubulin immunostaining on the same WT mDA differentiation plated at two cell densities, the sister wells of which were fixed at 7 and 9 weeks respectively after PFF treatment (Figure 5.2a). In cultures plated at 25,000 cells/cm^2, the level of pS129-αSyn pathology developed by 7 or 9 weeks was not significantly different. However, when plated at 80,000 cells/cm^2, 2 weeks of additional culture significantly increased the amount of pS129-αSyn pathology ($p = 0.001$). Plating at higher density increased the amount of pathology (Figure 5.2b, three-way ANOVA and post hoc comparisons with Sidak correction, $p = 0.2765$ at 7 weeks and $p < 0.0001$ at 9 weeks). These results suggested that higher neuron density contributed considerably to the level of pS129-αSyn pathology, while longer culture period after PFF treatment had a relatively minor but still positive effect, especially when neurons were plated at high density.

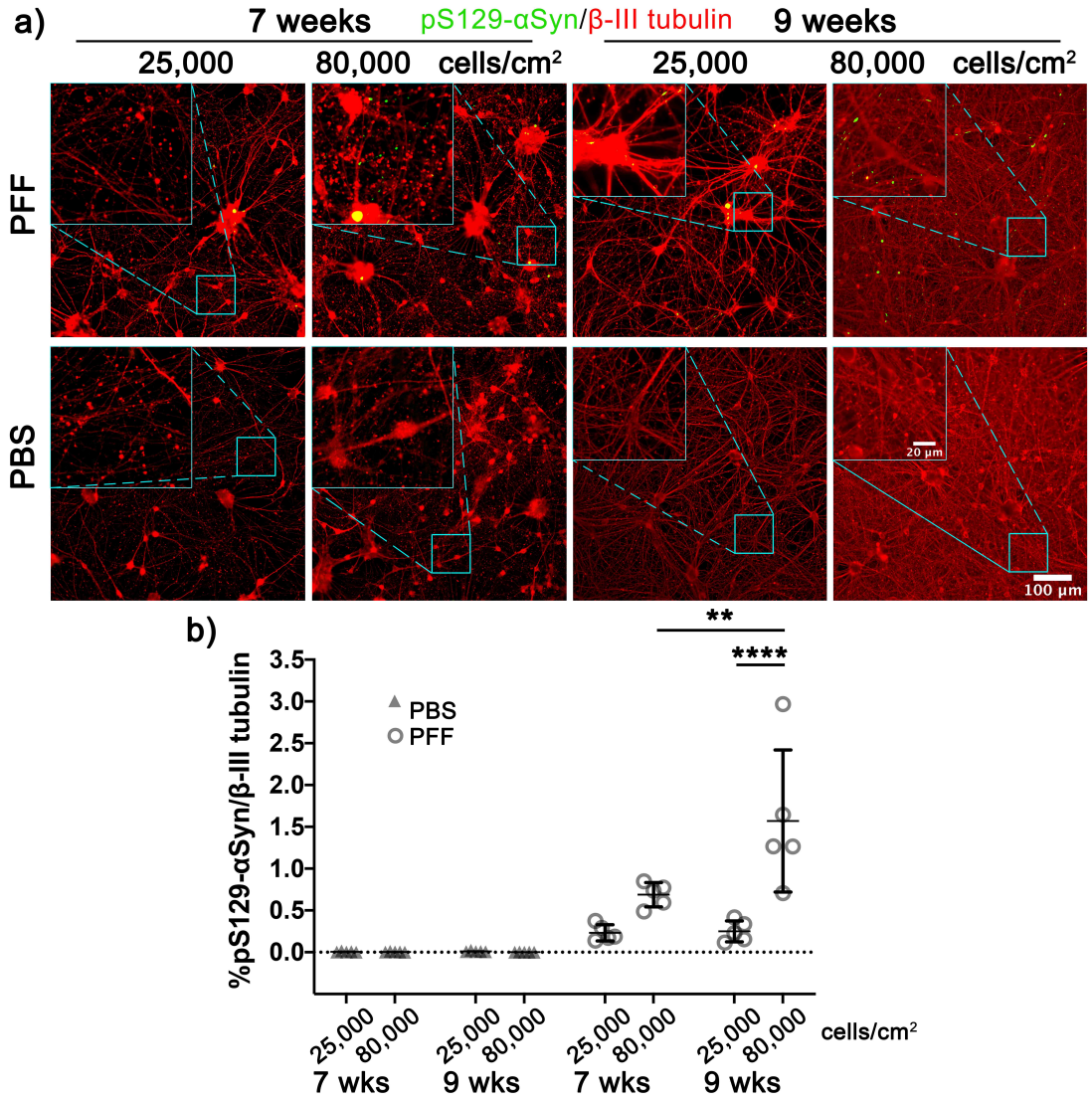

Figure 5.2 Longer culture period after PFF treatment and higher plating density of neurons increased the amount of pS129-αSyn pathology (normalised to area of β-III tubulin).

a) Sample fields of WT neurons plated at 25,000 cells/cm^2 and 80,000 cells/cm^2, treated with PFF and PBS control, and fixed at 7 and 9 weeks after treatment. Imaged at 20x.

b) Quantification of pS129-αSyn pathology overlapping with β-III tubulin area. n = 5 fields per condition. Bars indicate mean ± standard derivation. **** $p < 0.0001$, ** $p < 0.01$, three-way ANOVA, post hoc comparisons with Sidak correction.

To confirm the characteristics of the α-Syn pathology structures induced by PFFs, I stained for p62, another well-established Lewy body marker which is a common component in neuropathological inclusions (Kuusisto et al., 2003; Zatloukal et al., 2002). I performed p62 / pS129-αSyn / β-III tubulin immunostaining on two WT mDA

differentiations: one plated at 25,000 cells/cm^2 and cultured for 5 additional weeks after PFF treatment, the other plated at 80,000 cells/cm^2 and cultured for 9 additional weeks after PFF treatment. Although numerous pS129-αSyn structures were found in the first culture, they did not co-localized with p62 (Figure 5.3a). Only in the 9-week-post-treatment culture of 80,000 cells/cm^2, I found p62 co-staining with pS129-αSyn (indicated by white arrows in Figure 5.3b). This suggested that these pS129-αSyn structures resembled genuine Lewy bodies, but were only positive for p62 when relatively mature.

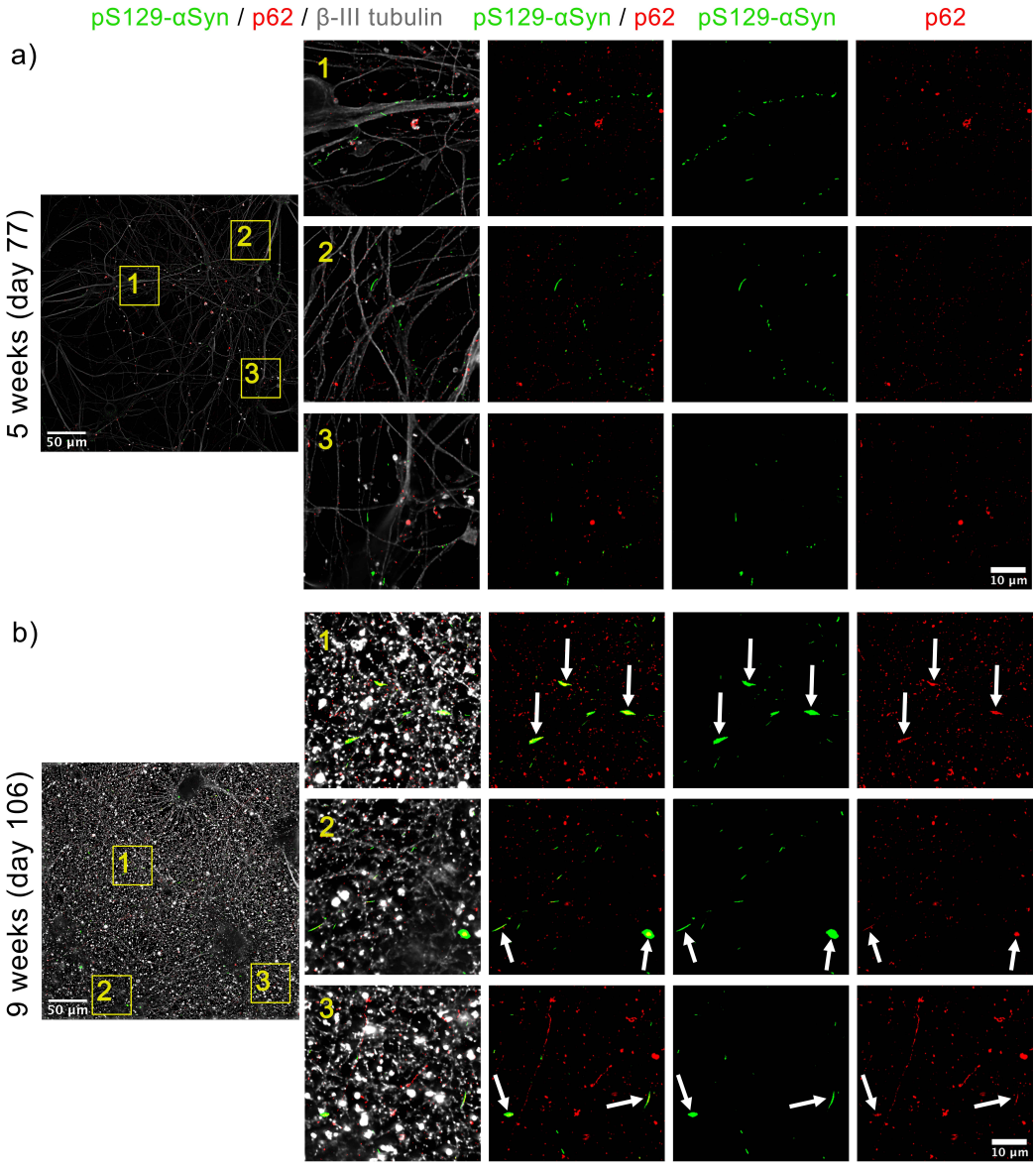

Figure 5.3 Co-localisation (indicated with white arrows) of p62 (red), another marker for Lewy bodies, with pS129-αSyn (green) was found in b) 80,000 cells/cm^2 WT mDA cultures

9 weeks after PFF treatment, but not in a) 25,000 cells/cm^2 WT mDA cultures 5 weeks after PFF treatment. Neurons were marked by β-III tubulin (grey).

5.2.2. PFFs did not induce cell death to a level detectable by LDH assay in the WT mDA cultures examined

To investigate whether PFF-induced pathology causes cell death in the current model, I performed lactate dehydrogenase (LDH) assay on the conditioned media from mDA cultures weeks after PFF treatment. LDH is a cytosolic enzyme which is released into surrounding media upon plasma membrane damage and is hence an indicator of cytotoxicity.

I collected conditioned media from 25,000 cells/cm^2 and 80,000 cells/cm^2 mDA cultures 3, 4 and 6 weeks after PFF treatment, respectively, and proceeded with LDH assay immediately. The amount of LDH was measured at 490 nm after coupled enzymatic reactions and subtracted by the background absorbance at 680 nm. Surprisingly, in all 3 experiments, LDH level in conditioned media from PFF-treated cultures was at a background level comparable to that in blank media or PBS vehicle-treated cultures (Figure 5.4). Cell lysate of a culture with the same number of cells (100% cell death) gave rise to absorbance of a positive level (Figure 5.4). This suggested that up to 6 weeks after PFF treatment, the cell death in these PFF-treated cultures was lower than the detection limit of LDH assay.

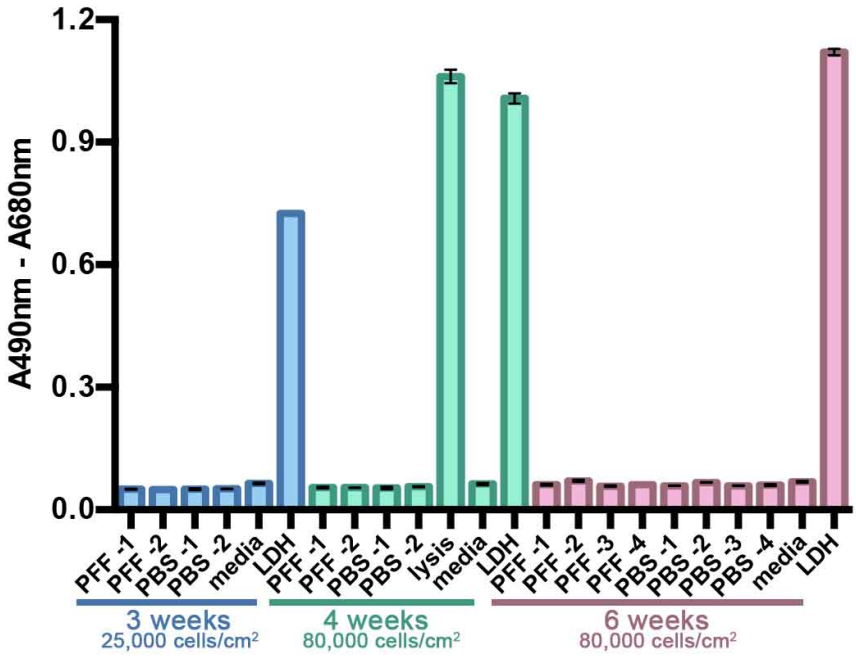

Figure 5.4 Lactate dehydrogenase (LDH) level in conditioned media collected from PFF-treated wells and PBS control wells were similar to that in blank media (negative control). Conditioned media were collected from 1 cm^2 cultures plated at different density and collected at various time point after PFF treatment: 3 weeks from 25,000 cell/cm^2 cultures, 4 weeks from 80,000 cell/cm^2 cultures and 6 weeks from 80,000 cell/cm^2 cultures. For all 3 experiments, the last half media change was 7 days before the collection of conditioned media. LDH enzyme and lysis of 80,000 cells were used as positive controls. Error bars were calculated from standard derivation of technical triplicates; suffix -1, -2, -3 and -4 in sample names indicated biological replicates.

5.2.3. PFFs did not affect synapse formation or maturity in WT mDA neurons

To study if PFF-induced pathology affects synapse formation and maturity in WT mDA neurons, I performed synapsin / PSD95 / β-III tubulin immunostaining on cultures plated at 25,000 cells/cm^2, 5 weeks after PFF or PBS vehicle treatment (Figure 5.5a). Although synapse formation and maturity varied between differentiations (Figure 4.10), it is theoretically possible to observe differences between PFF and PBS vehicle-treated wells within the same differentiation. Using the method described in Chapter 4, I quantified the number of total and mature synapsin and PSD95 particles normalised to the neuronal volume marked by β-III tubulin, as well as the maturity of synapsin and PSD95. For each of these aspects, not more than 1 out of 4 differentiation experiments showed significant difference between PFF-treated wells (red squares) and PBS vehicle-treated wells (black dots) (Figure 5.5b, two-way ANOVA and post hoc comparisons with Sidak correction). This suggested that the impact of PFF-induced pathology on synapse formation and maturity at 5 weeks after PFF treatment, if any, is too minor to be detected by this immunostaining and imaging conditions.

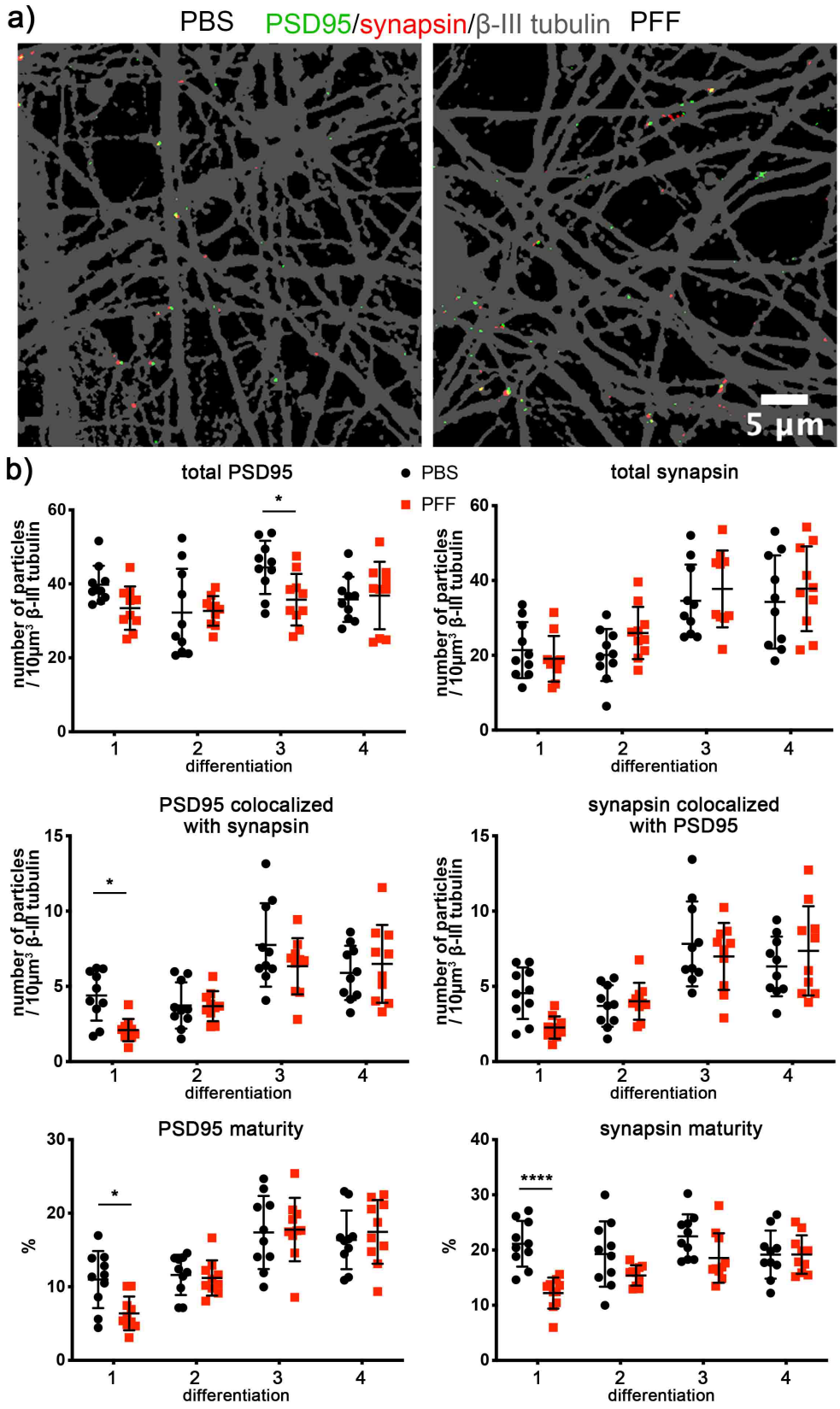

Figure 5.5 PFFs did not induce consistent decrease in total number or maturity of pre-synaptic marker synapsin or post-synaptic marker PSD95 in WT mDA cultures across 4 differentiations 5 weeks after PFF treatment.

a) Enlarged regions of synapsin (red) / PSD95 (green) / β-III tubulin (grey) immunostaining in PBS (left) and PFF (right) treated WT mDA cultures.
b) Quantification of total number of synapsin and PSD95 particles, number of mature synapsin and PSD95 particles normalised to the volume of neurons marked by β-III tubulin, as well as maturity of synapsin and PSD95. n = 10 fields from 2 wells per differentiation and 4 independent differentiation. Although the result varied between differentiations, it can be compared between PFF and PBS wells within the same differentiation. Bars indicate mean ± standard derivation. * $p < 0.05$, **** $p<0.001$, two-way ANOVA, post hoc comparisons with Sidak correction.

5.2.4. PFFs did not significantly impair spontaneous neuronal activities in WT mDA neurons

To investigate whether PFF-induced pathology has an impact on spontaneous neuronal activities in WT mDA neurons, I performed calcium imaging on cultures plated at 80,000 cells/cm^2, 7 weeks after PFF or PBS vehicle treatment. Similar to previous calcium imaging recordings (section 4.3.4), neurons were loaded with Fluo-4 and marked by response to KCl stimulus. Mg^{2+} concentration was decreased stepwise to encourage spontaneous activities. Spontaneous neuronal activities could be detected in neurons treated with PBS vehicles and also in those treated with PFFs. Both PFF-treated and PBS-treated cultures showed an increasing trend in the percentage of active cells as Mg^{2+} concentration decreased (Figure 5.6b). The frequency and magnitude of events in active cells in most of the cultures did not exhibit a clear response to the decreasing Mg^{2+} concentration (Figure 5.6b). However, the results were highly variable even between sister wells (Figure 5.6a, and data points denoted by the same shape in Figure 5.6b), which made it impossible to compare PFF-treated and PBS-treated wells with confidence.

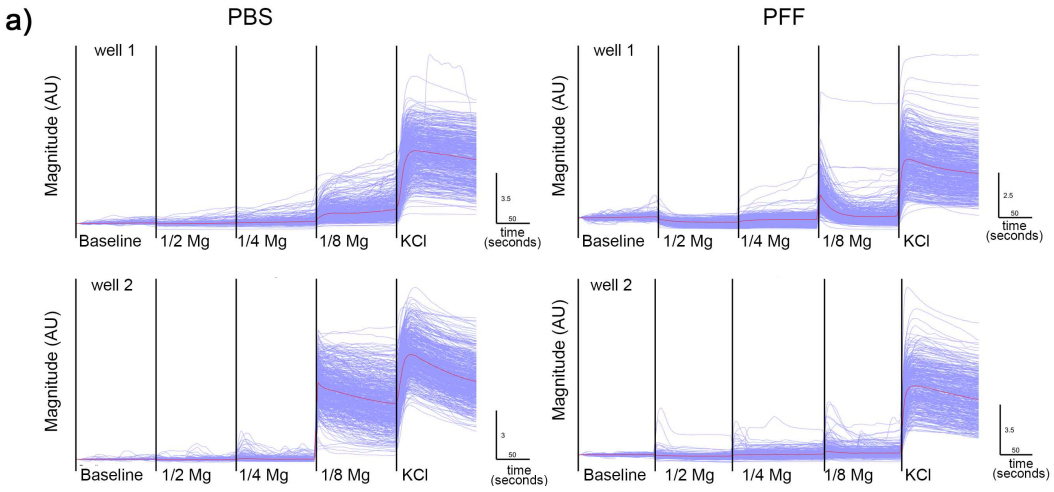

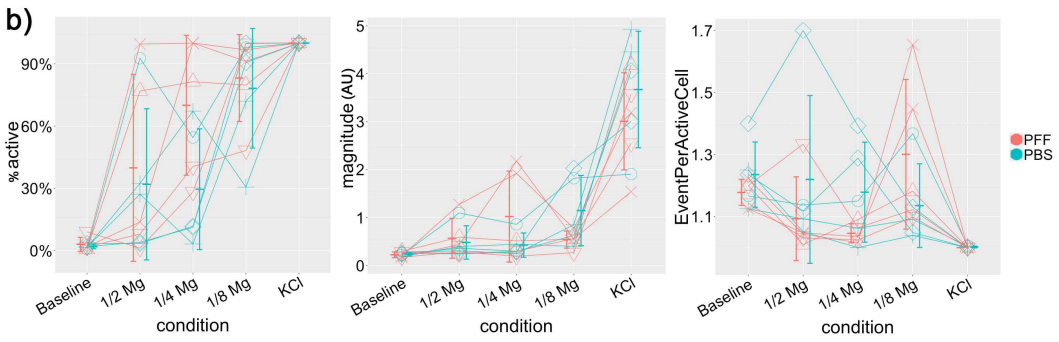

Figure 5.6 PFF treatment did not have significant impact on spontaneous neuronal activities, as detected by calcium imaging of WT mDA cultures 7 weeks after PFF treatment. Concentration of Mg^{2+} in the live imaging media was decreased stepwise to encourage spontaneous activities. KCl was added in the end to distinguish neurons by their response to this stimulus. Depending on the cell density of the imaged region, 400 – 800 cells with the most increase in Fluo-4 fluorescence intensity upon KCl exposure were analysed in each culture.

a) Sample traces of calcium imaging in PBS (left) and PFF (right) wells, which exhibited huge inconsistency between sister wells.

b) Spontaneous activities were observed in both neurons treated with PFFs (red) and PBS control (blue). The percentage of active cells showed an increasing trend as the concentration of Mg^{2+} decreased in the media, while there were no apparent trends in the magnitude of events and events per active cell. However, results were highly variable between differentiations and even between sister wells (indicated by the same shape of data points). n = 5 wells from 3 independent experiments. Bars indicate mean ± standard derivation.

5.2.5. PFFs did not induce significant changes in mitochondrial count, size or morphology in WT mDA neurons

As mitochondrial fragmentation occurs before mitochondrial dysfunction (Nakamura et al., 2011), I investigated whether PFF-induced pathology has an impact on the shape and size of mitochondria. I performed live imaging with TMRM, a fluorescent dye which accumulates in active mitochondria with intact membrane potentials. In both PFF-treated cultures and PBS control, TMRM was able to label mitochondria (Figure 5.7a), suggesting that mitochondrial membrane potential was intact in these cells. To image mitochondria for 3D reconstruction, I captured z-stack images of a neuronal cell body which did not overlap with other neurons. The cell bodies and a short portion of their neurites were then selected (yellow frames in Figure 5.7a) for thresholding into binary images. These binary images were analysed in 3D for their cell size, mitochondrial abundance, total and average mitochondrial volume

and surface, as well as mitochondrial shape (compactness and sphericity). At 7 weeks after PFF treatment in WT mDA culture plated at 80,000 cells/cm^2, I did not observe significant difference in any of these aspects after analysing 90 cells treated with PFF and 68 cells treated with PBS (Figure 5.7b, Student's t-test). This was further confirmed in WT mDA cultures plated at 25,000 cells/cm^2 9 weeks after PFF treatment, where I did not observe significant difference in any of aspects measured after analysing 29 cells treated with PFF and 25 cells treated with PBS (Figure 5.7c, Student's t-test). These results suggested the current amount of pS129-αSyn pathology did not have apparent effect on mitochondrial membrane potential and did not significantly affect mitochondrial count, size or morphology.

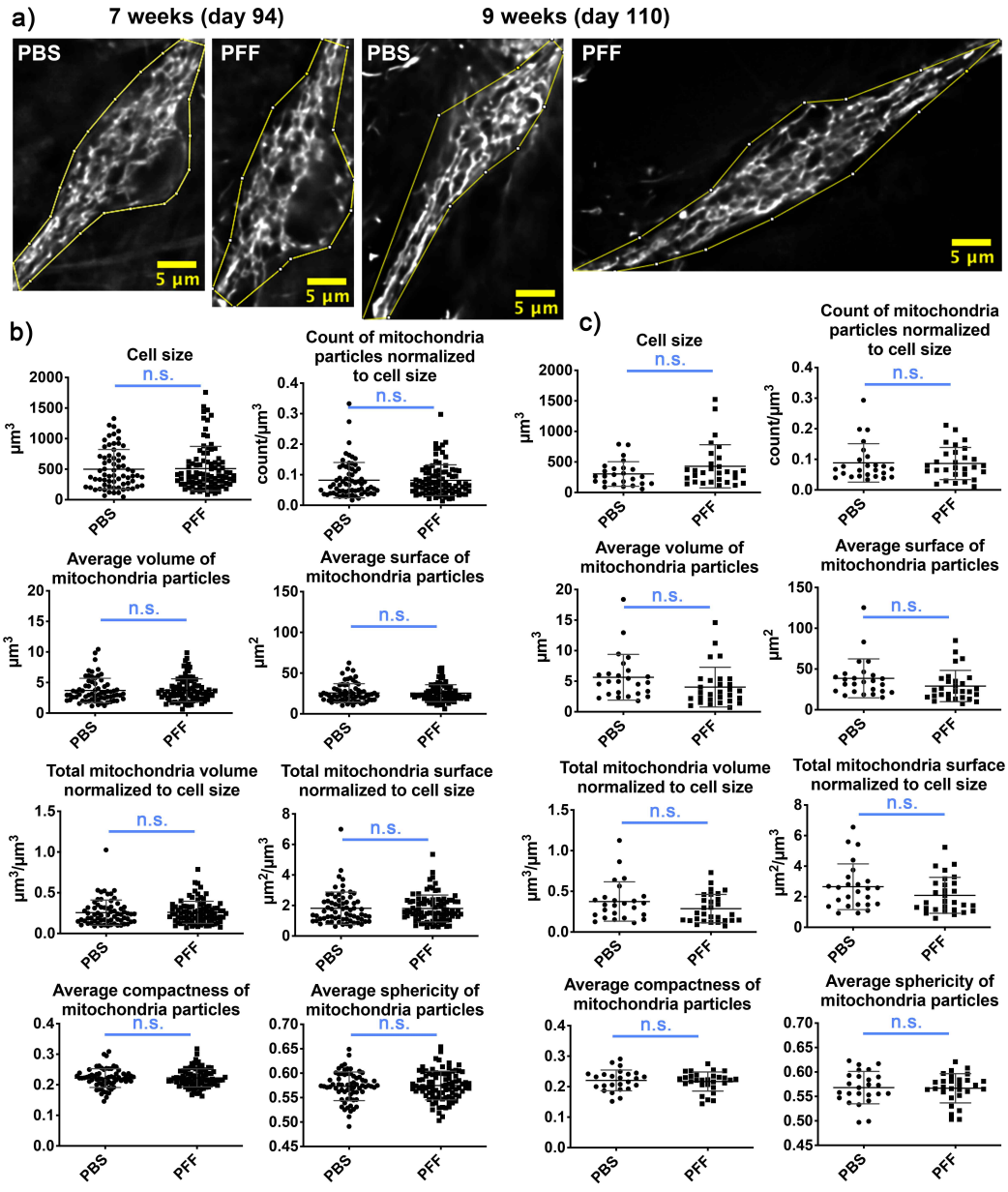

Figure 5.7 PFF treatment did not induced significant change in mitochondrial count, size or morphology in WT mDA cultures.

a) Sample images (z-slice 1/6) of mitochondria marked by TMRM, in 80,000 cells/cm^2 culture 7 weeks after PFF treatment and in 25,000 cells/cm^2 culture 9 weeks after PFF treatment, with their respective PBS control.

b) Quantification of mitochondria abundance, size and shape in 3D 7 weeks after PFF or PBS control treatment. n.s. not significant, Student's t-test. n = 90 and 68 cells for PFF-treated and PBS-treated wells respectively. Bars indicate mean ± standard derivation.

c) Quantification of mitochondria abundance, size and shape in 3D 9 weeks after PFF or PBS control treatment. n.s. not significant, Student's t-test. n = 29 and 25 cells for PFF-treated and PBS-treated wells respectively. Bars indicate mean ± standard derivation.

5.3. *SNCA*$^{-/-}$ neurons were resistant to synucleinopathy, while *SNCA*$^{+/-}$ neurons showed significantly reduced pathology

To investigate if α-Syn deletion reduces the neurons' susceptibility to synucleinopathy, I compared the level of pS129-αSyn pathology in *SNCA*$^{+/-}$, *SNCA*$^{-/-}$ and WT mDA neurons plated at 25,000 cells/cm^2, 5 weeks after PFF treatment. WT mDA neurons showed considerable pS129-αSyn structures due to PFF treatment (Figure 5.8a). *SNCA*$^{+/-}$ mDA neurons exhibited much less pS129-αSyn pathology, but small number of neurons showed punctate pS129-αSyn structures along axons (Figure 5.8a). *SNCA*$^{-/-}$ mDA neurons did not possess any pS129-αSyn structures along β-III tubulin-positive neurites or within β-III tubulin-positive neuronal cell bodies (Figure 5.8a). mDA neurons treated with PBS vehicle (Figure 5.8b) or α-Syn monomer (Figure 5.8c) as controls, did not form such pS129-αSyn structures in any of the mDA neuronal cultures.

Subsequently, I quantified the area of pS129-αSyn structures normalised to the area of β-III tubulin-positive neurons. In *SNCA*$^{+/-}$ and WT mDA neurons, PFF treatment induced significantly higher amount of pS129-αSyn staining compared to α-Syn monomer and PBS vehicle control treatment (Figure 5.8d, Brown-Forsythe and Welch ANOVA, post hoc comparisons with Dunnett's T3 correction). In contrast, area of pS129-αSyn staining was similar among PFF, monomer and PBS groups of *SNCA*$^{-/-}$ mDA neurons (Figure 5.8d). *SNCA*$^{+/-}$ and *SNCA*$^{-/-}$ mDA neurons developed significantly less pS129-αSyn pathology than WT neurons following α-Syn PFF treatment (Figure 5.8d).

To scrutinize the prevalence, size and shape of pS129-αSyn structures in WT and *SNCA*$^{+/-}$ mDA neurons, I performed particle analysis. The number of pS129-αSyn

structures did not significantly differ between WT and *SNCA*$^{+/-}$ mDA neurons, however, the structures in WT neurons were significantly larger in size, more elongated and thicker (Figure 5.8e, Student's t-test).

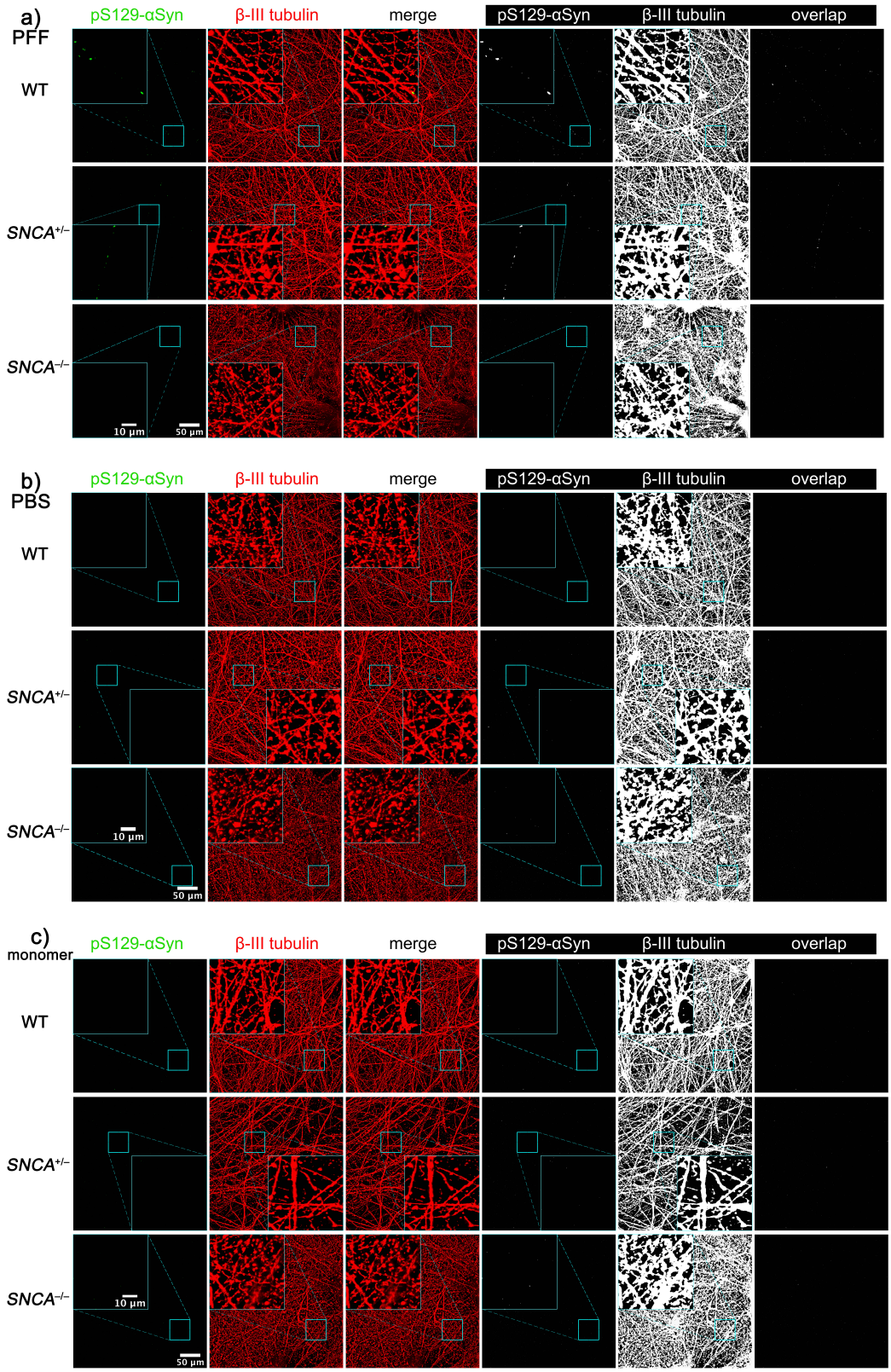

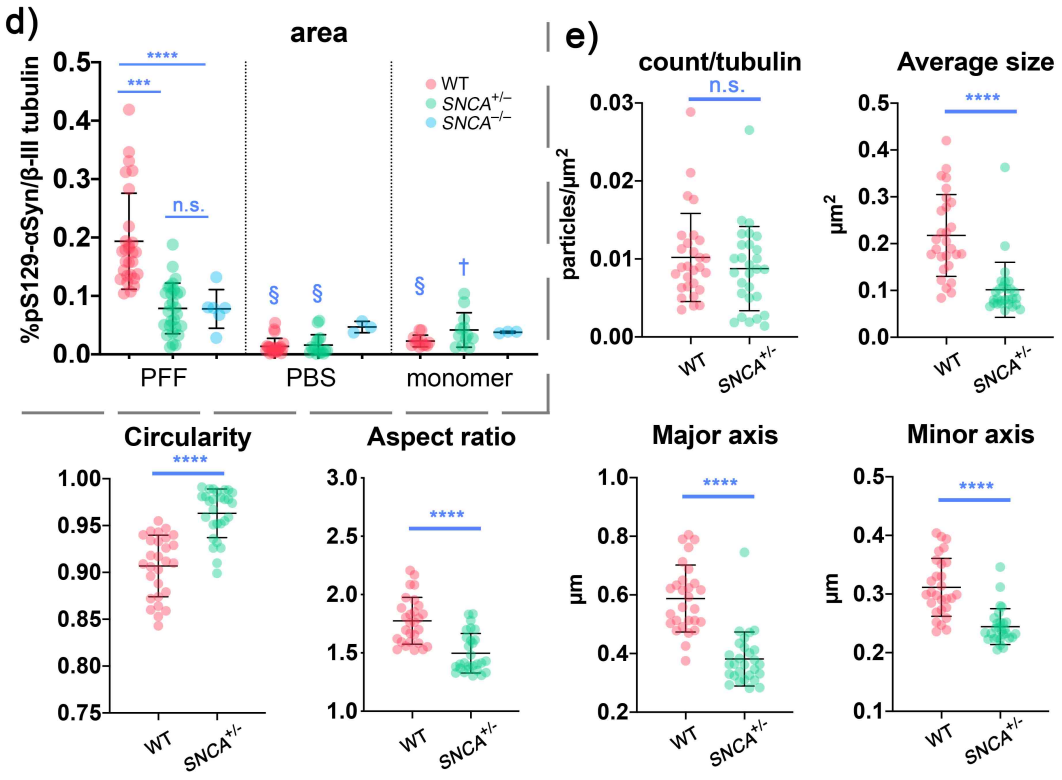

Figure 5.8 *SNCA*$^{-/-}$ and *SNCA*$^{+/-}$ mDA cultures displayed significantly less pS129-αSyn pathology than WT mDA cultures 5 weeks after PFF treatment.

a-c) Sample fields of *SNCA*$^{-/-}$, *SNCA*$^{+/-}$ and WT mDA cultures plated at 25,000 cells/cm^2, 5 weeks after treatment with a) α-Syn PFFs, b) PBS vehicle or c) α-Syn monomers. Imaged at 40x.

d) Quantification of total area of pS129-αSyn pathology overlapping with β-III tubulin area. Bars indicate mean ± standard derivation. **** $p < 0.0001$, *** $p < 0.001$, n.s. not significant, § $p < 0.0001$ compared to PFF counterpart, † $p < 0.05$ compared to PFF counterpart, Brown-Forsythe and Welch ANOVA, post hoc comparisons with Dunnett's T3 correction.

e) Quantification of count, average size and shape of β-III tubulin-overlapping pS129-αSyn structures in *SNCA*$^{+/-}$ and WT mDA cultures treated with PFFs. Bars indicate mean ± standard derivation. **** $p < 0.0001$, n.s. not significant, Student's t-test.

Genotype	Clone	Number of differentiations	Number of wells	Number of fields
SNCA$^{+/+}$	WT	3	8 for PFF, 6 for PBS, 4 for monomer	28 for PFF, 22 for PBS, 12 for monomer
SNCA$^{+/-}$	L5-4, 4-4	4	8 for PFF, 4 for PBS, 4 for monomer	28 for PFF, 16 for PBS, 12 for monomer
SNCA$^{-/-}$	M1-4	1	2 for PFF, 1 for PBS, 1 for monomer	6 for PFF, 3 for PBS, 3 for monomer

Table 5.1 N number summary for quantification of pS129-αSyn structures formed by *SNCA*$^{+/-}$, *SNCA*$^{-/-}$ and WT mDA neurons 5 weeks after PFF treatment. This includes data

points re-analysed from (Chen et al., 2019) by picking 13 out of 25 slices imaged at a step of 0.32 µm for z-stack (while the original analysis was 6 out of 25 slices). Hence, the z-projection covered a range of 4.2 µm and was comparable to later data, which was z-projection of all 15 slices imaged at a step of 0.3 µm for z-stack. Some of the *SNCA*$^{-/-}$ data points originally in the paper were excluded as they were later found to be from a PFF batch which was not able to induce pS129-αSyn structures in WT mDA neurons.

As shown previously, longer incubation periods and higher neurons density increased the amount of pS129-αSyn pathology (Figure 5.2). Therefore, I plated the neurons at 80,000 cells/cm^2 and quantified the level of pS129-αSyn pathology developed 9 weeks after PFF treatment in *SNCA*$^{+/-}$, *SNCA*$^{-/-}$ and WT mDA neurons. At this stage, WT mDA neurons exhibited extensive pS129-αSyn structures, while *SNCA*$^{+/-}$ mDA neurons only showed a few punctate pS129-αSyn structures along axons (Figure 5.9a). *SNCA*$^{-/-}$ mDA neurons treated with PFFs (Figure 5.9a) and all mDA neurons treated with PBS vehicle control (Figure 5.9b) did not possess any pS129-αSyn structures along β-III tubulin-positive neurites or within β-III tubulin-positive neuronal cell bodies.

Subsequently, I quantified the area of pS129-αSyn structures developed 9 weeks after PFF treatment, normalised to the area of β-III tubulin-positive neurons. PFF-treated WT and *SNCA*$^{+/-}$ mDA neurons had significantly more pS129-αSyn staining compared to their respective PBS controls (Figure 5.9c, Brown-Forsythe and Welch ANOVA, post hoc comparisons with Dunnett's T3 correction). In contrast, area of pS129-αSyn staining was not significantly different between PFF and PBS groups of *SNCA*$^{-/-}$ mDA neurons (Figure 5.9c). Both *SNCA*$^{+/-}$ and *SNCA*$^{-/-}$ mDA neurons developed significantly less pS129-αSyn pathology than WT neurons 9 weeks after PFF treatment (Figure 5.9c). It is worth noting that at this stage *SNCA*$^{+/-}$ mDA neurons exhibited significantly more pS129-αSyn pathology than *SNCA*$^{-/-}$ mDA neurons (Figure 5.9c).

To scrutinize the prevalence, size and shape of pS129-αSyn structures developed 9 weeks after PFF treatment in *SNCA*$^{+/-}$ and WT mDA neurons, I performed particle analysis. At this stage, the number of pS129-αSyn structures in *SNCA*$^{+/-}$ mDA neurons was significantly lower than in WT. They were also significantly smaller in size and less elongated, however, not significantly thinner compared to the pS129-αSyn structures in WT mDA neurons (Figure 5.9d, Student's t-test).

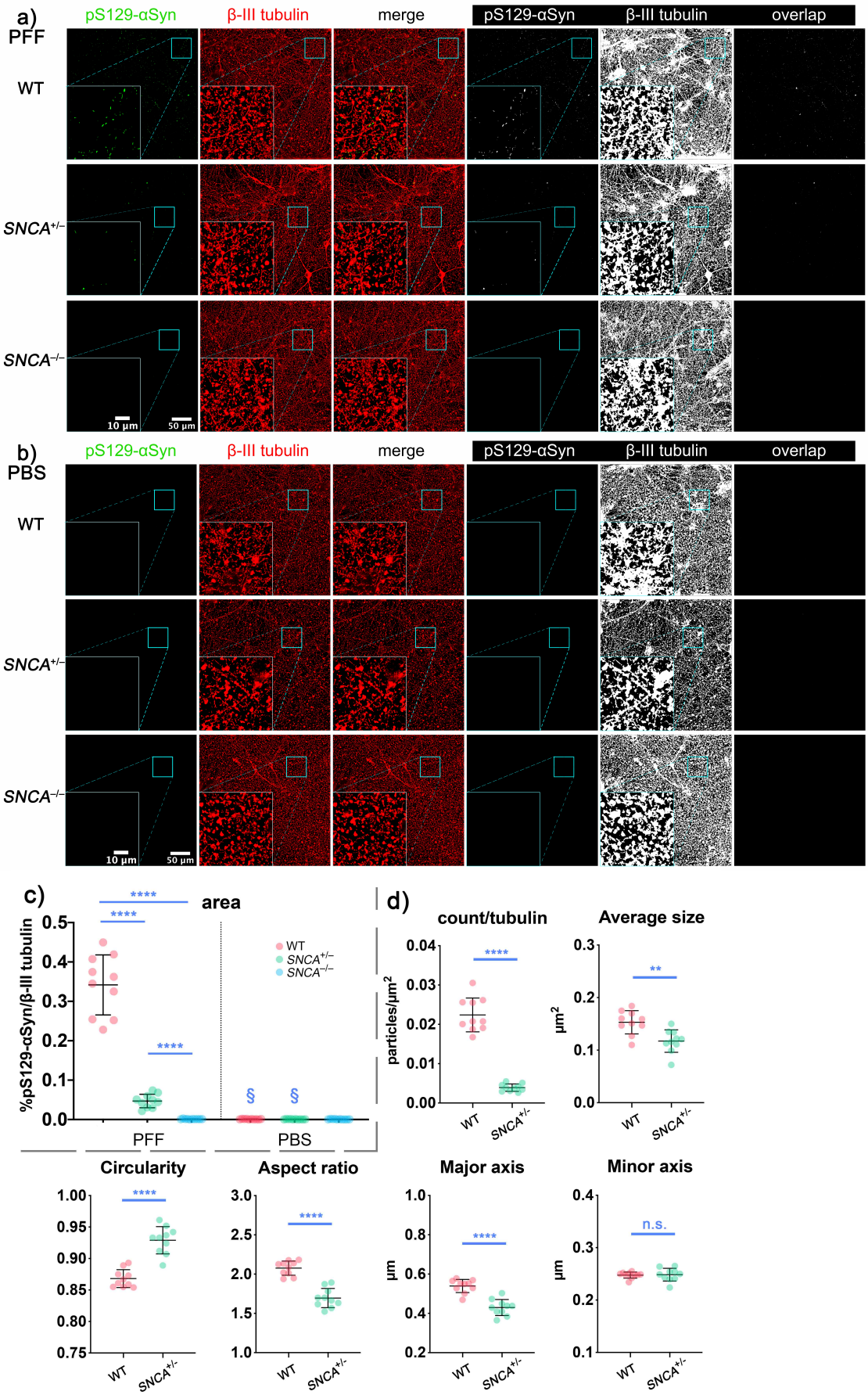
a)
PFF
pS129-αSyn
β-III tubulin
merge
pS129-αSyn
β-III tubulin
overlap
WT
SNCA+/–
SNCA–/–
10 µm
50 µm
b)
PBS
pS129-αSyn
β-III tubulin
merge
pS129-αSyn
β-III tubulin
overlap
WT
SNCA+/–
SNCA–/–
10 µm
50 µm
c)
area
%pS129-αSyn/β-III tubulin
WT
SNCA+/–
SNCA–/–
PFF
PBS
d)
count/tubulin
particles/µm2
Average size
µm2
Circularity
Aspect ratio
Major axis
Minor axis
µm
n.s.
WT
SNCA+/-

Figure 5.9 The level of pS129-αSyn pathology in *SNCA*$^{+/-}$ mDA cultures was significantly higher than that in *SNCA*$^{-/-}$ mDA cultures when neurons were plated at higher density and cultured for a longer period after PFF treatment, but was still significantly lower than the level in WT mDA cultures.

a-b) Sample fields of *SNCA*$^{-/-}$ (clone L5-3), *SNCA*$^{+/-}$ (clone L5-4) and WT mDA cultures plated at 80,000 cells/cm^2, 9 weeks after treatment with a) PFFs or b) PBS vehicle. Imaged at 40x.

c) Quantification of total area of pS129-αSyn pathology overlapping with β-III tubulin area. n = 10 fields from 2 wells of each genotype per condition. Bars indicate mean ± standard derivation. **** $p < 0.0001$, § $p < 0.0001$ compared to PFF counterpart, Brown-Forsythe and Welch ANOVA, post hoc comparisons with Dunnett's T3 correction.

d) Quantification of count, average size and shape of β-III tubulin-overlapping pS129-αSyn structures in *SNCA*$^{+/-}$ and WT mDA cultures treated with PFFs. Bars indicate mean ± standard derivation. **** $p < 0.0001$, ** $p < 0.01$, n.s. not significant, Student's t-test.

As p62 co-staining has been observed in pS129-αSyn structures developed 9 weeks after PFF treatment in WT mDA neurons plated at 80,000 cells/cm^2, I looked for p62 co-staining in their *SNCA*$^{+/-}$ equivalent. Although less prevalent than in WT mDA neurons, p62 co-staining could be found within some of the large pS129-αSyn structures in *SNCA*$^{+/-}$ mDA neurons (indicated by white arrows in Figure 5.10).

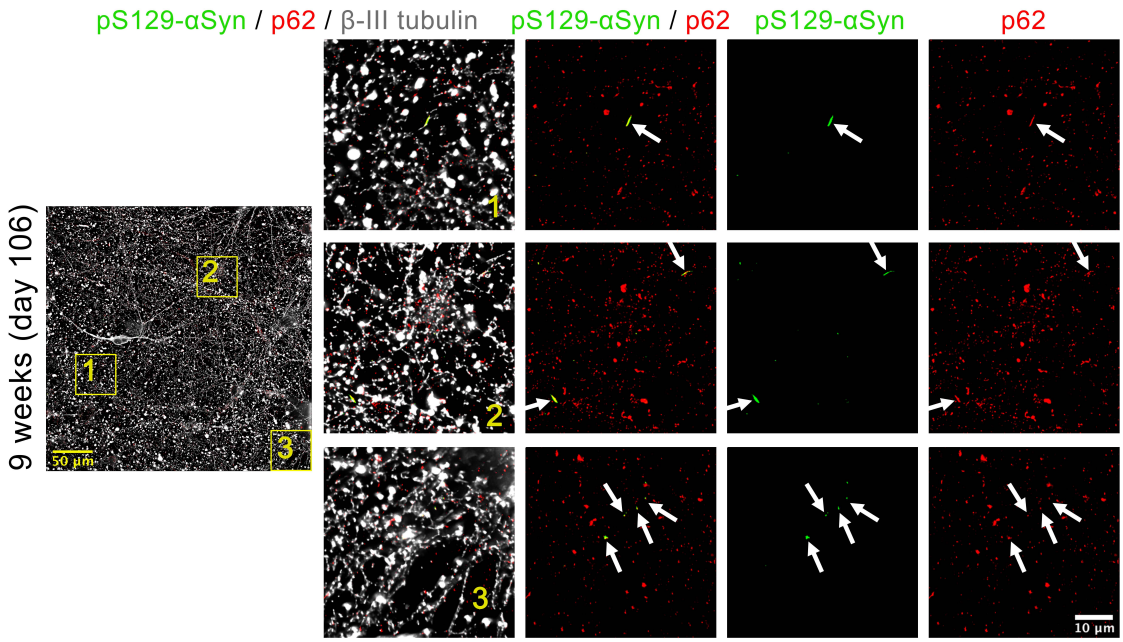

Figure 5.10 p62 (red) co-staining (indicated with white arrows) with pS129-αSyn (green) can be observed 9 weeks after PFF treatment in *SNCA*$^{+/-}$ (clone L5-4) mDA cultures plated at 80,000 cells/cm^2. Neurons were marked by β-III tubulin (grey).

5.4. *SNCA*$^{S87E/S87E}$ neurons displayed reduced susceptibility to synucleinopathy in comparison to WT neurons

To study whether *SNCA*$^{S87E/S87E}$ mutation reduces the neurons' susceptibility to synucleinopathy, I first compared the level of pS129-αSyn pathology formed 5 weeks after PFF treatment in WT and *SNCA*$^{S87E/S87E}$ (clones 21fB) mDA neurons plated at 25,000 cells/cm^2. Both WT and *SNCA*$^{S87E/S87E}$ mDA neurons developed considerable pS129-αSyn structures due to PFF treatment (Figure 5.11a). WT and *SNCA*$^{S87E/S87E}$ mDA neurons treated with PBS vehicle control did not form any pS129-αSyn structures along within β-III tubulin-positive neurites or within β-III tubulin-positive neuronal cell bodies (Figure 5.11b).

Subsequently, I quantified the area of pS129-αSyn structures, normalised to the area of β-III tubulin-positive neurons. PFF-treated mDA neurons, both WT and *SNCA*$^{S87E/S87E}$ (clone 21fB), exhibited significantly more pS129-αSyn staining compared to their respective PBS controls (Figure 5.11c, Brown-Forsythe and Welch ANOVA, post hoc comparisons with Dunnett's T3 correction). However, the area of pS129-αSyn staining in PFF-treated neurons was not significantly different between WT and *SNCA*$^{S87E/S87E}$ mDA neurons derived from clone 21fB (Figure 5.11c). To scrutinize if there is any difference in the prevalence, size and shape of pS129-αSyn structures in WT and *SNCA*$^{S87E/S87E}$ mDA neurons, I performed particle analysis. However, the pS129-αSyn structures in *SNCA*$^{S87E/S87E}$ mDA neurons (clone 21fB) were not significantly different from the ones in WT neurons in any measured aspects (Figure 5.11d, Student's t-test).

To further validate these findings, I imaged the above differentiation (Figure 5.11 a-d) at lower magnification, 20x. The amount of pS129-αSyn staining normalised to β-III tubulin area captured by 20x objective without z-stack was less than that captured with 40x with z-stack. Consistent with the 40x results, the area of pS129-αSyn staining in PFF-treated mDA neurons was not significantly different between WT and *SNCA*$^{S87E/S87E}$ (clone 21fB), and they both exhibited significantly higher amount of pS129-αSyn staining compared to their PBS control counterparts (Figure 5.11e). Therefore, I further validated these findings in mDA neurons differentiated from two other *SNCA*$^{S87E/S87E}$ hESC clones, B6L and 6hI. Consistent with results of clone 21fB, the area of pS129-αSyn staining in PFF-treated mDA neurons was not significantly different between WT and B6L, or between WT and

6hI, and they all exhibited significantly higher amount of pS129-αSyn staining compared to their PBS control counterparts (Figure 5.11f).

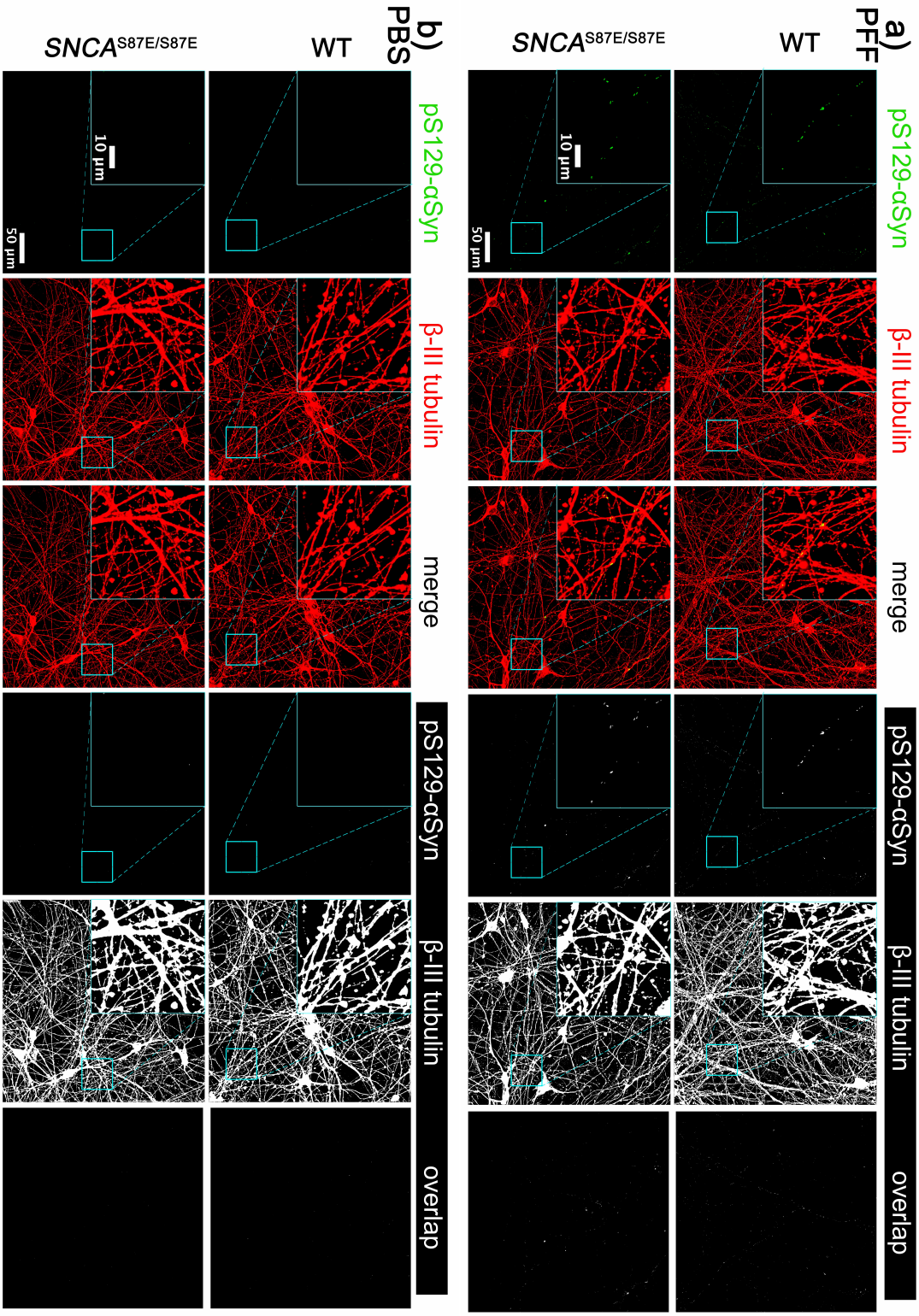

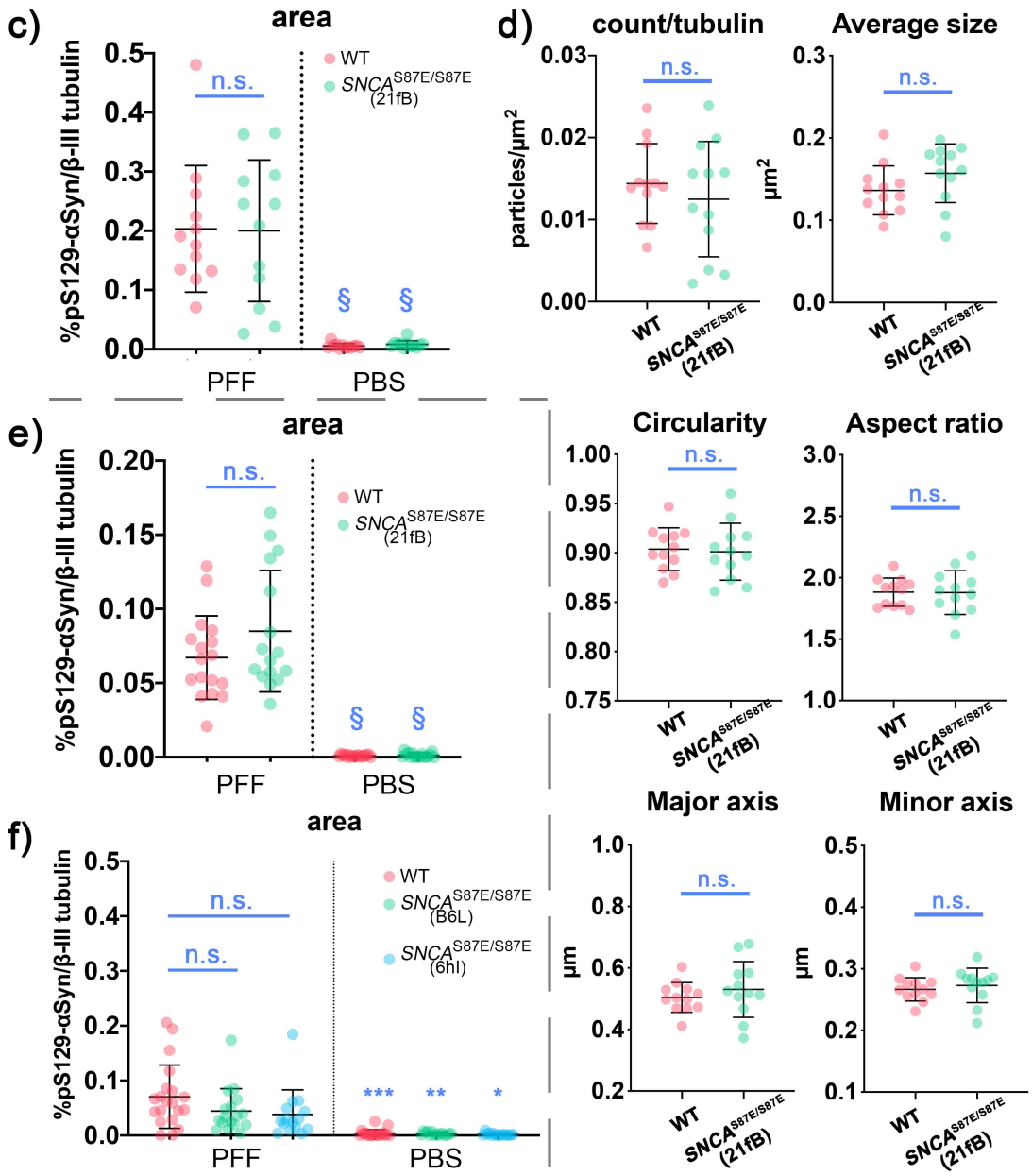

Figure 5.11 *SNCA*$^{S87E/S87E}$ mDA cultures displayed similar amount of PFF-induced pS129-αSyn pathology compared to WT mDA cultures 5 weeks after PFF treatment.

a-b) Sample fields of *SNCA*$^{S87E/S87E}$ (clone 21fB) and WT mDA cultures plated at 25,000 cells/cm^2, 5 weeks after treatment with a) PFFs or b) PBS vehicle. Imaged at 40x.

c) Quantification of total area of pS129-αSyn pathology overlapping with β-III tubulin area of *SNCA*$^{S87E/S87E}$ (clone 21fB) and WT mDA cultures, imaged at 40x. n = 12 fields from 2 wells per condition. Bars indicate mean ± standard derivation. n.s. not significant, § $p < 0.001$ compared to PFF counterpart, Brown-Forsythe and Welch ANOVA, post hoc comparisons with Dunnett's T3 correction.

d) Quantification of count, average size and shape of β-III tubulin-overlapping pS129-αSyn structures of *SNCA*$^{S87E/S87E}$ (clone 21fB) and WT mDA cultures. Bars indicate mean ± standard derivation. n.s. not significant, Student's t-test.

e) Quantification of total area of pS129-αSyn pathology overlapping with β-III tubulin area of the same differentiations in b) imaged at 20x. n = 17 fields from 2 wells per condition. Bars indicate mean ± standard derivation. n.s. not significant, § $p < 0.0001$ compared to PFF counterpart, Brown-Forsythe and Welch ANOVA, post hoc comparisons with Dunnett's T3 correction.

f) Quantification of total area of pS129-αSyn pathology overlapping with β-III tubulin area in *SNCA*$^{S87E/S87E}$ (clones 6hI and B6L) and WT mDA cultures plated at 25,000 cells/cm^2 5 weeks after PFF treatment, imaged at 20x. n = 15-20 fields from 3-4 wells per condition. Bars indicate mean ± standard derivation. n.s. not significant, *** $p < 0.001$, ** $p < 0.01$, * $p < 0.05$ compared to PFF counterpart, Brown-Forsythe and Welch ANOVA, post hoc comparisons with Dunnett's T3 correction.

Next, I investigated whether *SNCA*$^{S87E/S87E}$ and WT mDA neurons developed different levels of pS129-αSyn pathology when plated at higher density and cultured for longer after PFF treatment. The same differentiations in Figure 5.11 a-d were plated at 80,000 cells/cm^2 and cultured for 7 weeks after PFF treatment. Both WT and *SNCA*$^{S87E/S87E}$ (clone 21fB) mDA neurons developed extensive pS129-αSyn structures (Figure 5.12a). WT and *SNCA*$^{S87E/S87E}$ mDA neurons treated with PBS vehicle control (Figure 5.12b) did not show any pS129-αSyn structures along β-III tubulin-positive neurites or within β-III tubulin-positive neuronal cell bodies.

Subsequently, I quantified the area of pS129-αSyn structures developed 7 weeks after PFF treatment, normalised to the area of β-III tubulin-positive neurons. Both WT and *SNCA*$^{S87E/S87E}$ (clone 21fB) PFF-treated mDA neurons exhibited significantly higher level of pS129-αSyn pathology compared to their respective PBS controls (Figure 5.12c, Brown-Forsythe and Welch ANOVA, post hoc comparisons with Dunnett's T3 correction). It is worth noting that at 7 weeks after PFF treatment, *SNCA*$^{S87E/S87E}$ mDA neurons developed significantly less pS129-αSyn pathology than WT neurons (Figure 5.12c).

To scrutinize the prevalence, size and shape of pS129-αSyn structures developed 7 weeks after PFF treatment in *SNCA*$^{S87E/S87E}$ and WT mDA neurons, I performed particle analysis. At this stage, the number of pS129-αSyn structures in *SNCA*$^{S87E/S87E}$ mDA neurons was significantly lower than that in WT. They were also significantly smaller in size and thinner in shape, but not significantly shorter compared to the pS129-αSyn structures in WT mDA neurons (Figure 5.12d, Student's t-test).

a)
PFF
WT
SNCA S87E/S87E
pS129-αSyn
β-III tubulin
merge
pS129-αSyn
β-III tubulin
overlap
10 µm
50 µm
b)
PBS
WT
SNCA S87E/S87E
pS129-αSyn
β-III tubulin
merge
pS129-αSyn
β-III tubulin
overlap
10 µm
50 µm

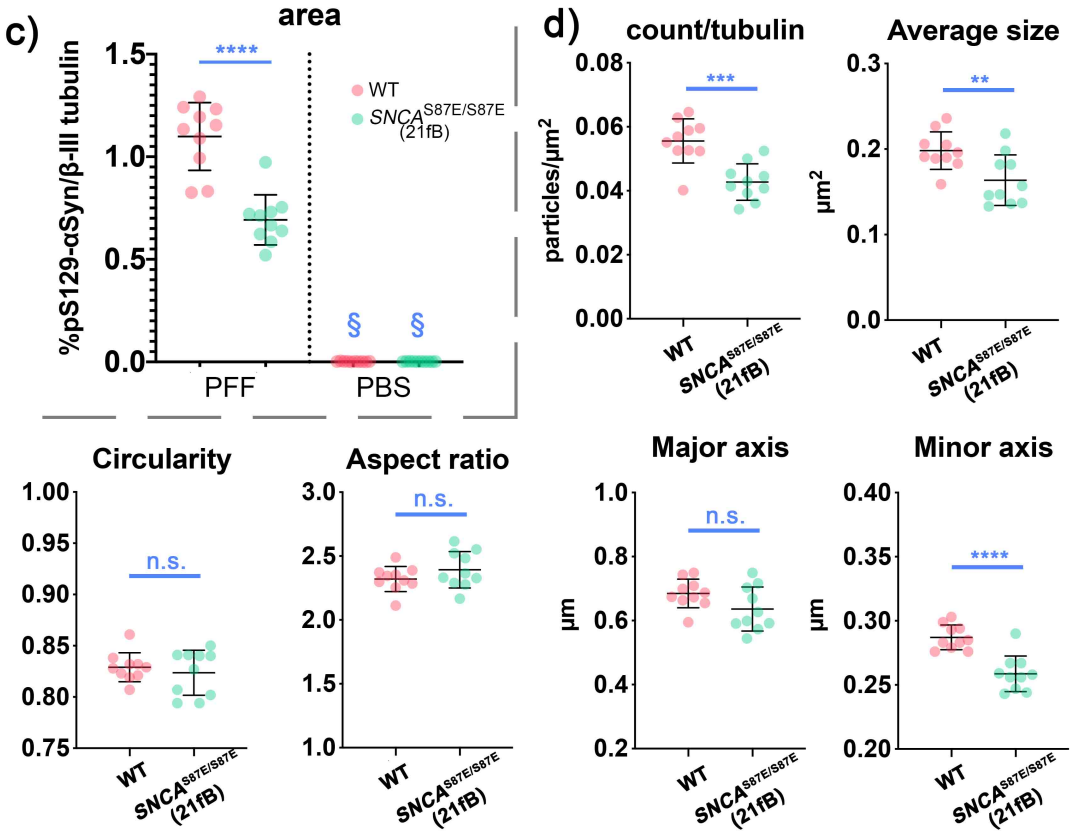

Figure 5.12 The level of pS129-αSyn pathology in *SNCA*$^{S87E/S87E}$ mDA cultures was significantly less than that in WT mDA cultures, when the same differentiations in Figure 5.11 a-d were plated at higher density and cultured for a longer period after PFF treatment.

a-b) Sample fields of *SNCA*$^{S87E/S87E}$ (clone 21fB) and WT mDA cultures plated at 80,000 cells/cm^2, 7 weeks after treatment with a) PFFs or b) PBS vehicle. Imaged at 40x.

c) Quantification of total area of pS129-αSyn pathology overlapping with β-III tubulin area imaged at 40x. n = 10 fields from 2 wells per condition. Bars indicate mean ± standard derivation. **** $p < 0.0001$, § $p < 0.0001$ compared to PFF counterpart, Brown-Forsythe and Welch ANOVA, post hoc comparisons with Dunnett's T3 correction.

d) Quantification of count, average size and shape of β-III tubulin-overlapping pS129-αSyn structures of *SNCA*$^{S87E/S87E}$ and WT mDA cultures treated with PFFs. Bars indicate mean ± standard derivation. **** $p < 0.0001$, *** $p < 0.001$, ** $p < 0.01$, n.s. not significant, Student's t-test.

5.5. Discussion

In this chapter, I demonstrated that mDA neurons derived from *SNCA*$^{-/-}$ hESCs were resistant to PFF-induced α-Syn pathology, while those derived from *SNCA*$^{+/-}$ hESC exhibited significantly reduced pathology compared to WT. mDA neurons derived from *SNCA*$^{S87E/S87E}$ hESCs displayed a significantly reduced level of pS129-αSyn pathology only at later endpoints. In addition, I explored a range of published PFF-induced

pathologies, but did not observe any significant alterations in synaptic staining, spontaneous activities and mitochonodrial structures in the current mDA neuron model. This could be due to the pS129-αSyn aggregates in PFF-treated cultures were in the transition from fibrillar form to Lewy body-like inclusions, a stage when most of the structural defects and functional impairments occur (Mahul-Mellier et al., 2019). Identification of Lewy body-inclusion requires detection of other proteins, lipids and membranous organelles such as mitochondria, autophagosomes, endosome and lysosome, in addition to the pS129-αSyn, Hsp70, ubiquitin and p62 that are readily detected in fibrillar aggregates (Gribaudo et al., 2019; Mahul-Mellier et al., 2019; Wakabayashi et al., 2013).

Given the fact that neurons plated at higher density were exposed to fewer PFFs per neuron, my observation of more pS129-αSyn pathology in denser neurons is likely due to the higher maturity these denser cultures achieved (Wagenaar et al., 2006). As revealed in a prior study, more pS129-αSyn structures would develop, if neurons were more mature at the time of PFF treatment (Volpicelli-Daley et al., 2011). This is most probably due to the increase in α-Syn expression as neurons mature (Clough et al., 2011; Taguchi et al., 2014; Volpicelli-Daley et al., 2011). The higher prevalence of pS129-αSyn aggregates in aged neurons might explain why the co-localisation of p62 with pS129-αSyn staining was found in 9-week cultures, but not in 5-week cultures. As the pS129-αSyn^{+}p62^{-} structures were recognised by the pS129-αSyn antibody, we can exclude the possibility that they were truncated degradation products which do not stain for ubiquitin or p62 (Grassi et al., 2018). It is likely that these structures await further maturation to be positive for p62, as the co-localisation p62 and ubiquitin with pS129-αSyn only appears after extended culture of the pS129-αSyn^{+} neurons (Mahul-Mellier et al., 2019).

Particle analysis of pS129-αSyn structures suggests that *SNCA*$^{S87E/S87E}$ appeared to add on to the α-Syn aggregates mainly along the major axis, making the structures similar in length as WT neurons but thinner in width. This parallels with prior observation in cells overexpressing A53T or E46K α-Syn monomers and treated with WT α-Syn PFFs, where the morphology of pS129-αSyn aggregates was dependent on the type of α-Syn monomers (Sacino et al., 2013b). Taking into account the prediction that S87E mutation repels E83 in the structure of α-Syn fibril (Figure 1.9) (Tuttle et al., 2016), this suggests that S87E mutation might change the orientation of α-Syn aggregation. Surprisingly, the

level of pS129-αSyn pathology in *SNCA*$^{S87E/S87E}$ mDA neurons was close to that in WT in this thesis. The discrepancy between my observation and what would be expected based on prior studies, might be resulted from the species of α-Syn used for assembling PFFs. While I used PFFs assembled from WT α-Syn, the S87E α-Syn was allowed to self-aggregate in prior studies (Lázaro et al., 2014; Oueslati et al., 2012; Paleologou et al., 2010). In fact, the aggregation-prone characteristic of the PFF template, rather than that of the α-Syn monomers, was shown to be the determinant factor for the level of PFF-induced pathology (Luk et al., 2016).

In the current model, cell death (as indicated by LDH level in conditioned media) was not observed in neurons plated at 25,000 cells/cm^2 or 80,000 cells/cm^2 at 3, 4 or 6 weeks after PFF treatment at 5 µg/ml. This is consistent with (Abounit et al., 2016; Gribaudo et al., 2019; Loria et al., 2017; Peelaerts et al., 2015), where no significant cell death was observed in PFF-treated neurons albeit the presence of multiple pathological phenotypes. Positive results were reported in relation with the use of high concentrations of PFF, relatively mature neurons and long culture period after PFF treatment (Mahul-Mellier et al., 2019, 2015; Volpicelli-Daley et al., 2011; Wu et al., 2019), all of which would give rise to more α-Syn pathology. Since mitochondrial morphology and neuronal activities were not significantly disrupted in the current model, it is highly likely that neurons were still in the development of dysfunction before cell death. As neuron death caused by PFFs or neuron-derived extracellular α-Syn is most likely to be an apoptosis process rather than necrosis (Desplats et al., 2009; Mahul-Mellier et al., 2019, 2015), caspase activity could be assayed in a time course manner to monitor changes in apoptosis activity.

Contrary to prior studies using primary hippocampal neurons (Mahul-Mellier et al., 2019; Tran et al., 2014; Volpicelli-Daley et al., 2011; Wu et al., 2019), I did not observe significant defects in the number of synaptic particles or in synapse formation in 25,000 cells/cm^2 mDA neurons 5 weeks after PFF treatment. This discrepancy could be due to cell types, but more likely due to a lower level of synucleinopathy developed by less mature neurons in the current model, which could result from the use of hESC-derived neurons rather than primary neurons and/or from a lower plating density (Volpicelli-Daley et al., 2011). As shown in section 5.2.1, neurons developed more pS129-αSyn pathology when plated at a higher density or cultured for longer after PFF treatment. Therefore, it would be interesting to investigate whether more pS129-αSyn pathology in denser

neurons would result in significant difference in synapse formation and maturity between PFF and vehicle-treated neurons. However, plating at higher density might increase the number of synapses per plating area but not necessarily the number normalised to neuronal area (Cullen et al., 2010). In addition, it would be challenging to accurately localise synaptic staining in a dense culture.

In fact, the depletion of functionable soluble α-Syn monomers upon PFF-induced aggregation (Kim et al., 2019; Mahul-Mellier et al., 2019; Osterberg et al., 2015; Volpicelli-Daley et al., 2011) might not have a significant impact on their numbers and maturity during the emergence and development of synapses (day 45 – 80 of current protocol). The absence of α-Syn did not have major impact on synapse development in *Snca*$^{-/-}$ mice (Abeliovich et al., 2000; Anwar et al., 2011; Cabin et al., 2002) and transgenic α-Syn overexpressing mice only developed a reduction in dendritic spine density when they aged (Blumenstock et al., 2017). Therefore, PFF-induced disruptions in synaptic structures and functions are more likely to be observed in aged neurons (Mahul-Mellier et al., 2019), or in mature neurons with synapses well-developed before PFF treatment (Mahul-Mellier et al., 2019; Tran et al., 2014; Volpicelli-Daley et al., 2011).

In the current model, the percentage of active cells, frequency and amplitude of spontaneous events showed considerable variation. This was most likely due to well-to-well variation during a lengthy differentiation protocol, as electrophysiology patterns of neuron cultures are notoriously variable between batches and even between sister wells (Wagenaar et al., 2006). Another factor which might contribute to the variation is that, at 7 weeks after PFF treatment (day 94 – 96), these mDA neurons were not mature enough to develop spontaneous activities with a regular firing pattern as observed in prior studies (Gribaudo et al., 2019; Peelaerts et al., 2015; Volpicelli-Daley et al., 2011). This is likely the case as the percentage of active cells at baseline is relatively low compared to day 141 cultures (Figure 4.11). The irregularity of spontaneous events could result in large variation during a short recording of 2 minutes.

Despite the absence of obvious differences in bulk events between PFF- and PBS vehicle-treated cultures, it is possible for PFF treatment to impair synchronicity of events and functional connectivity of neuronal network, which can be measured by synchronization cluster analysis and interactions between all pairs of neuron, respectively (Volpicelli-Daley et al., 2011). In addition, miniature changes in synaptic activities and

action potentials firing can be recorded by calcium imaging with high temporal resolution (> 20 Hz, currently at 2 Hz)., or by current-clamp recording at single cell level (Peelaerts et al., 2015; Scott et al., 2010; Wu et al., 2019).

At 7 to 9 weeks after PFF treatment, I did not observe significant changes in the size or morphology of mitochondria. Again, this could be due to the lack of overwhelming synucleinopathy. In addition, the current resolution (60x oil on a widefield microscope) is not sufficient for reconstructing an accurate 3D structure of mitochondria and therefore, was not able to capture smaller differences visible on a confocal microscope. An alternative method to assess mitochondrial health would be to measure the change in mitochondrial membrane potential, as indicated by the intensity of TMRM or MitoTracker dye (Grassi et al., 2018; Mahul-Mellier et al., 2019). The mitochondrial membrane potential could be measured at baseline as well as in response to oxidative stress, such as upon exposure to the phosphorylation uncoupler carbonyl cyanide 4-(trifluoromethoxy) phenylhydrazone (FCCP) (Ludtmann et al., 2018; Maio et al., 2016). Furthermore, due to high density of the current culture, the mitochondria analysed in each cell were limited to the ones in cell body and a short length of neurites close to cell body, to avoid overlap with the cell body or neurites of other neurons. As PFF-induced oxidative stress in mDA neurites increases with the distance from the soma (Dryanovski et al., 2013), it would be interesting to investigate the health of mitochondria in neurites distal to the cell body. This could be challenging as it would require neurons to be plated sparsely, which could have an undesirale adverse impact on neuron maturity and the subsequent development of synucleinopathy.

In conclusion, the current PFF model demonstrated that *SNCA*$^{-/-}$ mDA neurons harboured resistance to synucleinopathy, while *SNCA*$^{+/-}$ and *SNCA*$^{S87E/S87E}$ mDA neurons exhibited reduced synucleinopathy. Nonetheless, scrutinisation of functional impairments in PFF-treated mDA neurons *in vitro* could be addressed with finer methods and at later time points, which would reveal whether mDA neurons with α-Syn mutants retain normal functionalities. These α-Syn mutants can provide invaluable cell models for the investigation of pathological mechanism of PD. Provided satisfactory performance in animal models *in vivo*, they would be promising cell sources for cell replacement therapy for PD.

Chapter 6: Discussion

6.1. *SNCA*$^{-/-}$ and *SNCA*$^{+/-}$ hESC-derived mDA progenitors as novel cell products for PD cell replacement therapy

In this thesis, I demonstrated that *SNCA*$^{+/-}$ and *SNCA*$^{-/-}$ hESCs could be generated by CRISPR/Cas9n targeting and could be subsequently differentiated into mDA neurons highly resembling those differentiated from their WT parental line, RC17. This suggested that neither *SNCA* knockout nor the clonal derivation process had a substantial effect on mDA differentiation. In α-Syn PFF model, *SNCA*$^{+/-}$ and *SNCA*$^{-/-}$ hESC-derived mDA neurons exhibited a significantly lower level of pS129-αSyn pathology compared to WT neurons.

In rodent and non-human primate PD models, the performance of hESC/hiPSC-derived mDA progenitors was comparable to fetal tissue, which is the 'gold standard' of cell replacement therapy for PD. Hence, hESC/hiPSC-derived mDA progenitors have a vast potential in PD cell replacement therapy in the near future. In fact, the first patient of cell replacement therapy with iPSC-derived mDA progenitors was transplanted in 2018 (Cyranoski, 2018) and a few other groups are also in close preparation (Kirkeby et al., 2017b; Studer, 2017). However, as these mDA progenitors are derived from hESCs/hiPSCs with WT α-Syn, the resulting mDA neurons would be susceptible to the host-to-graft spread of Lewy body pathology, which was observed in clinical trials using fetal grafts (Kordower et al., 2017, 2008; Kurowska et al., 2011; Li et al., 2008, 2016). Therefore, *SNCA*$^{+/-}$ and *SNCA*$^{-/-}$ hESC-derived mDA neurons, which exhibited a significantly lower level of pS129-αSyn pathology in the PFF-treated mDA neuron model, could potentially extend the time before the grafts develop Lewy body pathology. This would give rise to longer-lasting grafts and benefit PD patients, especially those with an early onset form of the condition. In addition, patients with a heavy α-Syn burden due to genetic mutations, such as *SNCA* multiplication (Farrer et al., 2004; Miller et al., 2004; Olgiati et al., 2015; Sekine et al., 2010; Singleton, 2003) or glucocerebrosidase (gene *GBA)* mutation (Neumann et al., 2009) might also benefit from such grafts. In these patients, the high level of endogenous α-Syn would expose their grafts to a higher risk of developing α-Syn aggregates. *SNCA*$^{-/-}$ grafts might also provide some protection against

environmental neurotoxins such as MPTP, to which *SNCA*$^{-/-}$ mice exhibit a degree of resistance (Dauer et al., 2002; Robertson et al., 2004).

Nonetheless, any physiological roles α-Syn might play should be carefully evaluated in both *in vitro* and *in vivo* models, as *SNCA*$^{-/-}$ grafts might lack some crucial functions necessary for long-term neuronal health. One such function is the ability of the grafted neurons to protect themselves from viral infections (see section 6.2). *SNCA*$^{-/-}$ grafts might be susceptible to neuro-invasive viruses WNV and VEEV TC83 which might compromise graft survival following such infections. In addition, norovirus, reovirus T3D and *Salmonella typhimurium* could also spread to CNS, though it is unclear whether *SNCA*$^{-/-}$ mDA grafts would be compromised following enteric and respiratory infections. It would be vital to evaluate neuronal survival and functions following inoculation of these viruses and bacteria in *SNCA*$^{-/-}$ mDA cultures *in vitro*, as well as in PD animal models transplanted with *SNCA*$^{-/-}$grafts. Given that *SNCA*$^{+/-}$ mice were as resistant as WT mice to neuro-invasive viruses (Beatman et al., 2016), *SNCA*$^{+/-}$ grafts might exhibit resistance to these viral and bacterial infections. As I demonstrated that *SNCA*$^{+/-}$ mDA neurons developed significantly less pS129-αSyn pathology than WT neurons following PFF treatment (section 5.3), *SNCA*$^{+/-}$ graft might be a sensible compromise to maximise graft longevity and to balance the susceptibility to synucleinopathy and neural infections.

It is also important to ensure *SNCA*$^{-/-}$ grafts synthesise and release dopamine in a similar manner to WT grafts *in vivo*. The level of dopamine and dopamine metabolites such as DOPAC and HVA could be evaluated in the lysates of *SNCA*$^{-/-}$ mDA cultures *in vitro* and compared to that of WT mDA cultures. Dopamine release from graft mDA neurons could be measured in transplanted PD animal models *in vivo* using fast-scan cyclic voltammetry (Anwar et al., 2011) or similar techniques. If *SNCA*$^{-/-}$ and WT grafts significantly differ, it would be worthwhile to investigate whether *SNCA*$^{+/-}$ grafts exhibit an intermediate phenotype, which would reinforce the hypothesis that *SNCA*$^{+/-}$ grafts might be a sensible compromise between susceptibility to synucleinopathy and normal physiological functions.

To apply *SNCA*$^{+/-}$ and *SNCA*$^{-/-}$ grafts in a clinical setting, the gene-targeting to create *SNCA*$^{+/-}$ and *SNCA*$^{-/-}$ hESC clonal lines and their subsequent differentiation to mDA progenitors would need to be performed in a GMP environment. To knockout *SNCA*, the state-of-the-art method for delivering CRISPR/Cas9n is in the form of ribonucleoprotein

complex, which is more efficient, generates fewer off-target events and removes the risk of plasmid integration (as discussed in section 3.5). If there is a particular need for *SNCA*$^{+/-}$ hESCs, the frequency of heterozygous clones can be increased by using 1:1 mixed repair templates of WT sequence and *SNCA* knockout sequence, or by optimising the distance of double-strand break (DSB) from intended mutation (Paquet et al., 2016). Prior to differentiation for clinical application, the genomic integrity of clonal hESC lines should be assessed by whole genome sequencing or high-resolution SNP analysis. This would enable the detection of undesired large on-target deletions, off-target events and any other genomic abnormalities occurred during the cloning process. For large-scale mDA differentiation, it is essential to maintain predictable cell viability and to reduce batch-to-batch variation during the cryopreservation of mDA progenitors (Drummond et al., 2020). In addition, it might be crucial to perform pilot testing of the differentiation at a small scale, for example, for determining the optimal CHIR concentration. For subsequent scale-up, extra attention should to be paid to the accuracy of the scale-up process and the batch-to-batch variation of reagents, especially CHIR, which can shift the identity of neural progenitors by 0.1 µM difference in concentration.

Similar to WT hESC-derived mDA progenitors, the graft survival and functionality of *SNCA*$^{+/-}$ and *SNCA*$^{-/-}$ hESC-derived mDA grafts have to be validated in PD rodent models and subsequently in non-human primates. If they exhibit comparable efficiency and potency to WT hESC-derived mDA progenitors and to the 'gold-standard' fetal tissues, a clinical application is highly likely. *SNCA*$^{S87E/S87E}$ mDA progenitors are less likely to be useful for clinical application as synucleinopathy-resistant grafts, since *SNCA*$^{S87E/S87E}$ mDA cultures exhibited considerable amount of pS129-αSyn pathology in the PFF model *in vitro*. The level of pS129-αSyn pathology in *SNCA*$^{S87E/S87E}$ mDA cultures was significantly lower than that in WT only when cultures developed considerable amount of pathology, and was otherwise not significantly different from WT (section 5.4). Similar to cell replacement therapy with WT cells, multiple immunosuppression for at least 1 year would be essential to ensure graft survival. In addition, strict patient selection criteria similar to the ones in TRANSEURO and hESC/hiPSC-based trials would be required for an optimal outcome.

6.2. *SNCA*$^{-/-}$ and *SNCA*$^{+/-}$ hESC-derived cells are valuable models for studying the physiological role of α-Syn

α-Syn has been found to play a neuroprotective role against neuro-invasive viruses, such as WNV and VEEV (Beatman et al., 2016). WNV infection was lethal to *SNCA*$^{-/-}$ mice while *SNCA*$^{+/-}$ mice exhibited similar resistance as WT mice (Beatman et al., 2016). Therefore, we collaborated with the Beckham lab (University of Colorado, Denver) and used *SNCA*$^{-/-}$, *SNCA*$^{+/-}$ and WT hESC-derived mDA neurons for the investigation of susceptibility to WNV and to a less pathogenic neuro-invasive virus VEEV vaccine strain TC83. If α-Syn provides resistance to neuro-invasive viruses, inoculated mDA neurons would exhibited a *SNCA*$^{-/-}$ > *SNCA*$^{+/-}$ > WT gradient of viral loads and cell death. Having validated this initial hypothesis, it would be interesting to explore the expression profiles of the virus-inoculated versus mock *SNCA*$^{-/-}$, *SNCA*$^{+/-}$ and WT mDA neurons, with extra attention to the up-regulation of immune and apoptosis related genes.

As the interface between host and environment, the gastrointestinal tract and olfactory bulb have been proposed as possible origins of PD (Del Tredici and Braak, 2016). The expression of α-Syn at these locations might play a neuroprotective role against infections of bacteria and viruses such as norovirus (Stolzenberg et al., 2017), reovirus T3D and *Salmonella typhimurium* (Tomlinson et al., 2017). Although olfactory receptor neuron-like cells could be indirectly differentiated from mouse iPSCs at a low efficiency (Xiong et al., 2017), there is yet to be an efficient direct differentiation protocol for hESC-derived olfactory neurons. To investigate the neuroprotective function of α-Syn in enteric neurons, *SNCA*$^{-/-}$ and WT hESC-derived enteric neurons (Barber et al., 2019) can be used as an *in vitro* model. If endogenous α-Syn protects enteric neurons against norovirus, reovirus T3D and *Salmonella typhimurium*, the enteric neurons differentiated from *SNCA*$^{-/-}$ hESCs would exhibit higher viral load and more death than those differentiated from WT hESCs after inoculations. Similarly, the gene expression profiles of the inoculated enteric neurons might reveal differences in innate immune response between *SNCA*$^{-/-}$ and WT neurons.

In PFF-injected rodent models, microgliosis and astrogliosis were observed in association with pS129-αSyn positive inclusions (Breid et al., 2016; Duffy et al., 2018; Sacino et al., 2014a; Shimozawa et al., 2017; Sorrentino et al., 2018; Thakur et al., 2017), resembling those observed in PD patients (Damier et al., 1993; Gerhard et al., 2006; Ouchi et al., 2005). The α-Syn pathology clearance capacity of microglia and astrocytes (George et al., 2019; Lee et al., 2008b; Loria et al., 2017) was impaired when they are activated (Austin et al., 2006; George et al., 2019). The activation might be triggered by

reduction of endogenous α-Syn (Austin et al., 2006; Benskey et al., 2018), which could be modelled by *SNCA*$^{-/-}$ hESC-derived microglia-like cells *in vitro* (Abud et al., 2017; Muffat et al., 2016). If the *SNCA*$^{-/-}$ microglia-like cells exhibit a higher basal activation state than WT microglia-like cells (Table 6.1c 1), the reduction of endogenous α-Syn is likely to be responsible for microgliosis. However, extracellular α-Syn pathology initially developed in surrounding neurons might also trigger microglia activation (Zhang et al., 2005). To address this possibility, PFF treatment of *SNCA*$^{-/-}$ microglia-like cells, as well as plating *SNCA*$^{-/-}$ microglia-like cells on top of PFF-treated WT mDA neurons, would reveal whether exogenous α-Syn aggregates alone are sufficient for inducing activation of microglia-like cells (Table 6.1c 2&3). Similarly, whether endogenous α-Syn and/or exogenous α-Syn aggregates is involved in astrogliosis (Lee et al., 2010) could be elucidated in *SNCA*$^{-/-}$ hESC-derived astrocytes (Roybon et al., 2013; Shaltouki et al., 2013) models (Table 6.1c 4-6). In addition, PFF treatment of astrocytes revealed their capacity to present MHC-II antigen and to activate T-cells (Rostami et al., 2020). However, it remains to be elucidate whether the antigen presenting and T-cell activation behaviours are triggered by the exogenous PFFs alone or involve the aggregation of endogenous α-Syn. PFF treatment of *SNCA*$^{-/-}$ astrocytes, as well as plating *SNCA*$^{-/-}$ astrocytes on top of PFF-treated WT mDA neurons, would be interesting *in vitro* models for understanding the role of α-Syn in the antigen presenting behaviour of astrocytes (Table 6.1c 5&6).

α-Syn was also reported to play a role in DNA repair both *in vitro* and *in vivo*. In PFF-treated mouse model as well as in DLB patients, neurons bearing pS129-αSyn pathology showed a significantly higher level of DNA DSBs (Schaser et al., 2019). This is consistent with the observation that *Snca*$^{-/-}$ mice exhibited a significantly increased accumulation of DSBs compared to WT mice (Schaser et al., 2019). Interestingly, S129 phosphorylation of α-Syn seemed crucial for a rapid recruitment of α-Syn to DSBs, where it facilitated NHEJ (Schaser et al., 2019). Hence, the loss of α-Syn, by either KO or depletion of functionable monomers upon aggregation, might result in increased DSBs and eventually lead to apoptosis. Using *SNCA*$^{-/-}$ hESC-derived mDA neurons, it can be investigated whether the loss of α-Syn would result in accumulation of DSBs and subsequent degeneration of neurons.

Apart from the involvement in innate immunity, α-Syn might also play a physiological role in synaptic transmission and dopamine release. *Snca*$^{-/-}$ mice were reported to exhibit

a lower striatal tissue content of dopamine (Abeliovich et al., 2000; Al-Wandi et al., 2010; Anwar et al., 2011). Since α-Syn was found to negatively regulate dopamine synthesis (Alerte et al., 2008; Masliah et al., 2000; Perez et al., 2002; Tehranian et al., 2006), the low dopamine level in *Snca*$^{-/-}$ mice is most likely due to the reduction in dopamine storage (Abeliovich et al., 2000; Cabin et al., 2002; Murphy et al., 2000; Yavich et al., 2004) rather than dopamine synthesis. To investigate these *in vitro*, we can first compare the dopamine level in the lysate of *SNCA*$^{-/-}$ and WT mDA neurons. Next, it would be interesting to study whether *SNCA*$^{-/-}$ mDA cultures exhibit an increase in dopamine synthesis. The investigation could be focused on the enzymes involved in the dopamine synthesis, such as TH, the rate limiting enzymes in dopamine synthesis, and aromatic amino acid decarboxylase (AADC), which converts levodopa to dopamine. If the protein level and activity (phosphorylation level) of TH and AADC in *SNCA*$^{-/-}$ mDA cultures was found to be no lower than that in WT, it would support the hypothesis that the lower dopamine level in *Snca*$^{-/-}$ mice is not due to decreased dopamine synthesis. To elucidate whether the low dopamine level is due to a decrease in dopamine storage, we can investigate if the number of reserved vesicles and readily releasable vesicles is lower in *SNCA*$^{-/-}$ mDA neurons than in WT. Subsequently, electrophysiology experiments could be performed to measure whether *SNCA*$^{-/-}$ mDA neurons released more dopamine than WT in response to repetitive stimulations *in vitro*. In the case of significant differences found between *SNCA*$^{-/-}$ and WT mDA cultures, it would be worthwhile to investigate whether *SNCA*$^{+/-}$ mDA cultures exhibit an intermediate phenotype of these properties.

Physiological roles of α-Syn	Proposed experiments
a) Protect central nervous system against neuro-invasive viruses	Measure cell viability and expression of immune related genes in *SNCA*$^{-/-}$ versus WT hESC-derived mDA neurons, following inoculation of WNV and VEEV TC83, respectively
b) Protect gastrointestinal tract against bacteria and viruses	Measure cell viability and expression of immune related genes in *SNCA*$^{-/-}$ versus WT hESC-derived enteric neurons, following inoculation of norovirus, reovirus T3D, and *Salmonella typhimurium*, respectively
c) Neuroinflammation, such as microgliosis and astrogliosis	Measure the activation state of microglia-like cells in, 1) WT versus *SNCA*$^{-/-}$ hESC-derived microglia-like cells 2) PFF versus control-treated *SNCA*$^{-/-}$ hESC-derived microglia-like cells

	3) *SNCA*$^{-/-}$ microglia-like cells plated on top of PFF-treated versus those on top of control-treated WT mDA neurons Measure the activation state of astrocytes in, 4) WT versus *SNCA*$^{-/-}$ hESC-derived astrocytes Measure the activation state and MHC-II antigen presenting of astrocytes in, 5) PFF versus control-treated *SNCA*$^{-/-}$ hESC-derived astrocytes 6) *SNCA*$^{-/-}$ astrocytes plated on top of PFF-treated versus those on top of control-treated WT mDA neurons
d) Facilitating DNA repair	Measure the number of spontaneous / chemical-induced DSBs, efficiency of NHEJ, and cell death (apoptosis), in 1) *SNCA*$^{-/-}$ versus WT hESCs 2) *SNCA*$^{-/-}$ versus WT hESC-derived mDA neurons
e) Regulation of dopamine release	In *SNCA*$^{-/-}$ versus WT hESC-derived mDA neurons, measure 1) dopamine content and the expression and activity of TH and AADC in cell lysate 2) the number of reserved vesicles and readily releasable vesicles 3) dopamine release upon repetitive stimuli

Table 6.1 Summary of proposed experiments for investigating α-Syn functions with *SNCA*$^{-/-}$ hESC-derived cells.

6.3. PFF-treated hESC-derived mDA neuron model for drug screening

Apart from the applications in investigating physiological roles of α-Syn and producing mDA grafts as potential next-generation cell replacement therapy, *SNCA*$^{+/-}$ and *SNCA*$^{-/-}$ hESCs are also valuable cell sources for disease modelling in PD. In particular, the PFF-treated hESC-derived mDA neuron model established in this thesis could be used as an effective drug screening platform. With *SNCA*$^{-/-}$ hESC-derived mDA neurons and control-treated WT mDA neurons as negative controls, the efficacy of test compounds could be indicated by the unbiased quantification of pS129-αSyn pathology.

The compounds to be tested with priority should have been reported to reduce α-Syn expression or aggregation and can cross blood-brain barrier (BBB) for the ease of administration. In addition, drugs which are currently used to treat other conditions should be given top priority, as they are often commercially available and already demonstrated

for their safety in human use, enabling a more rapid advance to clinical applications once verified.

A recent screening in a human neuroblastoma cell line has identified salbutamol, clenbuterol and riluzole as hits in an assay to reduce *SNCA* transcription (Mittal et al., 2017). In 11-year follow-up study in Norway, the use of the asthma medication, salbutamol, was associated with reduced risk of developing PD (Mittal et al., 2017). Clenbuterol was found to exhibit a protective effect against the loss of mDA neurons in a MPTP-lesioned mouse model (Mittal et al., 2017). In neurons differentiated from *SNCA* triplication hiPSCs, clenbuterol was also found to reduce the mRNA and protein expression levels of α-Syn, as well as to rescue the mitochondrial oxidisation and cell death caused by the PD-inducing neurotoxin rotenone (Mittal et al., 2017). Riluzole, a medication for amyotrophic lateral sclerosis, has been shown to reduce the mDA neuron loss and rescued the amphetamine-induced rotational asymmetry in a 6-OHDA-lesioned rat model (Carbone et al., 2012). Posiphen, a new drug in Phase I trial for Alzhiemer's disease by QR Pharma (NCT02925650), might also benefit PD patients as it was shown to inhibit the production of α-Syn protein via interaction with its 5' UTR (Rogers et al., 2011). All four drugs (salbutamol, clenbuterol, riluzole and posiphen) are known to cross the BBB. Following addition to the culture media of WT mDA neurons, these drugs are expected to decrease the level of endogenous α-Syn and result in a reduction of pS129-αSyn pathology.

Apart from re-purposed drugs, compound libraries such as natural product libraries could be screened for compounds which reduce pS129-αSyn pathology in the PFF-treated mDA neuron model. In addition, screening of fragment libraries would enable discovery of lead compounds, which could subsequently inform the design and synthesis of novel ligands.

Such drug screening process could be carried out in a high-throughput format, with replica plating of WT mDA neurons in 96-well or 384-well plates and with drugs tested in serial dilutions. In addition, drug cocktails could be tested to evaluate whether the combinations of specific drugs are more effective than on their own. Furthermore, the timing of administration could be investigated, for example, applying the drug weeks before, at the same time with, or weeks after PFF treatment. These would enable efficient identification of effective drugs or drug combinations, along with the optimal concentration and timing which would result in the most significant reduction of the pS129-αSyn

pathology. Successful compounds identified in this initial screening *in vitro* could be further assessed in PD animal models, such as PFF-injected rodents. Based on results of the optimal administration timing in the *in vitro* testing, a range of administration time point during the disease development could be tested, for example, prior to the histological development of pS129-αSyn pathology, or after the emergence of severe motor impairments.

6.4. Future refinements of the α-Syn PFF-treated mDA neuron model

In the current study, a higher plating density of neurons and longer incubation periods after PFF treatment gave rise to more pS129-αSyn pathology. Nonetheless, a systematic approach is required for the investigation of the correlation between neuronal maturity and the level of pS129-αSyn pathology developed. For example, hESC-derived mDA progenitors/neurons plated at different densities can be exposed to PFFs at various time points of the differentiation, which could reflect the level of maturity of the neurons at the time of PFF treatment. Another variable that could be investigated is the length of incubation period after PFF treatment, before the neurons are fixed and used for quantification of pS129-αSyn pathology. Tuning of these variables would reveal the optimal time point and plating density for inducing maximum amount of pathology within a reasonable amount of time and potentially speed up the pathology modelling process. In addition, in clinical settings, hESC-derived mDA progenitors would be transplanted at early differentiation (day 16) for optimal graft survival and innervation, hence the progenitors would be exposed to a 'disease' environment as early as day 16. Hence, PFF treatment at day 16 might represent a more clinically relevant model for the 'host to graft' spread of α-Syn pathology, especially when comparing the relative susceptibility of *SNCA*$^{+/-}$ and WT grafts. Another clinically relevant condition to test in the PFF model would be the concurrent exposure of *SNCA*$^{+/-}$ or *SNCA*$^{-/-}$ hESC-derived mDA neurons to exogenous α-Syn monomers. Since α-Syn monomers can diffuse through cell membrane, the occurrence of pS129-αSyn pathology in *SNCA*$^{-/-}$ mDA neurons might be expected if the concentration of exogenous α-Syn monomers reaches a threshold. Correlating the α-Syn monomer concentration with the amount of pS129-αSyn pathology developed in *SNCA*$^{+/-}$ and *SNCA*$^{-/-}$ mDA neurons compared to WT, and relating that to the local α-Syn monomer concentration in PD striatum, would further the accuracy in predicting the longevity of a *SNCA*$^{+/-}$ or *SNCA*$^{-/-}$ grafts relative to a WT graft.

Surprisingly, contrary to prior reports where S87E mutation reduced the level of α-Syn aggregation (Lázaro et al., 2014; Oueslati et al., 2012; Paleologou et al., 2010), I only observed a minor decrease in pS129-αSyn levels in *SNCA*$^{S87E/S87E}$ mDA neurons compared to WT. A major difference from these prior studies, in which S87E α-Syn was allowed to self-aggregate, was that I used PFFs polymerised from WT α-Syn monomers as aggregation template. A prior study found that the level of PFF-induced pS129-αSyn pathology was more dependent on the aggregation-prone characteristics of the template, rather than that of the recruitable monomers (Luk et al., 2016). This could potentially explain why I observed more pS129-αSyn pathology than what was expected based on prior studies. Hence, treating WT and *SNCA*$^{S87E/S87E}$ mDA neurons with S87E and WT α-Syn PFFs, respectively, can provide deeper insight into the nucleation and aggregation mechanism of α-Syn. Hypothetically, PFFs polymerised from S87E α-Syn would induce less pS129-αSyn pathology in WT mDA neurons than PFFs polymerised from WT α-Syn. If that is the case, it would also suggest that α-Syn aggregates formed in *SNCA*$^{S87E/S87E}$ mDA neurons would induce a smaller amount of pathology than WT mDA neuerons, when they are released and subsequently induce α-Syn aggregation in other neurons. To validate this hypothesis, equivalent amount of insoluble α-Syn aggregates could be extracted from *SNCA*$^{S87E/S87E}$ mDA culture and WT mDA culture, both treated by WT PFFs ('passage 1') and added to recipient WT mDA cultures ('passage 2') (Mahul-Mellier et al., 2019). This *in vitro* 'passaging' model of α-Syn propagation would elucidate whether *SNCA*$^{S87E/S87E}$ mDA neurons would slow down the inter-neuronal propagation of the pathology in comparison to WT mDA neurons.

Most of single amino acids which are reported to reduce α-Syn aggregation reside in the non-amyloid-beta component (NAC) domain (61 – 95) of α-Syn (Table 1.2), which is crucial for the aggregation of soluble α-Syn (El-Agnaf et al., 1998; Pawar et al., 2005; Volpicelli-Daley et al., 2011). Region 71-82 was particularly essential, as 71-82 α-Syn alone was sufficient for α-Syn fibrilisation (Giasson et al., 2001) and ∆71-82 α-Syn PFFs induced no (Luk et al., 2009) or significantly less (Sacino et al., 2014a) pS129-αSyn pathology than WT PFFs in cell and animal models. In this region, introducing a charged substitution (R or E) at A76 reduced α-Syn fibrilisation *in vitro* (Giasson et al., 2001) and reduced α-Syn aggregation in a yeast model (Fiske et al., 2011). In contrast, substitution of A76 with non-charged residues (P, G or V) or simply deletion of A76 did not significantly

affected α-Syn fibrilisation (Waxman et al., 2009). Nonetheless, the evidence was limited to observations in protein fibrilisation *in vitro* and non-neuronal cell models. Whether ∆71-82, A76R or A76E mutation in endogenous α-Syn would reduce pS129-αSyn pathology in the PFF-treated mDA neuron model remains to be investigated.

To investigate whether any α-Syn mutants would have the potential to produce synucleinopathy-resistance grafts for PD cell replacement therapy, the following design of experiments could be implemented. After hESC clonal lines with the intended α-Syn mutation are generated by CRISPR/Cas9n, they would be differentiated into mDA neurons and tested for their susceptibility to pS129-αSyn pathology using the PFF model, as established in this thesis. Next, it is vital to test whether these mDA neurons would retain normal innate immune functions, such as resistance to WNV, as well as whether they would release dopamine in a physiological level and manner. These functions should be assessed initially in mDA cultures *in vitro* (as detailed in section 6.2) and if encouraging, subsequently confirmed in PD animal models *in vivo* (as detailed in section 6.1). Ideally, to be considered as putative synucleinopathy-resistance grafts, hESCs with α-Syn mutation(s) should exhibit normal differentiation to mDA neurons, which retain normal physiological functions of α-Syn and show resistance to pS129-αSyn pathology in the PFF model. However, it is possible that such an ideal α-Syn mutation does not exist, for example, if the fibrillar state of α-Syn is required for its innate immune functions.

In the current study, I did not observe apparent impairments in cellular and functional defects such as mitochondrial morphology, spontaneous neuronal activities and synapse formation, which were previously reported in PFF models (Grassi et al., 2018; Gribaudo et al., 2019; Mahul-Mellier et al., 2019; Peelaerts et al., 2015; Tran et al., 2014; Volpicelli-Daley et al., 2011; Wu et al., 2019). Possible explanations for these discrepancies and potential future experiments to further investigate these phenotypes have been discussed in section 5.5. Overall, a plausible general explanation for these differences is a lower maturity of the hESC-derived mDA neurons in this thesis than in prior studies. The hESC-derived mDA neurons in the current study exhibited a lower density of synapsin and PSD95 particles compared to (Gribaudo et al., 2019) as well as a lack of synchronised neuronal activities, such as calcium oscillation (Gribaudo et al., 2019; Peelaerts et al., 2015; Volpicelli-Daley et al., 2011).

It is worth noting that pS129-αSyn^{+} cells in the PFF-treated cultures exhibited significantly more fragmentation than pS129-αSyn^{-} cells in the PFF-treated cultures and than cells in monomer-treated cultures (Gribaudo et al., 2019). In addition, pS129-αSyn^{-} cells in the PFF-treated cultures were not significantly more fragmented than cells in monomer-treated cultures (Gribaudo et al., 2019). Therefore, comparison between pS129-αSyn^{+} and pS129-αSyn^{-} cells might reveal subtle PFF-induced difference in mitochondrial morphology and spontaneous neuronal activities, which are not apparent when simply comparing PFF and control-treated cultures. This could be achieved by live imaging followed by fixation, immunostaining and imaging of the same field. The challenge lies in the use of neurite tracing tools compatible with dense cultures, to identify individual neurons bearing pS129-αSyn structures, which could reside in soma or neurites overlapping with other neurons.

In the current model, cell death was not detectable by LDH assay in neurons plated at 25,000 cells/cm^2 or 80,000 cells/cm^2 at 3, 4 or 6 weeks after PFF treatment at 5 µg/ml. It is possible that prolonged culture after PFF treatment would eventually lead to evident cell death, as the mDA cultures develop more pS129-αSyn pathology. However, impairments in mitochondrial morphology, synapse formation and spontaneous activities were consistently found in the absence of (Gribaudo et al., 2019), or prior to (Mahul-Mellier et al., 2019; Volpicelli-Daley et al., 2011; Wu et al., 2019) significant cell death. As I did not observe apparent structural or functional impairments in the current model at 7 – 9 weeks after PFF treatment, the level of cell death is unlikely to be evident within the current experimental timeframe (up to 9 weeks).

In addition, a few phenotypes observed in PFF-injected animal models have not been modelled in neuronal cultures *in vitro*, such as a reduced dopamine content in striatum tissue (Karampetsou et al., 2017; Luk et al., 2012a; Paumier et al., 2015). However, in these *in vivo* studies, the dopamine content was not normalised to the number of dopaminergic neurons, which was also significantly reduced in these models (Patterson et al., 2019; Shimozawa et al., 2017; Thakur et al., 2017; Tran et al., 2014; Zhang et al., 2019). In addition, functional impairments were observed in PFF-injected rat model, including significant decrease in the amplitude and frequency of K^{+} evoked release and the frequency of reuptake of striatal dopamine (Thakur et al., 2017). Therefore, the PFF-treated mDA neuron model can be employed to study whether the level of neuronal

dopamine content or evoked release and reuptake of dopamine per neuron is altered when the mDA neurons are burdened with pS129-αSyn pathology *in vitro*.

6.5. Limitations of using hESC-derived neurons for disease modelling

Although hESC-derived mDA neurons successfully modelled various aspects of synucleinopathy in the current PFF model and could potentially be used for a wide range of other disease modelling studies, they shared some of the limitations in disease modelling with other hESC/hiPSC-derived cell models.

Firstly, the differentiation could not reach 100% efficiency that all hESCs/hiPSCs were converted to the intended cell type. In addition, the assessment of differentiation quality relies on classification of differentiated cells, which is solely based on marker expression, unlike the classification of tissues which could be guided by spatial organisations. Therefore, it is difficult to pinpoint the identity of the unintended cells or to classify them as differentiation artefacts, such as the fibroblast-like cells in the current study.

Secondly, even if the differentiation is extremely pure for the intended cell type, a uniformed culture might not be physiologically relevant. For example, in the present study, the hESC-derived culture consisted of highly pure mDA neurons, but they might not function as the ones found *in vivo* due to the lack of other SN cell types that are essential for physiological signaling and regulatory interactions. A co-culture system could potentially solve this problem, but it would be challenging to optimise the co-culture media, plating timing and the relative composition to mimic the *in vivo* environment.

Thirdly, due to the lack of systemic regulations, findings in cell models do not always translate to animal models or patients (Uchihara and Giasson, 2016). In the current model, *SNCA*$^{+/-}$ mDA neurons exhibited significantly less pS129-αSyn pathology compared to WT mDA neurons. However, based merely on the cell model data, it is impossible to predict how much longer a *SNCA*$^{+/-}$ graft would last than a WT graft when transplanted in PD animal models or patients.

Nonetheless, hESC/hiPSC-derived cells largely reduce the need for limited embryo resources and the sacrifice of animals. In addition, hESC/hiPSC-derived neurons can be cultured for a substantially longer period than primary neurons and hence enable prolonged drug treatments for disease modelling.

6.6. Conclusion

In this thesis, using CRISPR/Cas9n technology, I generated *SNCA*$^{+/-}$, *SNCA*$^{-/-}$ and *SNCA*$^{S87E/S87E}$ hESC lines, which are valuable cell sources for investigating the physiological role of α-Syn as well as for PD disease modelling. The mDA differentiation of these clonal lines was not affected by the α-Syn mutation or the selection and cloning process. The mDA neurons were subsequently used for α-Syn pathology modelling with PFF treatment. The results showed that *SNCA*$^{-/-}$ mDA neurons were fully resistant, and *SNCA*$^{+/-}$ mDA neurons were partially resistant to the pathology, while *SNCA*$^{S87E/S87E}$ mDA neurons exhibited a reduced level of pathology. Further *in vitro* phenotyping and transplantation in PD animal models will determine the potential of *SNCA*$^{+/-}$ and *SNCA*$^{-/-}$ mDA progenitors as novel grafts for PD cell replacement therapy.

Data accessibility

MATLAB scripts for analysing PSD95 / synapsin / β-III tubulin immunostaining and all raw data for graphs in Figures 4.2b, 4.7b, 4.7d&f, 4.7h, 4.10b, 4.11b, 4.12b, 5.2b, 5.4, 5.5b, 5.6b, 5.7b, 5.8d&e, 5.9c&d, 5.11c&d, 5.11e&f and 5.12c&d can be obtained from LabArchives.com at http://doi.org/10.25833/m1kq-xq79

Appendix 1: Catalogue numbers and supplier information

Reagent	Supplier	Cat. No.
1kb DNA ladder	New England Biolabs	N3232
6-well, 24-well, 48-well and 96-well Costar® flat-bottom TC-treated plates	Corning	3516, 3524, 3548, 3595
100 mm TC-treated culture dish	Corning	430167
Accutase	Sigma	A6964
Acquity in-line filter	Waters	205000343
Acquity UPLC BEH C18 column	Waters	186003540
Amaxa™ Human Stem Cell Nucleofector™ Kit 1	Lonza	VPH-5012
Amersham™ Protran™ Premium 0.45 µm NC membrane	GE Healthcare	10600096
Anti-Mouse IgG (H+L), HRP conjugate	Promega	W4028
*Asc*I	New England Biolabs	R0558
ascorbic acid	Sigma	A4403
*Ava*I	New England Biolabs	R0152
*Ava*II	New England Biolabs	R0153
B27 supplement	Thermo Fisher Scientific	12587-010
*Bbs*I-HF	New England Biolabs	R3539S
BioPur Safe-Lock tubes	Eppendorf	0030121.589
blocking-grade blocker	BioRad	1706404
brain-derived neurotrophic factor (BDNF)	Peprotech	450-02
*Bsr*DI	New England Biolabs	R0574
Carbenicillin	Fisher	BP2658-5
Centriprep 10K, 10,000 NMWL spin filter	Millipore	4305
CHIR99021	Miltenyi Biotec	130-103-926
CutSmart® buffer (10x)	New England Biolabs	B7204
DAPI	Thermo Fisher Scientific	D1306
DAPT	Tocris	2634
DH5α Competent *E. coli*	New England Biolabs	C2987
dibutyryl cyclic AMP	Sigma	D0627
DMEM/F12, no glutamine	Thermo Fisher Scientific	21331-020

donkey anti-goat Alexa Fluor-568	Thermo Fisher Scientific	A11057
donkey anti-mouse Alexa Fluor-488	Thermo Fisher Scientific	A21202
donkey anti-mouse Alexa Fluor-647	Abcam	Ab150107
donkey anti-rabbit Alexa Fluor-488	Thermo Fisher Scientific	A21206
donkey anti-rabbit Alexa Fluor-555	Thermo Fisher Scientific	A31572
donkey anti-rat IgG Alexa Fluor-488	Thermo Fisher Scientific	A21208
donkey anti-sheep IgG Alexa Fluor-488	Abcam	ab150177
donkey serum	Sigma	D9663
dopamine	Cerilliant	D-081
dopamine-1,1,2,4-	Cerilliant	D-072
DPBS with Mg^{2+} and Ca^{2+}	Thermo Fisher Scientific	14040-083
DPBS without Mg^{2+} and Ca^{2+}	Sigma	D8537
*Eco*RI	New England Biolabs	R0101
Enhancers 1 and 2	Thermo Fisher Scientific	1956760
Expi293 Expression Medium	Thermo Fisher Scientific	A1435101
Expi293fectamine	Thermo Fisher Scientific	1956760
fetal calf serum	Thermo Fisher Scientific	10270-106
FGF8b	R&D Systems	423-F8/CF
FlowFusor pyrogen free water	Fresenius Kabi	FBP7205
Fluo-4, AM	Thermo Fisher Scientific	F14201
Fluo-8, AM	Abcam	ab142773
formaldehyde solution 37-41%	Fisher	F/1501/PB08
glial cell line-derived neurotrophic factor (GDNF)	Peprotech	450-10
goat anti-HNF-3β/FOXA2 (M20)	Santa Cruz	sc-6554
goat anti-mouse IgG1 Alexa Fluor-488	Thermo Fisher Scientific	A21121
goat anti-mouse IgG2a Alexa Fluor-488	Thermo Fisher Scientific	A21131
goat anti-mouse IgG2a Alexa Fluor-568	Thermo Fisher Scientific	A21134
goat anti-mouse IgG2b Alexa Fluor-647	Thermo Fisher Scientific	A21242
goat anti-NANOG	R&D Systems	AF1997
goat anti-rabbit Alexa Fluor-555	Thermo Fisher Scientific	A21428
goat serum	Sigma	G9023

heparin	Sigma	H3149
High Sensitivity RNA ScreenTape	Agilent Technologies	5067-5579
High Sensitivity RNA ScreenTape Sample Buffer	Agilent Technologies	5067-5580
HiTrap Q FF column	GE Healthcare	17-5156-01
Hoechst	GeneCopoeia	C006
*Hpa*I	New England Biolabs	R0105
JC-1 dye	Thermo Fisher Scientific	T3168
Kanamycin	Fisher	BP906-5
L-Glutamine	Thermo Fisher Scientific	25030123
Laminin-111	Biolamina	LN111
Laminin-521	BioLamina	LN521
LDN-193189	Miltenyi Biotec	130-103-925
LightCycler® 480 Probes Master mix	Roche	04707494001
Limulus Amebocyte Lysate test	Charles River Laboratories	PTS20F
MasterPure™ Complete DNA and RNA Purification Kit	Epicentre	MC85200
Matrigel (Geltrex™ LDEV-Free, hESC-Qualified, Reduced Growth Factor Basement Membrane Matrix)	Thermo Fisher Scientific	A1413301
mouse anti-β-actin antibody, HRP conjugate	Abcam	ab20272
mouse IgG1 anti-α-Synuclein	BD Biosciences	610787
mouse IgG2a anti-p62 (SQSTM1)	Abcam	56416
mouse IgG2a anti-PSD95	Biolegend	810401
mouse IgG2a anti-tyrosine hydroxylase	Biolegend	818001
mouse IgG2b anti-OCT3/4	Santa Cruz	sc5279
mouse IgG2b anti-β-III tubulin	Abcam	T8660
N2 supplement	Thermo Fisher Scientific	17502-048
NEBuffer™ 2	New England Biolabs	B7002
NEBuffer™ 2.1 (10x)	New England Biolabs	B7202
Neurobasal Medium	Thermo Fisher Scientific	21103-049
*Nsi*I	New England Biolabs	R3127

Nuclease-free water	Thermo Fisher Scientific	AM9937
NuPAGE™ 4-12% Bis-Tris Protein Gel	Thermo Fisher Scientific	NP0322BOX
NuPAGE™ LDS loading dye (4x)	Thermo Fisher Scientific	NP0007
NuPAGE™ Sample Reducing Agent (10x) (DTT)	Thermo Fisher Scientific	NP0004
One Shot™ Stbl3™ Chemically Competent *E. coli*	Thermo Fisher Scientific	C737303
Opti-MEM	Thermo Fisher Scientific	11058021
*Pac*I	New England Biolabs	R0547
PBS	Thermo Fisher Scientific	18912-014
Phusion® High-Fidelity DNA Polymerase	New England Biolabs	M0530
Pierce™ BCA protein assay kit	Thermo Fisher Scientific	23227
Pierce™ ECL Western Blotting Substrate	Thermo Fisher Scientific	32109
Pierce™ LDH Cytotoxicity Assay Kit	Thermo Fisher Scientific	88953
poly-ornithine	Sigma	P4957
pSpCas9n-2A-Puro plasmid (pX462)	Addgene	48141
Q5® High-Fidelity DNA Polymerase	New England Biolabs	M0491
PureLink™ HiPure Plasmid Midiprep Kit	Thermo Fisher Scientific	K210004
QIAprep® Spin Miniprep Kit	QIAGEN	27104
Qubit HS RNA HS Assay Kits	Thermo Fisher Scientific	Q32852
Quick-Load® 100 bp DNA ladder	New England Biolabs	N0467
rabbit anti-LMX1A	Millipore	ab10533
rabbit anti-PDGFRα	Cell Signaling	5241
rabbit anti-phospho-S129 α-Synuclein	Abcam	A51253
rabbit anti-synapsin	Millipore	AB1543
rabbit anti-tyrosine hydroxylase	Millipore	AB152
rat IgG2a anti-CORIN	R&D Systems	MAB2209
rat IgG2a isotype control	R&D Systems	MAB006
Restore™ PLUS Western Blot Stripping Buffer	Thermo Fisher Scientific	46430
RIPA Lysis Buffer System	Santa Cruz	sc-24948
RNeasy Plus Micro Kit	QIAGEN	74034
SB431542	Millipore	616461
SeeBlue™ Plus2 pre-stained protein standard	Thermo Fisher Scientific	LC5925

sheep anti-COL1A1	R&D Systems	AF6220
Shh-C24II	R&D Systems	1845-SH-500
STEM-CELLBANKER - GMP Grade	ZENOAQ	11890
StemMACS iPS-Brew XF	Miltenyi Biotec	130-107-086
Strata Strong Cation Exchange (SCX) cartridges	Phenomenex	8B-S010-EAK
SuperScript™ IV Reverse Transcriptase	Thermo Fisher Scientific	18090010
T5 exonuclease	Epicentre	T5E4111K
T7 endonuclease I	New England Biolabs	M0302
Taq DNA polymerase with ThermoPol® Buffer	New England Biolabs	M0267
Tetramethylrhodamine, Methyl Ester, Perchlorate (TMRM)	Thermo Fisher Scientific	T668
TOPO® TA Cloning® Kit for Sequencing	Thermo Fisher Scientific	450030
Triton-X 100	Fisher	BP-151-100
UltraPure 0.5 M EDTA	Thermo Fisher Scientific	15575-038
UltraPure™ Agarose	Thermo Fisher Scientific	16500-500
Wizard® SV Gel and PCR Clean-Up System	Promega	A9281
Y27632	Tocris	1254
Zero Blunt® TOPO® PCR Cloning Kit	Thermo Fisher Scientific	450245
µ-Slide 8 Well	ibidi	80827

Appendix 2: R scripts for analysing RT-qPCR

1) For genes with efficiency = 2

```
# clear the environment
rm(list=ls())

genename <- readline(prompt = "enter gene name: ")

# choose the raw data .txt files
TBP <- read.delim("/Users/yixichen/Desktop/TBP.txt")
target_gene <- read.delim(file.choose())

library(dplyr)
library(ggplot2)

# add a new column to TBP with the mean of replicates for each sample
TBP <- TBP %>%
  filter(Name!="H2O" & !grepl("-RT", Name) & !grepl("Sample", Name)) %>%
  group_by(Name) %>%
  mutate(mean_of_replicates = mean(Cp))

# add a new colum to target gene with the difference between the cp value of TBP and its cp
value
# add a new colum to target gene with power(2,difference)
target_gene <- target_gene %>%
  filter(Name!="H2O" & !grepl("-RT", Name) & !grepl("Sample", Name)) %>%
  mutate(Cp_diff_TBP = TBP$mean_of_replicates - Cp) %>%
  mutate(pwr_diff = 2 ** Cp_diff_TBP)

# calculate the mean and standard deviation of the expression level (relative to TBP) of
replicates
target_gene_result <- target_gene %>%
  filter(!is.na(Cp)) %>%
  group_by(Name) %>%
  summarize(mean = mean(pwr_diff),std = sd(pwr_diff))

# export csv file with gene name
target_gene_result <- cbind(gene = genename, target_gene_result)
write.table(target_gene_result, "/Users/yixichen/Desktop/results.csv", append = TRUE,
sep=",", row.names=F)

# break x labels in to rows
levels(target_gene_result$Name) <- gsub(" ", "\n", levels(target_gene_result$Name))

# plot average with standard deviation
ggplot(data = target_gene_result) +
  ggtitle(genename) +
  xlab(NULL) +
  ylab("expression relative to TBP") +
  geom_col(aes(x=Name, y=mean), fill = "grey30", width = 0.6) +
```

```
  geom_errorbar(aes(x=Name, ymin=mean-std, ymax=mean+std), width=0.2, colour="black",
alpha=0.9, size=1) +
  theme(text = element_text(size=20, colour = "black"), axis.text.x = element_text(size=15,
colour = "black"), plot.title = element_text(size = 20, hjust = 0.5))

# auto save plots, need to change the format after both genename and device
ggsave(paste(genename,".png", sep = ""), plot = last_plot(), device = "png", path =
"/Users/yixichen/Desktop",
       scale = 1, width = NA, height = NA, units = c("in", "cm", "mm"),dpi = 300)
```

2) For genes with efficiency other than 2

```
# clear the environment
rm(list=ls())

# enter GOI and its known primer efficiency
genename <- readline(prompt = "enter gene name: ")
eGOI <- as.numeric(readline(prompt = "primer efficiency: "))

# choose the raw data .txt files
TBP <- read.delim("/Users/yixichen/Desktop/TBP.txt")
target_gene <- read.delim(file.choose())

library(dplyr)
library(ggplot2)

# add a new column to TBP with the mean of replicates for each sample
TBP <- TBP %>%
  filter(Name!="H2O" & !grepl("-RT", Name) & !grepl("Sample", Name)) %>%
  group_by(Name) %>%
  mutate(mean_of_replicates = mean(Cp))

# add a new colum to target gene with the difference between the cp value of TBP and its cp
value
# add a new colum to target gene with power(2,difference)
target_gene <- target_gene %>%
  filter(Name!="H2O" & !grepl("-RT", Name) & !grepl("Sample", Name)) %>%
  mutate(pwr_diff = 2 ** TBP$mean_of_replicates / eGOI ** Cp)

# calculate the mean and standard deviation of the expression level (relative to TBP) of
replicates
target_gene_result <- target_gene %>%
  filter(!is.na(Cp)) %>%
  group_by(Name) %>%
  summarize(mean = mean(pwr_diff),std = sd(pwr_diff))

# export csv file with gene name
target_gene_result <- cbind(gene = genename, target_gene_result)
write.table(target_gene_result, "/Users/yixichen/Desktop/results.csv", append = TRUE,
sep=",", row.names=F)
```

```
# break x labels in to rows
levels(target_gene_result$Name) <- gsub(" ", "\n", levels(target_gene_result$Name))

# plot average with standard deviation
ggplot(data = target_gene_result) +
  ggtitle(genename) +
  xlab(NULL) +
  ylab("expression relative to TBP") +
  geom_col(aes(x=Name, y=mean), fill = "grey30", width = 0.6) +
  geom_errorbar(aes(x=Name, ymin=mean-std, ymax=mean+std), width=0.2, colour="black",
alpha=0.9, size=1) +
  theme(text = element_text(size=20, colour = "black"), axis.text.x = element_text(size=15,
colour = "black"), plot.title = element_text(size = 20, hjust = 0.5))

# auto save plots, need to change the format after both genename and device
ggsave(paste(genename,".png", sep = ""), plot = last_plot(), device = "png", path =
"/Users/yixichen/Desktop",
       scale = 1, width = NA, height = NA, units = c("in", "cm", "mm"),dpi = 300)
```

Appendix 3:

ImageJ macro script for quantifying TH / β-III tubulin double positive cells

```
dir2=getDirectory("Save folder");
title=getTitle();
setSlice(1); // channel 1 - DAPI
run("Enhance Contrast", "saturated=0.35");
setSlice(2); // channel 2 - TH
run("Enhance Contrast", "saturated=0.35");
setSlice(3); // channel 3 - tubulin
run("Enhance Contrast", "saturated=0.35");
run("8-bit");
run("Split Channels");
selectWindow("C1-"+title); // channel 1 - DAPI
run("Auto Local Threshold", "method=Mean radius=15 parameter_1=0 parameter_2=0 white");
print(title+"*** threholded");
run("Watershed");
print(title+"*** watersheded");
roiManager("Delete");
print(title+"*** analyzing particles ***");
run("Analyze Particles...", "size=50-Infinity circularity=0.30-1.00 show=Outlines display clear
summarize add");
roiManager("Save", dir2+title+"_ROIs.zip"); //save ROIs
String.copyResults;
print(String.paste);

selectWindow("C2-"+title); // channel 2 - TH
run("Auto Threshold", "method=Yen white");
run("Clear Results");
roiManager("Measure");
String.copyResults;
print(String.paste);
close();
// copy DAPI & TH results from Log window

selectWindow("C3-"+title); //channel 3 - tubulin
run("Auto Threshold", "method=Default white");
run("Clear Results");
roiManager("Measure");
close();
// copy tubulin results from Result window
```

Appendix 4:

ImageJ macros for analysing pS129-αSyn / β-III tubulin immunostaining

1) area analysis

```
macro "pSyn overlap tubulin in zPro [F1]" {
setBatchMode(true);

dir1=getDirectory("Source folder");
dir2=getDirectory("Save folder");

list=getFileList(dir1); //Get the list of files in the input folder

for (i=0; i<list.length; i++){
    if (endsWith(list[i], ".ics")){
        processICS();
    }
}

function processICS(){
    open(dir1+list[i]);
    title=File.nameWithoutExtension;
    print(title);
    run("Z Project...", "start=1 stop=15 projection=[Max Intensity]"); // or stop = 13
    Stack.setChannel(1); //pSyn
    setMinAndMax(0,100000); // for each batch, select a maximum for a clear view of the
structures
    Stack.setChannel(2); //tubulin
    setMinAndMax(0,40000); // for each batch, select a maximum for a clear view of the
structures
    save(dir2+title+"_zPro.tif");
    run("Split Channels");

    selectWindow("C1-MAX_"+title+".ics");
    setThreshold(30000, 1e30); // for each batch, select a minimum to exclude noise
    run("Convert to Mask");
    run("Create Selection");
    run("Measure");
    save(dir2+title+"_pSyn_binary.tif");

    selectWindow("C2-MAX_"+title+".ics");
    setThreshold(2000, 1e30); // for each batch, select a minimum to exclude noise
    run("Convert to Mask");
    run("Create Selection");
    run("Measure");
    save(dir2+title+"_tubulin_binary.tif");

    imageCalculator("AND create", "C1-MAX_"+title+".ics", "C2-MAX_"+title+".ics");
    run("Create Selection");
    run("Make Inverse");
```

```
    run("Measure");
    save(dir2+title+"_AND_binary.tif");
    run("Close All");
}
}
```

2) particle analysis

```
macro "pSyn particle analysis [F2]" {
setBatchMode(true);

dir1=getDirectory("Source folder");
list=getFileList(dir1);

for (i=0; i<list.length; i++){
    if (endsWith(list[i], "AND_binary.tif")){
        processAND();
    }
}

function processAND(){
    open(dir1+list[i]);
    run("Set Measurements...", "area fit shape display redirect=None decimal=3");
    run("Analyze Particles...", "display clear summarize");
    run("Summarize"); // summarise measurements of all particles in this image in the
    Summary window
    String.copyResults;
    print(String.paste); // paste raw data of each particle in the Log window
    run("Close All");
}
}
```

Appendix 5: ImageJ macro script for thresholding PSD95 / synapsin / β-III tubulin immunostaining

```
macro "synaptic staining thresholding batch [F3]"{
setBatchMode(true);
dir1 = getDirectory("Input");
dir2 = getDirectory("Output");
listOfFiles = getFileList(dir1);

for (i=0; i<listOfFiles.length; i++) {
    if (endsWith(listOfFiles[i], ".ics")){
        path= dir1+listOfFiles[i];
        open(path);
        title = getTitle();
        print("*** Processing file= "+title+" ***");
        selectWindow(title);
        run("Split Channels");

        if (isOpen("C3-"+title)) {
            selectWindow("C3-"+title); // Channel #3 beta-tubulin thresholding
            c3Title = getTitle();
            setMinAndMax(0, 20000); // for each batch, select a maximum for a clear view of
    the structures
            setAutoThreshold("Default dark");
            setThreshold(600, 1e30); // for each batch, select a minimum to exclude noise
            run("Convert to Mask","method=Default background=Dark black");
            saveAs("tiff", dir2+"tub_"+title+"_thresholded");
        }
        if (isOpen("C2-"+title)) {
            selectWindow("C2-"+title); // Channel #2 synapsin thresholding
            setMinAndMax(0, 50000); // for each batch, select a maximum for a clear view of
        the structures
            setAutoThreshold("Default dark");
            setThreshold(12000, 1e30); // for each batch, select a minimum to exclude noise
            run("Convert to Mask","method=Default background=Dark black");
            saveAs("tiff", dir2+"syp_"+title+"_thresholded");
        }
        if (isOpen("C1-"+title)) {
            selectWindow("C1-"+title); // Channel #1 PSD95 thresholding
            setMinAndMax(0, 40000); // for each batch, select a maximum for a clear view of
        the structures
            setAutoThreshold("Default dark");
            setThreshold(10000, 1e30); // for each batch, select a minimum to exclude noise
            run("Convert to Mask","method=Default background=Dark black");
            saveAs("tiff", dir2+"psd_"+title+"_thresholded");
        }
    }
    run("Close All");
}
}
```

Appendix 6: R scripts for plotting calcium imaging results

1) Comparing cultures of different genotypes

```
# clear the environment
rm(list=ls())

# choose the data files, number indicate number of sheet to be plotted
library("readxl")
result <- read_excel(file.choose(), 1)

library(ggplot2)
# specify order of x-axis to avoid default order in R
result$condition <- factor(result$condition, levels = c("Baseline","1/2 Mg","1/4 Mg","1/8 Mg","1/16 Mg","KCl"))

# change y to magnitude, EventPerActiveCell, or active
ggplot(result, aes(x = condition, y = magnitude, colour = factor(genotype),
                   group = factor(result$line))) +
  geom_point(shape = 1, size = 6) +
  geom_line() +
  theme(text = element_text(size=35, colour = "black"),
        axis.text.x = element_text(size=30, colour = "black", angle = 45, hjust = 1),
        plot.title = element_text(size = 20, hjust = 0.5),
        legend.title = element_blank()) #+  # keep the + only for %active
  #scale_y_continuous(labels = function(x) paste0(x*100, "%")) # this line only for %active
```

2) Comparing PFF versus PBS-treated WT cultures

```
# clear the environment
rm(list=ls())

# choose the data files, number indicate number of sheet to be plotted
library("readxl")
result <- read_excel(file.choose(), 1)

library(ggplot2)
# specify order of x-axis to avoid default order in R
result$condition <- factor(result$condition, levels = c("Baseline","1/2 Mg","1/4 Mg","1/8 Mg","KCl"))
# specify order of groups to make PFF red and PBS blue
result$SorF <- factor(result$SorF, levels = c("PFF", "PBS"))

# change y to magnitude, EventPerActiveCell, or active
ggplot(result, aes(x = condition, y = magnitude, colour = factor(SorF),
                   group = factor(result$experiment))) +
  geom_point(shape = factor(result$sister), size = 3) +
  geom_line() +
  theme(text = element_text(size=35, colour = "black"),
        axis.text.x = element_text(size=30, colour = "black", angle = 30, hjust = 1),
        axis.text.y = element_text(size=30, colour = "black"),
```

```
      legend.title = element_blank()) +
stat_summary(aes(group = factor(result$SorF)),
             fun.y = "mean",
             fun.ymin = "mean",
             fun.ymax= "mean",
             size= 0.5, width = 0.3,
             geom = "crossbar",
             position = position_dodge(0.5)) +
geom_errorbar(aes(group = factor(result$SorF)),
              stat="summary", width = 0.2,size = 1,
              fun.ymin=function(x) {mean(x)-sd(x)},
              fun.ymax=function(x) {mean(x)+sd(x)},
              position = position_dodge(0.5)) #+  # keep the + only for %active
#scale_y_continuous(labels = function(x) paste0(x*100, "%")) # this line only for %active
```

Appendix 7: ImageJ macro scripts for analysing TMRM live imaging analysis

1) Select individual cells and thresholding

```
Stack.setChannel(1); //tubulin
setMinAndMax(0, 50000); // for each batch, select a maximum for a clear view of the structures
setTool(2); // select all the cells you want to analyse in tubulin channel with polygon tool
// MANUAL STEP: ctrl+T for each selection into ROI manager

Stack.setChannel(2); //TMRM
m = 30000; // for each image, select a maximum for a clear view of the structures
setMinAndMax(0, m);
print("MinMax = 0, "+m);

// select each of the ROIs & pick 6 most in-focus slices
start = getNumber("Start",5); // enter the start slice
end = start+5;
run("Duplicate...", "duplicate range="+start+"-"+end);
run("8-bit");
title=getTitle();
print(title,"\t",start,"\t",end);
dir2=getDirectory("Save folder");
save(dir2+title+".tif");
run("Auto Local Threshold", "method=Phansalkar radius=15 parameter_1=0 parameter_2=0
white stack");
run("Make Inverse"); // delete the unselected region
run("Clear", "slice");
run("Next Slice [>]");
run("Clear", "slice");
run("Next Slice [>]");
run("Clear", "slice");
run("Next Slice [>]");
run("Clear", "slice");
run("Next Slice [>]");
run("Clear", "slice");
run("Next Slice [>]");
run("Clear", "slice");
save(dir2+title+"_thresholded.tif"); // MANUALLY ctrl+shift+W close all after all the cells have
been saved
```

2) Measure size of thresholded cells

```
macro "Measure cell size of thresholded cells [F4]" {
setBatchMode(true);
dir1=getDirectory("Source folder");
list=getFileList(dir1);

for (i=0; i<list.length; i++){
    if (endsWith(list[i], "thresholded.tif")){
        measureCELLSIZE();
    }
```

```
}

function measureCELLSIZE(){
	open(dir1+list[i]);
	run("Set Measurements...", "area display redirect=None decimal=3");
	run("Measure");
	close();
}
```

3) Measure size of thresholded mitochondria

```
macro "Measure Size of Thresholded Mitochondria [F5]" {
setBatchMode(true);
dir1=getDirectory("Source folder");
list=getFileList(dir1);

for (i=0; i<list.length; i++){
	if (endsWith(list[i], "thresholded.tif")){
		measureGEOMETRY();
	}
}

function measureGEOMETRY(){
	open(dir1+list[i]);
	run("Clear Results");
	run("3D Geometrical Measure");
	close();
	selectWindow("Results");
	run("Summarize");
	String.copyResults;
	print(String.paste); // paste result in Log window
}
```

4) Measure shape of thresholded mitochondria

```
macro "Measure Shape of Thresholded Mitochondria [F6]" {
setBatchMode(true);
dir1=getDirectory("Source folder");
list=getFileList(dir1);

for (i=0; i<list.length; i++){
	if (endsWith(list[i], "thresholded.tif")){
		measureSHAPE();
	}
}

function measureSHAPE(){
	open(dir1+list[i]);
	run("Clear Results");
	run("3D Shape Measure");
	close();
```

```
    selectWindow("Results");
    run("Summarize");
    String.copyResults;
    print(String.paste); // paste result in Log window
}
```

5) Measure major and minor axes of thresholded mitochondria

```
macro "Measure Major and Minor Axes of Thresholded Mitochondria [F7]" {
setBatchMode(true);
dir1=getDirectory("Source folder");
list=getFileList(dir1);

for (i=0; i<list.length; i++){
    if (endsWith(list[i], "thresholded.tif")){
        measureAXES();
    }
}

function measureAXES(){
    open(dir1+list[i]);
    print(getTitle());
    run("Clear Results");
    run("3D Shape Measure");
    run("Clear Results");
    run("3D Ellipsoid Fitting", " ");
    run("Summarize");
    String.copyResults;
    print(String.paste); // paste result in Log window
}
```

References

Abdelmotilib, H., Maltbie, T., Delic, V., Liu, Z., Hu, X., Fraser, K.B., Moehle, M.S., Stoyka, L., Anabtawi, N., Krendelchtchikova, V., Volpicelli-Daley, L.A., West, A., 2017. α-Synuclein fibril-induced inclusion spread in rats and mice correlates with dopaminergic Neurodegeneration. Neurobiology of Disease 105, 84–98. https://doi.org/10.1016/j.nbd.2017.05.014

Abeliovich, A., Schmitz, Y., Fariñas, I., Choi-Lundberg, D., Ho, W.-H., Castillo, P.E., Shinsky, N., Verdugo, J.M.G., Armanini, M., Ryan, A., 2000. Mice lacking α-synuclein display functional deficits in the nigrostriatal dopamine system. Neuron 25, 239–252. https://doi.org/10.1016/S0896-6273(00)80886-7

Abounit, S., Bousset, L., Loria, F., Zhu, S., Chaumont, F., Pieri, L., Olivo-Marin, J., Melki, R., Zurzolo, C., 2016. Tunneling nanotubes spread fibrillar α-synuclein by intercellular trafficking of lysosomes. EMBO J 35, 2120–2138. https://doi.org/10.15252/embj.201593411

Abud, E.M., Ramirez, R.N., Martinez, E.S., Healy, L.M., Nguyen, C.H.H., Newman, S.A., Yeromin, A.V., Scarfone, V.M., Marsh, S.E., Fimbres, C., Caraway, C.A., Fote, G.M., Madany, A.M., Agrawal, A., Kayed, R., Gylys, K.H., Cahalan, M.D., Cummings, B.J., Antel, J.P., Mortazavi, A., Carson, M.J., Poon, W.W., Blurton-Jones, M., 2017. iPSC-Derived Human Microglia-like Cells to Study Neurological Diseases. Neuron 94, 278-293.e9. https://doi.org/10.1016/j.neuron.2017.03.042

Alerte, T.N.M., Akinfolarin, A.A., Friedrich, E.E., Mader, S.A., Hong, C.-S., Perez, R.G., 2008. α-Synuclein aggregation alters tyrosine hydroxylase phosphorylation and immunoreactivity: Lessons from viral transduction of knockout mice. Neuroscience Letters 435, 24–29. https://doi.org/10.1016/j.neulet.2008.02.014

Al-Wandi, A., Ninkina, N., Millership, S., Williamson, S.J., Jones, P.A., Buchman, V.L., 2010. Absence of α-synuclein affects dopamine metabolism and synaptic markers in the striatum of aging mice. Neurobiology of aging 31, 796–804. https://doi.org/10.1016/j.neurobiolaging.2008.11.001

Ana Gámez-Valero, Katrin Beyer, 2018. Alternative Splicing of Alpha- and Beta-Synuclein Genes Plays Differential Roles in Synucleinopathies. Genes 9, 63. https://doi.org/10.3390/genes9020063

Anderson, J.P., Walker, D.E., Goldstein, J.M., de Laat, R., Banducci, K., Caccavello, R.J., Barbour, R., Huang, J., Kling, K., Lee, M., Diep, L., Keim, P.S., Shen, X., Chataway, T., Schlossmacher, M.G., Seubert, P., Schenk, D., Sinha, S., Gai, W.P., Chilcote, T.J., 2006. Phosphorylation of Ser-129 Is the Dominant Pathological Modification of α-Synuclein in Familial and Sporadic Lewy Body Disease. J. Biol. Chem. 281, 29739–29752. https://doi.org/10.1074/jbc.M600933200

Andersson, E., Tryggvason, U., Deng, Q., Friling, S., Alekseenko, Z., Robert, B., Perlmann, T., Ericson, J., 2006. Identification of intrinsic determinants of midbrain dopamine neurons. Cell 124, 393–405. https://doi.org/10.1016/j.cell.2005.10.037

Angot, E., Steiner, J.A., Tomé, C.M.L., Ekström, P., Mattsson, B., Björklund, A., Brundin, P., 2012. Alpha-synuclein cell-to-cell transfer and seeding in grafted dopaminergic neurons in vivo. PLoS One 7, e39465. https://doi.org/10.1371/journal.pone.0039465

Anwar, S., Peters, O., Millership, S., Ninkina, N., Doig, N., Connor-Robson, N., Threlfell, S., Kooner, G., Deacon, R.M., Bannerman, D.M., Bolam, J.P., Chandra, S.S., Cragg, S.J., Wade-Martins, R., Buchman, V.L., 2011. Functional Alterations to the Nigrostriatal System in Mice Lacking All Three Members of the Synuclein Family. The Journal of Neuroscience 31, 7264–7274. https://doi.org/10.1523/jneurosci.6194-10.2011

Austin, S.A., Floden, A.M., Murphy, E.J., Combs, C.K., 2006. α-Synuclein Expression Modulates Microglial Activation Phenotype. Journal of Neuroscience 26, 10558–10563. https://doi.org/10.1523/JNEUROSCI.1799-06.2006

Ayers, J.I., Brooks, M.M., Rutherford, N.J., Howard, J.K., Sorrentino, Z.A., Riffe, C.J., Giasson, B.I., 2016. Robust CNS pathology in transgenic mice following peripheral injection of α-synuclein fibrils. Journal of Virology JVI. 02095-16. https://doi.org/10.1128/JVI.02095-16

Ayers, J.I., Riffe, C.J., Sorrentino, Z.A., Diamond, J., Fagerli, E., Brooks, M., Galaleldeen, A., Hart, P.J., Giasson, B.I., 2018. Localized Induction of Wild-Type and Mutant Alpha-Synuclein Aggregation Reveals Propagation along Neuroanatomical Tracts. Journal of Virology 92. https://doi.org/10.1128/JVI.00586-18

Bain, J., Plater, L., Elliott, M., Shpiro, N., Hastie, C.J., Mclauchlan, H., Klevernic, I., Arthur, J.S.C., Alessi, D.R., Cohen, P., 2007. The selectivity of protein kinase inhibitors: a further update. Biochem J 408, 297–315. https://doi.org/10.1042/BJ20070797

Baptista, M.J., O'Farrell, C., Daya, S., Ahmad, R., Miller, D.W., Hardy, J., Farrer, M.J., Cookson, M.R., 2003. Co-ordinate transcriptional regulation of dopamine synthesis genes by α-synuclein in human neuroblastoma cell lines: Microarray analysis of α-synuclein transfected cells. Journal of Neurochemistry 85, 957–968. https://doi.org/10.1046/j.1471-4159.2003.01742.x

Barbeau, A., 1969. L-dopa therapy in Parkinson's disease: a critical review of nine years' experience. Can Med Assoc J 101, 59–68.

Barber, K., Studer, L., Fattahi, F., 2019. Derivation of enteric neuron lineages from human pluripotent stem cells. Nat Protoc 14, 1261–1279. https://doi.org/10.1038/s41596-019-0141-y

Barker, R.A., Drouin-Ouellet, J., Parmar, M., 2015. Cell-based therapies for Parkinson disease-past insights and future potential. Nature reviews. Neurology 11, 492–503. https://doi.org/10.1038/nrneurol.2015.123

Beatman, E.L., Massey, A., Shives, K.D., Burrack, K.S., Chamanian, M., Morrison, T.E., Beckham, J.D., 2016. Alpha-Synuclein Expression Restricts RNA Viral Infections in the Brain. Journal of Virology 90, 2767–2782. https://doi.org/10.1128/JVI.02949-15

Benabid, A.L., 2003. Deep brain stimulation for Parkinson's disease. Current Opinion in Neurobiology 13, 696–706. https://doi.org/10.1016/j.conb.2003.11.001

Bennett, C.N., Ross, S.E., Longo, K.A., Bajnok, L., Hemati, N., Johnson, K.W., Harrison, S.D., MacDougald, O.A., 2002. Regulation of Wnt Signaling during Adipogenesis. J. Biol. Chem. 277, 30998–31004. https://doi.org/10.1074/jbc.M204527200

Benskey, M.J., Sellnow, R.C., Sandoval, I.M., Sortwell, C.E., Lipton, J.W., Manfredsson, F.P., 2018. Silencing Alpha Synuclein in Mature Nigral Neurons Results in Rapid Neuroinflammation and Subsequent Toxicity. Front. Mol. Neurosci. 11. https://doi.org/10.3389/fnmol.2018.00036

Besnard, V., Wert, S.E., Hull, W.M., Whitsett, J.A., 2004. Immunohistochemical localization of Foxa1 and Foxa2 in mouse embryos and adult tissues. Gene Expression Patterns 5, 193–208. https://doi.org/10.1016/j.modgep.2004.08.006

Bétemps, D., Verchère, J., Brot, S., Morignat, E., Bousset, L., Gaillard, D., Lakhdar, L., Melki, R., Baron, T., 2014. Alpha-synuclein spreading in M83 mice brain revealed by detection of pathological α-synuclein by enhanced ELISA. acta neuropathol commun 2, 29. https://doi.org/10.1186/2051-5960-2-29

Birkmayer, W., Hornykiewicz, O., 1961. [The L-3,4-dioxyphenylalanine (DOPA)-effect in Parkinson-akinesia]. Wien. Klin. Wochenschr. 73, 787–788.

Björklund, A., Stenevi, U., Dunnett, S.B., Iversen, S.D., 1981. Functional reactivation of the deafferented neostriatum by nigral transplants. Nature 289, 497–499. https://doi.org/10.1038/289497a0

Blumenstock, S., Rodrigues, E.F., Peters, F., Blazquez-Llorca, L., Schmidt, F., Giese, A., Herms, J., 2017. Seeding and transgenic overexpression of alpha-synuclein triggers dendritic spine pathology in the neocortex. EMBO Molecular Medicine 9, 716–731. https://doi.org/10.15252/emmm.201607305

Bothmer, A., Phadke, T., Barrera, L.A., Margulies, C.M., Lee, C.S., Buquicchio, F., Moss, S., Abdulkerim, H.S., Selleck, W., Jayaram, H., Myer, V.E., Cotta-Ramusino, C., 2017. Characterization of the interplay between DNA repair and CRISPR/Cas9-induced DNA lesions at an endogenous locus. Nat Commun 8, 1–12. https://doi.org/10.1038/ncomms13905

Bousset, L., Pieri, L., Ruiz-Arlandis, G., Gath, J., Jensen, P.H., Habenstein, B., Madiona, K., Olieric, V., Böckmann, A., Meier, B.H., 2013. Structural and functional characterization of two alpha-synuclein strains. Nature communications 4. https://doi.org/10.1038/ncomms3575

Braak, H., Tredici, K.D., Rüb, U., de Vos, R.A.I., Jansen Steur, E.N.H., Braak, E., 2003. Staging of brain pathology related to sporadic Parkinson's disease. Neurobiology of Aging 24, 197–211. https://doi.org/10.1016/S0197-4580(02)00065-9

Brahic, M., Bousset, L., Bieri, G., Melki, R., Gitler, A.D., 2016. Axonal transport and secretion of fibrillar forms of α-synuclein, Aβ42 peptide and HTTExon 1. Acta Neuropathol 131, 539–548. https://doi.org/10.1007/s00401-016-1538-0

Breid, S., Bernis, M.E., Babila, J.T., Garza, M.C., Wille, H., Tamgüney, G., 2016. Neuroinvasion of α-Synuclein Prionoids after Intraperitoneal and Intraglossal Inoculation. Journal of Virology 90, 9182–9193. https://doi.org/10.1128/JVI.01399-16

Brundin, P., Nilsson, O.G., Strecker, R.E., Lindvall, O., Åstedt, B., Björklund, A., 1986. Behavioural effects of human fetal dopamine neurons grafted in a rat model of Parkinson's disease. Experimental Brain Research 65, 235–240. https://doi.org/10.1007/BF00243848

Bye, C.R., Jonsson, M.E., Bjorklund, A., Parish, C.L., Thompson, L.H., 2015. Transcriptome analysis reveals transmembrane targets on transplantable midbrain dopamine progenitors. Proceedings of the National Academy of Sciences of the United States of America 112, E1946-55. https://doi.org/10.1073/pnas.1501989112

Cabin, D.E., Shimazu, K., Murphy, D., Cole, N.B., Gottschalk, W., McIlwain, K.L., Orrison, B., Chen, A., Ellis, C.E., Paylor, R., Lu, B., Nussbaum, R.L., 2002. Synaptic Vesicle Depletion Correlates with Attenuated Synaptic Responses to Prolonged Repetitive Stimulation in Mice Lacking α-Synuclein. The Journal of Neuroscience 22, 8797. https://doi.org/10.1523/JNEUROSCI.22-20-08797.2002

Canham, M.A., Van Deusen, A., Brison, D.R., De Sousa, P.A., Downie, J., Devito, L., Hewitt, Z.A., Ilic, D., Kimber, S.J., Moore, H.D., Murray, H., Kunath, T., 2015. The Molecular Karyotype of 25 Clinical-Grade Human Embryonic Stem Cell Lines. Sci Rep 5, 17258. https://doi.org/10.1038/srep17258

Carbone, M., Duty, S., Rattray, M., 2012. Riluzole neuroprotection in a parkinson's disease model involves suppression of reactive astrocytosis but not GLT-1 regulation. BMC Neurosci 13, 38. https://doi.org/10.1186/1471-2202-13-38

Challis, C., Hori, A., Sampson, T.R., Yoo, B.B., Challis, R.C., Hamilton, A.M., Mazmanian, S.K., Volpicelli-Daley, L.A., Gradinaru, V., 2020. Gut-seeded α-synuclein fibrils promote gut dysfunction and brain pathology specifically in aged mice. Nat Neurosci. https://doi.org/10.1038/s41593-020-0589-7

Chambers, S.M., Fasano, C.A., Papapetrou, E.P., Tomishima, M., Sadelain, M., Studer, L., 2009. Highly efficient neural conversion of human ES and iPS cells by dual inhibition of SMAD signaling. Nature Biotechnology 27, 275–280. https://doi.org/10.1038/nbt.1529

Chen, Y., Dolt, K.S., Kriek, M., Baker, T., Downey, P., Drummond, N.J., Canham, M.A., Natalwala, A., Rosser, S., Kunath, T., 2019. Engineering synucleinopathy-resistant human dopaminergic neurons by CRISPR-mediated deletion of the *SNCA* gene. Eur J Neurosci 49, 510–524. https://doi.org/10.1111/ejn.14286

Cho, S.W., Kim, S., Kim, Y., Kweon, J., Kim, H.S., Bae, S., Kim, J.-S., 2014. Analysis of off-target effects of CRISPR/Cas-derived RNA-guided endonucleases and nickases. Genome Res 24, 132–141. https://doi.org/10.1101/gr.162339.113

Chu, Y., Kordower, J.H., 2010. Lewy body pathology in fetal grafts. Annals of the New York Academy of Sciences 1184, 55–67. https://doi.org/10.1111/j.1749-6632.2009.05229.x

Chu, Y., Muller, S., Tavares, A., Barret, O., Alagille, D., Seibyl, J., Tamagnan, G., Marek, K., Luk, K.C., Trojanowski, J.Q., Lee, V.M.Y., Kordower, J.H., 2019. Intrastriatal alpha-synuclein fibrils in monkeys: spreading, imaging and neuropathological changes. Brain 142, 3565–3579. https://doi.org/10.1093/brain/awz296

Chung, H.K., Ho, H.-A., Pérez-Acuña, D., Lee, S.-J., 2019. Modeling α-Synuclein Propagation with Preformed Fibril Injections. JMD 12, 139–151. https://doi.org/10.14802/jmd.19046

Clough, R.L., Dermentzaki, G., Haritou, M., Petsakou, A., Stefanis, L., 2011. Regulation of α-synuclein expression in cultured cortical neurons. Journal of Neurochemistry 117, 275–285. https://doi.org/10.1111/j.1471-4159.2011.07199.x

Constantinescu, R., Eriksson, B., Jansson, Y., Johnels, B., Holmberg, B., Gudmundsdottir, T., Renck, A., Berglund, P., Bergquist, F., 2017. Key clinical milestones 15 years and onwards after DBS-STN surgery—A retrospective analysis of patients that underwent surgery between 1993 and 2001. Clinical Neurology and Neurosurgery 154, 43–48. https://doi.org/10.1016/j.clineuro.2017.01.010

Cradick, T.J., Fine, E.J., Antico, C.J., Bao, G., 2013. CRISPR/Cas9 systems targeting β-globin and CCR5 genes have substantial off-target activity. Nucleic Acids Res 41, 9584–9592. https://doi.org/10.1093/nar/gkt714

Cullen, D.K., Gilroy, M., Irons, H.R., LaPlaca, M.C., 2010. Synapse-to-neuron ratio is inversely related to neuronal density in mature neuronal cultures. Brain Res 1359, 44–55. https://doi.org/10.1016/j.brainres.2010.08.058

Cyranoski, D., 2018. 'Reprogrammed' stem cells implanted into patient with Parkinson's disease. Nature. https://doi.org/10.1038/d41586-018-07407-9

Damier, P., Hirsch, E.C., Zhang, P., Agid, Y., Javoy-Agid, F., 1993. Glutathione peroxidase, glial cells and Parkinson's disease. Neuroscience 52, 1–6. https://doi.org/10.1016/0306-4522(93)90175-F

Dauer, W., Kholodilov, N., Vila, M., Trillat, A.-C., Goodchild, R., Larsen, K.E., Staal, R., Tieu, K., Schmitz, Y., Yuan, C.A., Rocha, M., Jackson-Lewis, V., Hersch, S., Sulzer, D., Przedborski, S., Burke, R., Hen, R., 2002. Resistance of -synuclein null mice to the parkinsonian neurotoxin MPTP. Proceedings of the National Academy of Sciences 99, 14524–14529. https://doi.org/10.1073/pnas.172514599

Dauer, W., Przedborski, S., 2003. Parkinson's Disease: Mechanisms and Models. Neuron 39, 889–909. https://doi.org/10.1016/S0896-6273(03)00568-3

De Sousa, P.A., Tye, B.J., Bruce, K., Dand, P., Russell, G., Collins, D.M., Greenshields, A., McDonald, K., Bradburn, H., Canham, M.A., Kunath, T., Downie, J.M., Bateman, M., Courtney, A., 2016. Derivation of the clinical grade human embryonic stem cell line RCe013-A (RC-9). Stem Cell Research 17, 36–41. https://doi.org/10.1016/j.scr.2016.04.020

Del Tredici, K., Braak, H., 2016. Review: Sporadic Parkinson's disease: development and distribution of α-synuclein pathology. Neuropathol Appl Neurobiol 42, 33–50. https://doi.org/10.1111/nan.12298

Desplats, P., Lee, H.-J., Bae, E.-J., Patrick, C., Rockenstein, E., Crews, L., Spencer, B., Masliah, E., Lee, S.-J., 2009. Inclusion formation and neuronal cell death through neuron-to-neuron transmission of α-synuclein. Proceedings of the National Academy of Sciences 106, 13010–13015. https://doi.org/10.1073/pnas.0903691106

Devi, L., Raghavendran, V., Prabhu, B.M., Avadhani, N.G., Anandatheerthavarada, H.K., 2008. Mitochondrial Import and Accumulation of α-Synuclein Impair Complex I in Human Dopaminergic Neuronal Cultures and Parkinson Disease Brain. J. Biol. Chem. 283, 9089–9100. https://doi.org/10.1074/jbc.M710012200

Doi, D., Samata, B., Katsukawa, M., Kikuchi, T., Morizane, A., Ono, Y., Sekiguchi, K., Nakagawa, M., Parmar, M., Takahashi, J., 2014. Isolation of human induced pluripotent stem cell-derived dopaminergic progenitors by cell sorting for successful transplantation. Stem cell reports 2, 337–50. https://doi.org/10.1016/j.stemcr.2014.01.013

Domert, J., Sackmann, C., Severinsson, E., Agholme, L., Bergström, J., Ingelsson, M., Hallbeck, M., 2016. Aggregated Alpha-Synuclein Transfer Efficiently between Cultured Human Neuron-Like Cells and Localize to Lysosomes. PLoS ONE 11, e0168700. https://doi.org/10.1371/journal.pone.0168700

Dorsey, E.R., Elbaz, A., Nichols, E., Abd-Allah, F., Abdelalim, A., Adsuar, J.C., Ansha, M.G., Brayne, C., Choi, J.-Y.J., Collado-Mateo, D., Dahodwala, N., Do, H.P., Edessa, D., Endres, M., Fereshtehnejad, S.-M., Foreman, K.J., Gankpe, F.G., Gupta, R., Hankey, G.J., Hay, S.I., Hegazy, M.I., Hibstu, D.T., Kasaeian, A., Khader, Y., Khalil, I., Khang, Y.-H., Kim, Y.J., Kokubo, Y., Logroscino, G., Massano, J., Mohamed Ibrahim, N., Mohammed, M.A., Mohammadi, A., Moradi-Lakeh, M., Naghavi, M., Nguyen, B.T., Nirayo, Y.L., Ogbo, F.A., Owolabi, M.O., Pereira, D.M., Postma, M.J., Qorbani, M., Rahman, M.A., Roba, K.T., Safari, H., Safiri, S., Satpathy, M., Sawhney, M., Shafieesabet, A., Shiferaw, M.S., Smith, M., Szoeke, C.E.I., Tabarés-Seisdedos, R., Truong, N.T., Ukwaja, K.N., Venketasubramanian, N., Villafaina, S., weldegwergs, K. gidey, Westerman, R., Wijeratne, T., Winkler, A.S., Xuan, B.T., Yonemoto, N., Feigin, V.L., Vos, T., Murray, C.J.L., 2018. Global, regional, and national burden of Parkinson's disease, 1990–2016: a systematic analysis for the Global Burden of Disease Study 2016. The Lancet Neurology 17, 939–953. https://doi.org/10.1016/S1474-4422(18)30295-3

Drummond, N.J., Dolt, K.S., Canham, M.A., Kilbride, P., Morris, G.J., Kunath, T., 2020. Cryopreservation of midbrain dopaminergic neural cells differentiated from human embryonic stem cells (preprint). Cell Biology. https://doi.org/10.1101/2020.02.11.944272

Dryanovski, D.I., Guzman, J.N., Xie, Z., Galteri, D.J., Volpicelli-Daley, L.A., Lee, V.M.-Y., Miller, R.J., Schumacker, P.T., Surmeier, D.J., 2013. Calcium Entry and -Synuclein Inclusions Elevate Dendritic Mitochondrial Oxidant Stress in Dopaminergic Neurons. Journal of Neuroscience 33, 10154–10164. https://doi.org/10.1523/JNEUROSCI.5311-12.2013

Du, H.-N., Tang, L., Luo, X.-Y., Li, H.-T., Hu, J., Zhou, J.-W., Hu, H.-Y., 2003. A peptide motif consisting of glycine, alanine, and valine is required for the fibrillization and cytotoxicity of human α-synuclein. Biochemistry 42, 8870–8878. https://doi.org/10.1021/bi034028

Duffy, M.F., Collier, T.J., Patterson, J.R., Kemp, C.J., Luk, K.C., Tansey, M.G., Paumier, K.L., Kanaan, N.M., Fischer, D.L., Polinski, N.K., Barth, O.L., Howe, J.W., Vaikath, N.N., Majbour, N.K., El-Agnaf, O.M.A., Sortwell, C.E., 2018. Lewy body-like alpha-synuclein inclusions trigger reactive microgliosis prior to nigral degeneration. Journal of Neuroinflammation 15, 129. https://doi.org/10.1186/s12974-018-1171-z

El-Agnaf, O.M.A., Jakes, R., Curran, M.D., Middleton, D., Ingenito, R., Bianchi, E., Pessi, A., Neill, D., Wallace, A., 1998. Aggregates from mutant and wild-type α-synuclein proteins and NAC peptide induce apoptotic cell death in human neuroblastoma cells by formation of β-sheet and amyloid-like filaments. FEBS Letters 440, 71–75. https://doi.org/10.1016/S0014-5793(98)01418-5

Farrer, M., Kachergus, J., Forno, L., Lincoln, S., Wang, D.-S., Hulihan, M., Maraganore, D., Gwinn-Hardy, K., Wszolek, Z., Dickson, D., Langston, J.W., 2004. Comparison of kindreds with parkinsonism and α-synuclein genomic multiplications. Annals of neurology 55, 174–179. https://doi.org/10.1002/ana.10846

Fasano, C.A., Chambers, S.M., Lee, G., Tomishima, M.J., Studer, L., 2010. Efficient derivation of functional floor plate tissue from human embryonic stem cells. Cell stem cell 6, 336–47. https://doi.org/10.1016/j.stem.2010.03.001

Fiske, M., Valtierra, S., Solvang, K., Zorniak, M., White, M., Herrera, S., Konnikova, A., Brezinsky, R., DebBurman, S., 2011. Contribution of alanine-76 and serine phosphorylation in α-synuclein membrane association and aggregation in yeasts. Parkinson's Disease 2011. https://doi.org/10.4061/2011/392180

Flavin, W.P., Bousset, L., Green, Z.C., Chu, Y., Skarpathiotis, S., Chaney, M.J., Kordower, J.H., Melki, R., Campbell, E.M., 2017. Endocytic vesicle rupture is a conserved mechanism of cellular invasion by amyloid proteins. Acta Neuropathol 134, 629–653. https://doi.org/10.1007/s00401-017-1722-x

Freed, C.R., Breeze, R.E., Rosenberg, N.L., Schneck, S.A., Kriek, E., Qi, J., Lone, T., Zhang, Y., Snyder, J.A., Wells, T.H., Ramig, L.O., Thompson, L., Mazziotta, J.C., Huang, S.C., Grafton, S.T., Brooks, D., Sawle, G., Schroter, G., Ansari, A.A., 1992. Survival of Implanted Fetal Dopamine Cells and Neurologic Improvement 12 to 46 Months after Transplantation for Parkinson's Disease. N Engl J Med 327, 1549–1555. https://doi.org/10.1056/NEJM199211263272202

Freed, C.R., Greene, P.E., Breeze, R.E., Tsai, W.Y., DuMouchel, W., Kao, R., Dillon, S., Winfield, H., Culver, S., Trojanowski, J.Q., Eidelberg, D., Fahn, S., 2001. Transplantation of embryonic dopamine neurons for severe Parkinson's disease. New England Journal of Medicine 344, 710–719. https://doi.org/10.1056/nejm200103083441002

Freeman, D., Cedillos, R., Choyke, S., Lukic, Z., McGuire, K., Marvin, S., Burrage, A.M., Sudholt, S., Rana, A., O'Connor, C., Wiethoff, C.M., Campbell, E.M., 2013. Alpha-Synuclein Induces Lysosomal Rupture and Cathepsin Dependent Reactive Oxygen Species Following Endocytosis. PLoS ONE 8, e62143. https://doi.org/10.1371/journal.pone.0062143

Freeman, T.B., Olanow, C.W., Hauser, R.A., Nauert, G.M., Smith, D.A., Borlongan, C.V., Sanberg, P.R., Holt, D.A., Kordower, J.H., Vingerhoets, F.J.G., Snow, B.J., Calne, D., Gauger, L.L., 1995. Bilateral fetal nigral transplantation into the postcommissural putamen in Parkinson's disease. Ann Neurol. 38, 379–388. https://doi.org/10.1002/ana.410380307

Freundt, E.C., Maynard, N., Clancy, E.K., Roy, S., Bousset, L., Sourigues, Y., Covert, M., Melki, R., Kirkegaard, K., Brahic, M., 2012. Neuron-to-neuron transmission of α-synuclein fibrils through axonal transport. Annals of neurology 72, 517–524. https://doi.org/10.1002/ana.23747

Fu, Y., Foden, J.A., Khayter, C., Maeder, M.L., Reyon, D., Joung, J.K., Sander, J.D., 2013. High-frequency off-target mutagenesis induced by CRISPR-Cas nucleases in human cells. Nat Biotechnol 31, 822–826. https://doi.org/10.1038/nbt.2623

Fu, Y., Sander, J.D., Reyon, D., Cascio, V.M., Joung, J.K., 2014. Improving CRISPR-Cas nuclease specificity using truncated guide RNAs. Nat Biotechnol 32, 279–284. https://doi.org/10.1038/nbt.2808

Fujiwara, H., Hasegawa, M., Dohmae, N., Kawashima, A., Masliah, E., Goldberg, M.S., Shen, J., Takio, K., Iwatsubo, T., 2002. [alpha]-Synuclein is phosphorylated in synucleinopathy lesions. Nat Cell Biol 4, 160–164. https://doi.org/10.1038/ncb748

Galvin, J.E., Schuck, T.M., Lee, V.M.Y., Trojanowski, J.Q., 2001. Differential Expression and Distribution of α-, β-, and γ-Synuclein in the Developing Human Substantia Nigra. Experimental Neurology 168, 347–355. https://doi.org/10.1006/exnr.2000.7615

Gaspard, N., Vanderhaeghen, P., 2010. Mechanisms of neural specification from embryonic stem cells. Current Opinion in Neurobiology 20, 37–43. https://doi.org/10.1016/j.conb.2009.12.001

George, S., Rey, N.L., Tyson, T., Esquibel, C., Meyerdirk, L., Schulz, E., Pierce, S., Burmeister, A.R., Madaj, Z., Steiner, J.A., Escobar Galvis, M.L., Brundin, L., Brundin, P., 2019. Microglia affect α-synuclein cell-to-cell transfer in a mouse model of Parkinson's disease. Mol Neurodegeneration 14, 34. https://doi.org/10.1186/s13024-019-0335-3

Gerhard, A., Pavese, N., Hotton, G., Turkheimer, F., Es, M., Hammers, A., Eggert, K., Oertel, W., Banati, R.B., Brooks, D.J., 2006. In vivo imaging of microglial activation with [11C](R)-PK11195 PET in idiopathic Parkinson's disease. Neurobiology of Disease 21, 404–412. https://doi.org/10.1016/j.nbd.2005.08.002

Giasson, B.I., Duda, J.E., Quinn, S.M., Zhang, B., Trojanowski, J.Q., Lee, V.M.-Y., 2002. Neuronal α-Synucleinopathy with Severe Movement Disorder in Mice Expressing A53T Human α-Synuclein. Neuron 34, 521–533. https://doi.org/10.1016/S0896-6273(02)00682-7

Giasson, B.I., Murray, I.V., Trojanowski, J.Q., Lee, V.M.-Y., 2001. A hydrophobic stretch of 12 amino acid residues in the middle of α-synuclein is essential for filament assembly. Journal of Biological Chemistry 276, 2380–2386. https://doi.org/10.1074/jbc.M008919200

Gorbatyuk, O.S., Li, S., Nash, K., Gorbatyuk, M., Lewin, A.S., Sullivan, L.F., Mandel, R.J., Chen, W., Meyers, C., Manfredsson, F.P., Muzyczka, N., 2010. In Vivo RNAi-Mediated α-Synuclein Silencing Induces Nigrostriatal Degeneration. Molecular Therapy 18, 1450–1457. https://doi.org/10.1038/mt.2010.115

Grassi, D., Howard, S., Zhou, M., Diaz-Perez, N., Urban, N.T., Guerrero-Given, D., Kamasawa, N., Volpicelli-Daley, L.A., LoGrasso, P., Lasmézas, C.I., 2018. Identification of a highly neurotoxic α-synuclein species inducing mitochondrial damage and mitophagy in Parkinson's disease. Proc Natl Acad Sci USA 115, E2634–E2643. https://doi.org/10.1073/pnas.1713849115

Grealish, S., Diguet, E., Kirkeby, A., Mattsson, B., Heuer, A., Bramoulle, Y., Van Camp, N., Perrier, A.L., Hantraye, P., Bjorklund, A., Parmar, M., 2014. Human ESC-derived dopamine neurons show similar preclinical efficacy and potency to fetal neurons when grafted in a rat model of Parkinson's disease. Cell stem cell 15, 653–65. https://doi.org/10.1016/j.stem.2014.09.017

Gribaudo, S., Tixador, P., Bousset, L., Fenyi, A., Lino, P., Melki, R., Peyrin, J.-M., Perrier, A.L., 2019. Propagation of α-Synuclein Strains within Human Reconstructed Neuronal Network. Stem Cell Reports. https://doi.org/10.1016/j.stemcr.2018.12.007

Hackland, J., 2019. Top-Down Inhibition (TDi) and Baseline Activation (BLa): Controlling Signal Transduction When Endogenous Cytokines are Ruining Your Differentiation. Current Protocols in Stem Cell Biology 51. https://doi.org/10.1002/cpsc.98

Hackland, J.O.S., Frith, T.J.R., Thompson, O., Marin Navarro, A., Garcia-Castro, M.I., Unger, C., Andrews, P.W., 2017. Top-Down Inhibition of BMP Signaling Enables Robust Induction of hPSCs Into Neural Crest in Fully Defined, Xeno-free Conditions. Stem Cell Reports 9, 1043–1052. https://doi.org/10.1016/j.stemcr.2017.08.008

Hansen, C., Angot, E., Bergström, A.-L., Steiner, J.A., Pieri, L., Paul, G., Outeiro, T.F., Melki, R., Kallunki, P., Fog, K., 2011. α-Synuclein propagates from mouse brain to grafted dopaminergic neurons and seeds aggregation in cultured human cells. The Journal of Clinical Investigation 121, 715–725. https://doi.org/10.1172/JCI43366

Henderson, M.X., Covell, D.J., Chung, C.H.-Y., Pitkin, R.M., Sandler, R.M., Decker, S.C., Riddle, D.M., Zhang, B., Gathagan, R.J., James, M.J., Trojanowski, J.Q., Brunden, K.R., Lee, V.M.Y., Luk, K.C., 2020. Characterization of novel conformation-selective α-synuclein antibodies as potential immunotherapeutic agents for Parkinson's disease. Neurobiology of Disease 136, 104712. https://doi.org/10.1016/j.nbd.2019.104712

Holmes, B.B., DeVos, S.L., Kfoury, N., Li, M., Jacks, R., Yanamandra, K., Ouidja, M.O., Brodsky, F.M., Marasa, J., Bagchi, D.P., Kotzbauer, P.T., Miller, T.M., Papy-Garcia, D., Diamond, M.I., 2013. Heparan sulfate proteoglycans mediate internalization and propagation of specific proteopathic seeds. Proc. Natl. Acad. Sci. U.S.A. 110, E3138-3147. https://doi.org/10.1073/pnas.1301440110

Holmqvist, S., Chutna, O., Bousset, L., Aldrin-Kirk, P., Li, W., Björklund, T., Wang, Z.-Y., Roybon, L., Melki, R., Li, J.-Y., 2014. Direct evidence of Parkinson pathology spread from the gastrointestinal tract to the brain in rats. Acta neuropathologica 128, 805–820. https://doi.org/10.1007/s00401-014-1343-6

Hsu, P.D., Scott, D.A., Weinstein, J.A., Ran, F.A., Konermann, S., Agarwala, V., Li, Y., Fine, E.J., Wu, X., Shalem, O., Cradick, T.J., Marraffini, L.A., Bao, G., Zhang, F., 2013. DNA targeting specificity of RNA-guided Cas9 nucleases. Nat Biotechnol 31, 827–832. https://doi.org/10.1038/nbt.2647

Jang, H., Boltz, D., Sturm-Ramirez, K., Shepherd, K.R., Jiao, Y., Webster, R., Smeyne, R.J., 2009. Highly pathogenic H5N1 influenza virus can enter the central nervous system and induce neuroinflammation and neurodegeneration. Proceedings of the National Academy of Sciences 106, 14063–14068. https://doi.org/10.1073/pnas.0900096106

Jang, Haeman, Boltz, D.A., Webster, R.G., Smeyne, R.J., 2009. Viral parkinsonism. Biochimica et Biophysica Acta (BBA) - Molecular Basis of Disease 1792, 714–721. https://doi.org/10.1016/j.bbadis.2008.08.001

Jankovic, J., 2008. Parkinson's disease: clinical features and diagnosis. Journal of Neurology, Neurosurgery & Psychiatry 79, 368–376. https://doi.org/10.1136/jnnp.2007.131045

Jiang, P., Gan, M., Yen, S.-H., McLean, P.J., Dickson, D.W., 2017. Impaired endo-lysosomal membrane integrity accelerates the seeding progression of α-synuclein aggregates. Sci Rep 7, 7690. https://doi.org/10.1038/s41598-017-08149-w

Jinek, M., Chylinski, K., Fonfara, I., Hauer, M., Doudna, J.A., Charpentier, E., 2012. A programmable dual RNA-guided DNA endonuclease in adaptive bacterial immunity. Science 337, 816–821. https://doi.org/10.1126/science.1225829

Karampetsou, M., Ardah, M.T., Semitekolou, M., Polissidis, A., Samiotaki, M., Kalomoiri, M., Majbour, N., Xanthou, G., El-Agnaf, O.M.A., Vekrellis, K., 2017. Phosphorylated exogenous alpha-synuclein fibrils exacerbate pathology and induce neuronal dysfunction in mice. Scientific reports 7, 16533. https://doi.org/10.1038/s41598-017-15813-8

Karpowicz, R.J., Haney, C.M., Mihaila, T.S., Sandler, R.M., Petersson, E.J., Lee, V.M.-Y., 2017. Selective imaging of internalized proteopathic α-synuclein seeds in primary neurons reveals mechanistic insight into transmission of synucleinopathies. Journal of Biological Chemistry jbc. M117. 780296. https://doi.org/10.1074/jbc.M117.780296

Kaylor, J., Bodner, N., Edridge, S., Yamin, G., Hong, D.-P., Fink, A.L., 2005. Characterization of Oligomeric Intermediates in α-Synuclein Fibrillation: FRET Studies of Y125W/Y133F/Y136F α-Synuclein. Journal of Molecular Biology 353, 357–372. https://doi.org/10.1016/j.jmb.2005.08.046

Kee, N., Volakakis, N., Kirkeby, A., Dahl, L., Storvall, H., Nolbrant, S., Lahti, L., Björklund, Å.K., Gillberg, L., Joodmardi, E., Sandberg, R., Parmar, M., Perlmann, T., 2017. Single-Cell Analysis Reveals a Close Relationship between Differentiating Dopamine and Subthalamic Nucleus Neuronal Lineages. Cell Stem Cell 20, 29–40. https://doi.org/10.1016/j.stem.2016.10.003

Kefalopoulou, Z., Politis, M., Piccini, P., Mencacci, N., Bhatia, K., Jahanshahi, M., Widner, H., Rehncrona, S., Brundin, P., Björklund, A., 2014. Long-term clinical outcome of fetal cell transplantation for Parkinson disease: two case reports. JAMA neurology 71, 83–87. https://doi.org/10.1001/jamaneurol.2013.4749

Kerr, C.W., Lee, L.J., Romero, A.A., Stull, N.D., Iacovitti, L., 1994. Purification of dopamine neurons by flow cytometry. Brain Research 665, 300–306. https://doi.org/10.1016/0006-8993(94)91351-X

Khandelwal, P.J., Dumanis, S.B., Feng, L.R., Maguire-Zeiss, K., Rebeck, G.W., Lashuel, H.A., Moussa, C.E., 2010. Parkinson-related parkin reduces α-Synuclein phosphorylation in a gene transfer model. Molecular Neurodegeneration 5, 47. https://doi.org/10.1186/1750-1326-5-47

Kikuchi, T., Morizane, A., Doi, D., Magotani, H., Onoe, H., Hayashi, T., Mizuma, H., Takara, S., Takahashi, R., Inoue, H., Morita, S., Yamamoto, M., Okita, K., Nakagawa, M., Parmar, M., Takahashi, J., 2017. Human iPS cell-derived dopaminergic neurons function in a primate Parkinson's disease model. Nature 548, 592–596. https://doi.org/10.1038/nature23664

Kim, S., Kim, D., Cho, S.W., Kim, J., Kim, J.-S., 2014. Highly efficient RNA-guided genome editing in human cells via delivery of purified Cas9 ribonucleoproteins. Genome Res 24, 1012–1019. https://doi.org/10.1101/gr.171322.113

Kim, S., Kwon, S.-H., Kam, T.-I., Panicker, N., Karuppagounder, S.S., Lee, S., Lee, J.H., Kim, W.R., Kook, M., Foss, C.A., Shen, C., Lee, H., Kulkarni, S., Pasricha, P.J., Lee, G., Pomper, M.G., Dawson, V.L., Dawson, T.M., Ko, H.S., 2019. Transneuronal Propagation of Pathologic α-Synuclein from the Gut to the Brain Models Parkinson's Disease. Neuron 103, 627-641.e7. https://doi.org/10.1016/j.neuron.2019.05.035

Kirkeby, A., Grealish, S., Wolf, D.A., Nelander, J., Wood, J., Lundblad, M., Lindvall, O., Parmar, M., 2012. Generation of regionally specified neural progenitors and functional neurons from human embryonic stem cells under defined conditions. Cell reports 1, 703–14. https://doi.org/10.1016/j.celrep.2012.04.009

Kirkeby, A., Nelander, J., Parmar, M., 2013. Generating regionalized neuronal cells from pluripotency, a step-by-step protocol. Front. Cell. Neurosci. 6. https://doi.org/10.3389/fncel.2012.00064

Kirkeby, A., Nolbrant, S., Tiklova, K., Heuer, A., Kee, N., Cardoso, T., Ottosson, D.R., Lelos, M.J., Rifes, P., Dunnett, S.B., Grealish, S., Perlmann, T., Parmar, M., 2017a. Predictive Markers Guide Differentiation to Improve Graft Outcome in Clinical Translation of hESC-Based Therapy for Parkinson's Disease. Cell stem cell. https://doi.org/10.1016/j.stem.2016.09.004

Kirkeby, A., Parmar, M., Barker, R.A., 2017b. Chapter 7 - Strategies for bringing stem cell-derived dopamine neurons to the clinic: A European approach (STEM-PD), in: Dunnett, S.B., Björklund, A. (Eds.), Progress in Brain Research, Functional Neural Transplantation IV. Elsevier, pp. 165–190. https://doi.org/10.1016/bs.pbr.2016.11.011

Kleinstiver, B.P., Pattanayak, V., Prew, M.S., Tsai, S.Q., Nguyen, N.T., Zheng, Z., Joung, J.K., 2016. High-fidelity CRISPR–Cas9 nucleases with no detectable genome-wide off-target effects. Nature 529, 490–495. https://doi.org/10.1038/nature16526

Kordower, J.H., Chu, Y., Hauser, R.A., Freeman, T.B., Olanow, C.W., 2008. Lewy body–like pathology in long-term embryonic nigral transplants in Parkinson's disease. Nature medicine 14, 504–506. https://doi.org/10.1038/nm1747

Kordower, J.H., Dodiya, H.B., Kordower, A.M., Terpstra, B., Paumier, K., Madhavan, L., Sortwell, C., Steece-Collier, K., Collier, T.J., 2011. Transfer of host-derived alpha synuclein to grafted dopaminergic neurons in rat. Neurobiology of disease 43, 552–557. https://doi.org/10.1016/j.nbd.2011.05.001

Kordower, J.H., Freeman, T.B., Snow, B.J., Vingerhoets, F.J., Mufson, E.J., Sanberg, P.R., Hauser, R.A., Smith, D.A., Nauert, G.M., Perl, D.P., 1995. Neuropathological evidence of graft survival and striatal reinnervation after the transplantation of fetal mesencephalic tissue in a patient with Parkinson's disease. N. Engl. J. Med. 332, 1118–1124. https://doi.org/10.1056/NEJM199504273321702

Kordower, J.H., Goetz, C.G., Chu, Y., Halliday, G.M., Nicholson, D.A., Musial, T.F., Marmion, D.J., Stoessl, A.J., Sossi, V., Freeman, T.B., Olanow, C.W., 2017. Robust graft survival and normalized dopaminergic innervation do not obligate recovery in a Parkinson disease patient. Annals of neurology 81, 46–57. https://doi.org/10.1002/ana.24820

Kouroupi, G., Taoufik, E., Vlachos, I.S., Tsioras, K., Antoniou, N., Papastefanaki, F., Chroni-Tzartou, D., Wrasidlo, W., Bohl, D., Stellas, D., Politis, P.K., Vekrellis, K., Papadimitriou, D., Stefanis, L., Bregestovski, P., Hatzigeorgiou, A.G., Masliah, E., Matsas, R., 2017. Defective synaptic connectivity and axonal neuropathology in a human iPSC-based model of familial Parkinson's disease. Proceedings of the National Academy of Sciences. https://doi.org/10.1073/pnas.1617259114

Kramer, M.L., Schulz-Schaeffer, W.J., 2007. Presynaptic α-Synuclein Aggregates, Not Lewy Bodies, Cause Neurodegeneration in Dementia with Lewy Bodies. J Neurosci 27, 1405–1410. https://doi.org/10.1523/JNEUROSCI.4564-06.2007

Kriks, S., Shim, J.W., Piao, J., Ganat, Y.M., Wakeman, D.R., Xie, Z., Carrillo-Reid, L., Auyeung, G., Antonacci, C., Buch, A., Yang, L., Beal, M.F., Surmeier, D.J., Kordower, J.H., Tabar, V., Studer, L., 2011. Dopamine neurons derived from human ES cells efficiently engraft in animal models of Parkinson's disease. Nature 480, 547–51. https://doi.org/10.1038/nature10648

Kulikov, V., Guo, S.-M., Stone, M., Goodman, A., Carpenter, A., Bathe, M., Lempitsky, V., 2019. DoGNet: A deep architecture for synapse detection in multiplexed fluorescence images. PLoS Comput Biol 15, e1007012. https://doi.org/10.1371/journal.pcbi.1007012

Kurowska, Z., Englund, E., Widner, H., Lindvall, O., Li, J.-Y., Brundin, P., 2011. Signs of degeneration in 12–22-year old grafts of mesencephalic dopamine neurons in patients with Parkinson's disease. Journal of Parkinson's disease 1, 83–92. https://doi.org/10.3233/JPD-2011-11004

Kurtis, M.M., Rajah, T., Delgado, L.F., Dafsari, H.S., 2017. The effect of deep brain stimulation on the non-motor symptoms of Parkinson's disease: a critical review of the current evidence. npj Parkinson's Disease 3, 16024. https://doi.org/10.1038/npjparkd.2016.24

Kuusisto, E., Parkkinen, L., Alafuzoff, I., 2003. Morphogenesis of Lewy Bodies: Dissimilar Incorporation of α-Synuclein, Ubiquitin, and p62. J Neuropathol Exp Neurol 62, 1241–1253. https://doi.org/10.1093/jnen/62.12.1241

Lahti, L., Peltopuro, P., Piepponen, T.P., Partanen, J., 2012. Cell-autonomous FGF signaling regulates anteroposterior patterning and neuronal differentiation in the mesodiencephalic dopaminergic progenitor domain. Development 139, 894–905. https://doi.org/10.1242/dev.071936

Lázaro, D.F., Rodrigues, E.F., Langohr, R., Shahpasandzadeh, H., Ribeiro, T., Guerreiro, P., Gerhardt, E., Kröhnert, K., Klucken, J., Pereira, M.D., 2014. Systematic comparison of the effects of alpha-synuclein mutations on its oligomerization and aggregation. PLoS Genet 10, e1004741. https://doi.org/10.1371/journal.pgen.1004741

Lee, H.-J., Suk, J.-E., Bae, E.-J., Lee, J.-H., Paik, S.R., Lee, S.-J., 2008a. Assembly-dependent endocytosis and clearance of extracellular a-synuclein. The International Journal of Biochemistry & Cell Biology 40, 1835–1849. https://doi.org/10.1016/j.biocel.2008.01.017

Lee, H.-J., Suk, J.-E., Bae, E.-J., Lee, S.-J., 2008b. Clearance and deposition of extracellular α-synuclein aggregates in microglia. Biochemical and Biophysical Research Communications 372, 423–428. https://doi.org/10.1016/j.bbrc.2008.05.045

Lee, H.-J., Suk, J.-E., Patrick, C., Bae, E.-J., Cho, J.-H., Rho, S., Hwang, D., Masliah, E., Lee, S.-J., 2010. Direct Transfer of α-Synuclein from Neuron to Astroglia Causes Inflammatory Responses in Synucleinopathies. J. Biol. Chem. 285, 9262–9272. https://doi.org/10.1074/jbc.M109.081125

Lee, J.-H., Lee, I.-H., Choe, Y.-J., Kang, S., Kim, H.Y., Gai, W.-P., Hahn, J.-S., Paik, S.R., 2009. Real-time analysis of amyloid fibril formation of α-synuclein using a fibrillation-state-specific fluorescent probe of JC-1. Biochemical Journal 418, 311–323. https://doi.org/10.1042/BJ20081572

Lehnen, D., Barral, S., Cardoso, T., Grealish, S., Heuer, A., Smiyakin, A., Kirkeby, A., Kollet, J., Cremer, H., Parmar, M., Bosio, A., Knöbel, S., 2017. IAP-Based Cell Sorting Results in Homogeneous Transplantable Dopaminergic Precursor Cells Derived from Human Pluripotent Stem Cells. Stem Cell Reports 9, 1207–1220. https://doi.org/10.1016/j.stemcr.2017.08.016

Lewy, F.H., 1912. Paralysis agitans. I. Hundbuch der Neurologie III. 920–933.

Li, J.-Y., Englund, E., Holton, J.L., Soulet, D., Hagell, P., Lees, A.J., Lashley, T., Quinn, N.P., Rehncrona, S., Björklund, A., 2008. Lewy bodies in grafted neurons in subjects with Parkinson's disease suggest host-to-graft disease propagation. Nature medicine 14, 501–503. https://doi.org/10.1038/nm1746

Li, J.-Y., Englund, E., Widner, H., Rehncrona, S., Björklund, A., Lindvall, O., Brundin, P., 2010. Characterization of Lewy body pathology in 12-and 16-year-old intrastriatal mesencephalic grafts surviving in a patient with Parkinson's disease. Movement Disorders 25, 1091–1096. https://doi.org/10.1002/mds.23012

Li, J.Y.H., Joyner, A.L., 2001. Otx2 and Gbx2 are required for refinement and not induction of mid-hindbrain gene expression. Development 128, 4979.

Li, W., Englund, E., Widner, H., Mattsson, B., van Westen, D., Lätt, J., Rehncrona, S., Brundin, P., Björklund, A., Lindvall, O., 2016. Extensive graft-derived dopaminergic innervation is maintained 24 years after transplantation in the degenerating parkinsonian brain. Proceedings of the National Academy of Sciences 201605245. https://doi.org/10.1073/pnas.1605245113

Liang, X., Potter, J., Kumar, S., Zou, Y., Quintanilla, R., Sridharan, M., Carte, J., Chen, W., Roark, N., Ranganathan, S., Ravinder, N., Chesnut, J.D., 2015. Rapid and highly efficient mammalian cell engineering via Cas9 protein transfection. Journal of Biotechnology 208, 44–53. https://doi.org/10.1016/j.jbiotec.2015.04.024

Lindvall, O., Brundin, P., Widner, H., Rehncrona, S., Gustavii, B., Frackowiak, R., Leenders, K.L., Sawle, G., Rothwell, J.C., Marsden, C.D., Bjorklund, A., 1990. GRAFTS OF FETAL DOPAMINE NEURONS SURVIVE AND IMPROVE MOTOR FUNCTION IN PARKINSONS-DISEASE. Science 247, 574–577. https://doi.org/10.1126/science.2105529

Lindvall, O., Rehncrona, S., Brundin, P., Gustavii, B., Astedt, B., Widner, H., Lindholm, T., Bjorklund, A., Leenders, K.L., Rothwell, J.C., Frackowiak, R., Marsden, C.D., Johnels, B., Steg, G., Freedman, R., Hoffer, B.J., Seiger, A., Bygdeman, M., Stromberg, I., Olson, L., 1989. HUMAN-FETAL DOPAMINE NEURONS GRAFTED INTO THE STRIATUM IN 2 PATIENTS WITH SEVERE PARKINSONS-DISEASE - A DETAILED ACCOUNT OF METHODOLOGY AND A 6-MONTH FOLLOW-UP. Archives of Neurology 46, 615–631. https://doi.org/10.1001/archneur.1989.00520420033021

Lindvall, O., Sawle, G., Widner, H., Rothwell, J.C., Bjorklund, A., Brooks, D., Brundin, P., Frackowiak, R., Marsden, C.D., Odin, P., Rehncrona, S., 1994. EVIDENCE FOR LONG-TERM SURVIVAL AND FUNCTION OF DOPAMINERGIC GRAFTS IN PROGRESSIVE PARKINSONS-DISEASE. Annals of neurology 35, 172–180. https://doi.org/10.1002/ana.410350208

Lopes, C., Delezoide, A.-L., Delabar, J.-M., Rachidi, M., 2006. BARHL1 homeogene, the human ortholog of the mouse Barhl1 involved in cerebellum development, shows regional and cellular specificities in restricted domains of developing human central nervous system. Biochemical and Biophysical Research Communications 339, 296–304. https://doi.org/10.1016/j.bbrc.2005.11.021

Loria, F., Vargas, J.Y., Bousset, L., Syan, S., Salles, A., Melki, R., Zurzolo, C., 2017. α-Synuclein transfer between neurons and astrocytes indicates that astrocytes play a role in degradation rather than in spreading. Acta neuropathologica. https://doi.org/10.1007/s00401-017-1746-2

Ludtmann, M.H.R., Angelova, P.R., Horrocks, M.H., Choi, M.L., Rodrigues, M., Baev, A.Y., Berezhnov, A.V., Yao, Z., Little, D., Banushi, B., Al-Menhali, A.S., Ranasinghe, R.T., Whiten, D.R., Yapom, R., Dolt, K.S., Devine, M.J., Gissen, P., Kunath, T., Jaganjac, M., Pavlov, E.V., Klenerman, D., Abramov, A.Y., Gandhi, S., 2018. α-synuclein oligomers interact with ATP synthase and open the permeability transition pore in Parkinson's disease. Nature Communications 9, 2293. https://doi.org/10.1038/s41467-018-04422-2

Luk, K.C., Covell, D.J., Kehm, V.M., Zhang, B., Song, I.Y., Byrne, M.D., Pitkin, R.M., Decker, S.C., Trojanowski, J.Q., Lee, V.M.-Y., 2016. Molecular and Biological Compatibility with Host Alpha-Synuclein Influences Fibril Pathogenicity. Cell reports 16, 3373–3387. https://doi.org/10.1016/j.celrep.2016.08.053

Luk, K.C., Kehm, V., Carroll, J., Zhang, B., O'Brien, P., Trojanowski, J.Q., Lee, V.M.-Y., 2012a. Pathological α-Synuclein Transmission Initiates Parkinson-like Neurodegeneration in Nontransgenic Mice. Science 338, 949–953. https://doi.org/10.1126/science.1227157

Luk, K.C., Kehm, V.M., Zhang, B., O'Brien, P., Trojanowski, J.Q., Lee, V.M., 2012b. Intracerebral inoculation of pathological α-synuclein initiates a rapidly progressive neurodegenerative α-synucleinopathy in mice. The Journal of experimental medicine 209, 975–986. https://doi.org/10.1084/jem.20112457

Luk, K.C., Song, C., O'Brien, P., Stieber, A., Branch, J.R., Brunden, K.R., Trojanowski, J.Q., Lee, V.M.-Y., 2009. Exogenous α-synuclein fibrils seed the formation of Lewy body-like intracellular inclusions in cultured cells. Proceedings of the National Academy of Sciences 106, 20051–20056. https://doi.org/10.1073 pnas.0908005106

MacDonald, B.T., Tamai, K., He, X., 2009. Wnt/β-Catenin Signaling: Components, Mechanisms, and Diseases. Developmental Cell 17, 9–26. https://doi.org/10.1016/j.devcel.2009.06.016

Mahul-Mellier, A.-L., Burtscher, J., Maharjan, N., Weerens, L., Croisier, M., Kuttler, F., Leleu, M., Knott, G., Lashuel, H.A., 2019. The process of Lewy body formation, rather than simply alpha-synuclein fibrillization, is the major driver of neurodegeneration in synucleinopathies. bioRxiv 751891. https://doi.org/10.1101/751891

Mahul-Mellier, A.L., Vercruysse, F., Maco, B., Ait-Bouziad, N., De Roo, M., Muller, D., Lashuel, H.A., 2015. Fibril growth and seeding capacity play key roles in α-synuclein-mediated apoptotic cell death. Cell Death & Differentiation 22, 2107–2122. https://doi.org/10.1038/cdd.2015.79

Maio, R.D., Barrett, P.J., Hoffman, E.K., Barrett, C.W., Zharikov, A., Borah, A., Hu, X., McCoy, J., Chu, C.T., Burton, E.A., Hastings, T.G., Greenamyre, J.T., 2016. α-Synuclein binds to TOM20 and inhibits mitochondrial protein import in Parkinson's disease. Science Translational Medicine 8, 342ra78-342ra78. https://doi.org/10.1126/scitranslmed.aaf3634

Mali, P., Yang, L., Esvelt, K.M., Aach, J., Guell, M., DiCarlo, J.E., Norville, J.E., Church, G.M., 2013. RNA-Guided Human Genome Engineering via Cas9. Science 339, 823–826. https://doi.org/10.1126/science.1232033

Maneca, D.-L., Luo, W., Krahn, A., Del Cid Pellitero, E., Shlaifer, I., Beitel, L.K., Rao, T., Durcan, T.M., 2019. Production of Recombinant α Synuclein Monomers and Preformed Fibrils (PFFs). Zenodo. https://doi.org/10.5281/zenodo.3372888

Mao, X., Ou, M.T., Karuppagounder, S.S., Kam, T.-I., Yin, X., Xiong, Y., Ge, P., Umanah, G.E., Brahmachari, S., Shin, J.-H., Kang, H.C., Zhang, J., Xu, J., Chen, R., Park, H., Andrabi, S.A., Kang, S.U., Gonçalves, R.A., Liang, Y., Zhang, S., Qi, C., Lam, S., Keiler, J.A., Tyson, J., Kim, D., Panicker, N., Yun, S.P., Workman, C.J., Vignali, D.A.A., Dawson, V.L., Ko, H.S., Dawson, T.M., 2016. Pathological α-synuclein transmission initiated by binding lymphocyte-activation gene 3. Science 353, aah3374. https://doi.org/10.1126/science.aah3374

Marques, S., Zeisel, A., Codeluppi, S., Bruggen, D. van, Falcão, A.M., Xiao, L., Li, H., Häring, M., Hochgerner, H., Romanov, R.A., Gyllborg, D., Muñoz-Manchado, A.B., Manno, G.L., Lönnerberg, P., Floriddia, E.M., Rezayee, F., Ernfors, P., Arenas, E., Hjerling-Leffler, J., Harkany, T., Richardson, W.D., Linnarsson, S., Castelo-Branco, G., 2016. Oligodendrocyte heterogeneity in the mouse juvenile and adult central nervous system. Science 352, 1326–1329. https://doi.org/10.1126/science.aaf6463

Martens, M.A., Boesmans, W., Vanden Berghe, P., 2014. Calcium imaging at kHz frame rates resolves millisecond timing in neuronal circuits and varicosities. Biomed. Opt. Express 5, 2648. https://doi.org/10.1364/BOE.5.002648

Masliah, E., Rockenstein, E., Veinbergs, I., Mallory, M., Hashimoto, M., Takeda, A., Sagara, Y., Sisk, A., Mucke, L., 2000. Dopaminergic Loss and Inclusion Body Formation in α-Synuclein Mice: Implications for Neurodegenerative Disorders. Science 287, 1265. https://doi.org/10.1126/science.287.5456.1265

Masuda-Suzukake, M., Nonaka, T., Hosokawa, M., Kubo, M., Shimozawa, A., Akiyama, H., Hasegawa, M., 2014. Pathological alpha-synuclein propagates through neural networks. Acta neuropathologica communications 2, 1. https://doi.org/10.1186/s40478-014-0088-8

Masuda-Suzukake, M., Nonaka, T., Hosokawa, M., Oikawa, T., Arai, T., Akiyama, H., Mann, D.M., Hasegawa, M., 2013. Prion-like spreading of pathological α-synuclein in brain. Brain awt037. https://doi.org/10.1093/brain/awt037

Mendez, I., Dagher, A., Hong, M., Gaudet, P., Weerasinghe, S., McAlister, V., King, D., Desrosiers, J., Darvesh, S., Acorn, T., Robertson, H., 2002. Simultaneous intrastriatal and intranigral fetal dopaminergic grafts in patients with Parkinson disease: a pilot study - Report of three cases. Journal of Neurosurgery 96, 589–596. https://doi.org/10.3171/jns.2002.96.3.0589

Mendez, I., Viñuela, A., Astradsson, A., Mukhida, K., Hallett, P., Robertson, H., Tierney, T., Holness, R., Dagher, A., Trojanowski, J.Q., 2008. Dopamine neurons implanted into people with Parkinson's disease survive without pathology for 14 years. Nature medicine 14, 507. https://doi.org/10.1038/nm1752

Miller, D.W., Hague, S.M., Clarimon, J., Baptista, M., Gwinn-Hardy, K., Cookson, M.R., Singleton, A.B., 2004. α-Synuclein in blood and brain from familial Parkinson disease with SNCA locus triplication. Neurology 62, 1835–1838. https://doi.org/10.1212/01.WNL.0000127517.33208.F4

Mittal, S., Bjørnevik, K., Im, D.S., Flierl, A., Dong, X., Locascio, J.J., Abo, K.M., Long, E., Jin, M., Xu, B., Xiang, Y.K., Rochet, J.-C., Engeland, A., Rizzu, P., Heutink, P., Bartels, T., Selkoe, D.J., Caldarone, B.J., Glicksman, M.A., Khurana, V., Schüle, B., Park, D.S., Riise, T., Scherzer, C.R., 2017. β2-Adrenoreceptor is a regulator of the α-synuclein gene driving risk of Parkinson's disease. Science 357, 891–898. https://doi.org/10.1126/science.aaf3934

Mougenot, A.-L., Nicot, S., Bencsik, A., Morignat, E., Verchère, J., Lakhdar, L., Legastelois, S., Baron, T., 2012. Prion-like acceleration of a synucleinopathy in a transgenic mouse model. Neurobiology of aging 33, 2225–2228. https://doi.org/10.1016/j.neurobiolaging.2011.06.022

Muffat, J., Li, Y., Yuan, B., Mitalipova, M., Omer, A., Corcoran, S., Bakiasi, G., Tsai, L.-H., Aubourg, P., Ransohoff, R.M., Jaenisch, R., 2016. Efficient derivation of microglia-like cells from human pluripotent stem cells. Nat Med 22, 1358–1367. https://doi.org/10.1038/nm.4189

Murphy, D.D., Rueter, S.M., Trojanowski, J.Q., Lee, V.M.-Y., 2000. Synucleins Are Developmentally Expressed, and α-Synuclein Regulates the Size of the Presynaptic Vesicular Pool in Primary Hippocampal Neurons. J. Neurosci. 20, 3214–3220. https://doi.org/10.1523/JNEUROSCI.20-09-03214.2000

Nakamura, K., Nemani, V.M., Azarbal, F., Skibinski, G., Levy, J.M., Egami, K., Munishkina, L., Zhang, J., Gardner, B., Wakabayashi, J., Sesaki, H., Cheng, Y., Finkbeiner, S., Nussbaum, R.L., Masliah, E., Edwards, R.H., 2011. Direct Membrane Association Drives Mitochondrial Fission by the Parkinson Disease-associated Protein α-Synuclein. J Biol Chem 286, 20710–20726. https://doi.org/10.1074/jbc.M110.213538

Neumann, J., Bras, J., Deas, E., O'Sullivan, S.S., Parkkinen, L., Lachmann, R.H., Li, A., Holton, J., Guerreiro, R., Paudel, R., Segarane, B., Singleton, A., Lees, A., Hardy, J., Houlden, H., Revesz, T., Wood, N.W., 2009. Glucocerebrosidase mutations in clinical and pathologically proven Parkinson's disease. Brain 132, 1783–1794. https://doi.org/10.1093/brain/awp044

Nolbrant, S., Heuer, A., Parmar, M., Kirkeby, A., 2017. Generation of high-purity human ventral midbrain dopaminergic progenitors for in vitro maturation and intracerebral transplantation. Nature Protocols 12, 1962–1979. https://doi.org/10.1038/nprot.2017.078

Nonaka, T., Watanabe, S.T., Iwatsubo, T., Hasegawa, M., 2010. Seeded Aggregation and Toxicity of α-Synuclein and Tau CELLULAR MODELS OF NEURODEGENERATIVE DISEASES. Journal of Biological Chemistry 285, 34885–34898. https://doi.org/10.1074/jbc.M110.148460

Nouri, N., Awatramani, R., 2017. A novel floor plate boundary defined by adjacent En1 and Dbx1 microdomains distinguishes midbrain dopamine and hypothalamic neurons. Development 144, 916–927. https://doi.org/10.1242/dev.144949

Obeso, J.A., Olanow, C.W., Nutt, J.G., 2000. Levodopa motor complications in Parkinson's disease. Trends in Neurosciences 23, S2–S7. https://doi.org/10.1016/S1471-1931(00)00031-8

Okuzumi, A., Kurosawa, M., Hatano, T., Takanashi, M., Nojiri, S., Fukuhara, T., Yamanaka, T., Miyazaki, H., Yoshinaga, S., Furukawa, Y., Shimogori, T., Hattori, N., Nukina, N., 2018. Rapid dissemination of alpha-synuclein seeds through neural circuits in an in-vivo prion-like seeding experiment. Acta Neuropathologica Communications 6, 96. https://doi.org/10.1186/s40478-018-0587-0

Olanow, C.W., Goetz, C.G., Kordower, J.H., Stoessl, A.J., Sossi, V., Brin, M.F., Shannon, K.M., Nauert, G.M., Perl, D.P., Godbold, J., Freeman, T.B., 2003. A double-blind controlled trial of bilateral fetal nigral transplantation in Parkinson's disease. Annals of neurology 54, 403–14. https://doi.org/10.1002/ana.10720

Olgiati, S., Thomas, A., Quadri, M., Breedveld, G.J., Graafland, J., Eussen, H., Douben, H., de Klein, A., Onofrj, M., Bonifati, V., 2015. Early-onset parkinsonism caused by alpha-synuclein gene triplication: Clinical and genetic findings in a novel family. Parkinsonism & Related Disorders 21, 981–986. https://doi.org/10.1016/j.parkreldis.2015.06.005

Ono, Y., Nakatani, T., Sakamoto, Y., Mizuhara, E., Minaki, Y., Kumai, M., Hamaguchi, A., Nishimura, M., Inoue, Y., Hayashi, H., Takahashi, J., Imai, T., 2007. Differences in neurogenic potential in floor plate cells along an anteroposterior location: midbrain dopaminergic neurons originate from mesencephalic floor plate cells. Development 134, 3213–25. https://doi.org/10.1242/dev.02879

Osterberg, V.R., Spinelli, K.J., Weston, L.J., Luk, K.C., Woltjer, R.L., Unni, V.K., 2015. Progressive aggregation of alpha-synuclein and selective degeneration of lewy inclusion-bearing neurons in a mouse model of parkinsonism. Cell reports 10, 1252–1260. https://doi.org/10.1016/j.celrep.2015.01.060

Ouchi, Y., Yoshikawa, E., Sekine, Y., Futatsubashi, M., Kanno, T., Ogusu, T., Torizuka, T., 2005. Microglial activation and dopamine terminal loss in early Parkinson's disease. Ann Neurol. 57, 168–175. https://doi.org/10.1002/ana.20338

Oueslati, A., 2016. Implication of Alpha-Synuclein Phosphorylation at S129 in Synucleinopathies: What Have We Learned in the Last Decade? Journal of Parkinson's disease 6, 39–51. https://doi.org/10.3233/JPD-160779

Oueslati, A., Paleologou, K.E., Schneider, B.L., Aebischer, P., Lashuel, H.A., 2012. Mimicking Phosphorylation at Serine 87 Inhibits the Aggregation of Human α-Synuclein and Protects against Its Toxicity in a Rat Model of Parkinson's Disease. The Journal of Neuroscience 32, 1536. https://doi.org/10.1523/JNEUROSCI.3784-11.2012

Owens, D.D.G., Caulder, A., Frontera, V., Harman, J.R., Allan, A.J., Bucakci, A., Greder, L., Codner, G.F., Hublitz, P., McHugh, P.J., Teboul, L., de Bruijn, M.F.T.R., 2019. Microhomologies are prevalent at Cas9-induced larger deletions. Nucleic Acids Research 47, 7402–7417. https://doi.org/10.1093/nar/gkz459

Pacelli, C., Giguère, N., Bourque, M.-J., Lévesque, M., Slack, R.S., Trudeau, L.-É., 2015. Elevated Mitochondrial Bioenergetics and Axonal Arborization Size Are Key Contributors to the Vulnerability of Dopamine Neurons. Current Biology 25, 2349–2360. https://doi.org/10.1016/j.cub.2015.07.050

Paleologou, K.E., Oueslati, A., Shakked, G., Rospigliosi, C.C., Kim, H.-Y., Lamberto, G.R., Fernandez, C.O., Schmid, A., Chegini, F., Gai, W.P., Chiappe, D., Moniatte, M., Schneider, B.L., Aebischer, P., Eliezer, D., Zweckstetter, M., Masliah, E., Lashuel, H.A., 2010. Phosphorylation at S87 Is Enhanced in Synucleinopathies, Inhibits α-Synuclein Oligomerization, and Influences Synuclein-Membrane Interactions. The Journal of Neuroscience 30, 3184–3198. https://doi.org/10.1523/jneurosci.5922-09.2010

Paquet, D., Kwart, D., Chen, A., Sproul, A., Jacob, S., Teo, S., Olsen, K.M., Gregg, A., Noggle, S., Tessier-Lavigne, M., 2016. Efficient introduction of specific homozygous and heterozygous mutations using CRISPR/Cas9. Nature 533, 125–129. https://doi.org/10.1038/nature17664

Parikh, B.A., Beckman, D.L., Patel, S.J., White, J.M., Yokoyama, W.M., 2015. Detailed Phenotypic and Molecular Analyses of Genetically Modified Mice Generated by CRISPR-Cas9-Mediated Editing. PLoS One 10. https://doi.org/10.1371/journal.pone.0116484

Parkinson, J., 1817. An Essay on the Shaking Palsy. JNP 14, 223–236. https://doi.org/10.1176/jnp.14.2.223

Parkinson's UK, 2018. The incidence and prevalence of Parkinson's in the UK: Results from the Clinical Practice Research Datalink Summary report.

Pattanayak, V., Lin, S., Guilinger, J.P., Ma, E., Doudna, J.A., Liu, D.R., 2013. High-throughput profiling of off-target DNA cleavage reveals RNA-programmed Cas9 nuclease specificity. Nat Biotechnol 31, 839–843. https://doi.org/10.1038/nbt.2673

Patterson, J.R., Duffy, M.F., Kemp, C.J., Howe, J.W., Collier, T.J., Stoll, A.C., Miller, K.M., Patel, P., Levine, N., Moore, D.J., Luk, K.C., Fleming, S.M., Kanaan, N.M., Paumier, K.L., El-Agnaf, O.M.A., Sortwell, C.E., 2019. Time course and magnitude of alpha-synuclein inclusion formation and nigrostriatal degeneration in the rat model of synucleinopathy triggered by intrastriatal α-synuclein preformed fibrils. Neurobiology of Disease 130, 104525. https://doi.org/10.1016/j.nbd.2019.104525

Paumier, K.L., Luk, K.C., Manfredsson, F.P., Kanaan, N.M., Lipton, J.W., Collier, T.J., Steece-Collier, K., Kemp, C.J., Celano, S., Schulz, E., 2015. Intrastriatal injection of pre-formed mouse α-synuclein fibrils into rats triggers α-synuclein pathology and bilateral nigrostriatal degeneration. Neurobiology of disease 82, 185–199. https://doi.org/10.1016/j.nbd.2015.06.003

Pawar, A.P., DuBay, K.F., Zurdo, J., Chiti, F., Vendruscolo, M., Dobson, C.M., 2005. Prediction of “aggregation-prone” and “aggregation-susceptible” regions in proteins associated with neurodegenerative diseases. Journal of molecular biology 350, 379–392. https://doi.org/10.1016/j.jmb.2005.04.016

Peelaerts, W., Bousset, L., Van der Perren, A., Moskalyuk, A., Pulizzi, R., Giugliano, M., Van den Haute, C., Melki, R., Baekelandt, V., 2015. α-Synuclein strains cause distinct synucleinopathies after local and systemic administration. Nature 522, 340–344. https://doi.org/10.1038/nature14547

Perez, R.G., Waymire, J.C., Lin, E., Liu, J.J., Guo, F., Zigmond, M.J., 2002. A role for α-synuclein in the regulation of dopamine biosynthesis. The Journal of Neuroscience 22, 3090–3099. https://doi.org/10.1523/JNEUROSCI.22-08-03090.2002

Piccini, P., Pavese, N., Hagell, P., Reimer, J., Björklund, A., Oertel, W.H., Quinn, N.P., Brooks, D.J., Lindvall, O., 2005. Factors affecting the clinical outcome after neural transplantation in Parkinson’s disease. Brain 128, 2977–2986. https://doi.org/10.1093/brain/awh649

Polinski, N.K., Volpicelli-Daley, L.A., Sortwell, C.E., Luk, K.C., Cremades, N., Gottler, L.M., Froula, J., Duffy, M.F., Lee, V.M.Y., Martinez, T.N., Dave, K.D., 2018. Best Practices for Generating and Using Alpha-Synuclein Pre-Formed Fibrils to Model Parkinson’s Disease in Rodents. J Parkinsons Dis 8, 303–322. https://doi.org/10.3233/JPD-171248

Politis, M., Oertel, W.H., Wu, K., Quinn, N.P., Pogarell, O., Brooks, D.J., Bjorklund, A., Lindvall, O., Piccini, P., 2011. Graft-induced dyskinesias in Parkinson’s disease: High striatal serotonin/dopamine transporter ratio. Movement disorders : official journal of the Movement Disorder Society 26, 1997–2003. https://doi.org/10.1002/mds.23743

Polymeropoulos, M.H., 1997. Mutation in the -Synuclein Gene Identified in Families with Parkinson’s Disease. Science 276, 2045–2047. https://doi.org/10.1126/science.276.5321.2045

Poulin, J.F., Zou, J., Drouin-Ouellet, J., Kim, K.Y., Cicchetti, F., Awatramani, R.B., 2014. Defining midbrain dopaminergic neuron diversity by single-cell gene expression profiling. Cell reports 9, 930–43. https://doi.org/10.1016/j.celrep.2014.10.008

Quinn, J.G., Coulson, D.T.R., Brockbank, S., Beyer, N., Ravid, R., Hellemans, J., Irvine, G.B., Johnston, J.A., 2012. α-Synuclein mRNA and soluble α-synuclein protein levels in post-mortem brain from patients with Parkinson’s disease, dementia with Lewy bodies, and Alzheimer’s disease. Brain Research 1459, 71–80. https://doi.org/10.1016/j.brainres.2012.04.018

Ran, F.A., Hsu, P.D., Lin, C.-Y., Gootenberg, J.S., Konermann, S., Trevino, A., Scott, D.A., Inoue, A., Matoba, S., Zhang, Y., Zhang, F., 2013a. Double nicking by RNA-guided CRISPR Cas9 for enhanced genome editing specificity. Cell 154, 1380–1389. https://doi.org/10.1016/j.cell.2013.08.021

Ran, F.A., Hsu, P.D., Wright, J., Agarwala, V., Scott, D.A., Zhang, F., 2013b. Genome engineering using the CRISPR-Cas9 system. Nat Protoc 8, 2281–2308. https://doi.org/10.1038/nprot.2013.143

Recasens, A., Dehay, B., Bové, J., Carballo-Carbajal, I., Dovero, S., Pérez-Villalba, A., Fernagut, P.-O., Blesa, J., Parent, A., Perier, C., Fariñas, I., Obeso, J.A., Bezard, E., Vila, M., 2014. Lewy body extracts from Parkinson disease brains trigger α-synuclein pathology and neurodegeneration in mice and monkeys. Annals of Neurology 75, 351–362. https://doi.org/10.1002/ana.24066

Rey, N.L., George, S., Steiner, J.A., Madaj, Z., Luk, K.C., Trojanowski, J.Q., Lee, V.M.-Y., Brundin, P., 2018. Spread of aggregates after olfactory bulb injection of α-synuclein fibrils is associated with early neuronal loss and is reduced long term. Acta Neuropathol 135, 65–83. https://doi.org/10.1007/s00401-017-1792-9

Rey, N.L., Steiner, J.A., Maroof, N., Luk, K.C., Madaj, Z., Trojanowski, J.Q., Lee, V.M.-Y., Brundin, P., 2016. Widespread transneuronal propagation of α-synucleinopathy triggered in olfactory bulb mimics prodromal Parkinson's disease. The Journal of experimental medicine 213, 1759–1778. https://doi.org/10.1084/jem.20160368

Robertson, D.C., Schmidt, O., Ninkina, N., Jones, P.A., Sharkey, J., Buchman, V.L., 2004. Developmental loss and resistance to MPTP toxicity of dopaminergic neurones in substantia nigra pars compacta of γ-synuclein, α-synuclein and double α/γ-synuclein null mutant mice. Journal of Neurochemistry 89, 1126–1136. https://doi.org/10.1111/j.1471-4159.2004.02378.x

Robertson, G., Bushell, T.J., Zagnoni, M., 2014. Chemically induced synaptic activity between mixed primary hippocampal co-cultures in a microfluidic system. Integrative Biology 6, 636–644. https://doi.org/10.1039/c3ib40221e

Rogers, J.T., Mikkilineni, S., Cantuti-Castelvetri, I., Smith, D.H., Huang, X., Bandyopadhyay, S., Cahill, C.M., Maccecchini, M.L., Lahiri, D.K., Greig, N.H., 2011. The alpha-synuclein 5'untranslated region targeted translation blockers: anti-alpha synuclein efficacy of cardiac glycosides and Posiphen. J Neural Transm (Vienna) 118, 493–507. https://doi.org/10.1007/s00702-010-0513-5

Rostami, J., Fotaki, G., Sirois, J., Mzezewa, R., Bergström, J., Essand, M., Healy, L., Erlandsson, A., 2020. Astrocytes have the capacity to act as antigen-presenting cells in the Parkinson's disease brain. J Neuroinflammation 17, 119. https://doi.org/10.1186/s12974-020-01776-7

Roybon, L., Lamas, N.J., Garcia-Diaz, A., Yang, E.J., Sattler, R., Jackson-Lewis, V., Kim, Y.A., Kachel, C.A., Rothstein, J.D., Przedborski, S., Wichterle, H., Henderson, C.E., 2013. Human Stem Cell-Derived Spinal Cord Astrocytes with Defined Mature or Reactive Phenotypes. Cell Reports 4, 1035–1048. https://doi.org/10.1016/j.celrep.2013.06.021

Sacino, A.N., Brooks, M., McGarvey, N.H., McKinney, A.B., Thomas, M.A., Levites, Y., Ran, Y., Golde, T.E., Giasson, B.I., 2013a. Induction of CNS α-synuclein pathology by fibrillar and non-amyloidogenic recombinant α-synuclein. Acta neuropathologica communications 1, 1. https://doi.org/10.1186/2051-5960-1-38

Sacino, A.N., Brooks, M., McKinney, A.B., Thomas, M.A., Shaw, G., Golde, T.E., Giasson, B.I., 2014a. Brain injection of α-synuclein induces multiple proteinopathies, gliosis, and a neuronal injury marker. The Journal of Neuroscience 34, 12368–12378. https://doi.org/10.1523/JNEUROSCI.2102-14.2014

Sacino, A.N., Brooks, M., Thomas, M.A., McKinney, A.B., Lee, S., Regenhardt, R.W., McGarvey, N.H., Ayers, J.I., Notterpek, L., Borchelt, D.R., 2014b. Intramuscular injection of α-synuclein induces CNS α-synuclein pathology and a rapid-onset motor phenotype in transgenic mice. Proceedings of the National Academy of Sciences 111, 10732–10737. https://doi.org/10.1073/pnas.1321785111

Sacino, A.N., Brooks, M., Thomas, M.A., McKinney, A.B., McGarvey, N.H., Rutherford, N.J., Ceballos-Diaz, C., Robertson, J., Golde, T.E., Giasson, B.I., 2014c. Amyloidogenic α-

synuclein seeds do not invariably induce rapid, widespread pathology in mice. Acta neuropathologica 127, 645–665. https://doi.org/10.1007/s00401-014-1268-0

Sacino, A.N., Brooks, M.M., Chakrabarty, P., Saha, K., Khoshbouei, H., Golde, T.E., Giasson, B.I., 2017. Proteolysis of α-synuclein fibrils in the lysosomal pathway limits induction of inclusion pathology. J. Neurochem. 140, 662–678. https://doi.org/10.1111/jnc.13743

Sacino, A.N., Thomas, M.A., Ceballos-Diaz, C., Cruz, P.E., Rosario, A.M., Lewis, J., Giasson, B.I., Golde, T.E., 2013b. Conformational templating of α-synuclein aggregates in neuronal-glial cultures. Mol Neurodegeneration 8, 17. https://doi.org/10.1186/1750-1326-8-17

Samata, B., Doi, D., Nishimura, K., Kikuchi, T., Watanabe, A., Sakamoto, Y., Kakuta, J., Ono, Y., Takahashi, J., 2016. Purification of functional human ES and iPSC-derived midbrain dopaminergic progenitors using LRTM1. Nature Communications 7, 13097. https://doi.org/10.1038/ncomms13097

Schaser, A.J., Osterberg, V.R., Dent, S.E., Stackhouse, T.L., Wakeham, C.M., Boutros, S.W., Weston, L.J., Owen, N., Weissman, T.A., Luna, E., Raber, J., Luk, K.C., McCullough, A.K., Woltjer, R.L., Unni, V.K., 2019. Alpha-synuclein is a DNA binding protein that modulates DNA repair with implications for Lewy body disorders. Sci Rep 9, 1–19. https://doi.org/10.1038/s41598-019-47227-z

Scott, D.A., Tabarean, I., Tang, Y., Cartier, A., Masliah, E., Roy, S., 2010. A Pathologic Cascade Leading to Synaptic Dysfunction in α-Synuclein-Induced Neurodegeneration. J. Neurosci. 30, 8083–8095. https://doi.org/10.1523/JNEUROSCI.1091-10.2010

Sejvar, J.J., 2003. Neurologic Manifestations and Outcome of West Nile Virus Infection. JAMA 290, 511. https://doi.org/10.1001/jama.290.4.511

Sekine, T., Kagaya, H., Funayama, M., Li, Y., Yoshino, H., Tomiyama, H., Hattori, N., 2010. Clinical course of the first Asian family with Parkinsonism related to SNCA triplication: SNCA Triplication in Japan. Mov. Disord. 25, 2871–2875. https://doi.org/10.1002/mds.23313

Shaltouki, A., Peng, J., Liu, Q., Rao, M.S., Zeng, X., 2013. Efficient Generation of Astrocytes from Human Pluripotent Stem Cells in Defined Conditions. STEM CELLS 31, 941–952. https://doi.org/10.1002/stem.1334

Shew, W.L., Bellay, T., Plenz, D., 2010. Simultaneous multi-electrode array recording and two-photon calcium imaging of neural activity. Journal of Neuroscience Methods 192, 75–82. https://doi.org/10.1016/j.jneumeth.2010.07.023

Shimozawa, A., Ono, M., Takahara, D., Tarutani, A., Imura, S., Masuda-Suzukake, M., Higuchi, M., Yanai, K., Hisanaga, S., Hasegawa, M., 2017. Propagation of pathological α-synuclein in marmoset brain. Acta Neuropathologica Communications 5, 12. https://doi.org/10.1186/s40478-017-0413-0

Singh, A.M., Adjan Steffey, V.V., Yeshi, T., Allison, D.W., 2015. Gene Editing in Human Pluripotent Stem Cells: Choosing the Correct Path. J Stem Cell Regen Biol 1.

Singleton, A.B., 2003. α-Synuclein Locus Triplication Causes Parkinson's Disease. Science 302, 841–841. https://doi.org/10.1126/science.1090278

Sode, K., Ochiai, S., Kobayashi, N., Usuzaka, E., 2007. Effect of Reparation of Repeat Sequences in the Human α-Synuclein on Fibrillation Ability. Int. J. Biol. Sci. 1–7. https://doi.org/10.7150/ijbs.3.1

Sorrentino, Z.A., Xia, Y., Funk, C., Riffe, C.J., Rutherford, N.J., Ceballos Diaz, C., Sacino, A.N., Price, N.D., Golde, T.E., Giasson, B.I., Chakrabarty, P., 2018. Motor neuron loss and neuroinflammation in a model of α-synuclein-induced neurodegeneration. Neurobiology of Disease 120, 98–106. https://doi.org/10.1016/j.nbd.2018.09.005

Specht, C.G., Schoepfer, R., 2001. Deletion of the alpha-synuclein locus in a subpopulation of C57BL/6J inbred mice. BMC neuroscience 2, 1. https://doi.org/10.1186/1471-2202-2-11

Spillantini, M.G., Crowther, R.A., Jakes, R., Hasegawa, M., Goedert, M., 1998. α-Synuclein in filamentous inclusions of Lewy bodies from Parkinson's disease and dementia with Lewy

bodies. Proceedings of the National Academy of Sciences 95, 6469–6473. https://doi.org/10.1073/pnas.95.11.6469

Spillantini, M.G., Schmidt, M.L., Lee, V.M.Y., Trojanowski, J.Q., Jakes, R., Goedert, M., 1997. α-Synuclein in Lewy bodies. Nature 388, 839. https://doi.org/10.1038/42166

Stolzenberg, E., Berry, D., Yang, D., Lee, E.Y., Kroemer, A., Kaufman, S., Wong, G.C.L., Oppenheim, J.J., Sen, S., Fishbein, T., Bax, A., Harris, B., Barbut, D., Zasloff, M.A., 2017. A Role for Neuronal Alpha-Synuclein in Gastrointestinal Immunity. J Innate Immun 9, 456–463. https://doi.org/10.1159/000477990

Stoyka, L.E., Arrant, A.E., Thrasher, D.R., Russell, D.L., Freire, J., Mahoney, C.L., Narayanan, A., Dib, A.G., Standaert, D.G., Volpicelli-Daley, L.A., 2020. Behavioral defects associated with amygdala and cortical dysfunction in mice with seeded α-synuclein inclusions. Neurobiology of Disease 134, 104708. https://doi.org/10.1016/j.nbd.2019.104708

Studer, L., 2017. Chapter 8 - Strategies for bringing stem cell-derived dopamine neurons to the clinic—The NYSTEM trial, in: Dunnett, S.B., Björklund, A. (Eds.), Progress in Brain Research, Functional Neural Transplantation IV. Elsevier, pp. 191–212. https://doi.org/10.1016/bs.pbr.2017.02.008

Su, X., Fischer, D.L., Li, X., Bankiewicz, K., Sortwell, C.E., Federoff, H.J., 2017. Alpha-Synuclein mRNA Is Not Increased in Sporadic PD and Alpha-Synuclein Accumulation Does Not Block GDNF Signaling in Parkinson's Disease and Disease Models. Molecular Therapy 25, 2231–2235. https://doi.org/10.1016/j.ymthe.2017.04.018

Sunmonu, N.A., Li, K., Guo, Q., Li, J.Y.H., 2011. Gbx2 and Fgf8 are sequentially required for formation of the midbrain-hindbrain compartment boundary. Development 138, 725–734. https://doi.org/10.1242/dev.055665

Taguchi, K., Watanabe, Y., Tsujimura, A., Tatebe, H., Miyata, S., Tokuda, T., Mizuno, T., Tanaka, M., 2014. Differential Expression of Alpha-Synuclein in Hippocampal Neurons. PLoS ONE 9, e89327. https://doi.org/10.1371/journal.pone.0089327

Takahashi, K., Yamanaka, S., 2006. Induction of pluripotent stem cells from mouse embryonic and adult fibroblast cultures by defined factors. Cell 126, 663–676. https://doi.org/10.1016/j.cell.2006.07.024

Tarutani, A., Suzuki, G., Shimozawa, A., Nonaka, T., Akiyama, H., Hisanaga, S., Hasegawa, M., 2016. The Effect of Fragmented Pathogenic α-Synuclein Seeds on Prion-like Propagation. J. Biol. Chem. 291, 18675–18688. https://doi.org/10.1074/jbc.M116.734707

Tehranian, R., Montoya, S.E., Van Laar, A.D., Hastings, T.G., Perez, R.G., 2006. Alpha-synuclein inhibits aromatic amino acid decarboxylase activity in dopaminergic cells. J Neurochem 99, 1188–1196. https://doi.org/10.1111/j.1471-4159.2006.04146.x

Thakur, P., Breger, L.S., Lundblad, M., Wan, O.W., Mattsson, B., Luk, K.C., Lee, V.M.Y., Trojanowski, J.Q., Björklund, A., 2017. Modeling Parkinson's disease pathology by combination of fibril seeds and α-synuclein overexpression in the rat brain. PNAS 114, E8284–E8293. https://doi.org/10.1073/pnas.1710442114

Thevenon, J., Callier, P., Andrieux, J., Delobel, B., David, A., Sukno, S., Minot, D., Mosca Anne, L., Marle, N., Sanlaville, D., Bonnet, M., Masurel-Paulet, A., Levy, F., Gaunt, L., Farrell, S., Le Caignec, C., Toutain, A., Carmignac, V., Mugneret, F., Clayton-Smith, J., Thauvin-Robinet, C., Faivre, L., 2013. 12p13.33 microdeletion including ELKS/ERC1, a new locus associated with childhood apraxia of speech. Eur J Hum Genet 21, 82–88. https://doi.org/10.1038/ejhg.2012.116

Tiklová, K., Nolbrant, S., Fiorenzano, A., Björklund, Å.K., Sharma, Y., Heuer, A., Gillberg, L., Hoban, D.B., Cardoso, T., Adler, A.F., Birtele, M., Lundén-Miguel, H., Volakakis, N., Kirkeby, A., Perlmann, T., Parmar, M., 2019. Single Cell Gene Expression Analysis Reveals Human Stem Cell-Derived Graft Composition in a Cell Therapy Model of Parkinson's Disease (preprint). Neuroscience. https://doi.org/10.1101/720870

Tomlinson, J.J., Shutinoski, B., Dong, L., Meng, F., Elleithy, D., Lengacher, N.A., Nguyen, A.P., Cron, G.O., Jiang, Q., Roberson, E.D., Nussbaum, R.L., Majbour, N.K., El-Agnaf, O.M., Bennett, S.A., Lagace, D.C., Woulfe, J.M., Sad, S., Brown, E.G., Schlossmacher, M.G., 2017. Holocranohistochemistry enables the visualization of α-synuclein expression in the murine olfactory system and discovery of its systemic anti-microbial effects. J Neural Transm 124, 721–738. https://doi.org/10.1007/s00702-017-1726-7

Tran, H.T., Chung, C.H.-Y., Iba, M., Zhang, B., Trojanowski, J.Q., Luk, K.C., Lee, V.M.Y., 2014. α-Synuclein Immunotherapy Blocks Uptake and Templated Propagation of Misfolded α-Synuclein and Neurodegeneration. Cell Reports 7, 2054–2065. https://doi.org/10.1016/j.celrep.2014.05.033

TRANSEURO consortium, Barker, R.A., 2019. Designing stem-cell-based dopamine cell replacement trials for Parkinson's disease. Nat Med 25, 1045–1053. https://doi.org/10.1038/s41591-019-0507-2

Tretiakoff, K., 1919. Contribution a l'etude de l'anatomie pathologique du locus niger de Soemmering avec quelques deductions relatives a la pathogenie des troubles du tonus musculaire et de la maladie de Parkinson.

Tuttle, M.D., Comellas, G., Nieuwkoop, A.J., Covell, D.J., Berthold, D.A., Kloepper, K.D., Courtney, J.M., Kim, J.K., Barclay, A.M., Kendall, A., Wan, W., Stubbs, G., Schwieters, C.D., Lee, V.M.Y., George, J.M., Rienstra, C.M., 2016. Solid-state NMR structure of a pathogenic fibril of full-length human [alpha]-synuclein. Nat Struct Mol Biol 23, 409–415. https://doi.org/10.1038/nsmb.3194

Uchihara, T., Giasson, B.I., 2016. Propagation of alpha-synuclein pathology: hypotheses, discoveries, and yet unresolved questions from experimental and human brain studies. Acta neuropathologica 131, 49–73. https://doi.org/10.1007/s00401-015-1485-1

Uéda, K., Fukushima, H., Masliah, E., Xia, Y., Iwai, A., Yoshimoto, M., Otero, D.A., Kondo, J., Ihara, Y., Saitoh, T., 1993. Molecular cloning of cDNA encoding an unrecognized component of amyloid in Alzheimer disease. PNAS 90, 11282–11286. https://doi.org/10.1073/pnas.90.23.11282

Uemura, N., Yagi, H., Uemura, M.T., Hatanaka, Y., Yamakado, H., Takahashi, R., 2018. Inoculation of α-synuclein preformed fibrils into the mouse gastrointestinal tract induces Lewy body-like aggregates in the brainstem via the vagus nerve. Molecular Neurodegeneration 13, 21. https://doi.org/10.1186/s13024-018-0257-5

Ungerstedt, U., Arbuthnott, G.W., 1970. Quantitative recording of rotational behavior in rats after 6-hydroxy-dopamine lesions of the nigrostriatal dopamine system. Brain Research 24, 485–493. https://doi.org/10.1016/0006-8993(70)90187-3

Vanlandewijck, M., He, L., Mäe, M.A., Andrae, J., Ando, K., Del Gaudio, F., Nahar, K., Lebouvier, T., Laviña, B., Gouveia, L., Sun, Y., Raschperger, E., Räsänen, M., Zarb, Y., Mochizuki, N., Keller, A., Lendahl, U., Betsholtz, C., 2018. A molecular atlas of cell types and zonation in the brain vasculature. Nature 554, 475–480. https://doi.org/10.1038/nature25739

Volpicelli-Daley, L.A., Luk, K.C., Lee, V.M., 2014. Addition of exogenous α-synuclein preformed fibrils to primary neuronal cultures to seed recruitment of endogenous α-synuclein to Lewy body and Lewy neurite–like aggregates. Nature protocols 9, 2135–2146. https://doi.org/10.1038/nprot.2014.143

Volpicelli-Daley, L.A., Luk, K.C., Patel, T.P., Tanik, S.A., Riddle, D.M., Stieber, A., Meaney, D.F., Trojanowski, J.Q., Lee, V.M.-Y., 2011. Exogenous α-synuclein fibrils induce Lewy body pathology leading to synaptic dysfunction and neuron death. Neuron 72, 57–71. https://doi.org/10.1016/j.neuron.2011.08.033

Wagenaar, D.A., Pine, J., Potter, S.M., 2006. An extremely rich repertoire of bursting patterns during the development of cortical cultures. BMC Neurosci 7, 11. https://doi.org/10.1186/1471-2202-7-11

Wakabayashi, K., Tanji, K., Odagiri, S., Miki, Y., Mori, F., Takahashi, H., 2013. The Lewy Body in Parkinson's Disease and Related Neurodegenerative Disorders. Mol Neurobiol 47, 495–508. https://doi.org/10.1007/s12035-012-8280-y

Wang, Yizhi, Wang, C., Ranefall, P., Broussard, G.J., Wang, Yinxue, Shi, G., Lyu, B., Wu, C.-T., Wang, Yue, Tian, L., Yu, G., 2019. SynQuant: an automatic tool to quantify synapses from microscopy images. Bioinformatics btz760. https://doi.org/10.1093/bioinformatics/btz760

Waxman, E.A., Emmer, K.L., Giasson, B.I., 2010. Residue Glu83 plays a major role in negatively regulating α-synuclein amyloid formation. Biochemical and biophysical research communications 391, 1415–1420. https://doi.org/10.1016/j.bbrc.2009.12.079

Waxman, E.A., Giasson, B.I., 2010. A novel, high-efficiency cellular model of fibrillar α-synuclein inclusions and the examination of mutations that inhibit amyloid formation. Journal of neurochemistry 113, 374–388. https://doi.org/10.1111/j.1471-4159.2010.06592.x

Waxman, E.A., Mazzulli, J.R., Giasson, B.I., 2009. Characterization of hydrophobic residue requirements for α-synuclein fibrillization. Biochemistry 48, 9427–9436. https://doi.org/10.1021/bi900539p

Wenning, G.K., Odin, P., Morrish, P., Rehncrona, S., Widner, H., Brundin, P., Rothwell, J.C., Brown, R., Gustavii, B., Hagell, P., Jahanshahi, M., Sawle, G., Björklund, A., Brooks, D.J., Marsden, C.D., Quinn, N.P., Lindvall, O., 1997. Short- and long-term survival and function of unilateral intrastriatal dopaminergic grafts in Parkinson's disease. Ann. Neurol. 42, 95–107. https://doi.org/10.1002/ana.410420115

Widner, H., Tetrud, J., Rehncrona, S., Snow, B., Brundin, P., Gustavii, B., Bjorklund, A., Lindvall, O., Langston, J.W., 1992. Bilateral fetal mesencephalic grafting in 2 patients with parkinsonism induced by 1-methyl-4-phenyl-1,2,3,6-tetrahydropyridine (MPTP). New England Journal of Medicine 327, 1556–1563. https://doi.org/10.1056/nejm199211263272203

Wierson, W.A., Simone, B.W., WareJoncas, Z., Mann, C., Welker, J.M., Kar, B., Emch, M.J., Friedberg, I., Gendron, W.A.C., Barry, M.A., Clark, K.J., Dobbs, D.L., McGrail, M.A., Ekker, S.C., Essner, J.J., 2019. Expanding the CRISPR Toolbox with ErCas12a in Zebrafish and Human Cells. The CRISPR Journal 2, 417–433. https://doi.org/10.1089/crispr.2019.0026

Wood, S.J., Wypych, J., Steavenson, S., Louis, J.-C., Citron, M., Biere, A.L., 1999. α-Synuclein Fibrillogenesis Is Nucleation-dependent IMPLICATIONS FOR THE PATHOGENESIS OF PARKINSON′S DISEASE. J. Biol. Chem. 274, 19509–19512. https://doi.org/10.1074/jbc.274.28.19509

Wu, Q., Takano, H., Riddle, D.M., Trojanowski, J.Q., Coulter, D.A., Lee, V.M.-Y., 2019. Alpha-synuclein (αSyn) preformed fibrils induce endogenous αSyn aggregation, compromise synaptic activity and enhance synapse loss in cultured excitatory hippocampal neurons. J. Neurosci. 0060–19. https://doi.org/10.1523/JNEUROSCI.0060-19.2019

Xi, J., Liu, Y., Liu, H., Chen, H., Emborg, M.E., Zhang, S.-C., 2012. Specification of Midbrain Dopamine Neurons from Primate Pluripotent Stem Cells. Stem cells 30, 1655–1663. https://doi.org/10.1002/stem.1152

Xiong, S., Zhang, S., Guan, L., Chen, J., Tu, X., Li, Q., Jiang, H., 2017. Differentiation of induced pluripotent stem cells for future olfactory repair using an indirect co-culture technique. Int J Clin Exp Pathol 10, 8072–8081.

Yagi, H., Takeuchi, H., Ogawa, S., Ito, N., Sakane, I., Hongo, K., Mizobata, T., Goto, Y., Kawata, Y., 2010. Isolation of short peptide fragments from α-synuclein fibril core identifies a residue important for fibril nucleation: A possible implication for diagnostic applications. Biochimica et Biophysica Acta (BBA)-Proteins and Proteomics 1804, 2077–2087. https://doi.org/10.1016/j.bbapap.2010.07.007

Yan, S., Schubert, M., Young, M., Wang, B., 2017. Applications of Cas9 nickases for genome engineering. genome editing 10.

Yavich, L., Tanila, H., Vepsäläinen, S., Jäkälä, P., 2004. Role of α-Synuclein in Presynaptic Dopamine Recruitment. J. Neurosci. 24, 11165–11170. https://doi.org/10.1523/JNEUROSCI.2559-04.2004

Yu, J., Vodyanik, M.A., Smuga-Otto, K., Antosiewicz-Bourget, J., Frane, J.L., Tian, S., Nie, J., Jonsdottir, G.A., Ruotti, V., Stewart, R., Slukvin, I.I., Thomson, J.A., 2007. Induced pluripotent stem cell lines derived from human somatic cells. Science 318, 1917–1920. https://doi.org/10.1126/science.1151526

Yu, S., Zuo, X., Li, Y., Zhang, C., Zhou, M., Zhang, Y.A., Uéda, K., Chan, P., 2004. Inhibition of tyrosine hydroxylase expression in α-synuclein-transfected dopaminergic neuronal cells. Neuroscience Letters 367, 34–39. https://doi.org/10.1016/j.neulet.2004.05.118

Yusa, K., 2013. Seamless genome editing in human pluripotent stem cells using custom endonuclease–based gene targeting and the piggyBac transposon. Nature protocols 8, 2061. https://doi.org/10.1038/nprot.2013.126

Yusa, K., Zhou, L., Li, M.A., Bradley, A., Craig, N.L., 2011. A hyperactive piggyBac transposase for mammalian applications. Proceedings of the National Academy of Sciences 108, 1531–1536. https://doi.org/10.1073/pnas.1008322108

Zatloukal, K., Stumptner, C., Fuchsbichler, A., Heid, H., Schnoelzer, M., Kenner, L., Kleinert, R., Prinz, M., Aguzzi, A., Denk, H., 2002. p62 Is a Common Component of Cytoplasmic Inclusions in Protein Aggregation Diseases. The American Journal of Pathology 160, 255–263. https://doi.org/10.1016/S0002-9440(10)64369-6

Zeisel, A., Hochgerner, H., Lönnerberg, P., Johnsson, A., Memic, F., van der Zwan, J., Häring, M., Braun, E., Borm, L.E., La Manno, G., Codeluppi, S., Furlan, A., Lee, K., Skene, N., Harris, K.D., Hjerling-Leffler, J., Arenas, E., Ernfors, P., Marklund, U., Linnarsson, S., 2018. Molecular Architecture of the Mouse Nervous System. Cell 174, 999-1014.e22. https://doi.org/10.1016/j.cell.2018.06.021

Zhang, D., Wu, L., Chow, D.S.-L., Tam, V.H., Rios, D.R., 2016. Quantitative determination of dopamine in human plasma by a highly sensitive LC–MS/MS assay: Application in preterm neonates. Journal of Pharmaceutical and Biomedical Analysis 117, 227–231. https://doi.org/10.1016/j.jpba.2015.09.003

Zhang, J., Park, E.S., Park, H.-J., Yan, R., Grudniewska, M., Zhang, X., Oh, S., Yang, X., Baum, J., Mouradian, M.M., 2019. Apoptosis Signal Regulating Kinase 1 Deletion Mitigates the α-Synuclein Pre-formed Fibril Propagation Model in Mice. Neurobiology of Aging. https://doi.org/10.1016/j.neurobiolaging.2019.09.012

Zhang, Wei, Wang, T., Pei, Z., Miller, D.S., Wu, X., Block, M.L., Wilson, B., Zhang, Wanqin, Zhou, Y., Hong, J.-S., Zhang, J., 2005. Aggregated α-synuclein activates microglia: a process leading to disease progression in Parkinson's disease. The FASEB Journal 19, 533–542. https://doi.org/10.1096/fj.04-2751com